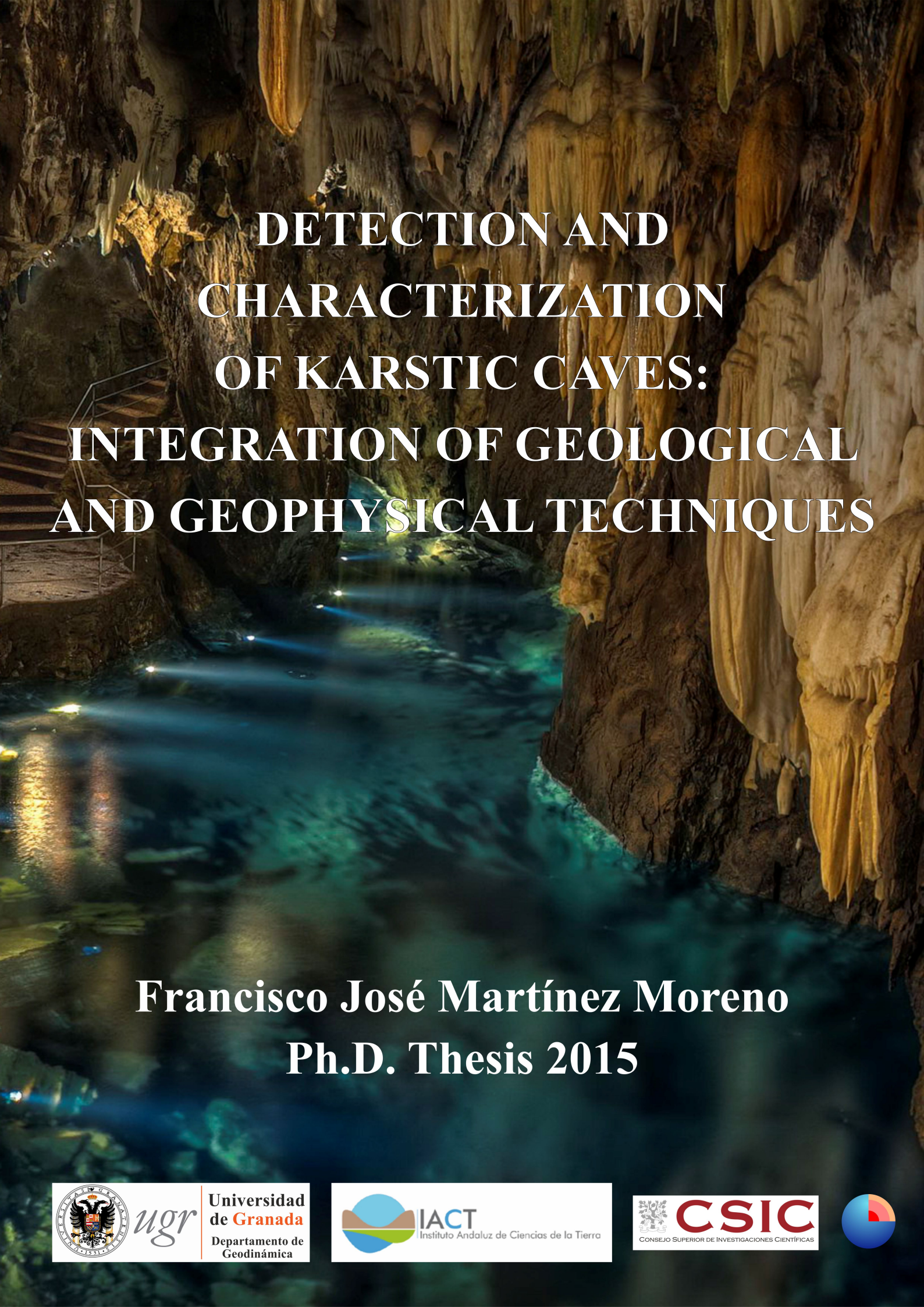

# DETECTION AND CHARACTERIZATION OF KARSTIC CAVES: INTEGRATION OF GEOLOGICAL AND GEOPHYSICAL TECHNIQUES

**Francisco José Martínez Moreno**

**Ph.D. Thesis 2015**

ugr Universidad de Granada Departamento de Geodinámica

IACT Instituto Andaluz de Ciencias de la Tierra

CSIC Consejo Superior de Investigaciones Científicas

Editorial: Universidad de Granada. Tesis Doctorales
Autor: Francisco José Martínez Moreno
ISBN: 978-84-9125-078-4
URI: http://hdl.handle.net/10481/40049

Departamento de Geodinámica

# DETECTION AND CHARACTERIZATION OF KARSTIC CAVES: INTEGRATION OF GEOLOGICAL AND GEOPHYSICAL TECHNIQUES

**Francisco José Martínez Moreno**

**Ph.D. Thesis 2015**

Departamento de Geodinámica – Universidad de Granada

Instituto Andaluz de Ciencias de la Tierra CSIC-UGR

Universidad de Granada
Departamento de Geodinámica

IACT Instituto Andaluz de Ciencias de la Tierra
CSIC Consejo Superior de Investigaciones Científicas

**Jesús Galindo Zaldívar**, Catedrático de Geodinámica Interna de la Universidad de Granada, y **Antonio Pedrera Parias**, Doctor en Ciencias Geológicas por la Universidad de Granada.

HACEN CONSTAR:

Que la presente tesis titulada "**Detection and characterization of karstic caves: Integration of geological and geophysical techniques**" ha sido realizada bajo nuestra dirección coordinada y cumple las condiciones suficientes para que su autor, **Francisco José Martínez Moreno**, opte al grado de Doctor en Ciencias Geológicas por la Universidad de Granada.

**Granada, Febrero de 2015**

**Vº Bº de los Directores**

**Fdo. Jesús Galindo Zaldívar** **Fdo. Antonio Pedrera Parias**

**Fdo. Francisco José Martínez Moreno**

El doctorando **Francisco José Martínez Moreno** y los directores de la tesis, Catedrático **Jesús Galindo Zaldívar** y Dr. **Antonio Pedrera Parias** garantizamos, al firmar esta tesis doctoral, que el trabajo ha sido realizado por el doctorando bajo la dirección de los directores de la tesis y hasta donde nuestro conocimiento alcanza, en la realización del trabajo, se han respetado los derechos de otros autores a ser citados, cuando se han utilizado sus resultados o publicaciones.

**Granada, Febrero de 2015**

**Directores de la Tesis**

**Fdo. Jesús Galindo Zaldívar** **Fdo. Antonio Pedrera Parias**

**Doctorando**

**Fdo. Francisco José Martínez Moreno**

*A mi familia*

*Para tener éxito,*

*no tienes que hacer cosas extraordinarias.*

*Haz cosas ordinarias, extraordinariamente bien.*

*(Jim Rohn, 1930-2009)*

**AGRADECIMIENTOS**

En estas líneas quiero expresar mi gratitud a todas aquellas personas que han contribuido en este trabajo. Sin su colaboración, ayuda y consejos no hubiera sido posible conseguirlo.

En primer lugar, quisiera destacar el papel fundamental desempeñado por mis directores, D. Jesús Galindo Zaldívar y D. Antonio Pedrera Parias. A Jesús le debo estar donde estoy. Desde el primer momento confió en mí y en la forma de desarrollar mi trabajo. Siempre me ha ofrecido oportunidades que han servido para conseguir finalizar esta tesis en poco tiempo. Gracias a sus ideas y largas conversaciones científicas, han salido la mayoría de trabajos que aquí se presentan. Sin olvidar su apoyo personal en esos momentos en que, a lo largo de mi etapa de doctorando, necesitaba para seguir adelante.

A Antonio quisiera agradecerle haberme introducido en el mundo de las cuevas. Durante mi época de estudiante de máster comencé con este tipo de estudios que se han mantenido hasta la actualidad. Por otro lado, sus rápidas y eficaces revisiones y sugerencias en todo este trabajo me han permitido trabajar de una forma más efectiva. Además, me ha transmitido su ánimo y consejos, lo cual ha facilitado todo mi trabajo.

Durante mi estancia a Lisboa conocí al que se convertiría en otro pilar fundamental para mi tesis, Fernando Monteiro. En los tres meses que pasé en la Universidad de Lisboa me enseñó, además de geofísica, que la ciencia es algo más y tiene muchas formas de verse y ejecutarse. Quisiera agradecer también la acogida que tuvieron todos los miembros del Departamento de Geofísica e Instituto Dom Luiz de la misma universidad.

A lo largo de la carrera encuentras a personas que llegan a convertirse en imprescindibles. En ese camino tuve la suerte de cruzarme con Lourdes, la cual me ha guiado hasta el final de esta tesis. Sus sabios consejos y recomendaciones para cada paso que daba, así como su colaboración y discusiones científicas sobre todo tipo de temas que

aquí se incluyen, han conseguido una mayor calidad en todo lo que aquí se expone. Formamos un gran equipo, el cual nunca debe separarse para lograr grandes cosas en un futuro cercano.

Durante las numerosas campañas de campo que he tenido que realizar para esta tesis, he contado con la colaboración de un gran equipo que me ha aportado ideas, conocimientos y planificación tanto en campo como en procesado de datos. Además, hemos pasado muy buenos momentos que nunca olvidaré.

A Teresa Teixidó y José Antonio Peña quisiera agradecerle todo su apoyo científico, ímpetu y efectividad a la hora de emprender nuevos proyectos científicos. A Patricia Ruano por su disponibilidad y ayuda para todo lo que la he necesitado. A Ana Ruiz, porque incluso estando en avanzado estado del embarazo, vino al campo a colaborar. A Sergio Martos por descubrir esas cuevas mediante sondeos en Estepa, lo que permitió lanzarme a este mundo de la geofísica en cuevas. A Carlos Marín por sus modelos con datos geofísicos que me han permitido tener una mejor visión de los resultados obtenidos. Antonio Azor me dio una clase magistral sobre geología en el Cerro del Castillo que me ayudó a iniciarme en el estudio de cuevas desde otros campos. José María Calaforra siempre ha estado dispuesto a colaborar conmigo en investigaciones sobre cavidades e hidrogeología. Gracias a eternas discusiones sobre los distintos orígenes de las cuevas he aprendido que existen múltiples opciones que deben ser demostradas. A Emilio Guirado por su colaboración en las investigaciones llevadas a cabo en las cuevas de Sorbas.

Las personas que voy a citar a continuación merecen un reconocimiento especial por mi parte. Wenceslao Martín impulsó el proyecto científico de Aracena, el cual es parte importante dentro de este trabajo. Me ha ofrecido oportunidades que siempre he valorado. Con Manolo López Chicano he mantenido largas conversaciones y discusiones científicas que me han hecho abrir la mente hacia otros campos. Espero poder seguir disfrutando de

estas conversaciones de aquí en adelante. Con Rafa Rodríguez Durán fue la primera persona con la que empecé a trabajar en Aracena, y hoy en día aunque está triunfando en otros ámbitos de la geología distintos al mío, sigo contando con su colaboración. Con él empezó todo, y con él he disfrutado el descubrimiento de las nuevas cavidades de la Gruta. Adela Hódar fue la segunda persona que colaboró conmigo en la misma investigación. Fue una campaña dura en la que tenía que 'dejarla expresarse' mientras disfrutábamos tomando las medidas de campo.

También quisiera agradecer a otras personas que, aunque no han estado directamente involucradas en este trabajo, de una forma u otra, son parte fundamental. A mis compañeros de becaría y amigos: Juampe, Inma, Idaira, Eduardo González, Irene, Pedro, Lara, Manuel, Ángel, Yasmina, Carlos, Julia, Enric, Eduardo Molina… A mis compañeros de máster con los que tan buenos y variados ratos pasamos juntos disfrutando de esas tardes de clase y cafetería. A Carlos Sanz y Ángel Carlos por ser tan buenos conmigo siempre. A Manolo Avilés por ayudarme en todo lo referente a GPS y por su santa paciencia. A Fernando Bohoyo por ayudarme a salir del agujero en el momento que más lo necesitaba. A mis compañeros de Lisboa, Ivo, Susana, Joana y Khalil, por su buena acogida y ayuda en las campañas de campo.

Ha habido muchas personas e instituciones que me han hecho posible que mis trabajos de campo se realizaran de una forma mucho más sencilla. El personal de la Gruta de las Maravillas siempre ha estado dispuesto a echarme una mano cada vez que lo necesitaba; y no han sido pocas. Quisiera destacar el trabajo y ayuda de Eva, Mari, Rocío y Eduardo, entre muchos otros que han aportado sus conocimientos para guiarme en mis investigaciones. Gracias también al Excmo. Ayuntamiento de Aracena por confiar en nosotros para realizar las campañas geofísicas del Cerro del Castillo y confirmar nuestros resultados con sondeos. A José por abrirme las puertas de la torre del Castillo para instalar la antena GPS. A Álvaro y su familia, del mesón San Ginés, por alimentarme tan bien en

mis largas estancias en Aracena. Gracias a la empresa Love the Frame, y en especial al productor Pedro Pablo Figueroa, por cederme la imagen que representa a este trabajo y que es imagen de portada. A Victor Ferrer por dejarme utilizar la fantástica imagen del capítulo de introducción, cuyo autor es él mismo y que correspondiente al libro 'Grandes Cuevas y Simas del Mediterráneo'. Al Paraje Natural Karst en Yesos de Sorbas por no poner impedimento en la realización de medidas geofísicas. A Francisco José Cabello, de la finca La Algaidilla, por colaborar siempre con nosotros y al Instituto Geológico y Minero de España.

A todo el personal del hospital de Traumatología - Virgen de las Nieves, en especial a los doctores Rafael Osuna y Juan Jesús Sánchez Munuera, a la enfermera Lola y la fisioterapeuta Mamen. También a la mutua Fremap por cuidar de mí.

Por último, y no por ello menos importante, quisiera agradecer a mi familia el apoyo recibido durante todos estos años. Ha sido un largo tiempo de mucho trabajo y ausencias en casa que han sabido comprender y apoyar. A mis padres, Mari Carmen y Teófilo, a mis hermanos y cuñados, Teo, Mari, Patri y Manu; a mis tíos Paqui y Carlos, y a mis primas, María y Paula. A mis amigos, los cuales he tenido abandonados durante algún tiempo por mi trabajo y siempre han estado ahí, en especial a Caro, Luis, Mari y Paco.

Este trabajo ha sido posible gracias a un contrato de investigación del proyecto P09-RNM-5388 de la Junta de Andalucía que me concedió a través del Instituto Andaluz de Ciencias de la Tierra-CSIC-UGR, a los medios materiales del grupo de investigación RNM-148 y del Departamento de Geodinámica de la Universidad de Granada, y a los proyectos CSD2006-00041, CGL-2008-03474-E/BTE, CGL2010-21048, P09-RNM-5388, RNM148, C-3726-00 y C-3727-00.

# ABSTRACT

The integration of geophysical and geological methods is a sound means of studying cavities that are not accessible from the surface. In this Ph.D. Thesis, cavities under different geological, size and depth conditions were studied to establish the suitability of different techniques for void detection and characterization. The Gruta de las Maravillas cave, located within pyrite-bearing marbles in the Cerro del Castillo hill (Aracena, SW Spain), was explored through a combination of techniques: microgravity, magnetic, electrical resistivity tomography (ERT), induced polarization (IP), seismic refraction and reflection, ground penetrating radar (GPR) and geological field mapping. The geophysical anomalies obtained for the known cave were extrapolated to other parts of the hill, revealing the presence of new cavities. In addition, the sensitivity of each geophysical method for detecting caves in metallic mineralized sectors was analysed. Regarding microgravity prospection, a detailed analysis of already available regional-residual anomaly separation methods was carried out. High resolution residual gravity maps were obtained by means of first order polynomial fitting. Meanwhile, the Algaidilla cave (Estepa, Southern Spain), partially saturated with salty water and enclosed in carbonates disconnected from the surface, was studied through microgravity, ERT and IP methods. Joint interpretation made it possible to derive the approximate morphology of the cavity. Finally, a combination of microgravity and ERT techniques in 3D array were applied over the shallow gypsum caves of Sorbas (Almería, SE Spain); the measurements repeated in time-lapse allow these geophysical methods to be tested in sectors having a low contrast in physical parameters. Application of the geophysical techniques in different contexts leads to the conclusion that microgravity and ray tracing coverage in seismic refraction are, in general, the most suitable methodologies for cave detection.

# RESUMEN

La combinación técnicas geofísicas e investigaciones geológicas es la mejor forma de estudiar cavidades que son inaccesibles desde el exterior. En este trabajo se ha realizado el estudio de cavidades que se encuentran bajo diferentes condiciones tanto geológicas, como de dimensión y profundidad para estimar la eficacia de los diferentes métodos en su detección y caracterización. La Gruta de las Maravillas, emplazada en mármoles con bandas de pirita en el Cerro del Castillo (Aracena, SO de España), ha sido estudiada mediante la combinación de microgravimetría, magnetometría, tomografía eléctrica de resistividad (ERT), polarización inducida (IP), sísmica de refracción y reflexión, georradar (GPR) y un estudio geológico detallado. Las anomalías obtenidas sobre la cavidad conocida se han extrapolado a otras zonas del cerro y se han descubierto nuevas cavidades. Además, se ha analizado cómo responde cada método a la presencia de huecos en condiciones de cavidad con mineralizaciones metálicas. En gravimetría, se ha realizado una revisión de los métodos de separación de anomalía regional y residual. El mejor método para obtener dicha separación es el ajuste polinomial de primer orden. La cueva de la Algaidilla (Estepa, sur de España), parcialmente saturada en agua salobre, formada en carbonatos, y desconectada del exterior, ha sido estudiada mediante la combinación de microgravimetría, ERT e IP, lo que ha permitido una interpretación conjunta de los resultados y la obtención de una morfología aproximada de la cavidad. Por último, se ha combinado microgravimetría y ERT en 3D en las superficiales cuevas de yeso de Sorbas (Almería, SE de España), con repetición de medidas separadas en el tiempo, para la detección de cavidades superficiales con menor contraste en sus parámetros físicos. La aplicación de métodos geofísicos en contextos geológicos diferentes ha permitido determinar que la microgravimetría y cobertura de rayos en sísmica de refracción son la mejor combinación de metodologías generales de trabajo para detección de cavidades.

# EXTENDED ABSTRACT

The study of karstic cavities has undergone substantial growth due to its high socio-economic and scientific value. In addition to attracting tourists and having economic potential, caves imply large reservoirs of water and may even serve for housing, wine cellars or food preservation. The study of caves that are accessible from the outside can be conducted in a direct way, using classical geodetic and geological techniques. However, there are many undiscovered cavities lacking direct access, and their study must be conducted indirectly.

Geophysical methods are presented as a suitable tool for new cavity detection. Still, each cave has different boundary conditions to be taken into account. Geological features such as lithology, bedding, foliation, dip, faults and joints, as well as the hydrogeological features, determine cave morphologies and therefore condition the interpretation of results when applying geophysical prospecting techniques.

In this Ph.D. Thesis, a combination of geophysical techniques was applied over cavities having different morphologies and geological settings. Included are caves hosted in marbles (Gruta de las Maravillas cave, Aracena, Southwest Spain), limestone (Algaidilla Cave, Estepa, Southern Spain), and gypsum (El Bosque cave, Sorbas, Southeast Spain). Diverse physical properties between the cavity and surrounding rock (density, resistivity, seismic wave velocity or dielectric contrast) are analysed to detect the presence of cavities. The response of the applied techniques varies due to the different boundary conditions: caves partially submerged in water (Gruta de las Maravillas and Algaidilla), metallic mineralized walls (Gruta de las Maravillas), or completely dry caves

(El Bosque). Another essential aspect is the depth and magnitude of the void, from small and shallow caves (Gruta de las Maravillas and El Bosque), to deep and large ones (Gruta de las Maravillas and Algaidilla).

By integrating various geophysical methods, more reliable results are ensured. Microgravity, magnetic, electrical methods (resistivity and induced polarization), seismic methods (refraction and reflection) and electromagnetic (Ground Penetrating Radar) were combined in this research. All the geophysical procedures were supported by high-precision geodetic techniques for the positioning and adjustment of field measurements.

This combination of geophysical methods was furthermore complemented by a detailed geological survey of the areas surrounding the cavity. Such data aids the interpretation of findings, so that they better fit reality.

The obtained results show that regional microgravity studies, performed at regular grid measurement spacing according to the expected size and depths of the studied cavity, may be used as a first approximation to locate and estimate sectors with a high probability of containing cavities. A comparison of the different methods for separating the Bouguer anomaly into regional and residual anomalies indicated that low-order polynomial fitting was most adequate for this purpose. Because gravity methods offer a non-unique solution for morphology, size and depth estimations, they must be complemented with other geophysical methods. Electrical resistivity tomography and velocity profiles in seismic refraction provide high resolution with accurate cave morphologies, which can be tested using direct gravity 2.5D models. Unlike electric, magnetic and GPR methods, microgravity and ray tracing coverage in seismic refraction methods are not restricted to the boundary conditions exclusively for cave detection. Time-lapse electrical tomography measurements served to reveal that variable soil humidity conditions increase the resistivity contrast between the unsaturated cavity and host rock.

By combining geophysical methods applied in different settings, the morphologies of unexplored cavities could be identified (Algaidilla cave and continuity of the Gruta de las Maravillas). The main features of the anomalies related to the cavities, according to each technique applied, may help detect unknown cavities under similar conditions. In sum, microgravity and ray tracing coverage in seismic refraction are the most reliable methods overall for cave detection.

# RESUMEN EXTENDIDO

El estudio de cavidades cársticas ha experimentado un alto crecimiento debido a su alto valor socioeconómico y científico. Las cavidades representan un alto potencial turístico y económico, así como un gran reservorio de agua y otros usos, tales como viviendas, bodega de vinos o conserva de alimentos. El estudio de cuevas que tienen acceso desde el exterior se puede abordar de una forma directa mediante técnicas geodésicas y geológicas clásicas. Sin embargo, existe un gran número de cavidades sin descubrir y sin acceso desde el exterior. El estudio de este tipo de cavidades se debe abordar de forma indirecta.

Los métodos geofísicos se presentan como una herramienta adecuada para la detección de nuevas cavidades. Sin embargo, cada cueva tiene condiciones de contorno diferentes que deben ser tenidas en cuenta. Los parámetros geológicos, tales como litología, foliación, estratificación, buzamiento, fallas, diaclasas así como las características hidrogeológicas van a determinar la morfología de las cavidades presentes y, por tanto, facilitará la interpretación de los resultados de prospección geofísica aplicados.

En este trabajo se realiza una combinación de varias técnicas geofísicas aplicadas a cavidades con morfologías y contextos geológicos diferentes. Se han investigado cuevas encajadas en mármoles (Gruta de las Maravillas, Aracena, suroeste de España), calizas (Cueva de la Algaidilla, Estepa, sur de España), y yesos (Cuevas de Sorbas, Sorbas, sureste de España). Las diferentes propiedades físicas entre cavidad y roca encajante (densidad, resistividad, velocidad de ondas sísmicas o contraste dieléctrico) son analizadas para detectar y determinar las cavidades presentes. Además, en las

cavidades estudiadas cambian la respuesta esperada en cada una de las técnicas aplicadas ya que tiene condiciones de contorno diferentes que incluyen: cuevas parcialmente sumergidas en agua (Cueva de la Algaidilla y Gruta de las Maravillas), con paredes tapizadas de mineralizaciones metálicas (Gruta de las Maravillas) y cuevas totalmente secas (Cuevas de Sorbas). Además también influyen las diferentes profundidades y tamaños, desde pequeñas y superficiales (Cuevas de Sorbas y Gruta de las Maravillas), hasta profundas y grandes (Cueva de la Algaidilla y Gruta de las Maravillas).

La integración de diferentes metodologías geofísicas permite obtener unos resultados más fiables. Se ha realizado una combinación de métodos microgravimétricos, magnéticos, eléctricos (resistividad y polarización inducida), sísmicos (refracción y reflexión) y electromagnéticos (Georradar). Todos estos métodos geofísicos han sido acompañados de métodos geodésicos de alta precisión para un buen posicionamiento y ajuste de las medidas de campo.

Esta combinación de métodos geofísicos ha sido acompañada de un detallado estudio geológico de las áreas circundantes a la cavidad. Estas observaciones geológicas han permitido interpretar los resultados de forma que se ajuste mejor a la realidad y ha conseguido subsanar la mayor parte de los errores de interpretación.

Los resultados obtenidos muestran que los estudios microgravimétricos regionales en malla regular, con un espaciado apropiado a las dimensiones y profundidades esperadas para la cavidad estudiada, son la primera aproximación para una buena localización y estimación de zonas con alta probabilidad de contener cavidades. Además, se ha realizado una comparativa de los diferentes métodos de separación de la anomalía de Bouguer en anomalía regional y residual, y se ha determinado que los mejores resultados se obtienen mediante ajuste polinomial de bajo orden. Debido a que

los métodos gravimétricos no ofrecen una solución única en la estimación de morfologías, tamaños y profundidades, estos deben ser combinados con otros métodos geofísicos. Los perfiles de tomografía eléctrica de resistividad y perfil de velocidades en sísmica de refracción ofrecen resultados que se aproximan a morfologías reales, que pueden ser comprobadas con modelos gravimétricos directos en 2.5D. Además, los métodos de cobertura de rayos en sísmica de refracción y microgravimetría no están tan restringidos a las condiciones de contorno de la cavidad para su detección, como sí lo están los métodos eléctricos, magnéticos o de georradar. Las medidas de tomografía eléctrica separadas en el tiempo revelan que la variación en las condiciones de humedad del suelo aumenta el contraste de resistividad entre la cueva insaturada y la roca encajante.

La mejor combinación de metodologías geofísicas aplicadas en las diferentes cuevas estudiadas ha permitido definir morfologías de cavidades desconocidas hasta ahora (Cueva de la Algaidilla y continuidad de la Gruta de las Maravillas). Además ayuda a caracterizar las anomalías asociadas a cavidades en las diferentes técnicas aplicadas, para poder detectar otras cavidades desconocidas en condiciones similares en el futuro. La combinación de métodos geofísicos en diferentes contextos geológicos ha permitido determinar que la microgravimetría y la cobertura de trazado de rayos en sísmica de refracción son la mejor metodología de trabajo para la detección de cavidades.

# TABLE OF CONTENTS

**Page**

## PART I

## PART II

# Part I

1. Introduction
2. Objectives
3. Geological, geodetical and geophysical methods
4. Outlines

# Chapter 1

## Introduction

A cave, cavity o cavern is defined as an underground hollow generally placed into the hill of a mountain region. The caves usually are formed by natural processes or artificially by anthropic action, in different contexts and origins, and they can be connected with the outside or remain disconnected. The speleology is the science of cave exploration studying all aspect of caves and the cave environment (Moore and Nicholas, 1967), although the action to visit or explore cave is also called caving, potholing or spelunking.

Caves have been used since ancient times as shelter or primary residence (Angelucci *et al.*, 2009). Nowadays caves have aroused great interest both from socioeconomic point of view as for scientific research, especially geological and biological researches.

As socioeconomic factor, the caves of tourist use represent a significant income generating employment in areas surrounding the cavities. Geotourism has experiment a rapidly development in the last two years (Garofano and Govoni, 2012), and the most significant segment is underground geotourism. The beauty in its formations and speleothems denote a significant attractive for uptake tourism. Furthermore, saturated caves are a natural water reservoir that can be used to supply the population. The water found in caves usually has high quality for direct consumption.

The study of caves is also important in the fields of civil engineering. Construction made over karst system with cave presence can have specific impact on subsidence by collapse. There are some examples of collapse produced in this kind of zones, both in carbonate rocks (Canakci, 2007; Murphy *et al.*, 2008; Martínez-Pagán *et al.*, 2013) and evaporites (Poupelloz and Toulemont, 1981; Cooper, 1986, 1995; Paukštys *et al.*, 1999; Cooper and Saunders, 2002; Alberto *et al.*, 2008). This fact remarks the importance of a detailed study over the area of interest previous the constructions start.

Moreover caves themselves has become a remarkable laboratory due to their biologic and geologic oddities that need to be explained (Culver and White, 2005). From the geological point of view there are numerous elements that must be studied. Sediments and speleothems register paleoclimatic and hydrologic changes in surrounding areas. The climatic conditions controlled the timing of speleothem growth, because the formation and growth rates of speleothems depend on the availability of water (Vaks *et al.*, 2003). Cave passages and morphologies are usually defined both by the geological structure and by the hydrogeology of the host rock. Active caves give direct insight about the aquifer hydrochemistry and hydrodynamic, allowing direct hydrogeology measurements. Dating techniques provide information relative to the evolutionary history of the geology (Bar-Matthews *et al.*, 1998), in addition to the evolution of the surface topography. Furthermore the study of secondary mineralogy deposited along the cavity also provides information about the cave formation and evolution.

From the biological standpoint caves are used as laboratory for ecology and evolutionary researches. There are numerous species that are only developed and conserved in caves (Yager, 1994), where occur unique air and/or water environment relative to the humidity, as well as constant temperature and luminosity. The main question that occupied the attention of biologist is investigate how the species have transformed themselves for lose their eyes and pigment to accommodate to these conditions.

Cave are also repositories for archaeologists and palaeontologists researchers. Within cavities have been found abundant archaeological remains and paintings over the cave walls that allow study lifestyle of the past. In addition, caves appear frequently in legends, mythology, folk tales and in the religions of many people. Caves always enclose an aura of mystery that is used from literature to cinema.

The geological process and context that explain caves formation are varied, and they can be explained by multitude of them. Relative to the process formation, caves are divided in two general groups: primary and secondary caves (Fig. 1.1). Primary caves are formed at the same time as the host rock where they are emplaced. To these caves belong the so-called volcanic caves, formed on the sides of volcanoes within streams of lava by a process called inflation or crusting over the channels. This process originates the caves known as Lava tubes. Lava flows down and the outer part solidified by cooling resulting in a solid crust. Internally the lava continues flowing until the channel is empty and results in tubes morphologies (Calvari and Pinkerton, 1998). These caves have conduit morphologies with widths of few meters and a length up to kilometres. Other caves formed through volcanic activity include blister caves, vents, rift caves, lava mold caves, open vertical conduit and inflationary caves. These caves are formed in volcanic areas such as Hawaii, Galapagos, Canaries (Cueva de los Verdes, Lanzarote; Fig. 1.2a) and Azores, among others (Waters *et al.*, 1990).

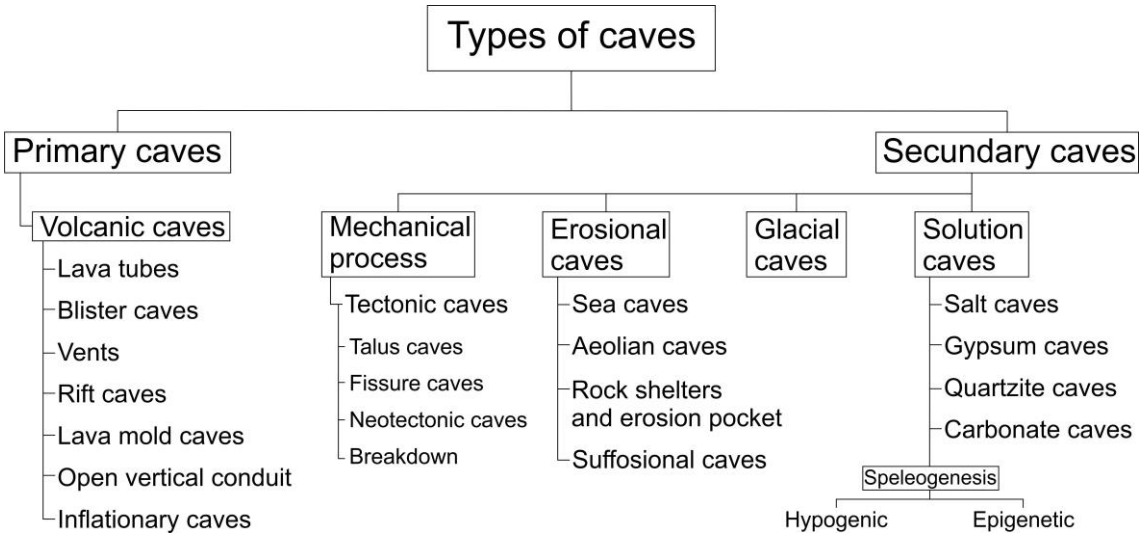


Figure 1.1: classification of the type of caves (Modified from Encyclopedia of caves, Culver and White, 2005)

Secondary caves are formed when the formation of the host rocks is already completed. The rock lithification is the primary stage, where the rock is formed without caves. The caves begging to form in a secondary stage. Secondary caves are linked to a wide range of formation processes: mechanical processes, erosional caves, glacial caves and solution caves.

Caves formed by mechanical process are those that bulk masses of rock are affected by faults or fractures and shifted leading to collapses. These collapses resulting in disordered rocks leaving connected void spaces formed between the rock masses and give rise to a subtype of caves called tectonic caves. They are formed in massive and hard rocks, resulting in small caves. The most common tectonic caves are Talus caves, which are formed by rock slides and collapses (Smith, 2007). Tiny Falls caves (Washington, Fig. 1.2b), Ice Caves Mountain, Polar Caves Park and Pinnacles National Monument, all of them located in USA., are some examples. Less common are the fissure caves which are also formed by rock slides, but in a different way (Goetz Höhle, Germany; Fig. 1.2c). Fissure caves are formed by mechanic widening of thin fissures in the rocks, forming narrow, high, long, and mostly triangular shaped crevices (Gale, 1984). Often there are several, not connected, parallel crevices. Sometimes they open downwards, sometimes upwards. But if they are open upwards, with no roof, they are not really caves, they are more like gorges.

The Neotectonic caves are related to fast isostatic adjustments like those occurred by recent glacial processes in Scandinavia (Sjöberg, 1986). Isostasy is the theory of the balance between the gravity, which tends to depress, and the buoyancy, which tends to raise the crust. These cavities are typical in Scandinavian countries. Examples of these types of caves are Torkulla Kyrka (Fig. 1.2d), Gillberga Gryt, and Bodagrottorna, in

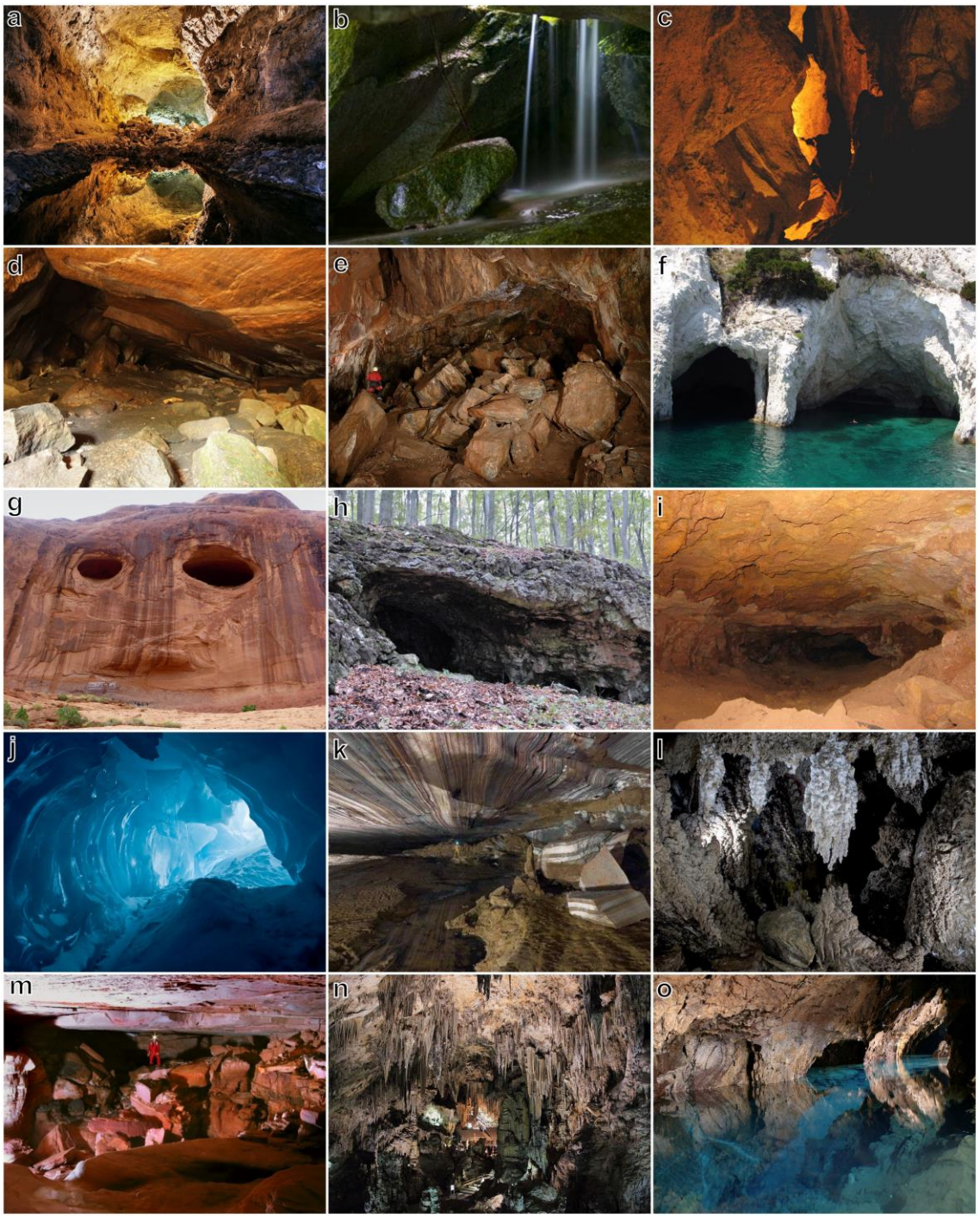


Figure 1.2: Examples of the types of caves. (a) Volcanic cave (Cueva de los Verdes, Lanzarote, Spain). (b) Talus cave (Tiny Falls caves, Washington, USA). (c) Fisure cave (Goetz Höhle, Germany). (d) Neotectonic cave (Torkulla Kyrka, Sweden). (e) Breakdown (Gruta de las Maravillas, Aracena, Spain). (f) Sea cave (Greek Isles). (g) Aeolian cave (Potash Road, Utah, USA). (h) Rock shelter (Little Carpathians, Slovak). (i) Suffosional cave Badlands National Monument, South Dakota, USA). (j) Glacial caves (Antarctica) (k) Salt cave (Qeshm Island, Persian Gulf, Iran). (l) Gypsum cave (Sorbas, Almería, Spain). (m) Silieous cave (Ojos de Cristal cave, Venezuela). (n) Caves in Limestone (Cuevas de Nerja, Málaga, Spain). (o) Caves in Marbles (Gruta de las Maravillas, Aracena, Spain).

Sweden. And finally there is a related process happening inside caves, which is thus generally interpreted as an aging process of caves. It is called breakdown and is the collapse of rock inside caves. It does not create new caves but may change existing caves substantially (Great Lake in Gruta de las Maravillas, Spain; Fig. 1.2e).

Erosion process define the category of erosional caves, which are formed by the action of water or wind, carrying abrasive particles capable of carving rock. These type of caves include sea caves, aeolian caves, rock shelter or erosion pocket, and suffosional caves. Sea caves are formed by the power of the ocean (or in some cases, lakes) attacking zones of weakness in coastal cliffs (Moore, 1954). The weak zone is usually a fault, or fractured zone formed during slippage. Another type of weak zone is formed where dissimilar types of rocks are interbedded and one is weaker than the other. Typically this weak zone is a dike, or intrusive vein of more easily eroded rock found within a stronger host rock. Yet a third instance is in sedimentary rocks where a layer of softer rock is interbedded between harder layers. These caves extend from a few meters to a few hundred meters into the sea cliff. Some examples are found in the Pacific coast of the USA, Greek Isles (Fig. 1.2f), British Isles and New Zealand.

Aeolian caves are formed by wind action (e.g. Potash Road, Utah, USA; Fig. 1.2g). They are common in desert areas where they are formed in massive sandstone cliffs. Wind sweeping around such a cavity erodes the walls, floor, and ceiling, resulting in a bottle-shaped chamber usually of greater diameter than the entrance. Aeolian caves are rarely longer than a few tens of metres.

A rock shelter is a shallow cave-like opening at the base of a bluff or cliff. These caves are produced by bedrock erosion in insoluble rocks. A common setting is where a resistant rock such as sandstone overlies shale or some other relatively weak rock. Surface weathering or stream action dresses away the shale, cutting it back into the hillside. The

sandstone is left behind as a roof to the rock shelter. Rock shelters are minor features as caves, and they not extend to total darkness, but many are used as refuge. Some examples of rock shelter are found in Little Carpathians (Slovak, Fig. 1.2h) or Connecticut (New York, USA).

Suffosional caves are formed by the sweep of fine-grained or poorly consolidated sediment by the storm waters action. Sediment flushed by storm water and produce small cavities in the loosely consolidated silts and clays. Some examples of these caves are located in the Badlands National Monument in western South Dakota (USA) (Fig. 1.2i), or Svyataya Cave, in Russia.

Other type of secondary caves is found into the glaciers, resulting in what is known as glacial or ices caves. The formation of this caves is the result of the water circulation through ice fissures into the glaciers. The circulating warmer water slowly defrost the ice and it is slightly carves out along tunnels that open at the front of the glaciers. Glacial caves are ice tunnels with floor, walls and ceiling of ice. Many examples of these kind of caves are found in Antarctica (Shackleton, 1911; Fig. 1.2j) and Alaska, USA (Peterson and McKenzie, 1968; Gulley, 2009).

The caves formation process more important are the solution caves. These form by chemical dissolution of the host rock by direct circulating groundwater. There are four main lithologies where solution caves are formed: salts, gypsum, quartzites and carbonates. Salt caves are easily form because is a very soluble material, but such caves are unusual because salt only survive in a few extremely arid region. The best example is found in Qeshm Island in the Persian Gulf (Iran; Fig. 1.2k).

Gypsum caves are preserved in arid regions. They are formed by direct rainwater dissolution of evaporite deposits of gypsums throughout stratification or fractures. The

landform originated is called as gypsum karst systems. The more significant examples of gypsum caves are Cave of Crystal (Naica, Mexico) or Sorbas Caves (Almeria, Spain; Fig. 1.2l).

Caves also can be developed in very low soluble lithologies as Quartzites and siliceous sandstones. These kind of caves are developed by two process, first where the silica cement can be removed by dissolution and the less soluble residual grains are then efficiently swept away by flowing waters. There are few examples of quartzite caves around the world, but have been documented some of them in South America (Ojos de Cristal cave, Venezuela; Fig. 1.2m).

The more widespread secondary cave systems are developed in carbonates by direct dissolution. These caves are settled in several lithologies as limestones, dolostones or marbles. Rock is dissolved by natural acid carbonate in groundwater that seep through bedding-planes, fault or joints. This dissolution process produces a distinctive landform known as karst, characterized by underground drainage systems with sinkholes, dolines, and caves. The acid carbonate precipitates in secondary minerals as calcite or aragonite, resulting in what is known as speleothems. The speleothems have a great variety of morphologies: stalactites, stalagmites, columns, soda straws, drapery, helectites, moonmilk, rimstone, shield, tower cones, shelfstones, flowstones, coralloids or frostworks are some of them. There are numerous caves developed in Limestones (Cuevas de Nerja, Spain (Fig. 1.2n); Grutas de Cacahuamilpa, Mexico), Dolostone (Castañar caves, Spain), and Marbles (Gruta de las Maravillas, Spain, Fig. 1.2o; Marble Arch Caves, Ireland).

The speleogenesis, which is the origin and development of the cave, can be divided mainly in two process: hypogenic and epigenetic. Epigenetic karst is formed by aggressive recharge descending from the land surface (Tennyson *et al.*, 2008). Hypogenic

karst is defined for two properties: predominance of the deep-seated sources of aggressiveness of karst water, independent of the environment at the overlying or immediately adjacent surface; and recharge of soluble formation from below, independent of recharge from overlying or immediately adjacent surface (Dublyansky, 2014).

The speleology combines multidisciplinary knowledge of geology, physics, chemistry, biology, meteorology and cartography. Caves open to the outside can be studied and explored in a direct way. But sometimes caves remain inaccessible or masked and they should be studied from the surface. For this purpose the development of geophysical methods applied to caves is a key issue.

Geophysical methods began to be applied in the investigation and evaluation of geotechnical problems related to voids, sinkholes or epikarst structures since the 1950s (Chalikakis, 2011). The first studies were carried out throughout electrical resistivity methods (Cook and Nostrand, 1954; Vincenz, 1968; Dutta *et al.*, 1970; Smith and Randazzo, 1975; Greenfield, 1979; Militzer *et al.*, 1979; Owen, 1983; Smith, 1986; Chamon and Dobereiner, 1988). Simultaneously, microgravity and gravity gradient techniques were other shallow methods applied for cave detection (Colley, 1963; Chico, 1964; Neumann, 1965; Arzi, 1975; Blížkovský, 1979; Butler 1984). Seismic methods were applied since 1960s to identify cavities (Cook 1965; Steeples *et al.*, 1986). Finally, electromagnetic methods started to be used from 1970s to detect caves (Kašpar and Pecen, 1975; Ballard *et al.*, 1982; Vogelsang, 1987).

From 1990s the use of geophysical methods applied to cave studies improved notably. Technological developments, simpler field procedures, lower costs and more rapid inversion and interpretation of data helped to promote new researches for cave detection. Although the use of a single geophysical method have been applied over

different geological context for cave detection, the use of a unique geophysical technique only provide information about one physic property of the underground. The use of combined geophysical methods is the more widespread procedure used in recent years. The integration of several methods provides information about different physical properties, it better highlights the presence of caves and avoids misinterpretation.

Numerous geophysical methods have been combined along the time: electrical resistivity tomography (ERT), induced polarization (IP), vertical electrical soundings (VES), mise-à-la-masse and Capacity-Coupled Geoelectrics (CCG) (for electrical methods). Electromagnetic (EM), Ground Penetrating Radar (GPR), Natural Potential (NP), Very Low Frequency (VLF), Gamma Ray (γ) and Time Domain Electromagnetic (TDEM) (as electromagnetic methods). Magnetic and magnetic resonance sounding (in magnetic methods). Gravity and microgravity (for gravity methods). Seismic refraction/reflection tomography (SRT), diffracted waves, Rayleigh waves and Seismic Wavefield (as seismic methods).

The firsts combinations of geophysical methods were in 1980s (McCann *et al.*, 1987; Chamon and Dobereiner, 1988). Later, have been combined two methods (Holub and Dumitrescu, 1994; Guérin and Benderitter, 1995; Gautam *et al.*, 2000; Beres *et al.*, 2001; McGrath *et al.*, 2002; Vouillamoz *et al.*, 2003; Gibson *et al.*, 2004; El Qady *et al.*, 2005; Leucci and Giorgi, 2005, 2010; Debeglia *et al.*, 2006; Carpenter and Ekberg, 2006; Leucci, 2006; Piscitelli *et al.*, 2007; Rădulescu *et al.*, 2007; Xia *et al.*, 2007; Cardarelli *et al.*, 2010; Keydar *et al.*, 2010; Valois *et al.*, 2010; Gambetta *et al.*, 2011; Gómez-Ortiz and Martín-Crespo, 2012; Vadillo *et al.*, 2012; Carrière *et al.*, 2013; Orlando, 2013; Giorgi and Leucci, 2014), three methods (Bozzo *et al.*, 1996; Lange, 1999; Cardarelli *et al.*, 2003; Thierry *et al.*, 2004; Ulugergerli and Akca, 2006; Mochales *et al.*, 2008), and four or more methods (Brown *et al.*, 2011; Guérin *et al.*, 2009).

The caves are developed in different geological context and present variables physical conditions: air-filled or water-filled cavities, different dimensions and depths or metallic mineralized caves, which can provoke changes in its detection for geophysical methods. It is necessary carry out combined geophysical methods in caves with different features and geological settings to define a guide for selecting the optimal geophysical tools.

# Chapter 2

## Objectives

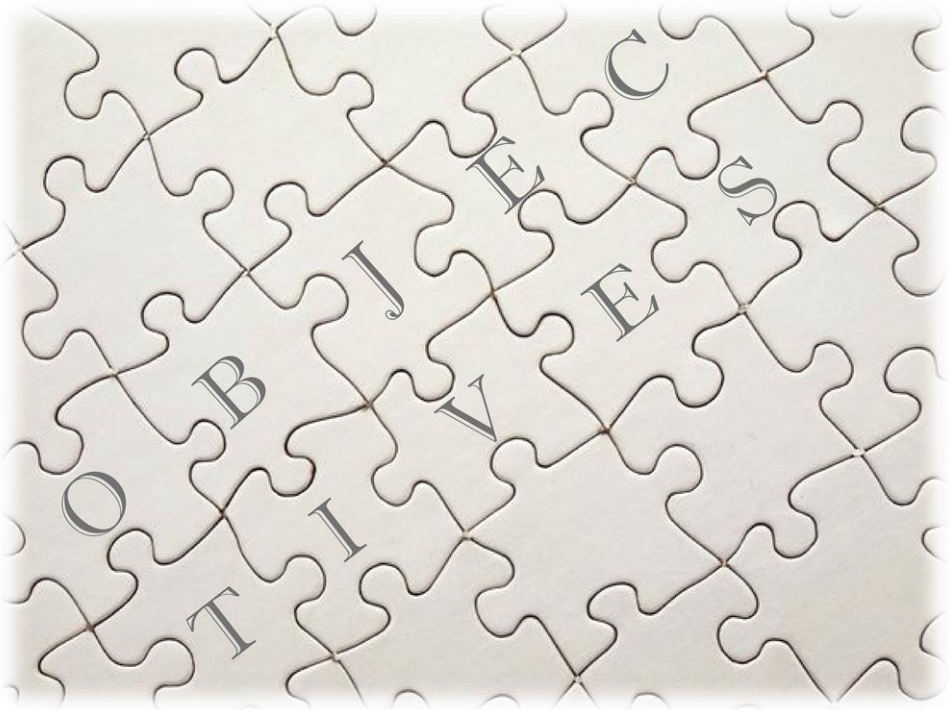

This Ph.D. Thesis aims to improve the knowledge about the detection and characterization of karstic caves with different features, formed in marbles, limestones, dolostones and gypsum, combining geophysical methods. In addition, the study of the Gruta de las Maravillas contributes to improve the knowledge on the origin of sulphur related caves. The study is focused in the next objectives:

1) Discussing the role of sulphur mineralization enclosed in carbonates during solution cave formation and cave evolution.

2) Combining several geophysical methods (gravity, magnetic, electrical resistivity and induced polarization tomography, refraction and reflection seismic tomography and ground penetrating radar supported by differential GPS) to determine the anomalies related to known caves enclosed in different geophysical settings.

3) Studying how the humidity variations influences the resolution of electric methods for cavity detection.

4) Discussing the best methods of regional-residual anomaly separation in microgravity researches related to cave studies.

5) Establishing the accuracy of each geophysical method on known caves and determining the geometry of unknown caves through joint interpretation and forwards models of these methods.

6) Proposing the most suitable succession of geophysical techniques according to the geological setting of each region to identify new cavities.

# Chapter 3

## Geological, geodetical and geophysical methods

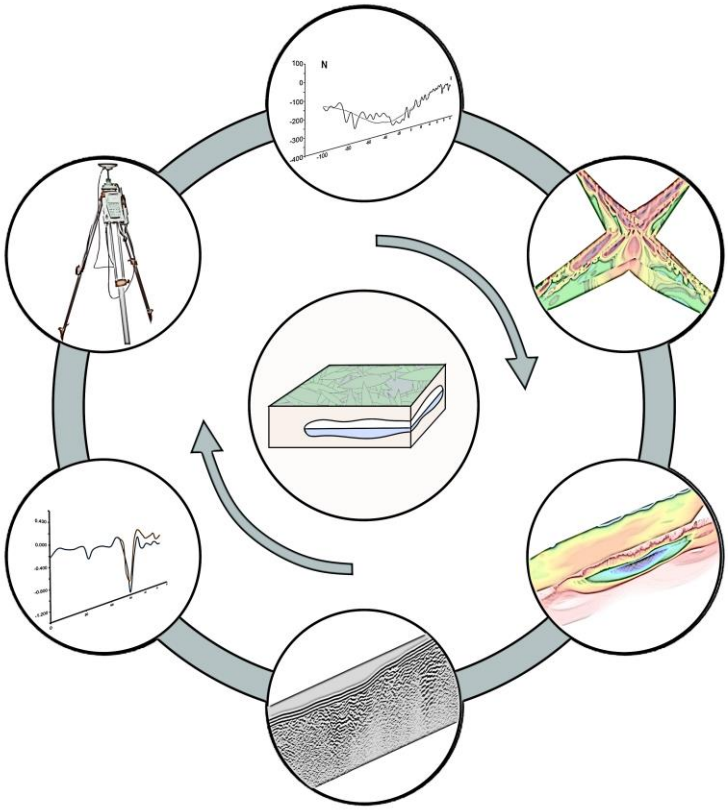

Integration of geological and geophysical methods becomes necessary to obtain optimal results in cave research. Characterization of cave morphology and properties constrained by geological data provides information about its development and increases the probability to identify unknown cavities. In addition, the interpretation of geophysical results compared with geological information is recommendable to avoid misinterpretation.

## 4.1 GEOLOGICAL METHODS

In order to characterize cave formation, morphology and their possible unknown continuity, a detailed geological research has been performed mainly in the study area of Aracena and Estepa. The MAGNA (1:50.000) geological maps, in combination with later geological studies developed in the region, constitute a valuable base for geological fieldwork. These maps allow the main lithologies and structures to be identified, in an initial step before the development of more detailed studies. These geological data have been fulfilled with detailed geological mapping of the regions nearby the studied caves providing a basic structural interpretation of the deep structure of each region.

Moreover, the study of microstructures has been revealed essential to understand the processes of development and evolution of caves because it determines the main rock anisotropies. The most accurate study of ductile and brittle deformation structures and bedding/foliation attitude measurements is carried out in the studied areas where the caves are located. As ductile structures, fold, shears zones and boudins are analysed to understand their role during cave formation. Moreover, the analysis of fractures, including faults and joints, are carried out. Faults and joints are scarce in recent rocks of the studied area, and their orientation (strike and dip, and fault kinematics) has been

considered in order to determine the paleostresses according to classical criteria (Hancock, 1985). The cave speleothems are taken into account to understand the hydrogeological conditions during its formation. In addition, the different lithologies have been studied in detail with petrographic analysis in microscopy.

## 4.2 GEODETICAL METHODS

### 4.2.1 Cave topography

The measurements of shallow morphologies opencast can be performed with numerous equipment supported by GPS (Global Positioning System) for their location. The measurement of cave topography and position respect to the surface should be completed in a different way and it cannot be supported by GPS system exclusively.

The method consists in obtaining the x, y, z position or stations within the cavity from a station with known coordinates located outside the cave using a GPS equipment for their location. From this station with known coordinates, distance, strike and dip to the next station is obtained. Thus are calculated coordinates x, y, z of the new station from the previous station, and the process can be repeated along the shaped cavity in consecutive measures determining singular points of the cave morphology. Furthermore, additional measures on each station (laterals and top) are obtained to define a more detailed morphology.

The formulas used (Albert Martinez i Rius, 1992) for calculating the positions of each station are:

| | |
|---|---|
| Horizontal distance between stations | $D_h = L*\cos(I)$ |
| Vertical distance between stations | $D_v = L*\text{sen}(I)$ |
| Absolute X position | $X = X_i\ D_h *\text{sen}(R)$ |
| Absolute Y position | $Y = Y_i\ D_h *\cos(R)$ |
| Absolute Z position | $Z = Z_i + D_v$ |

Where *L* is the distance measured between stations, *I* is the inclination and *R* is the trend. To calculate the final locations, the absolute positions of the previous station (Xi, Yi, Zi) are used.

For high accuracy in absolute coordinates, the measurements can be performed in loop, i.e. starts and ends at the same point, so that it gets a difference in the common measurement stations due to instrumental or operator errors. These measurement errors in X and Y positions are corrected by the following formulas:

$$\varepsilon x = \frac{Ex}{\sum_1^n Li}\ Li \tag{3.1}$$

Where $\varepsilon x$ is the variation in X, *Ex* is the difference in distance among common stations at the start and end of the loop. *Li*, is the relative distance among stations and $\sum_1^n Li$ is the total distance accumulated. For vertical distance correction, the next formula is applied:

$$tg\ d\ \beta i = \frac{Ez}{\sum_1^n Li \cos[\beta i]} \tag{3.2}$$

Where $tg\ d\ \beta i$ calculates the variation in Z, *Ez* is the vertical difference among common points at the start and end of the loop; $\beta i$ is the variation in degrees between stations and $\sum_1^n Li$ is the relative vertical difference between stations.

- *Equipment*

The measurements were performed with the distance meter laser Leica Disto A3 on tripod and target (Fig. 3.1). Through the laser device it obtains the distance between its position and the target, emplaced on the next measurement station. In addition, the device contains a digital inclinometer to measure the inclination in degrees between successive measurement points. A compass or meter direction has been incorporated into measuring equipment. This meter is able to measuring the trend between the measurement station and the target point.

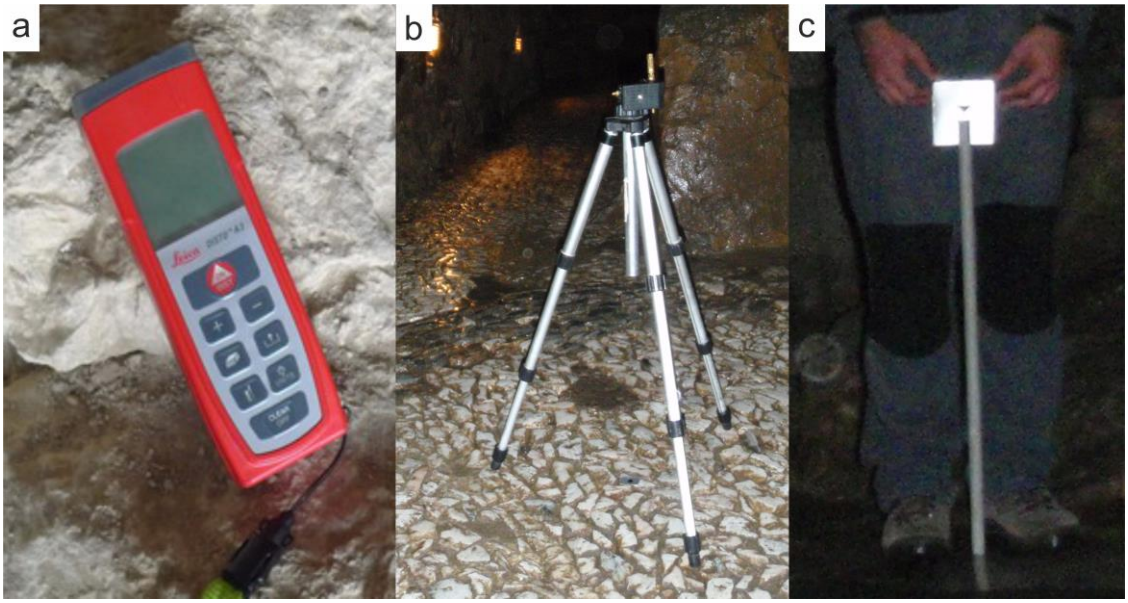


Figure 3.1: Equipment used for the caves topography. (a) Distance meter laser Leica Disto A3, (b) tripod on which equipment is supported and (c) target where laser is projected.

### 4.2.2 High precision positioning

The adjustment of microtopography by high-precision positioning measures is very important for the data processing carried out in this work. In very detailed studies, a height error of ± 1 m during survey data produced very different results in microgravimetry models and may lead to interpretation errors and mistakes during the analysis of results.

For this reason, particular attention has been paid to the measurement accuracy. In addition, it is necessary a great precision of the measured stations to apply other methods on the same stations with low margin of error. For this study we used the GPS Leica Differential 1200 and 1200 + equipment, and a Laser Level SP-30.

#### *4.2.2.1 Leica Differential GPS*

- *Basic fundaments of the method*

The Global Positioning System (GPS) is a method that allows the precise geographic location in different zones around the world. It comprises three different components (Fig. 3.2):

- Satellites: form a constellation of 24 satellites that circle Earth orbit, at a distance of 20.200 km. Although there are often 6 or 7 visible satellites, 4 is the minimum number of visible satellites above an elevation angle of 15º from any point on Earth's surface for 24 hours a day. Each satellite broadcasts a specific code that is decoded by the GPS pseudorange measurements and thereafter, calculates the position.
- Control segment: consists of monitoring stations on land and close to the equator. They are 5 in total, of which one is used as a master. Its function is to calibrate satellite at any instant to avoid any error.
- Users: is the signals reception from satellites by any user and received for GPS to determine position.

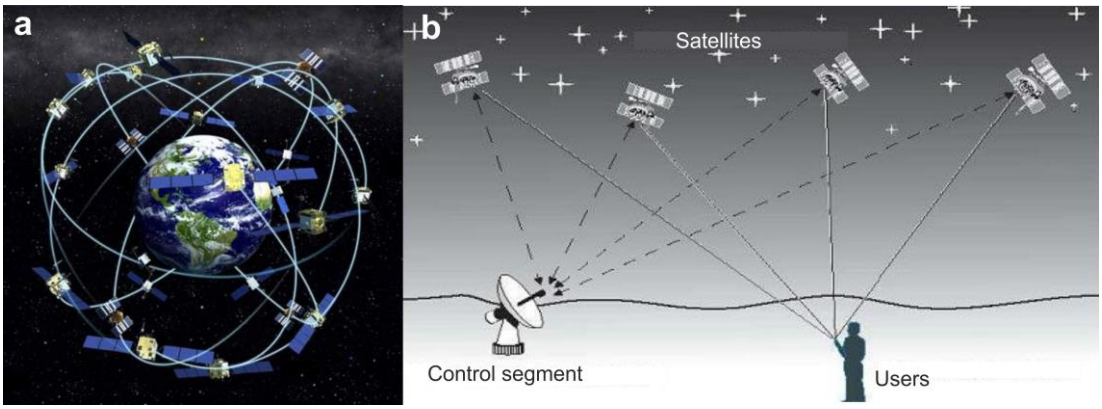


Figure 3.2: Global Positioning System (GPS). (a) Satellites present in the orbit of the Earth and (b) system components. Modified from U.S. Govt Source.

This system leads to a series of errors and corrections to consider, such as ionospheric and atmospheric delays, multipath effects, dilution of precision, selective availability and anti-spoofing. There are three methods to obtain a position using GPS. The choice of one method or another depends on the resolution that is required, and the type of study to be performed:

- Autonomous navigation: nearest from 5 to 100 m accuracy. In this method, one single receiver is used.
- Corrected Differential Positioning: accuracies of 0.5-5 m. Commonly used in coastal navigation, GIS data acquisition, automated farming, etc.
- Phase Differential Positioning: 0.5-20 mm accuracy is obtained. This method is applied on detailed studies.

The method used for this work is the phase differential positioning with high accuracy obtained in the data. Determining the GPS position is referenced to the geodetic coordinate system based on the geoid. The reason for the geoid reference is to get a more accurate position in X, Y coordinates, since due to the topographic irregularities, distortions occur during the measurement.

- *Equipment*

Measurements were made with two Differential GPS Leica 1200 equipments, with an accuracy of 0.5 to 20 mm. It is a method in which errors affecting the distance measurement satellites are eliminated or drastically reduced. It is a technique that requires extensive statistical analysis.

The equipment is composed by the following elements (Fig. 3.3):

- Reference Station (Leica System 1200): On a known point of reference, the receiver or base station is positioned. This receiver is able to estimate very accurately the distance to each satellite by the Andalusian Network Positioning (RAP, Junta de Andalucía, 2014). With this network, it define a geodetic reference frame only using 22 reference stations strategically located throughout Andalusia to ensure the same quality of whole region. Thus, the receiver calculates the difference between the calculated position and the measured position, and obtains corrections. Through radio antenna, the reference receiver transmits corrections to the rover.
- Rover (Leica System 1200+): Placed over station measurements. It has a radio data link for receiving the transmitted reference receiver correction. This receiver also calculates the distance to the satellites, and then applies the corrections obtained from the reference receiver. So much more accurate position (up to 10 mm) is obtained, and all errors are removed.

- *Acquisition and processing*

For stations arranged in profiles, the measures were taken directly. For data acquisition in regular grid, has been used the stakeout program, built into the operating


Figure 3.3: Differential GPS Leica 1200 and 1200+ equipment, respectively. (a) Reference Station fixed on a point that covers the whole study area. (b) Taking data into a measuring station with the rover GPS.

system of the equipment. This program allows from two points, create a baseline and an origin of coordinates in the workspace. These references help to create a data grid with uniform spacing. Furthermore, it allows any station measured previously in future research to be located.

Data processing has been done by the LEICA Geo Office program v.6.0 (Leica Geosystems AG) and Transformaciones Cartográficas v.9.2 software. The data are recorded in the memory card from GPS. These data are transmitted to a computer using the LEICA Geo Office software and a data file is obtained with geographical coordinates referred to the geoid. These coordinates are obtained in the ERTS89 system, and ellipsoidal height (referenced to the ellipsoid). Transformaciones Cartográficas software calculates the orthometric height (referenced to the topography) of the measures. These processed data obtain the X, Y, Z positions to fit the coordinate system used.

*4.2.2.2 Auto Laser Level*

- *Basics concepts of the method*

This method supports GPS data profiles. Along profiles, a precise GPS data is acquired at the beginning and at the end of the profile to obtain X and Y coordinates. The X and Y data is calculated over the measurement points equidistant along the profile with trigonometric calculation. The Z data is obtained with relative topographic changes with respect to a known base. Over this known base (usually placed outside and centered respect to the profile to cover a great area) the Auto Laser levelled on tripod is settled. The laser receptor (laser sight) may be placed consecutively over the different measurement stations to obtain the relative topography difference with respect to the base. This method provides topographic data with an error under a few of millimetres.

- *Equipment*

A laser SP-30 on tripod and a laser sight LC-2 (Fig. 3.4) constitutes the equipment. To obtain the base coordinates, the differential GPS Leica 1200+ has been used. The equipment comprises an automatic level with an invisible laser with rotary laser ray diode. It has a horizontal structure with a sweep of 300 revolution per minute and auto-off in case of unlevelled. The levelling ratio is ±0.17 mm with a transmitter laser and a receptor expandable to 120 m.

- *Acquisition and processing*

In profiles longer than 120 m or topography higher than the laser sight height, is necessary to displace the laser base. To do that, a new base is established. Some previous measures are repeated to correct the errors produced for the base change. The X and Y position is calculated with the coordinates from the beginning and the end of the profile throughout trigonometric determinations. Moreover, the Z coordinate is calculated with

the Z value obtained in the base and the relative changes respect to the base in the different measurement stations.

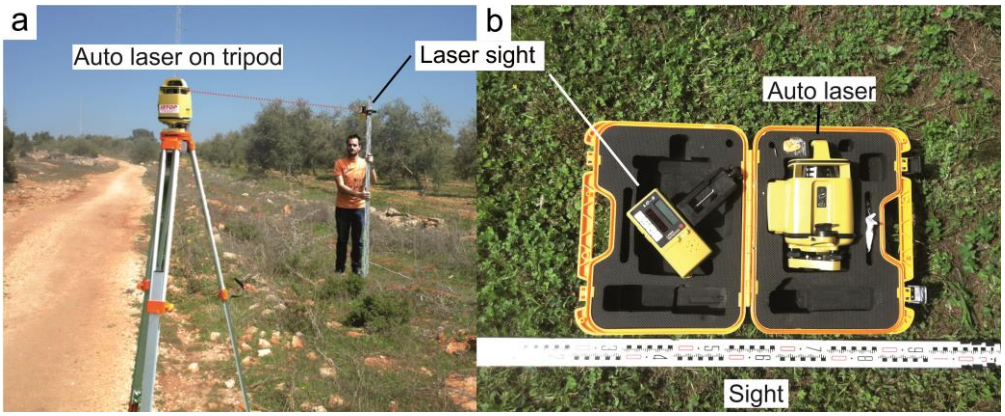


Figure 3.4: Laser level SP-30 equipment. (a) Laser level on tripod and laser sight during a field measure. (b) Detail of the equipment.

## 4.3 GEOPHYSICAL METHODS

Several geophysical techniques have been applied and combined in the different researches for the study of known and unknown cavities. The study of a known cave in the study areas, make possible understand how the new caves may be detected by the applied geophysical methods. For this purpose, firstly a regional study through microgravity has been performed, which indicate the area with high probability of contain caves. Secondly, other geophysical methods are applied over the area of interest to confirm the presence or not of a cave and to know the anomalies produced by the caves that are detected using each method.

### 4.3.1 Microgravity prospection

*- Basic fundaments of the method*

Gravity prospection is the geophysical technique that detects density variations of the subsurface materials. The density of a body is the mass referenced to the volume and is typically expressed in $g/cm^3$ or $kg/m^3$. Density contrasts are determined from the

difference between real and theoretical value of the gravity acceleration at each measurement point on the Earth's surface. These acceleration differences are called 'gravity anomalies'. The determination of the origin of these anomalies in an area is done by models that include simple geometries formed by a configuration of polygons with different density contrast compared to the homogeneous background. It is necessary to make several corrections to the measured values to remove the effects of temporal and spatial variation.

Temporal variations are produced as a result of the sun and moon attraction, and instrumental drift. To correct these variations, 'tide correction' is performed and the instrumental drift of the gravimeter is calculated too. Therefore, the measurements are performed in closed cycles. The real value used is called observed gravity ($g_{obs}$). Later, it is renamed as measured gravity ($g_{measured}$) when applied to the $g_{obs}$ corrections.

There are other factors affecting the gravity value as a result of the movement and the geometry of the Earth. These factors are:

- Latitude: the value of gravity increases progressively from the equator to the poles due to the decreasing of terrestrial radio and centrifugal force. The theoretical value of gravity at sea level depending on the latitude over the spheroid is determined by the formula proposed by the Geodetic Reference System (GRS, 1967).

$$g_{theor} = 978031{,}849\ (1+0{,}005278895\ \sin^2\varphi + 0{,}000023462\ \sin^4\varphi)\ (mGal) \qquad (3.3)$$

($\varphi$ = latitude expressed in degrees)

- Altitude and relief: The different height between sea level and the measurement point will condition the following corrections:

- Free Air correction ($C_{FA}$), which depends on the height (h) where the measured point is located, without considered the effect of the rocks below and using sea level as a reference level.

$$C_{FA} = + 0.3086\ h\ (mGal) \quad (3.4)$$

(h= height over sea level)

- Bouguer correction ($C_B$), eliminates the attraction occurs due to the presence of a flat layer between the topographic surface and the sea level. It takes into account the average mass density, generally considered as 2.67 g/cm$^3$.

$$C_B = - (0.04193\ \rho\ h)\ (mGal) \quad (3.5)$$

($\rho$ = average mass density measure in g/cm$^3$)

- Topography correction (TC), due to the influence of the topography around the point of measurement. Maximun gravity values are reached in flat topography areas.

The Free Air Anomaly ($g_{FA}$) is obtained from the differences between the theoretical and observed gravity values, and applied them the Free Air correction:

$$g_{FA} = g_{obs} + 0{,}3086\ h - g_{theor}\ (mGal) \quad (3.6)$$

If all gravity corrections are applied to the measured values and the theoretical value of gravity is subtracted, the Bouguer anomaly is obtained. This anomaly can include topographic correction ($g_{Bt}$). Nevertheless, sometimes, it can be calculated with no topographic correction ($g_B$). This anomaly is associated only to the density change underground, and allows anomalous bodies distribution to be established using models.

$$g_B = g_{obs} + (0.3086\ h) - (0.04193\ \rho\ h) - g_{theor}\ (mGal) \quad (3.7)$$

$$g_{Bt} = g_{obs} + (0.3086\ h) - (0.04193\ \rho\ h) + TC - g_{theor}\ (mGal) \quad (3.8)$$

- *Equipment*

Gravity measurements were acquired with a Scintrex CG-5 AutoGrav gravimeter on tripod (Fig. 3.5). The equipment has an accuracy up to 0.001 miliGals (mGal) and a standard deviation less than 0.005 mGal. It has an internal memory to storage the measurements, and built-in GPS for approximate positioning and precision in time and date of the measurements. It also incorporates an electronic level for a correct positioning of the equipment prior to measurements.

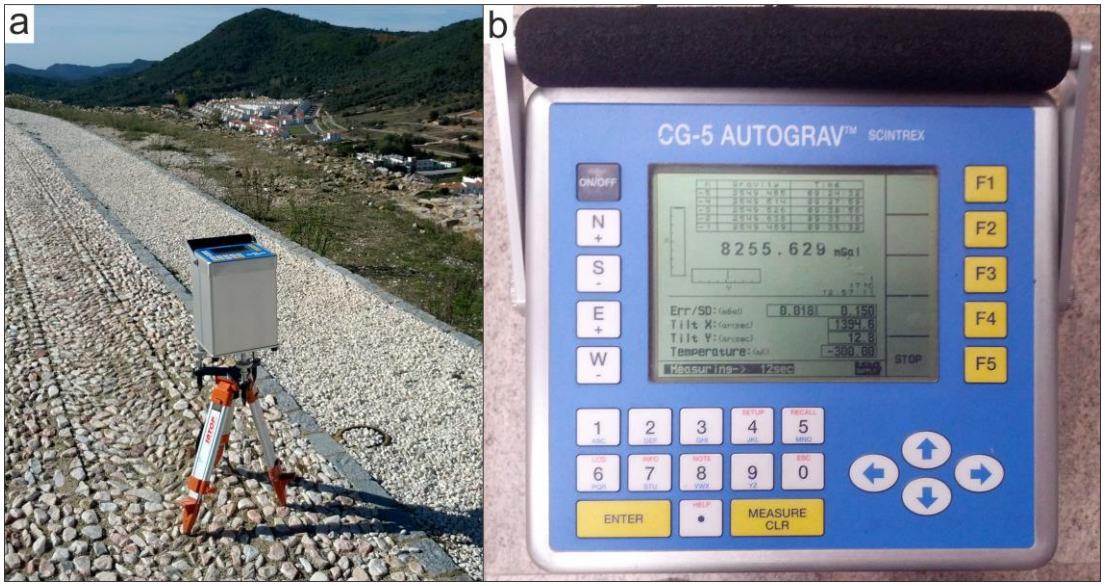


Figure 3.5: Equipment of gravity measurements acquisition Scintrex CG-5 Autograv. (a) Gravimeter on tripod over a measurement station. (b) Equipment during the acquisition of a measurement.

- *Processing and modelling*

For proper data acquisition in microgravity, it is necessary an equipment calibration steps prior measuring. In this case, the equipment has remained plugged in 48 hours prior to each measurement campaign to reach the correct temperature measurement. In addition, during the 12 hours before the start of the measures, the charge has been made on tripod with levelling equipment. This eliminates hysteresis errors in the measurement, i.e. errors due to distortion in the calibrated spring. Finally, at the base station the

equipment has remained levelled on tripod 15 minutes before start each cycle to avoid this problem.

The measures were acquired in cycles, starting and ending on a gravimetric basis. The gravimetric basis are stablished for each study area, and they are referred to the nearest gravimetric station of the Instituto Geográfico Nacional (IGN). The Bouguer anomaly was obtained by means of CICLOS and ANOMALIA programs developed by J. Galindo Zaldívar, and by Oasis Montaj from Geosoft Inc. Both programs calculate the instrumental drift correction firstly, in linear mode in function of the time difference between measurements. The difference in mGal between the measures taken on the basis at the beginning and the end of the cycle is distributed according to the time separation between the other measures of the cycle. Secondly, the Free Air and Bouguer anomaly are calculated by the above described formulas (4 and 5). The topography correction has been calculated using the Hammer circles method (Hammer 1939, 1982), through Gravmaster software v. 1.30d. For topographic correction it is used the digital elevation model (DEM) performed with flight LIDAR from Instituto Geográfico Nacional with a resolution of 5 m and the digital terrain model of Andalusia (Junta de Andalucía, 2005) with a resolution of 10 m. Moreover, this correction has been calculated with Oasis Montaj software to compare both calculations, obtaining similar results.

The Bouguer anomaly is the sum of the local attractions of shallow bodies (surface noise) in geological depth range of interest ones (responsible for the residual anomaly), and regional attractions due to the presence of deep bodies and far reliefs (producing the regional anomaly). Therefore, to obtain the residual anomaly is necessary to subtract from Bouguer anomaly the surface noise and the contribution of the regional anomaly before modelling the geological bodies of interest. The residual anomaly is calculated through the polynomial calculation of first order (both profiles and maps), which calculates

regional anomaly from Bouguer anomaly. With the subtraction of regional data from Bouguer data is obtained the residual anomaly. This anomaly is used for data interpretation and forward modelling of caves and geological structures.

The forward models were calculated in 2.5D profiles with Gravmag v.1.7 software, from British Geological Survey (Pedley *et al*., 1993). This software allows assigning a perpendicular length to the profile to each modelled polygon to develop 2.5D models. To create the forward models, the available geological and geophysical information have been taken into account, as well as density of the rocks obtained from previous researches (in the cases where was posible) or calculated for this specific study on several samples of the study area through the method of double weight. This method is applied with the following formula:

$$\rho = \frac{W_{dry}}{W_{ds} - W_{aw}} \tag{3.9}$$

Where $W_{dry}$ is the weight of the sample in dry conditions; $W_{aw}$ is the apparent weight, when the rock is weighed submerged in water; and $W_{ds}$ is the weight of the sample with dried surface after removing of the water.

### 4.3.2 Magnetic prospection

*- Basics fundaments of the method*

Earth's magnetic field is shaped similar to that produced by a magnet geocentric slightly inclined to the axis of rotation. It is mainly due to internal causes associated with the friction produced as a result of the movement of the inner core and on the internal convection cells generated in the liquid outer core whose main components, Fe and Ni, are excellent conductors. The overall intensity of Earth's magnetic field is approximately

30,000 nT at the equator and 60,000 nT at the poles. Internal changes are predictable and are characterized by the International Geomagnetic Reference Field (IGRF) calculated from magnetic observatories distributed over the World.

External causes, mainly the influence of the sun and moon, produced 3% of Earth's Magnetic Field . Diurnal variations thereof, associated with this factor as a result of the rotation of the Earth on its axis, are important from the standpoint of magnetic exploration. They are characterized by continuous recording observatories. In addition, other external causes disturb the magnetic field as the aurora borealis, magnetic storms and agitations. The magnetic survey is based on the analysis of magnetic anomalies due to the local distortion of the geomagnetic field by the presence of rocks with a magnetization that differs from the host rock. The two magnetic properties that determine these anomalies are the remnant magnetism and induced magnetization. The relationship between these magnetisms is established by Koenigsberger ratio. These anomalies are mainly caused by the presence in the subsoil of bodies containing magnetite or other ferromagnetic minerals. The shape of the anomalies depends on the intensity of the total field and inclination of the field in addition to other features related to the anomalous bodies like: the position, size, shape and nature and their remnant magnetism and the magnetic susceptibility. Magnetic techniques utilized in this research analyse the variations of the total magnetic field strength.

- *Equipment*

For measuring the total magnetic field intensity has been used a magnetometer GSM - 9 proton precession magnetometer with a maximum precision of 1 nT (Fig. 3.6). Direct measurements of the magnetic susceptibility of the exposed rocks were performed with a susceptometer Exploranium kappameter KT-9.


Figure 3.6: Magnetic equipments. (a) GSM - 9 standard proton precession magnetometer. (b) Susceptometer Exploranium kappameter KT-9. (c) Acquisition of a magnetic measure in the field.

- *Acquisition and processing*

The profiles have been measured in N-S direction to cross orthogonally the anomaly dipoles and the position of the measurement stations were taken with differential GPS. The data processing is carried out as follows: first are removed the diurnal variations from intensity data measured total magnetic field station of San Fernando (Cádiz) located at the Royal Observatory Navy. These data can be obtained from the Web site of Intermagnet (www.intermagnet.org). The residue of diurnal variations is removed by comparing the values obtained from periodic returns to a measurement base. The magnetic anomaly has been calculated substracting the value of IGRF 2010 (IAGA, 2010). For the anomaly calculation have been used, as in gravity, CICLOS and ANOMALIA Fortran programs from J. Galindo Zaldivar. The data positioning in profiles has been obtained by PERFIL program from the same author.

### 4.3.3 Electrical tomography

- *Basic fundaments of the method*

When electric current is introduced into the ground, it can spread in three different ways through the ground: dielectric conduction (associated with very low conductive or insulating materials), electronic conduction (associated with materials with free electrons, such as metals) and electrolytic conduction (associated with the motion of the ions present in the interstitial fluid terrain).

Electrolytic conduction is the most important mode of propagation, and in which are based the resistivity methods. This magnitude determines the difficulty of the electric current passing through a material independently of its shape. In a homogeneous isotropic half space of resistivity '$\rho$' subjected to a current '$I$', the potential value '$V$' from a point at a distance '$r$' with respect to a single electrode is:

$$V = \frac{I\rho}{2\pi r} \tag{3.10}$$

To introduce electric current in the ground, four electrodes are used conventionally: an electric field of direct current through two current electrodes (A, B) connected to a milliampere meter; and two electrodes (M, N) connected to a millivoltimeter. With this device, the difference in electrical potential ΔV is measured between points M and N and the current intensity between A and B, measures from which can be calculated the value of apparent or theoretical resistivity.

For a common electrode arrangement, the potential measured by the measurement electrodes M and N is:

$$V_M = \frac{I\rho}{2\pi}\left[\frac{1}{AM} - \frac{1}{BM}\right]; V_N = \frac{I\rho}{2\pi}\left[\frac{1}{AN} - \frac{1}{BN}\right] \tag{3.11}$$

And the potential difference $\Delta V_{MN}$ between both electrodes is:

$$\Delta V_{MN} = \frac{I\rho}{2\pi}\left[\frac{1}{AM} - \frac{1}{BM} - \frac{1}{AN} + \frac{1}{BN}\right] \tag{3.12}$$

If ρ is cleared, the value of the resistivity to the midpoint of the device is obtained. Within heterogeneous semispace or comprising for different layers, on each measure is obtained an intermediate resistivity called apparent resistivity $\rho_a$:

$$\rho_a = R \cdot K \tag{3.13}$$

Where $\rho_a$ is measured in Ohms per meter (ohm.m). R is a resistance term gave by R = ΔV/I. The term K is the "geometric factor" or "electrode array" and depend on the distance between the electrodes and the selected device. I in amperes and V in volts

$$K = \frac{2\pi}{\left[\frac{1}{AM} - \frac{1}{BM} - \frac{1}{AN} + \frac{1}{BN}\right]} \tag{3.14}$$

The resistivity calculated by the expression (3.13) corresponds to the apparent resistivity of the ground and is not the real resistivity. This is because the ground is usually composed of different materials, so that the electric field introduced into the ground affects simultaneously various layers, so that the measured resistivity corresponds to an intermediate value of all of them. The measured value of resistivity coincide with the real resistivity only in homogeneous soils or very shallow depths of investigation. From measurements of apparent resistivity, the real resistivity of different materials is obtained by the inversion process. For this purpose the data matrix called Jacobian matrix is used. Through an iterative process, it seeks the real resistivity model which best fit the model of apparent resistivity measurements in the field.

The induced polarization (IP) phenomenon is produced by electrolytic conduction in which a time delay is recorded to establish a charge balance. This polarization or relaxation time (to remove the potential difference) is measurable instrumentally. The time constant associated with this process allows the presence of bodies with metallic conductivity to be inferred (some metallic minerals and graphite) or clays. Once

established the ions flow, the aqueous medium sinuosity induce the generation of polarized barriers with opposite charges. The measurement is performed simultaneously with the resistivity measurements.

The aim of this method, when operating in 2D mode, is based on obtaining an underground section of real resistivities and induced polarization. For this purpose is necessary, after data acquisition, the use of inversion programs to transform the apparent resistivities obtained in the field, to real values of resistivity and induced polarization.

- *Measurement arrays*

There are different measuring arrays used in electrical tomography. They can be divided into two groups in function of the electrode disposition: symmetric and asymmetric arrays. In the symmetrical electrode array AB and MN (current and voltage, respectively) lie on a straight line so that the potential electrodes MN are placed symmetrically relative to the centre. In asymmetric electrode array such arrangement shall be disregarded and also requires forward and reverse current injections to avoid distortions.

The asymmetric arrays group include pole-pole, pole-dipole and dipole-dipole. These devices offer greater penetration into a smaller space but distort the morphology of the registered bodies. This array is optimal to detect underground flat layers. Moreover, remote electrodes are necessary and they should be positioned away from the profile. Among the symmetrical arrays it found Wenner, Schlumberger and Wenner-Schlumberger (Fig. 3.7). These arrays provide less penetration, but the morphology of the bodies that records present lower distortion and the field measurement becomes easier due to the remote electrode is avoided.

The Wenner α method consists in varying the spacing between the electrodes and they maintain the condition of equal distance between AM - MN - NB. In the Schlumberger method just electrodes A and B are extended, and maintain a constant spacing between the electrodes MN. Mixed array, Wenner-Schlumberger, is a combination of both.

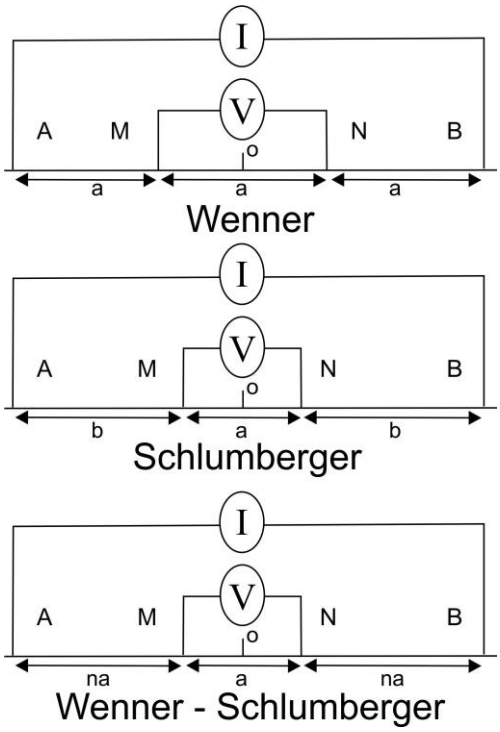


Figure 3.7: Sketch of symmetric arrays used in electrical tomography.

The development of electrical tomography techniques has allowed the design of new measuring arrays based on four channels equipment. These devices are capable of recording 4 measurements of potential difference in one current injection. The arrays applied is the gradient array, which uses an ‘alfa’ type electrode arrangement where the potential electrodes are between the current ones (ABEM, 2006; Loke, 2014). The field measurement order by the different electrodes arranged along the profile (forming for 81 electrodes) is called protocol. A measurement protocol in electrical tomography is the programming and command definition measured by electrode (Fig. 3.8). For this work it has used the protocol "4-channel multiple gradient" that takes the measures in two cycles

called GRAD4LX8 and GRAD4S8. This combination of protocols offers a resolution greater than the Wenner and Schlumberger method. The four measurement channels increase the data acquisition rate, which is faster than single channel equipment. This protocol begins with a long cycle (GRAD4LX8) and at the end of this, the measurement is performed with a short cycle (GRAD4S8). In the long cycle steps, the measurements are conducted between the electrodes of four cables, and in the short cycle only the two central cables are used.

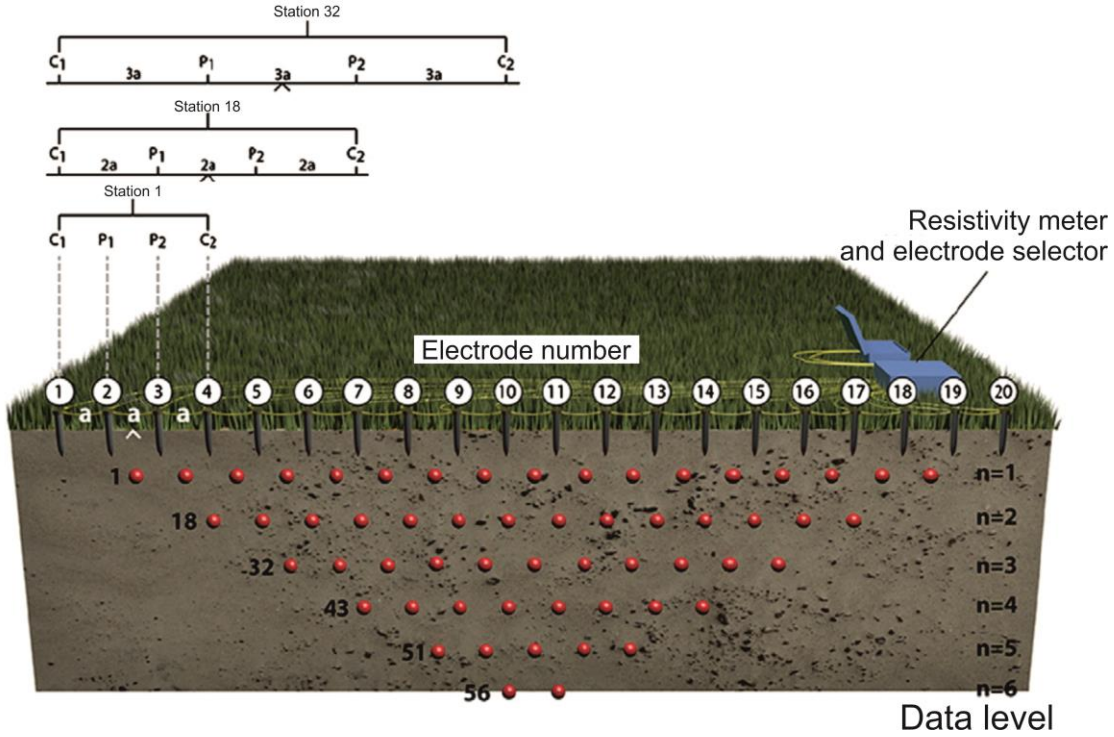


Figure 3.8: Schematic diagram of tomography data acquisition. Protocol example scheduled from station 1 to 32. Modified from Loke 2013.

- *Equipment*

To perform the measurements was used the resistivity meter Terrameter SAS 4000 which has a resolution of 1 μV (theoretical, 1 second integration time), three automatic measurement ranges (± 250 mV, ± 10 V and ± 400 V) and accuracy and security greater than 1% in the entire temperature range. It also has four measurement channels, that is,

in one emission current performs four measures at a time. This method reduces measurement time relative to other equipments with a single channel, and gets a larger amount of data.

The equipment consists of a central unit containing a central computer to store, programming and broadcasting data from the microcomputer inserted into the equipment, a power supply battery and an electrode selector ES10-64C (Fig. 3.9). It has also used the LUND cable system consists of 4 cables of 100 m long each with a maximum output current spacing of 5 m and 21 takeouts, 81 steel electrodes and connectors to send and receive electrical currents in the terrain. The current consists of pulses of opposite polarity with a maximum current of 1-ampere waiting periods separated by 7 seconds.


Figure 3.9: Electrical resistivity tomography equipment: (a) Terrameter SAS 4000, (b) electrode selector ES10-64C and ($b_1$ y $b_2$) cable connectors, (c) cable and ($c_1$) connectors between cables, (d) steel electrodes, (e) connectors cable-electrode and (f) battery supply.

- *Acquisition and processing*

The data acquisition is performed along profiles of different length. For each profile, four cables are deployed, which generate three intersections between cables. The

electrode spacing defines the penetration depth, so that for every meter of interspace between electrodes is reached a depth of approximately ~14 meters.

The protocols used to measure profiles are GRAD4S8 and GRAD4LX8, designed by ABEM Company. Both protocols were measured at each cables intersection. Usually six protocols are measured in 3 seasons for a profile with 4 cables, and obtained over 1100 data points. The roll-a-long technique consist in connect the back cable to the front one, so that it possible obtain long profiles. Data acquisition is programmed and recorded into the equipment previously, so that successive measurements are made. If the results of the first two measures match, the equipment moves to the next electrodes combination. If no match would be made up to 4 measures with 1 second delay and the median of the measurements are used, i.e. those data farthest are discarded.

Once collected, the data are transmitted from the microcomputer equipment to a computer where the data is converted into a text file with inversion programs format. Within the text file, the topographic data of each electrode measured with GPS are manually introduced at each electrode position. The data inversion processing is performed with RES2DINV v.3.59 and RES3DINV V.2.16 softwares from Geotomo Software, for resistivity and induced polarization data in 2D and 3D array respectively. It is an inversion program that calculates the real resistivities from the pseudosection of apparent measured resistivity. The program uses the least squares method and finite differences. In this way, real resistivity and induced polarization models are obtained to fit the apparent resistivity and induced polarization measured in the field.

The steps followed during processing and modelling of electrical data (Loke, 2014) are:

- *Data Filtering*: It is performed in two steps. The first of them is to remove anomalous data that do not conform to their environment (Fig. 3.10a). The second step is to make a data inversion with default inversion parameters of the program. Later, a statistical analysis of the results is made in which the data are displayed in a bar chart with the number of data and the error percentage (Fig. 3.10b). For this filtering those data with an error higher than 60-80% are removed. Once filtered data, a new data file is generated only with those apparent resistivities and IP measures that have not affected by large measurement errors.

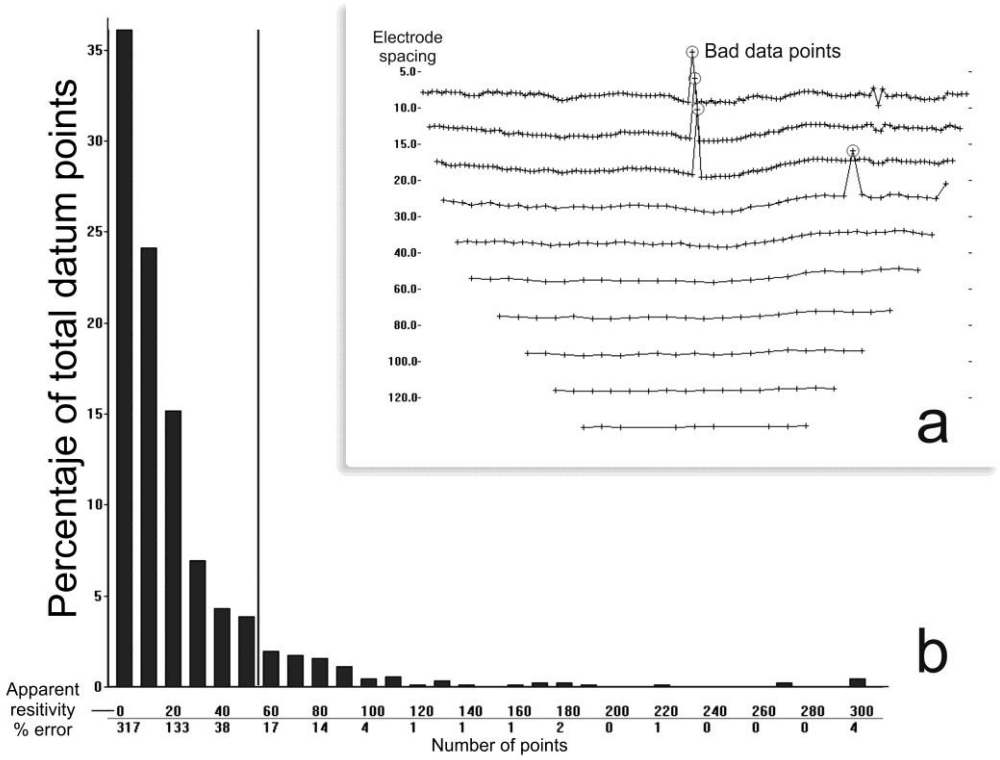


Figure 3.10: Data filtering. (a) Exterminate bad datum points. (b) RMS error statistic, eliminating data with high error rate (vertical thin line).

- Inversion parameters: the success or failure of the results depends largely on the inversion parameters chosen before the calculation of real resistivities. The parameters selected are:

- Block model: a model in increasing depth is used. Furthermore, the large amount of data obtained allows a refined model which divides the space to the half-cell of electrode spacing (Fig. 3.11).
- Inversion method: smoothed, which provides more realistic and fitted morphologies.
- Direct type model: finite difference with trapezoidal element.
- Four nodes per unit electrode spacing.
- Topographic model: grid finite element uniformly distorted for smooth topographies and SC transformation (Schwartz-Christoffel) for rouged ones, since it is the method that produces a more natural aspect in the block model if exist a large curvature on the topographic model.

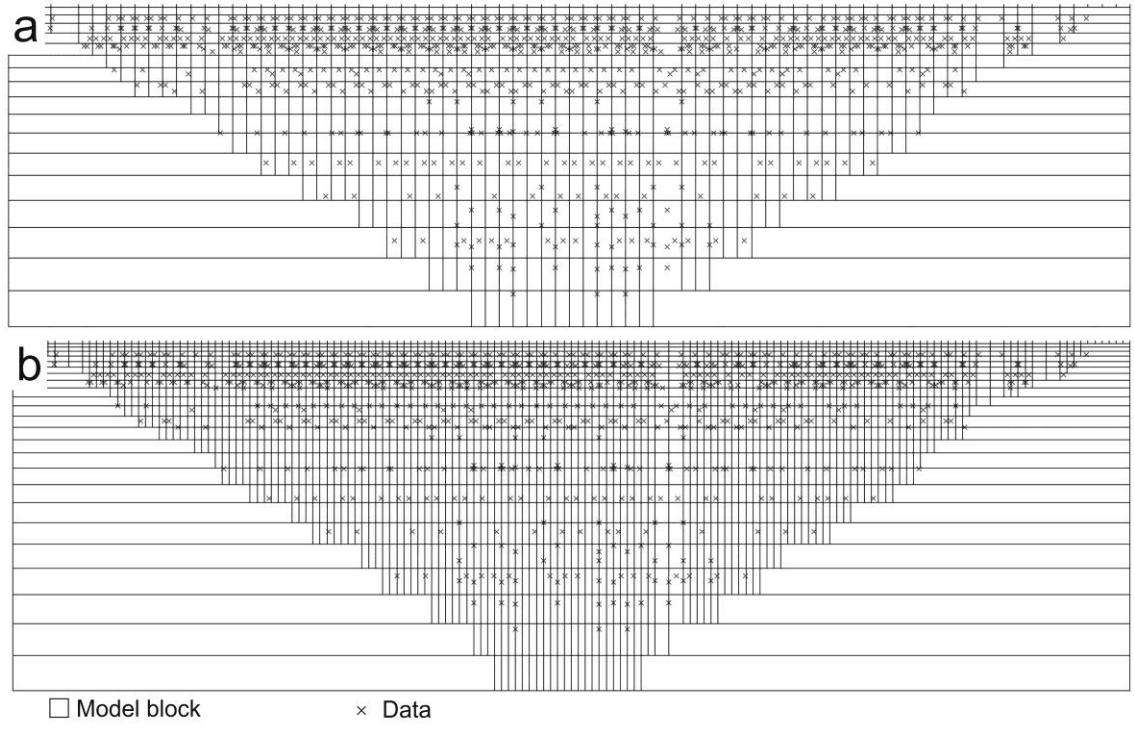


Figure 3.11: Selection of a fitted model blocks. (a) Model blocks where the width of the model cells is the same as the unit electrode spacing. (b) Model block where the width of the cells is half the unit electrode spacing.

After setting the parameters, the inversion model is obtained. The error model obtained through iterations must be less than 10% so that the results are acceptable. The results are exported to x, z, d data file (distance, depth and resistivity or IP) to display the data results. For this purpose, Surfer v.12 and Voxler v.3.3 softwares from Golden Software are used.

- *Normalized depth of investigation index (DOI)*

To ensure that the calculated resistivity profile is real up to the depth indicated, it is necessary calculate the empirical depth of investigation (DOI) index. This method was introduced by Oldenburg and Li (1999) and modified by Marescot *et al*. (2003). To determine the DOI it is necessary to carry out, at least, two inversions of the data using different resistivity backgrounds. The second reference model should be obtained from an initial resistivity background 10 to 100 times higher than the first one (Loke, 2014). The equation below makes it possible to calculate a DOI index (R) of the model cell by cell:

$$R_{1,2}(x,z) = \frac{m_1(x,z) - m_2(x,z)}{m_{1r} - m_{2r}} \quad (3.15)$$

where $m_{1r}$ and $m_{2r}$ are the resistivity of the first and second reference models, and $m_1$ (x, z) and $m_2$ (x, z) are the resistivity of each cell of these models. The DOI index (R) will approach zero where the two inversions produce the same resistivity values, regardless of the value of the initial reference model. In cells where the value is far from zero, it means that the resistivity value depends on the background resistivity value assigned to the reference model; such a result is not reliable. The normalized DOI index is calculated to reduce the effect of the damping factor and the selection of the initial reference model (Robert *et al*., 2011). To normalize the DOI index, is used the maximum value of R ($R_{max}$) calculated with equation (3.15):

$$R(x,z) = \frac{m_1(x,z) - m_2(x,z)}{R_{max}\ (m_{1r} - m_{2r})} \quad (3.16)$$

The main difficulty lies in deciding the cut-off value where the inversion values are trusted. For the normalized DOI index, Marescot *et al*. (2003) recommended a cut-off value of 0.1 or 0.2. The computation of the normalized DOI index was performed with RES2DINV v.3.59.

- *Forward Modelling*

The use of electrical tomography provides a resistivity results sometimes difficult to interpret. For their analysis is necessary to obtain field information and response of the materials present as much as possible. Unfortunately, the results do not always match the expected response due to multiple factors. Forward Modelling is used to approximate the obtained result to the subsurface materials (Loke, 2002). A theoretical profile with known resistivity bodies and simple morphology is modelled to analyse the electrical response. To make these models has been used RES2DMOD software, from Geotomo Software.

This program calculates the apparent resistivity pseudosections for a defined synthetic model. For these apparent resistivity pseudosections generated, the real resistivity is calculated by RES2DINV v.3.59 software, like a field measured profile. To calculate the real resistivity are used the same inversion parameters for the profiles measured in the field. In addition to this posteriori analysis for the materials composing the resistivity profile, has made a priori analysis to define which measuring array should be used for best results.

### 4.3.4 Seismic tomography

*- Basic fundaments of the method*

Seismic waves are a type of elastic waves produced by large faults and leading to large earthquakes, or minor disturbances, such as strokes caused by a bulldozer, and give rise to movements imperceptible by humans. They may be produced artificially by weight drop or explosions.

The seismic waves propagate through the bodies, and are divided into two groups of waves: internal and surface waves. Internal waves travel through the interior of the Earth, and surface waves do by the surface similar to the sea waves. Four types of seismic waves exist (Fig. 3.12): P waves (or compression) which spread in the same direction of the particle motion; S waves (or shear), which propagate in perpendicular direction to the particle displacement; Love waves that are surface waves and move surface particles transversely to the direction of wave propagation; and Rayleigh waves, also surface waves, and the particles move with a backward movement from direction of wave spread.

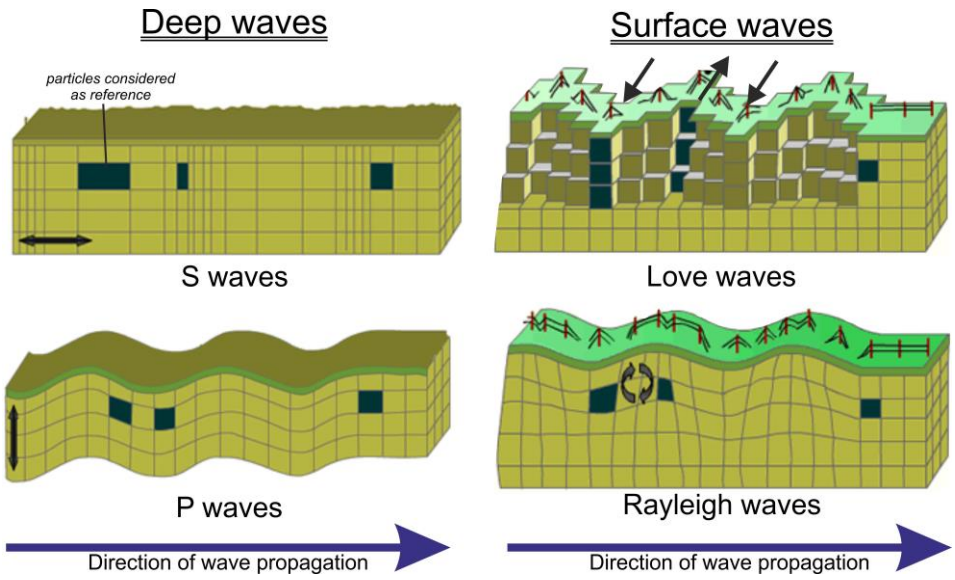


Figure 3.12: Types of seismic waves. Deep waves (P and S waves) and surface waves (Love and Rayleigh waves). Modified from Grotzinger and Jordan, 2010.

When it exerts a force on the ground, this is deformed in proportion to the force applied. This proportionality between distortion and stress is characterized by the elastic constants of the medium and they are defined by the elastic modulus. These are the characteristic physical parameters of each rock:

- *Young Modulus* (E): is the relationship between the unit compressive stress and the unit longitudinal deformation.

$$E = \frac{F/A}{\Delta L/L} \tag{3.17}$$

  Where $F/A$ is the unit effort and $\Delta L/L$ is the unit deformation.

- Poisson's Ratio ($\mu$): relates the unit change of the cross-sectional area ($\Delta W/W$) to the unit longitudinal strain ($\Delta L/L$):

$$\mu = \frac{\Delta W/W}{\Delta L/L} \tag{3.18}$$

- *Bulk modulus* ($K$): When an object is subjected to a uniform compressive stress on all sides, the object will experience a reduction in volume. This module relate compression with the unit change volume:

$$K = \frac{\Delta P}{\Delta V/V} \tag{3.19}$$

  Where $\Delta P$ is pressure increase, and $\Delta V$ is volume increase.

- *Shear modulus* ($G$): is the ratio of the unit lateral force ($F/A$) and the relative displacement of the slip planes ($\Delta x/y$):

$$G = \frac{F/A}{\Delta x/y} \tag{3.20}$$

When waves propagation within the earth find a change in the elastic properties of the material, some of the energy goes through the same medium (incident wave), other

portion is reflected (reflected waves), and the remainder waves are transmitted to other mediums (refracted waves) with changes in propagation direction, speed and vibration mode.

Seismic refraction is based on the critically refracted rays. Reading the first arrivals and the spacing between geophones provide the data necessary to apply the equations of the critical rays trajectories, and to calculate the velocities of waves propagation on the surface and the depth at which they do (Grandjean *et al*., 2004; Fiore *et al*., 2013). This method provides seismic refraction pseudosections showing the velocity distribution of the subsoil and deep through the velocity field V (x, z).

Seismic reflection consists on register over the surface the reflected waves front produced as consequence of a controlled explosion or provoked perturbation produced on the surface (shot). Among the different trajectories produced are only considered those due to the reflection over the layer that composes the subsoil. The result is a set of seismic traces reordered in common depth point (CDP) whose contain information about the reflectors. The method provides seismic reflection pseudosection that group the CDP traces and also contain the approximate information about materials velocities. Usually only P waves are used, but in researches with complex geology, the S waves are also used.

- *Equipment*

To obtain the seismic profiles, it has been used the StrataVisor-NZ seismometer from Geometrics (Fig. 3.13). This equipment has a central computer, 24 channels of simultaneous measurement and 20 kHz bandwidth (from 0.02 ms to 16 ms sampling) for high-resolution investigations. It also used 48 vertical geophones of 40 Hz, a starter geophone and two cables of 120 m long with a maximum takeout spacing of 5 m.

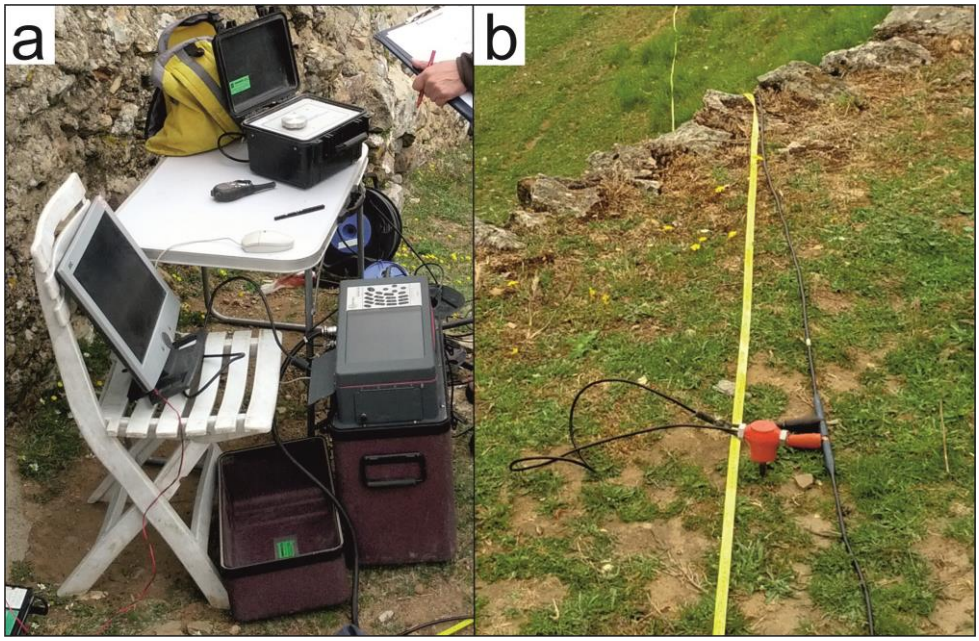


Figure 3.13: Seismic equipment. (a) Measuring equipment StrataVisor NZ seismometer. (b) Measuring geophone along a profile.

- *Acquisition and processing*

The seismic data acquisition, as in electrical tomography, is performed along profiles. Each profile has a maximum of 48 geophones, of which only through 24 of them measure at the same time, with an offset that varies between different profiles. Moreover, the roll-a-long technique allows obtain longer profiles, where the back cable is emplaced in the front of the profile. To generate the seismic wave has been used an 8 kg hammer on steel plate located near the starter geophone. This starter geophone indicates to the equipment at what time the shot was made and marks the beginning of the measure. There has been a shot in the mid-point between each geophone and other on each side of the profile, so that for a profile with 48 geophones were recorded 49 shots. In some sections, in addition to the shot made by the hammer, has used a small explosive charge for better penetration and resolution measures.

Measurements were taken using symmetric and asymmetric geometry (Fig. 3.14). In asymmetric geometry the receptor and measure geophones of the seismic waves are outside shooting, and reach a greater depth and lower resolution. In symmetric geometry, the shot is performed at the midpoint of measuring seismic geophone signal, so that there are 12 geophones on each side of the shot. In profiles with 48 measurement geophones, in which only is measured by 24 of them, permits vary between symmetric and asymmetric geometry without changing the geophones position.

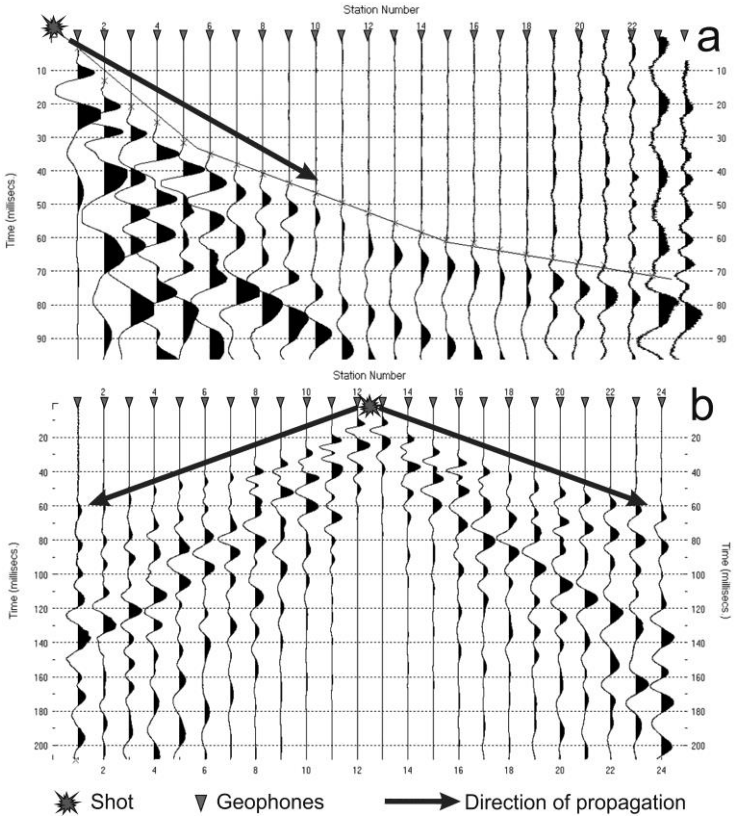


Figure 3.14: Seismic measurement in asymmetric (a) and symmetric (b) geometry.

- *Seismic refraction*

The data processing was performed with RayFract v.2.52 software. Then, the measured data are transferred in the field from the internal microcomputer to a PC, where the processing is done in several steps:

- ✓ *Geophones geometry definition*: for each data file is defined the number of geophones corresponding measures and the shot position.
- ✓ *Definition of geometry x, y, z*: the coordinates are assigned to each geophone. These coordinates are relative, so the X starts at 0, the Y is always 0 if measures have been taken in a single profile, and Z is normalized to 0 for the lowest topographic level.
- ✓ *First arrivals Reading (picking)*: Manually, input points is marked in the domocronas wave curves generated in each geophone, for the graphical space/time.
- ✓ *Velocity model*: a model of real seismic velocities for a profile is obtained.
- ✓ *Inversion of initial model*: through Delta T-V method. Fifty iterations are performed to achieve a lower error rate not exceeding 5%.
- ✓ *Time setting*: experimental times and times calculated are compared. They are adjusted manually to get a new model through a new inversion data with 50 iterations.

This processing obtains the initial velocity model, the real velocity model and ray tracing coverage. These models are displayed and analysed in the Surfer v.11 software.

- *Seismic reflection*

The seismic reflection processing is more complex than in seismic refraction. The more important challenge is isolate the reflection register from other waves (direct waves, refraction, noise, etc.). This process is performed with multisignal treatment (filters, deconvolutions, etc.) that should be done carefully to avoid artefact and false reflectors. Other conflictive point is the reflectors layers are in double time in the travel time (incidence and rebound). The process of the raw seismic data, the VSUNT-Pro 21

(Geofoft, Inc.) commercial code and SU (Seismic Unix, Center of wave phenomena) free routines code has been used. The common offset short-receiver sections over the instantaneous frequency images are generated.

### 4.3.5 Ground Penetrating Radar (GPR)

- *Basic fundaments of the method*

This technique is based on the emission of electromagnetic pulses underground and reception of the reflections produced by electromagnetic discontinuities found in the material. GPR generally consists on emitter, receiver and mainframe (Fig. 3.15) (Xu *et al*., 2010). GPR frequency ranging between 10 MHz and 1 GHz, corresponding to a pulse width of nanoseconds to dozens of nanoseconds. High frequency signal penetrates to smaller depth beneath ground but shows higher resolution than low frequency signal. Short pulse is sent into the ground via emission antenna, while transmission of electromagnetic wave in underground depends upon the attribute of the media it penetrates; as for the media its conductivity controls the signal attenuation, its dielectric constant controls the rate of signal transmission. Part of the signals emitted will be reflected at the interface between two materials with different electric properties, and they can be received, magnified, digitized by the receiver. Finally, they are transmitted to the mainframe for storage and processing.

The wave velocity of electromagnetic wave V for soil or rocks, and also fresh water, can be expressed as follows (Flohrer and Pöpel, 1996):

$$V = \frac{c}{\sqrt{\varepsilon\gamma}} \tag{3.21}$$

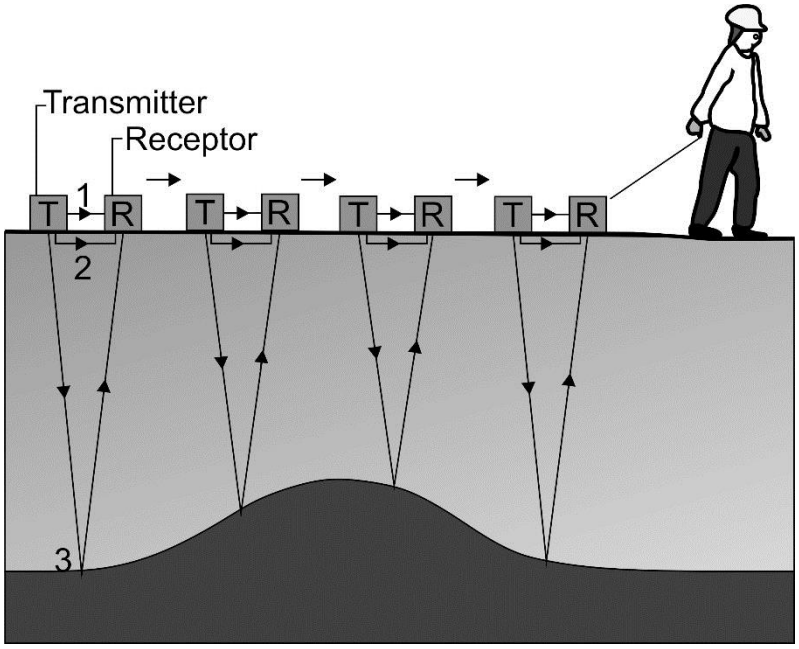


Figure 3.15: Schema of GPR data acquisition in profiles in the field. Modified from Daniels (2004).

Where *C* is the rate for light transmission, and $\varepsilon\gamma$ is the dielectric constant of the media. From the above equation the distance *D* between the antenna and a reflection point can be calculated as follows:

$$D = \frac{\mathrm{V}\cdot\Delta\mathrm{t}}{2} \tag{3.22}$$

Where $\Delta t$ refers to the time required from emitting to receiving of an electromagnetic wave. When electromagnetic wave reaches the interface between two different electromagnetic properties layers, its reflection amount depends upon the difference in dielectric constant between the two materials, while the reflecting coefficient R for the interface between them can be expressed as follows:

$$R = \frac{1-\sqrt{\varepsilon_2/\varepsilon_1}}{1+\sqrt{\varepsilon_2/\varepsilon_1}} \tag{3.23}$$

Where $\varepsilon_1$ and $\varepsilon_2$ refer respectively to the dielectric constants of the two materials.

- *Equipment*

Generally, the GPR equipment is constituted by a central computer that register the signal, connected to the transmitter and receptor units called antennas. The equipment used is GSSI and two types of antennas have been employed (Fig. 3.16). First a more shallow antennas of 80 MHz with a separation of transmitter-receptor of 2 m; and secondly, a deeper antennas of 40 MHz with an antennas separation of 3 m.


Figure 3.16: GPS equipment. (a) 80 MHZ antenna and (b) 40 MHz antenna.

- *Acquisition and processing*

The data was acquired along profiles with measurement interval of 0.1 m, 1024 samples for a time window of 400 ns. The data processing is performed with the software RADAN (v.6.5, GSSI, Inc.). For the processing, only a simple flow (background removal, filtering horizontal pass-band and topographic correction) was applied because the objective was to emphasize only the relevant diffraction-reflections. This meant not compensating the amplitude attenuation due to geometrical divergence and not migrating the radargrams. The depths provided for the profiles is approximate, due to the EM wave velocities could then be estimated.

# Chapter 4

## Outlines

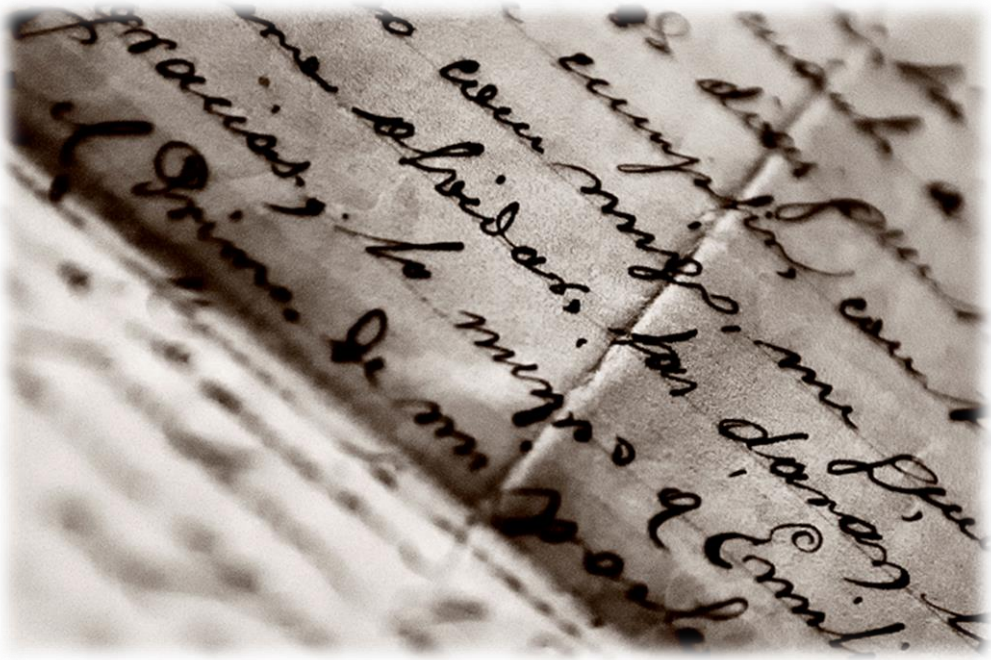

In this section is explained briefly the structure in which it has raised this Ph.D. Thesis and how the chapters are organized. It mainly focuses on the detection of cavities by the integration of geophysical and geological techniques. For them it has conducted a review of previous work in both study areas and on geophysical techniques applied and combined.

The main part of the Thesis, **Part II**, consists of six chapter of which five of them are articles. They describe a sequence of different combinations of geophysical techniques applied on different geological environments and cave features.

**Chapter 5**, '*The Gruta de las Maravillas (Aracena, South-West Iberia): setting and origin of a sulphur-bearing marble-related cave*', provides a description of the main geological features of the Cerro del Castillo hill, where is emplaced de Gruta de las Maravillas cave. The cavity is placed in marbles, with metallic mineralizations, having rooms of variable sizes and depths. The geological parameters measured try to relate surface geological structures with the cave morphology and features.

**Chapter 6**, '*Integrated geophysical methods for studying the karst system of Gruta de las Maravillas (Aracena, Southwest Spain)*' combines eight geophysical method in the Cerro del Castillo to study the continuity of the Gruta de las Maravillas. These methods are applied over the known cave and compared with the profiles measured over zones where there is suspicion of its continuity. The geological features, such as host rock, pyrite band near the cave or iron oxides at cave walls, provide remarkable geophysical anomalies.

**Chapter 7**, '*Regional and residual anomaly separation in microgravity maps for caves detection: the case study of Gruta de las Maravillas (SW Spain)*' is an overview about the techniques applied for Bouguer anomaly separation, and some of them are

applied and compared over the microgravity data obtained in Cerro del Castillo hill. Finally, a discussion on each of ones will provide the best methods for this purpose.

**Chapter 8,** *'Cave detection with geophysical methods and drills exploration in Cerro del Castillo'* exposes the results obtained during the drill exploration in the hill scheduled in view of the geophysical and geological obtained data. It is performed on the areas pointing as minima of residual anomaly which high probability to content caves. The drill exploration results show the new caves detected in the area.

**Chapter 9**, '*Combined microgravity, electrical resistivity tomography and induced polarization to detect deeply buried caves: Algaidilla cave (Southern Spain)*' is the integration of geophysical methods over a known cave detected by boreholes but of unknown geometry. The cave is emplaced in limestones, uncovered and placed in deep, and partially submerged in water. The combination of three geophysical methods allow obtain approximate real morphology of the unexplored cave, and estimate its volume.

**Chapter 10**, '*Detecting gypsum caves with microgravity and ERT under soil water content variations (Sorbas, SE Spain)*' shows the combination of two geophysical methods, measured using a 3D array, over a shallow cave emplaced in gypsum and dry. The electrical methods are applied in time-lapse to compare cave detection with variation in humidity conditions.

Within **Part III, Chapter 11** provides a general discussion about the application of different geophysical methods in different geological conditions and cave features, choosing the best way to use such methods for each case of study. Finally, **Chapter 12** foreground the main conclusions, and **Chapter 13** tries to structure the future perspective in cave detection.

# Part II

5. Geology of Gruta de las Maravillas
6. Geophysics of Gruta de las Maravillas
7. Regional and residual anomaly separation
8. Cave detection with geophysical methods and drills exploration in Cerro del Castillo
9. Algaidilla cave
10. El Bosque cave

# Chapter 5

## Geology of Gruta de las Maravillas

# The Gruta de las Maravillas (Aracena, South-West Iberia): setting and origin of a sulphur-bearing marble-related cave

F.J. Martínez-Moreno[a], A. Pedrera[b], J. Galindo-Zaldívar[a,b], M. López-Chicano[a], A. Azor[a], W. Martín-Rosales[a], P. Ruano[a,b], J. M. Calaforra[c], A. Hódar-Pérez[a]

[a] Departamento de Geodinámica, Universidad de Granada, 18071-Granada, Spain.

[b] Instituto Andaluz de Ciencias de la Tierra, CSIC-Universidad de Granada, 18071-Granada, Spain.

[c] Water Resources and Environmental Geology, University of Almería, 04120-Almería, Spain.

*Under review*

Submitted on November 23, 2014 to

**Journal of Iberian Geology**

## ABSTRACT

The Gruta de las Maravillas is located at the WNW side of the Cerro del Castillo hill in Aracena (Huelva, SW Spain). The cavity is hosted within marbles included in a strip of high-grade metamorphic rocks belonging to the so-called Aracena Massif in the southernmost Ossa-Morena Zone. The hill is made up, from structural tectonic bottom to top, of granodiorites, marbles, quartzites, and gneisses, with the foliation trending N110ºE and dipping roughly 60º- 80º toward NE. The marbles appear highly deformed in ductile conditions, with isoclinal folds of different sizes, boudins, porphyroblasts with sigmoidal morphology, and left-lateral S-C shear fabrics. Close to the granodiorite contact, the marbles include a thin band of disseminated and massive pyrite, partially transformed to Fe-oxides. Analysis of the brittle deformation and the associated paleostresses indicates a NE-SW oriented maximum compression, probably related to the latest Variscan collisional tectonics (300 Ma; Late Carboniferous). The Gruta de las Maravillas is divided into three main levels (located at ~650, ~665 and ~685 m.a.s.l.), the dissolution having progressed from top to bottom in different stages of stability of the water table, pertaining to a carbonate aquifer. The initial dissolution phases were probably favoured by the presence of pyrite in the host rock, which, in turn, would have caused acidification of the circulating water. Hence, a thin layer of Fe-oxides covers some parts of the cave walls, locally including gypsum in the latest stages of the cave formation. The developmental process of the Gruta de las Maravillas is intriguing as compared to other caves developed in carbonates. The morphology and structure of the cavity result from interaction between the general NNE dipping foliation with sub-perpendicular joints, the pyrite-bearing band in the host marbles, and the descending water table that determines different dissolution levels.


**Keywords:** Aracena Metamorphic Belt, cave formation, pyrite band, acidic water, horizontal dissolution levels.

**RESUMEN**

La Gruta de las Maravillas se localiza al ONO del Cerro del Castillo en Aracena (Huelva, SO de España). La cavidad se encuentra en mármoles incluidos en una banda de rocas de alto grado metamórfico pertenecientes al Macizo de Aracena en el sector más meridional de la Zona de Ossa-Morena. En el cerro afloran, de muro a techo, granodioritas, mármoles, cuarcitas y gneises, con foliación N110ºE y buzamiento aproximado de 60º-80º hacia NE. Los mármoles aparecen altamente deformados en condiciones dúctiles, con pliegues isoclinales de diferentes tamaños, boudines, porfiroblastos con morfología sigmoidal y estructuras S-C. Cerca del contacto con granodioritas, los mármoles incluyen una fina banda de pirita masiva y diseminada, parcialmente transformada en óxidos de hierro. El análisis de las deformaciones frágiles y paleoesfuerzos asociado indica un esfuerzo máximo de compresión en la dirección NE-SO, probablemente relacionada con la colisión tectónica Varisca tardía (300 Ma; Carbonífero superior). La Gruta de las Maravillas se divide en 3 niveles principales (situados a ~650, ~665 y ~685 m.s.n.m.), cuya disolución ha progresado desde el nivel superior al inferior en distintas etapas de estabilidad del nivel freático correspondiente al acuífero carbonatado. Las primeras fases de disolución fueron probablemente favorecidas por la presencia de pirita en la roca encajante, la cual habría provocado acidificación en las aguas circulantes. Como resultado, una fina capa de óxidos de hierro cubre parte de las paredes de la cavidad, que puntualmente incluye yeso, generada en las últimas etapas de formación. El desarrollo de la Gruta de las Maravillas es particular en comparación con otras cuevas desarrolladas en carbonatos. La morfología y estructura de la cavidad es el resultado de la interacción entre la foliación buzante NNE con diaclasas sub-perpendiculares, banda de pirita en la roca encajante y el descenso del nivel freático que determina los diferentes niveles de disolución.

**Palabras clave:** Banda metamórfica de Aracena, formación de la cavidad, banda de pirita, aguas ácidas, niveles de disolución horizontal

## 5.1 INTRODUCTION

The dissolution of limestones and marbles by meteoric water enriched in $CO_2$ is by far the most common speleogenesis process (Palmer, 1991), and it has been extensively described (Klimchouk, 2007, 2009; Palmer, 2011; Tisato *et al.*, 2012). A particular type of karst system is associated with the dissolution of carbonates by water enriched in sulphuric acid (Lechuguilla and Carlsbad caves, Davis, 2000). This setting could result from $H_2S$ associated with deep hydrocarbon reservoirs, magmatic activity, and sulphate mineral reduction. The $H_2S$ rich waters mix with meteoric oxygen-enriched waters, thus generating sulphuric acid, which in turn dissolves the carbonate rocks (Egemeier, 1981; White *et al.*, 1995; Hose and Pisarowicz, 1999). Sulphuric acid corrosion causes distinctive morphological features (e.g. ramiform maze, Palmer, 1991) and promotes the formation of secondary sulphate minerals, mainly gypsum (Polyak *et al.*, 1998).

Caves formed by sulphuric acid develop irregular rooms and dead-end galleries near the water table, leading to sponge work and network mazes. In a mature speleogenesis stage, the mixing of meteoric and deep waters could become the dominant process, and highly soluble sulphate minerals could be dissolved and removed by subsaturated water (Hose and Macalady, 2006). Although oxidation zones of pyrite deposits hosted in carbonate rocks are favourable sectors for cave formation, there are scarce examples of sulphur-related caves described in such a context (Auler and Smart, 2003; Audra, 2004; Onac *et al.*, 2011; Tisato *et al.*, 2012). The active Cueva de Villa Luz (Mexico), probably linked to volcanic $H_2S$ emissions (Hose and Pisarowicz, 1999), the Kane and Guadalupe caves (U.S.A., Palmer and Palmer, 2000), which are related to nearby petroleum reservoirs (Egemeier, 1971; Hill, 2000; Palmer, 2006), and the Frasassi Gorge cave (Italy), associated with the reduction of underlying anhydrite and gypsum beds (Galdenzi and Menichetti, 1995), are some of the best-known examples.

Sulphur deposits, mostly pyrite ($FeS_2$), are oxidized when exposed to water and oxygen (Descotes *et al.*, 2002) and can thus react to form sulphuric acid ($H_2SO_4$), according to the equation (5.1) (Nicholson *et al.*, 1988):

$$FeS_2 + \frac{15}{4} O_2 + \frac{7}{2} H_2O \Rightarrow Fe(OH)_3 + 2SO_4^{2-} + 4H^+ \quad (5.1)$$

The dissolution of calcite in carbonates causes an increase in pH. This makes the ferric iron and aluminium hydrolize and precipitate as oxyhydroxide over the carbonates (Ziemkiewicz *et al.*, 1997; Cravotta and Traham, 1999; Al *et al.*, 2000; Hammarstrom *et al.*, 2003):

$$Fe^{2+} + 0.25O_2 + 2CaCO_2 + 2.5H_2O \Leftrightarrow Fe(OH)_3 + 2Ca^{2+} + 2HCO_3 \quad (5.2)$$

Moreover, gypsum can precipitate on the carbonate surface if the solution is supersaturated in sulfates (Booth *et al.*, 1997; Wilkins *et al.*, 2001; Hammarstom *et al.*, 2003):

$$Ca^{2+} + 2SO_4^{2-} + 2H_2O = CaSO_4 \cdot 2H_2O \text{ (gypsum)} \quad (5.3)$$

The Gruta de las Maravillas, located in the SW Iberian Peninsula, is hosted in marbles that include some pyrite-rich levels. The cave was discovered by iron mining explorers at the end of the nineteenth century (Romero Bomba *et al.*, 2010). There are no written references to it before that date. This fact, coupled with the absence of archaeological remains and organic debris, justifies the assumption that the cave was inaccessible to humans during its evolution. In 1914 the cavity was opened to tourism, and it is currently one of the most visited caves in Spain (Martín-Rosales *et al.*, 2012). Subsequent speleological research exposed new galleries and cavities that were also opened to tourists. Recent geophysical results reveal there are still unexplored cavities within this endokarst system (Martínez-Moreno *et al.*, 2014).

The aim of this paper is to discuss the Gruta de las Maravillas development mechanism. To do so, we have characterized the geological structure of the Cerro del Castillo hill where the cave is located, the tectonic deformations, the hydrogeology, the cavity morphology and the mineralogy of host rocks and cave deposits.

## 5.2 GEOLOGICAL AND GEOMORPHIC SETTINGS

The Gruta de las Maravillas is located in Aracena, North of Huelva, in western Andalusia (Spain) (Fig. 5.1). The cave formed through the dissolution of marbles belonging to the Aracena Metamorphic Belt. This metamorphic band is located along the contact between two major zones of the Palaeozoic Iberian Massif (Fig. 5.1): the Ossa-Morena Zone (OMZ) and the South Portuguese Zone (SPZ). The Metamorphic Aracena Belt is formed by Precambrian–Carboniferous rocks affected by high-temperature/low-pressure metamorphism and bounded to the south by the Beja-Acebuches Amphibolites. This region is characterized by a high ductile, ductile-brittle and brittle Variscan deformation associated with a general context of sinistral transpressional/collisional tectonics (Simancas *et al.*, 2006).

The Aracena Massif presents a rugged orography with alternating ranges and plains elongated in an ESE-WNW direction. Overall, it is a corrugated landscape with moderate average altitude, ranging from 160 to 1000 m.a.s.l. The Gruta de las Maravillas is located in the Cerro del Castillo hill (Fig. 5.2), which stands 100 meters above the surrounding Aracena town (from 650 to 750 m.a.s.l.) and has an extension of ≈ 0.25 $km^2$.

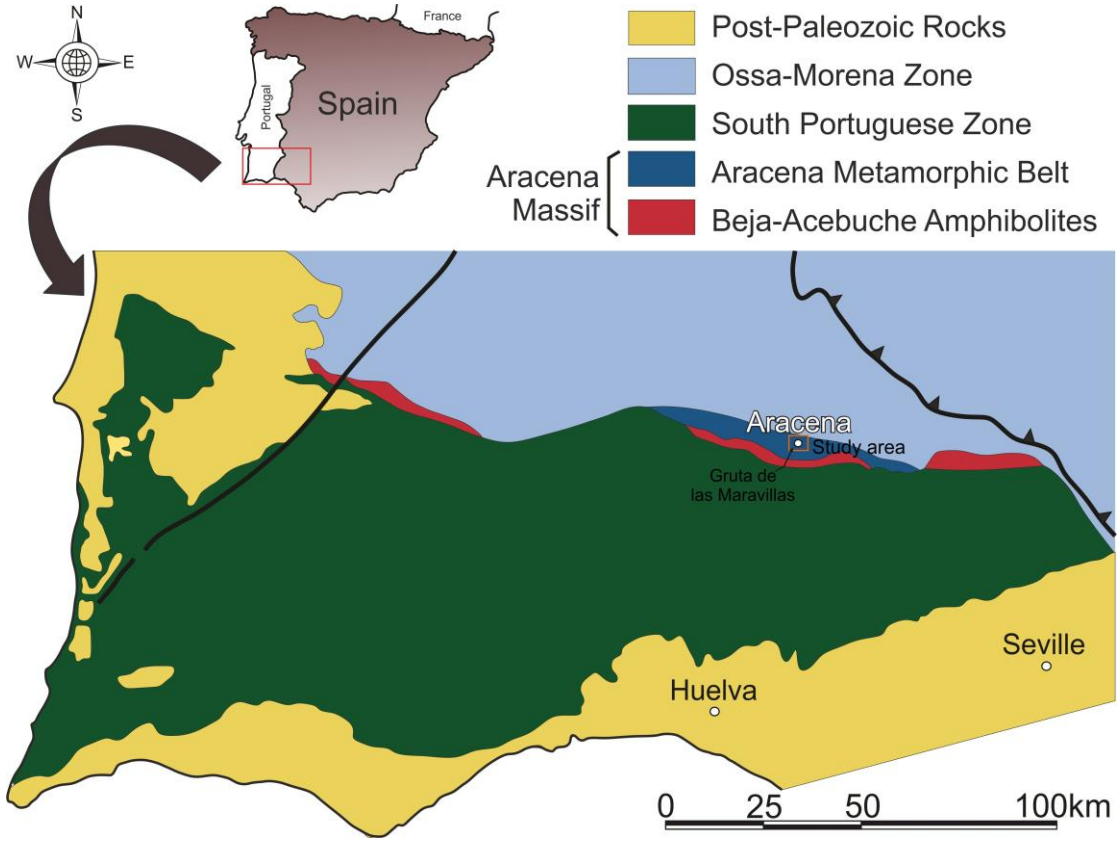


Figure 5.1: Location of the town of Aracena, SW Iberian Peninsula. Simplified regional geological sketch.

## 5.3 STRUCTURE AND DEFORMATIONS OF THE GRUTA DE LAS MARAVILLAS AREA

The Late Precambrian–Cambrian volcano-sedimentary sequence includes carbonate levels like those outcropping in the Cerro del Castillo hill (Fig. 5.2). From structural bottom to top, the hill is made up of granodiorites and marbles with intercalated quartzites and gneisses (Fig. 5.2b). The granodiorites crop out on the southwestern side of the hill, showing typical granitic textures; weathering in these rocks increases towards the NNE. The contact with the marbles is parallel to the regional metamorphic foliation, though locally metric-to-decametric granitic dykes intrude the marbles (Fig. 5.2a, 714060E / 4196420N – UTM H29); some marble xenoliths within the granodiorites have also been

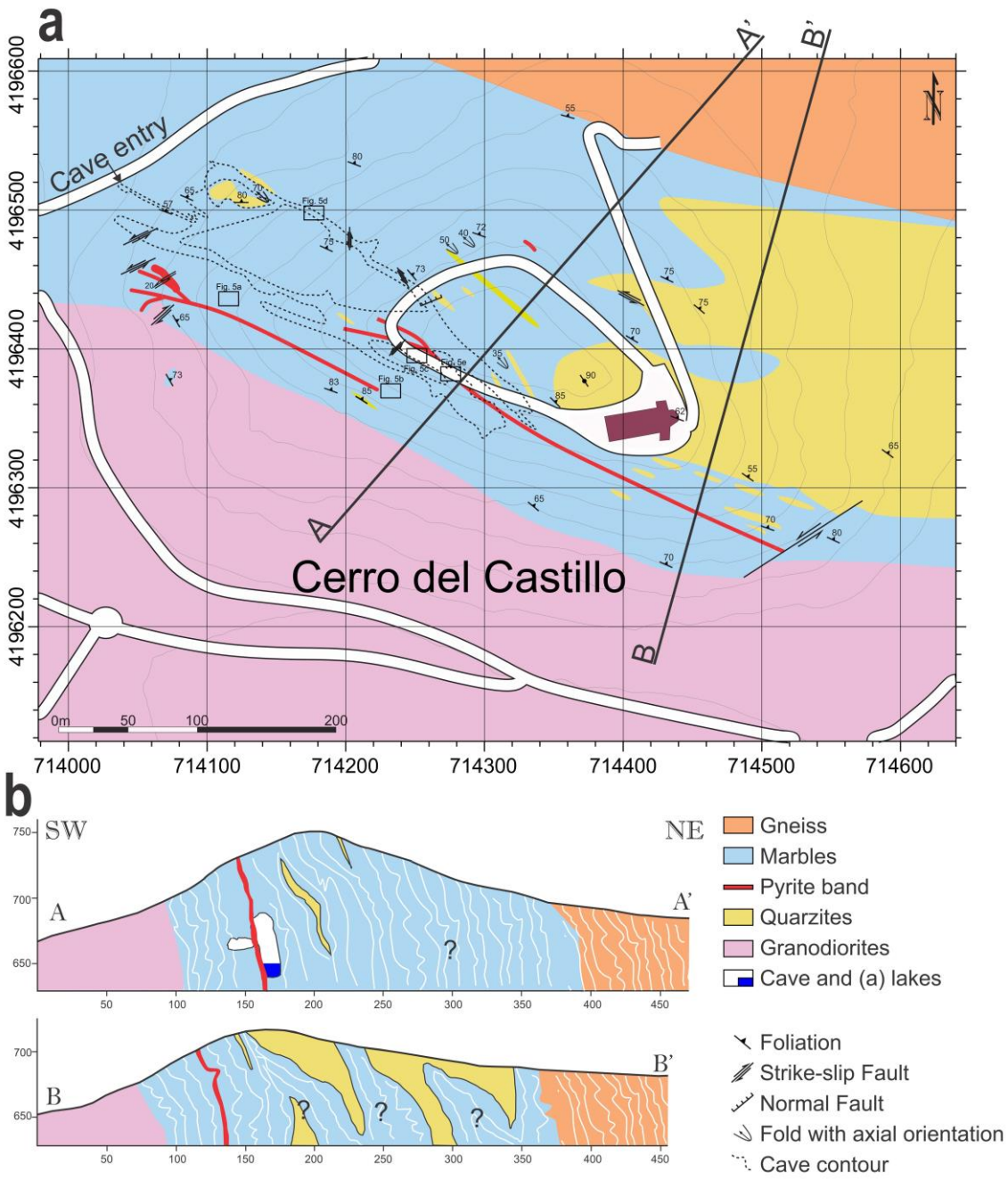


Figure 5.2: Geological map of Cerro del Castillo hill. (a) Study area, position in Figure 5.1. (b) Geological section marked in Figure 5.2a.

observed (Fig. 5.2a, 714075E / 4196380N – UTM H29). Marble foliation is defined by alternating dark and light bands formed by deformed calcite crystals with minor contents of K-feldspar and quartz. The foliation on average strikes N110ºE and dips 60º to 80º towards the NE (Fig. 5.2a). Interfingered with marbles, some quartzite levels crop out on the eastern side of the hill, and at some places they are the dominant lithology. The contact

between marbles and intercalated quartzites has an irregular geometry in detail, but in general it lies parallel to the regional foliation. These Quartzite intercalations have tabular morphologies, with thicknesses of 2-5 m and lateral continuities of ≈ 100 m. The top of the lithological sequence in the Cerro del Castillo corresponds to gneisses (Fig. 5.2b) in direct contact with the marbles. The gneisses extend under the buildings of Aracena, showing foliation orientations parallel to the marble.

Close to the contact with the granodiorites and interbedded within the marbles, several narrow pyrite bands with oxidized massive sulphurs appear (Figs. 5.2 and 5.3a). Disseminated pyrite crystals (Fig. 5.3b), at times transformed to iron oxides, are also recognized (Fig. 5.3c). Pyrite and related minerals are mainly located along two parallel bands, with ramifications toward the WNW, showing dimensions of ≈ 500 m in length and some centimetres to 1-2 m in width.

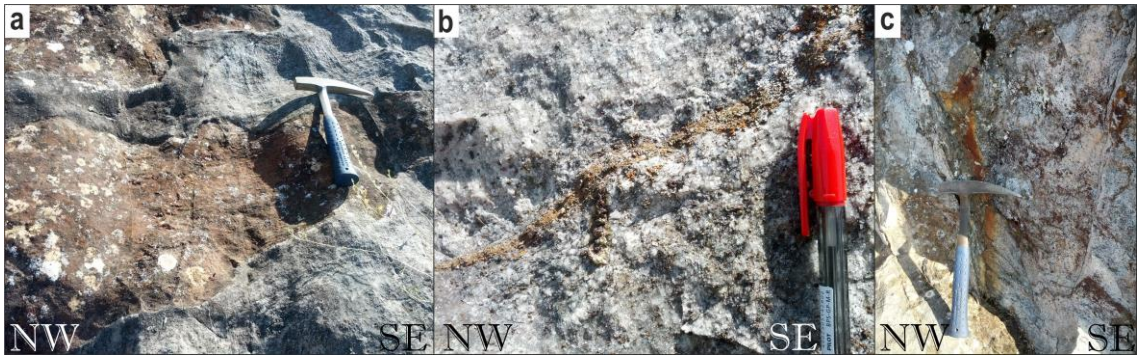


Figure 5.3: Pyrite band partially transformed to iron oxides included within marbles. (a) Massive oxidized sulphurs. (b) Disseminated pyrite crystals. (c) Pyrite transformed in iron oxides.

The petrographic analysis performed on the different lithologies (Fig. 5.4) shows high contents of carbonate in marbles, mainly calcite (Figs. 5.4.1a and 5.4.1b), in addition to quartz, biotite, K-feldspar, and small pyrite crystals. A sample with high pyrite content (Figs. 5.4.2a and 5.4.2b) features small pyrite crystals and high proportions of Fe-oxides, with quartz and carbonates (calcite). The granodiorites (Figs. 5.4.3a and 5.4.3b) have high

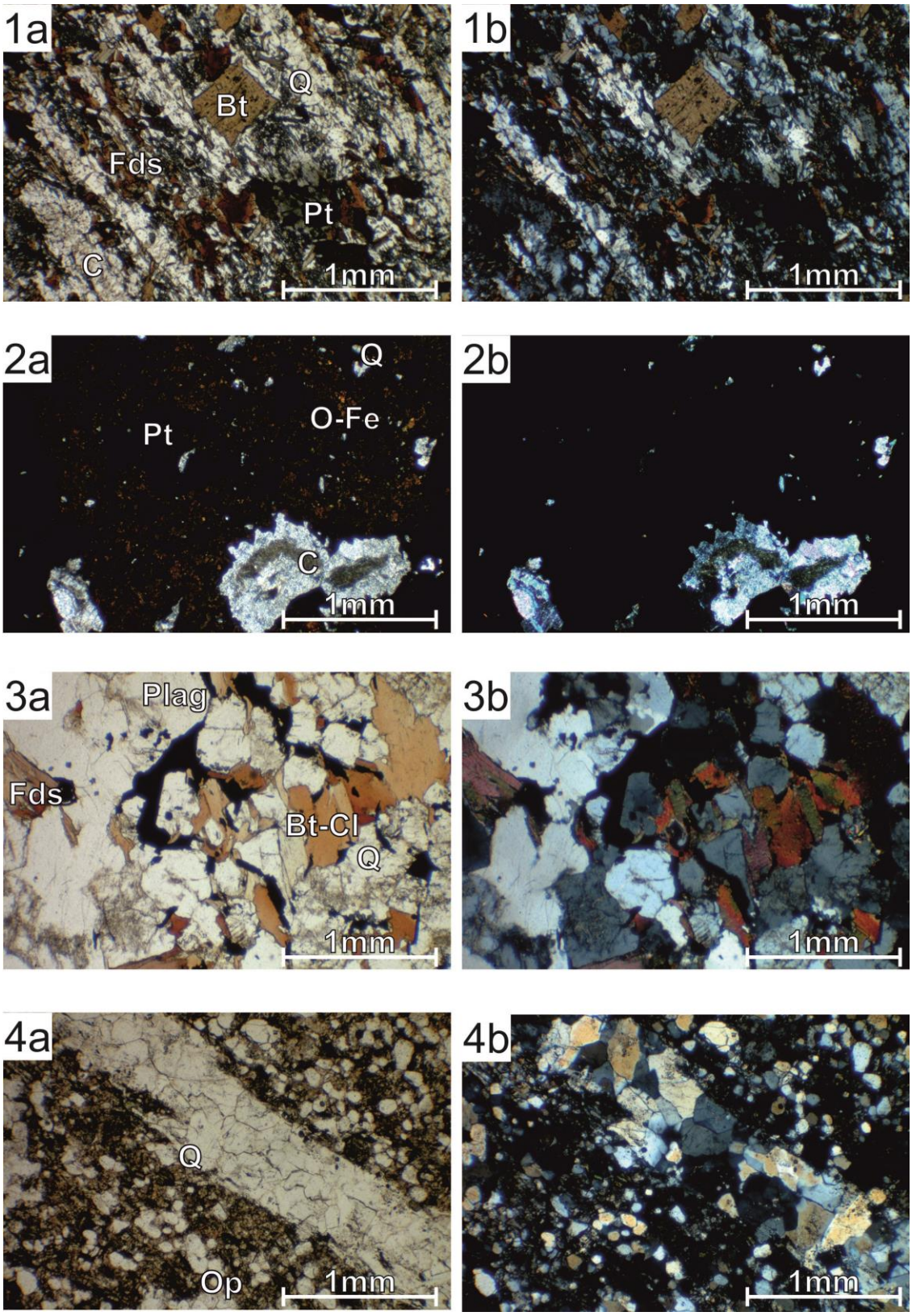


Figure 5.4: Petrographic analysis in microscope with transmitted (a) and polarized light (b). The samples represented are: (1) marbles, (2) high content pyrite sample, (3) granodiorites and (4) quartzites. C: carbonate; Q: quartz; Bt: biotite; Cl: chlorite; Plag: plagioclase; Fds: K-Feldspar; Pt: Pyrite; O-Fe: iron oxides; Op: opaques.

content in plagioclase and biotite-chlorite, with minor proportions of K-feldspar and quartz. The quartzites (Fig. 5.4.4a and 5.4.4b) are mainly constituted by quartz, with small amounts of ore minerals.

The marbles, quartzites and gneisses are affected by ductile deformation, the main result being the penetrative regional foliation described above. At mesoscale, the marble foliation is very warped and folded, locally showing isoclinal folds of centimetric to decametric size, with axes generally WNW-ESE oriented and plunges towards the WNW (Figs. 5.2a, 5.5a and 5.5b). Many of these folds present moderate hinge thickening that suggests ductile shearing (Figs. 5.5a, 5.5b and 5.5e). Moreover, the presence of some boudins (symmetric type, blocky boudins, Fig. 5.5c) indicates elongation parallel to the layers with perpendicular flattening (Fernández and Díaz-Azpiroz, 2008). Furthermore,

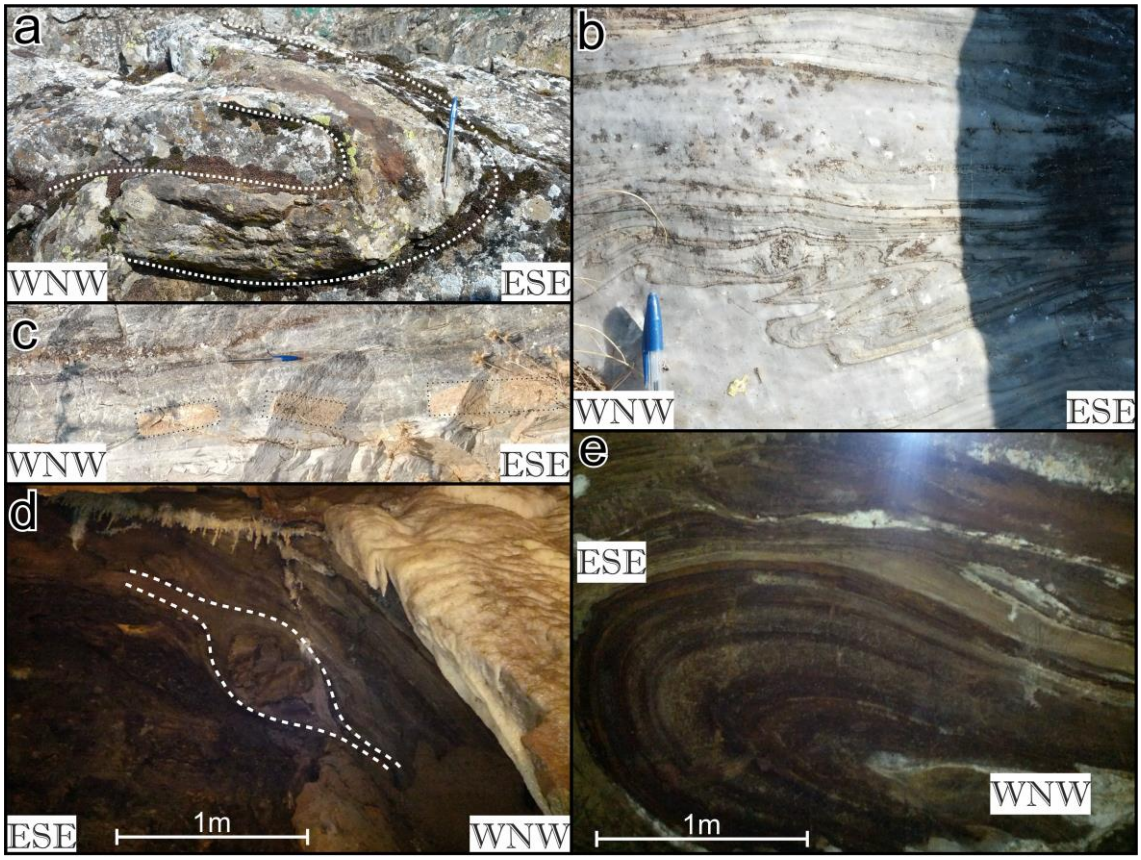


Figure 5.5: Ductile deformation structures observed both on the hill surface (a, b, c) and inside the cave (d, e). Isoclinal folds (a, b, e). Boudins (c). S-C fabric (d). Location in Figure 5.2a.

there are some porphyroblasts (quartzite) with sigmoidal morphology and S-C fabrics, which point to a left-lateral component in the main deformation affecting these rocks (ductile shearing; Fig. 5.5d).

Brittle deformation in the marbles gave way to a main system of joints, most having an opening of a few millimetres; they often show fillings of iron and manganese oxides (Fig. 5.6) that can be measured at surface and inside the cave. Fractures are generally vertical and trend NE-SW. In some locations (stations 7, 9 and 12), two conjugated joint sets have been observed. At station 7, the two sets of joints show an angle of ≈ 60º, suggesting an origin related to conjugate shear joints; at stations 9 and 12, the angle between joint sets is lower than 60º, thus being considered as hybrid joints (Hancock, 1985;

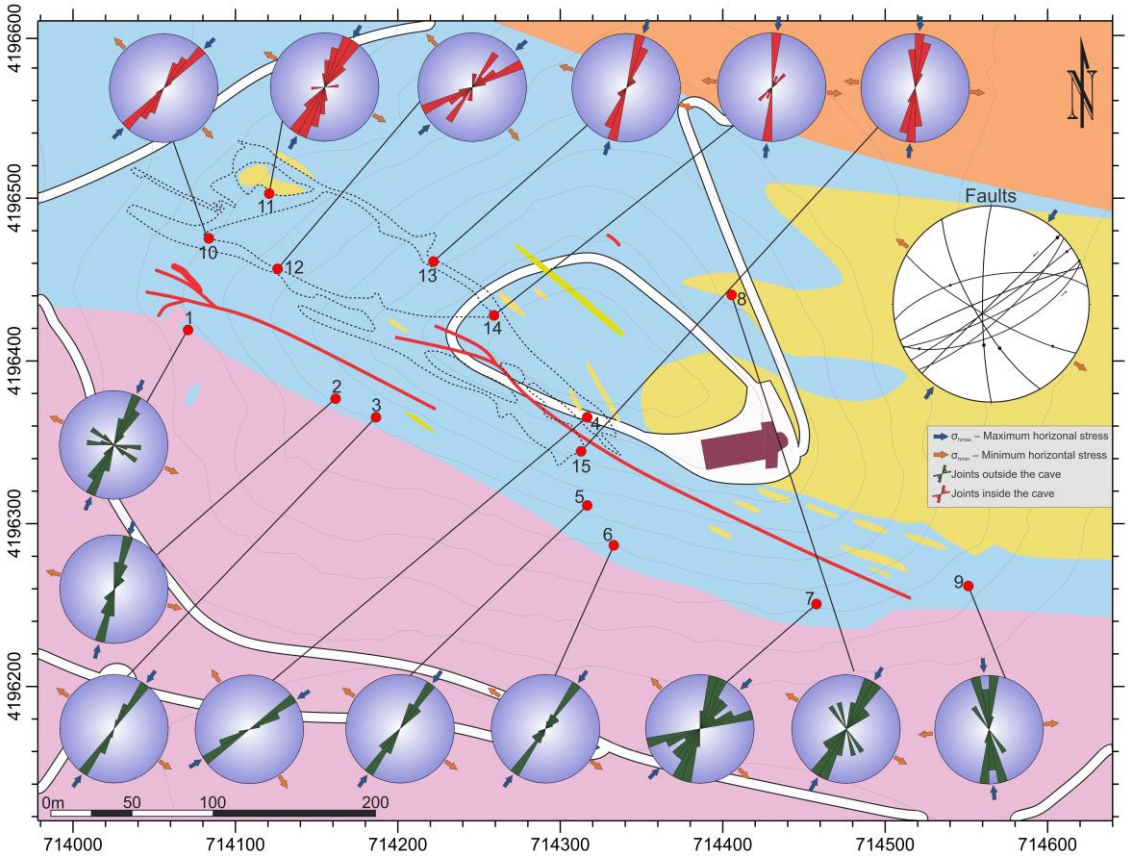


Figure 5.6: Paleostress analysis with faults and joints. The joints set measurements pertain to the hill surface (green rose diagrams) and inside the cave (red rose diagrams). Orientation of small size faults in stereographic projection, lower hemisphere.

Hancock and Engelder, 1989). The joint system recognized is compatible with a stress regime that would produce extension in a NW-SE direction with orthogonal NE-SW compression. Several small-scale faults can be observed at surface and inside the cave (Fig. 5.6). The most common fault set is oriented NE-SW and has sinistral kinematics, suggesting that the paleostresses were similar to those deduced from the joint sets. Nevertheless, the population of observed faults is too small to apply conventional statistical techniques for paleostress determination.

## 5.4 CAVE MORPHOLOGY

The cave presents a predominantly horizontal development, with irregular rooms and dead-end passages. It is formed by a succession of large passages, erosional rock floors and plenty of dome ceilings. It is 350 m long and 80 m wide, having a path that is 2130 m long, an approximate perimeter of 1065 m and an area of 16775 $m^2$. The cave volume is estimated at 70000 $m^3$, deduced from topographic observations. It is divided into three main levels (Fig. 5.7), the bottom level located at ~645 m.a.s.l. and having a height of 7-10 m. At present, the water table is found at 650 m.a.s.l. (Fig 8a) and it is constant throughout the cave. In the areas close to the hill contour, where the cavity is just 3-4 m beneath the surface, tree roots penetrate the cavity. Level 2, located at ~670 m.a.s.l. (Fig. 5.7), presents a minor horizontal development with regard to the known and explored galleries. It has an average height of 10 m and shows the greatest development of speleothems of the entire cave. The dating of speleothem samples from this area gives an average age of 50 ± 10 Ka BP (Martín-Rosales *et al.*, 2008). In addition, there are hanging lakes located in this level (Figs. 5.7 and 5.8b). Level 3 lies ~685 m.a.s.l. and has a greater length than level 2, with a height of 5-10 m. The passages belonging to level 3 are only accessible by climbing —it is

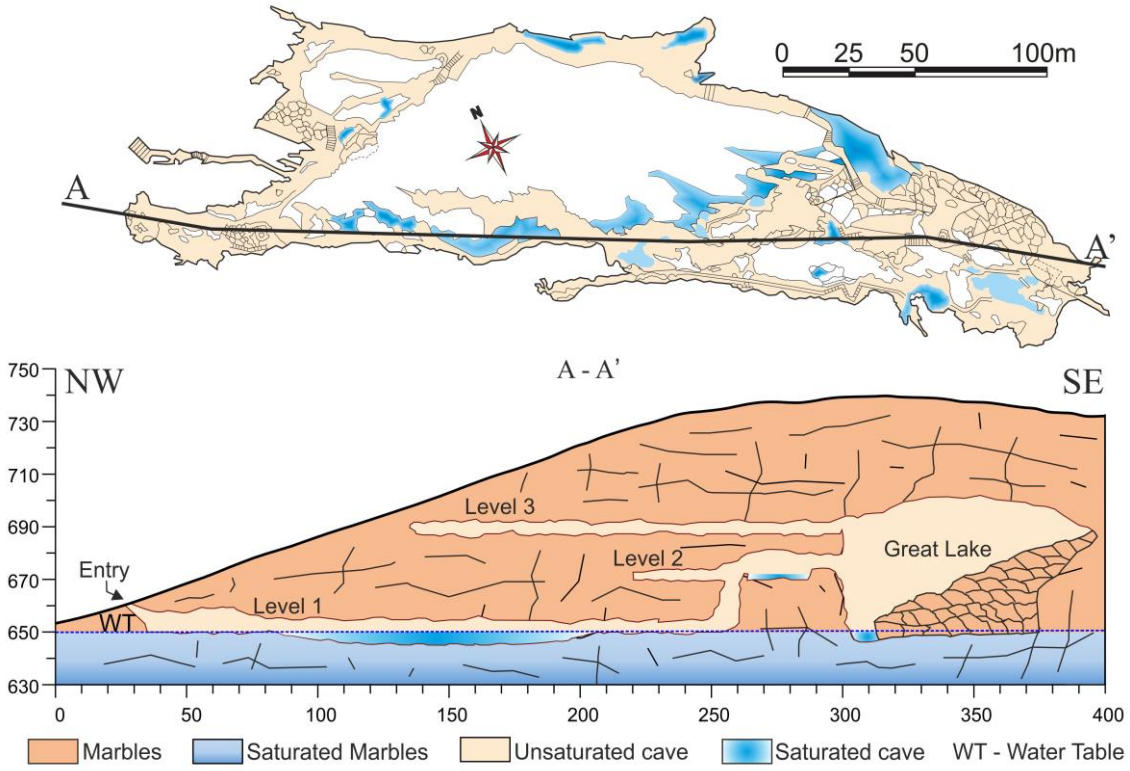


Figure 5.7: Gruta de las Maravillas cave. Cave section showing flat morphology of the cavity and the three dissolution levels (Modified from Speleological Group of Malaga).

not open to tourism. It has well preserved and corroded speleothems due to its location near the surface and the action of the vegetation roots crossing the galleries.

The vast part of the cave known as the Great Lake (Figs. 5.7 and 5.8c) deserves special attention. This part is found toward the end of the cave, in the central part of the hill, where it reaches greater elevation and matches the location of the pyrite band crossing the cave (Fig. 5.2). It is the largest section of the cave: 25 m wide, 100 m long and 50 m high. Its topographic elevation ranges from ~645 to ~700 m.a.s.l., taking in all three levels described. The bottom of the cavity presents chaotically arranged large fall blocks from the collapse of level 2 and 3 floors. The dating carried out on speleothems developed on steep boulders suggests that the collapse occurred about 10 Ka BP (Martín-Rosales *et al.*, 2008).

The cave is developed parallel to the foliation strike (N110ºE, Fig. 5.2 and Fig. 5.8c, De Val and Hernández, 1989). The morphology of the galleries, in transverse and

longitudinal section, presents a shape that coincides with the foliation dip (80-85º N) and strike (N110ºE). Generally, the cavity fits a pattern of large passages connected together by smaller galleries and narrow passages. The end of the ramifications has network maze morphology. The connection between parallel galleries is associated with joint direction.

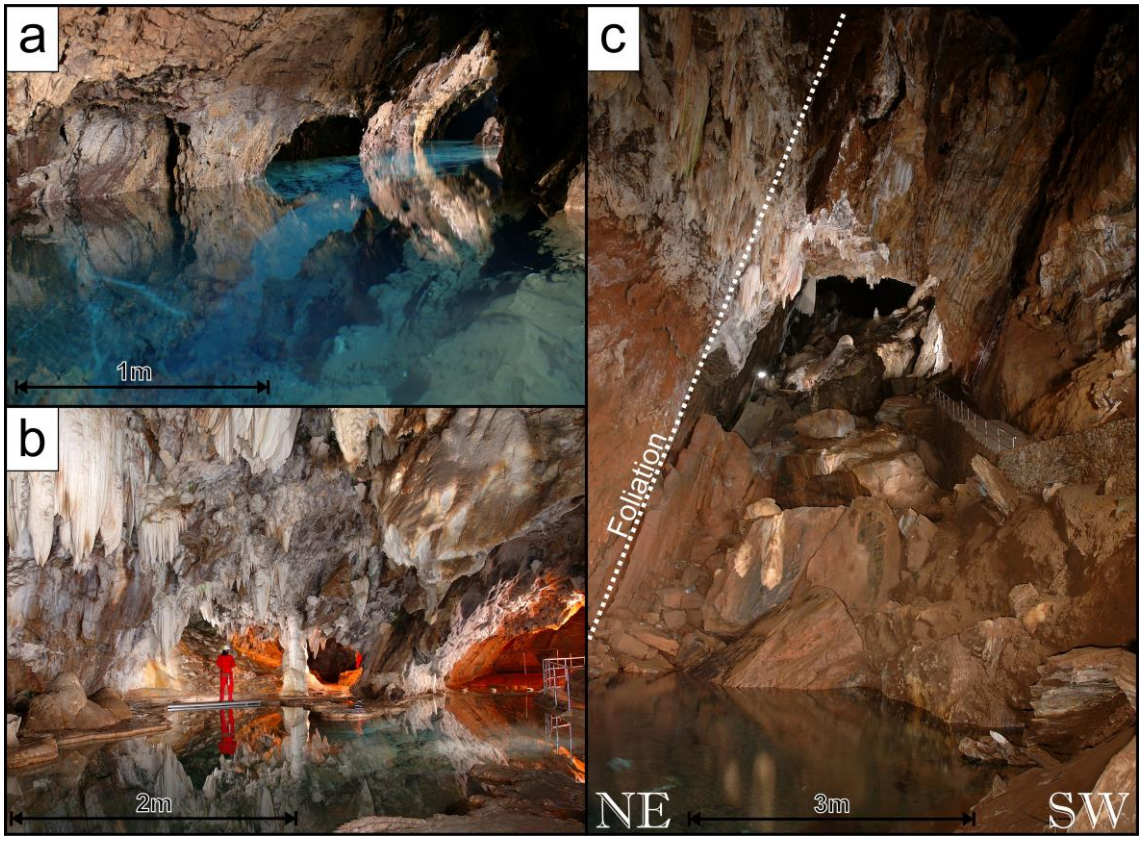


Figure 5.8: Cave morphology. (a) Current water table. (b) Hanging lakes or gours. (c) Great Lake Room and chaotic blocks.

## 5.5 SPELEOTHEMS AND OTHER DEPOSITS

The cave features a great variety of speleothems: stalactites, stalagmites, columns, drapery, flowstone, sinterfahne, precipitate and pavement forms (shelfstone, gours, rimstone), helictites and coraloide calcite (Fig. 5.8b). They are made up mainly of calcite, predominantly in the lower cave levels, while aragonite is mostly preserved in the upper part. The variability in the precipitation of different carbonate forms can be linked to

microclimatic changes, as has been demonstrated in many other cavities (Fernandez-Cortes *et al.*, 2010). The thin section analysis performed on some speleothems from level 2 revealed the existence of fibrous aragonite textures developed on calcite crystals, showing changes in the physico-chemical water conditions, probably associated with hydrological and/or paleoclimate changes in the region (Martín-Rosales *et al.*, 1995).

Speleothems developed over and below water conditions coexist in the lower level, in an area hydrologically disconnected from the water table. There are subaquatic speleothems of substantial dimensions placed directly upon the host rock. Secondary vadose formations, with the presence of aragonite, are located over them. Lastly, flatwater and oversaturated formations (gours) and, finally, vadose formation culminate the superposition of speleothems, dated as 15 Ka BP (Martín-Rosales *et al.*, 1995).

In the lower level, the galleries located to the SW show a greater development of speleothems than the galleries located to the NE. The flooded and fluctuating water areas contain fewer speleothems, as corrosion predominates over precipitation in these sectors. This process affected ancient speleothems developed at this level, as also observed in the northern sector, where debris flows and stalagmites affected by corrosion are identified (8-10 meters above the current water table). This implies that the position of the water table was above its current position during a significant period of time. Therefore, numerous corrosion notches and stable water morphologies are observed (Martín-Rosales *et al.*, 1995). The uppermost levels 2 and 3 contain a great variety of speleothems that completely hide the wall morphologies. Abundant underwater speleothems originate in gours, some very unique, such as the calcite raft cones dated at 101 ± 5 ka BP (Martín-Rosales *et al.*, 2008).

There are additional allochthonous deposits (clays) derived from surface percolation, as well as autochthonous ones (chaotic blocks). Minerals resulting from the pyrite

transformation cover the cave walls under the speleothems. The most visible products are iron oxides (Figs. 5.9a and 5.9b): goethite, lepidocrite, psilomelana, rutile, ilmenite and brookite (Martín-Rosales *et al.*, 1995). Gypsum microcrystals were detected under the speleothems of the lower level using Raman spectroscopy (Fig. 5.9c).

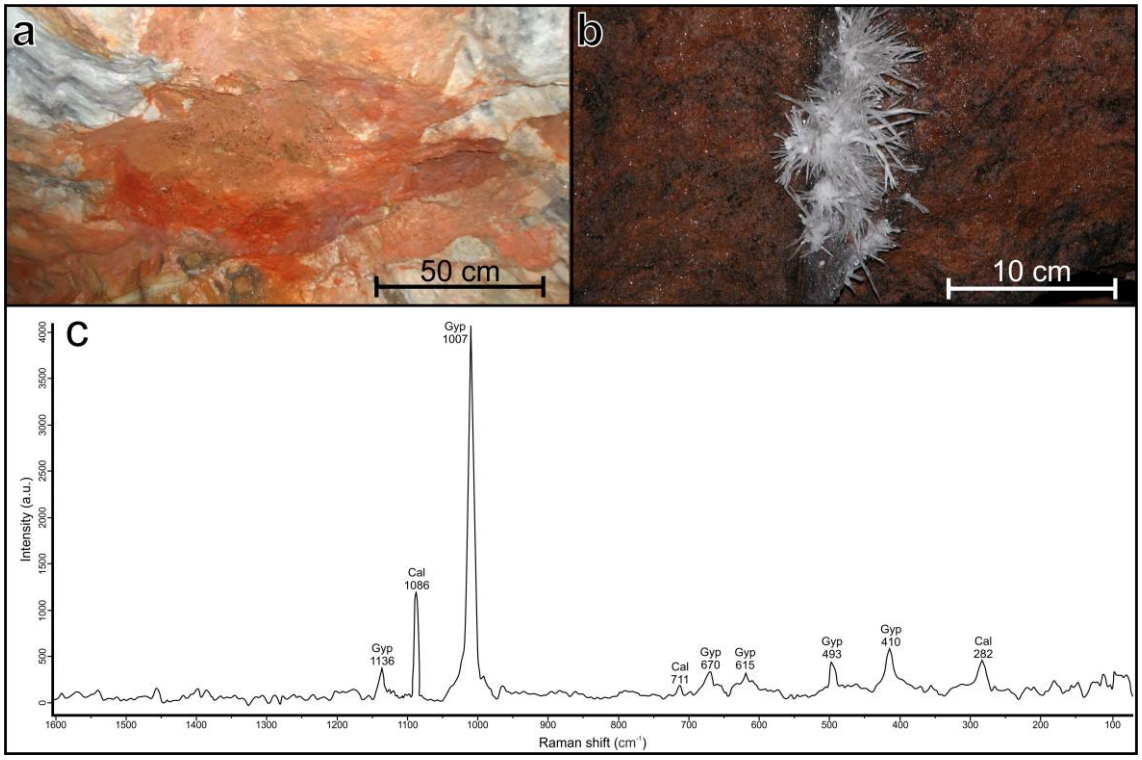


Figure 5.9: Pyrite transformation products on cave walls. (a, b) Iron oxides forming a thin layer under speleothems. (c) Raman results detecting gypsum (ExoMars project).

## 5.6 HYDROGEOLOGY

The Cerro del Castillo hill, where the cave is emplaced, pertains to the Sierra de Aracena aquifer (IGME, 2006). It is constituted by marbles, intercalated within low permeability quartzites and gneisses, laterally covered by recent sedimentary deposits around the hill. The dolomitic marbles have low thickness and minor lateral extension, and their permeability is largely due to fractures and karstic conduits and caves. Recharge occurs by direct infiltration from rain water. Reloading appears to exceed 400 mm/yr. Given the small extension of the aquifer, the natural discharge should be about 3 l/s (Pulido

Bosch *et al.*, 1997). The water entering the system, especially during autumn and winter rain, creates maximum groundwater level fluctuations of about 3 m; yet natural fluctuation should be higher, since artificial drainage systems are operated when there is a risk of flooding in the galleries visited by tourists. There are water connections between the saturated zone of the Cerro del Castillo and wells located more than 300 m from the cavity, dug in alluvial detrital materials beneath the village, producing simultaneous fluctuations of groundwater level (Pulido Bosch *et al.*, 1997).

To obtain further information on the hydrogeological aquifer system and its extension, piezometric observations were made in the Cerro del Castillo and surrounding area from March to April 2013. Little data is available on the circulation flow system in the carbonates of the hill due to the absence of drills. Interpretation is restricted to the surrounding drill information and one point cave observations. The general flow system is characterised by the circulation of two flows surrounding the hill, from NNE to SSW, and it bifurcates at the contact with isotropic granodiorites. The flows converge southwest of the study area (Fig. 5.10) where there are at least three springs that could explain the natural drainage of this small carbonate outcrop.

The isohypses map in Figure 5.10 points to the entry of water into the aquifer from Cambrian carbonate-Quaternary detrital sediments to the N, a largely urbanized area. There may be leaks of sewer water from the town, which would explain the relatively high concentrations of nitrates and nitrites in the waters of the Great Lake within the cave (Jiménez-Sánchez *et al.*, 2008).

The hydrochemical information corresponds to various water sampling campaigns conducted during 2005 and 2006 (López-Chicano *et al.*, 2010) within the cavity. The most mineralized waters (0.7-0.8 g/l of dissolved salts) correspond to the Great Lake, and are

similar to those from springs south of the hill. The remaining sampled points inside (or from dripping stalactite gours) have less mineralized waters, but almost systematically

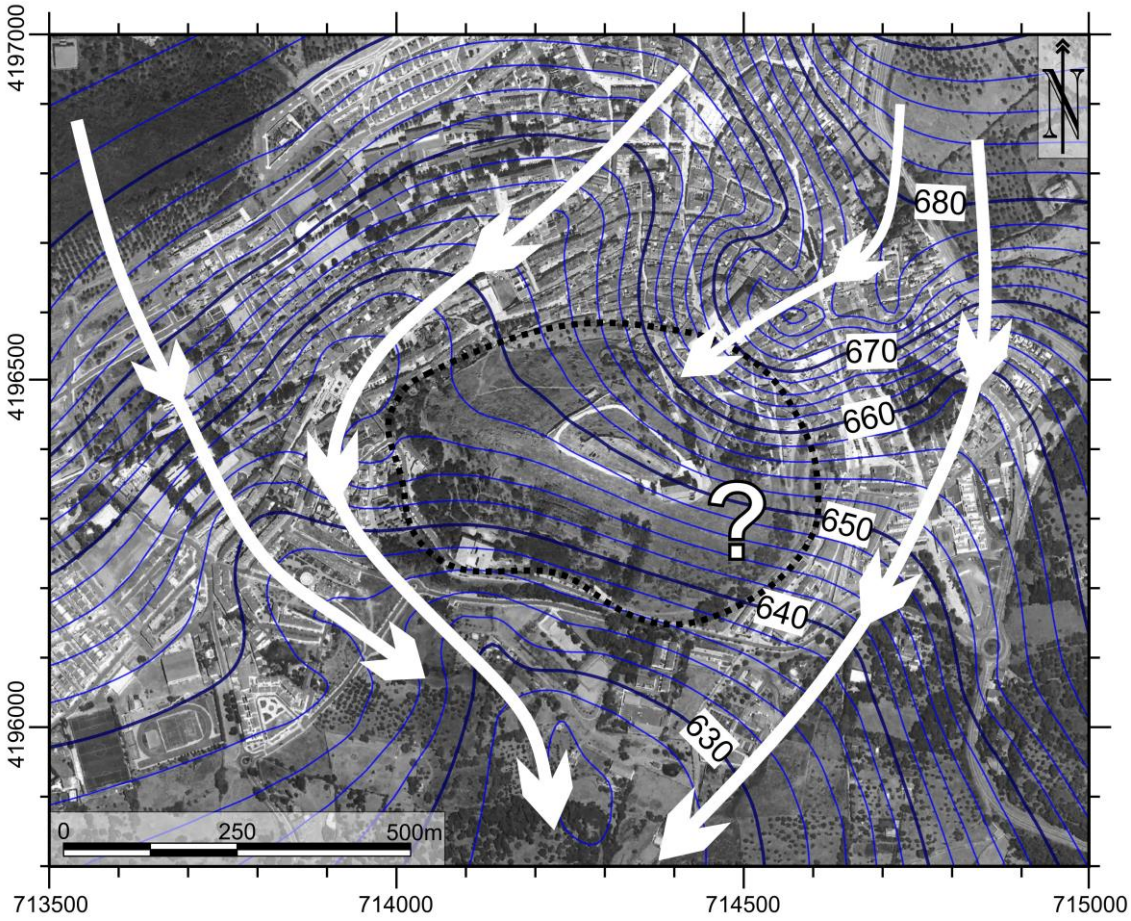


Figure 5.10: Maps of isohypses. Water table location is given in meters above sea level. Hill contours highlighted with dashed black line.

saturated or supersaturated in calcite and aragonite. However, this is not the case of the Great Lake groundwater (Table 5.1), where sampling campaigns revealed the waters to be in balance or subsaturated in calcite and aragonite.

All campaigns show water enrichments in $SO_4^{2-}$ with respect to storm and infiltration water, which could come from the oxidation of sulphide mineralized host rock. Also observed are significant enrichments in Cl-, Na + and $NO^{3-}$.

| Place | Data (dd/mm/yr) | CE | pH | Eh | $O_2$ | $Cl^-$ | $SO_4^{2-}$ | $HCO_4^-$ | $Ca^{2+}$ | $Mg^{2+}$ | $Na^+$ | $K^+$ | $NO_3^-$ |
|---|---|---|---|---|---|---|---|---|---|---|---|---|---|
| Great Lake | 21/10/2005 | 598 | 7.79 | | | 24.5 | 55.0 | 234.0 | 92.0 | 12.8 | 18.3 | 1.9 | 34.9 |
| | 12/11/2005 | 592 | 8.21 | | | 24.6 | 55.6 | 234.5 | 92.9 | 13.0 | 18.5 | 2.1 | 35.1 |
| | 21/12/2005 | 572 | 7.69 | | | 22.7 | 52.1 | 223.3 | 89.0 | 12.3 | 16.9 | 2.9 | 32.4 |
| | 07/02/2006 | 582 | 7.27 | 226 | 6.19 | 23.2 | 53.5 | 231.9 | 89.7 | 12.2 | 17.0 | 2.7 | 32.4 |
| | 28/03/2006 | 532 | 7.36 | 299 | 6.42 | 19.2 | 40.9 | 213.6 | 84.5 | 10.4 | 14.2 | 3.1 | 30.5 |
| | 27/09/2006 | 586 | 7.19 | 232 | 4.39 | 24.5 | 48.9 | 253.2 | 53.2 | 8.7 | 14.8 | 2.4 | 32.4 |

| Place | Data (dd/mm/yr) | IS Aragonite | IS Calcite | IS Dolomite | IS Gypsum | IS Anhidrite |
|---|---|---|---|---|---|---|
| Great Lake | 21/10/2005 | 0.44 | 0.59 | 0.56 | -1.77 | -2.01 |
| | 12/11/2005 | 0.84 | 0.99 | 1.38 | -1.77 | -2.01 |
| | 21/12/2005 | 0.31 | 0.46 | 0.30 | -1.80 | -2.04 |
| | 07/02/2006 | -0.09 | 0.06 | -0.50 | -1.79 | -2.03 |
| | 28/03/2006 | -0.05 | 0.10 | -0.46 | -1.91 | -2.15 |
| | 27/09/2006 | -0.33 | -0.18 | -0.91 | -2.00 | -2.24 |

Table 5.1. Analytical results of water samples for the Great Lake. The electrical conductivity (EC) is expressed in μS/cm at 25 °C, redox potential (Eh) in mvolt, pH in units and all other concentrations in mg/l. IS expresses the saturation index of the mineral.

## 5.7 DISCUSSION

The Gruta de las Maravillas cave formed as the result of the interaction of the tectonic structure —particularly relevant are the pyrite bands intercalated within the marbles— and the evolution of the water table. Analysis of each one of these factors led us to the proposal of a new model for the origin and evolution of sulphur-bearing marble and limestone related caves.

### 5.7.1 Geological structures and their relationship with Gruta de las Maravillas

The lithological sequence of the Cerro del Castillo, from bottom to top, consists of granodiorites, marbles, quartzites and gneisses. The granodiorites were emplaced during the thermal peak of the regional metamorphism affecting the Aracena Belt.

The marbles constitute the karst system harbouring the cave. The main foliation trends N110ºE and dips roughly 60º-80º NE. Ductile deformation structures are widely distributed and include NW-SE oriented folds, S-C fabric, boudins and porphyroblasts with sigmoidal morphology that roughly suggest sinistral transpressive shearing, according to regional studies (e.g., Díaz-Azpiroz and Fernández, 2005). Paleostress analysis shows that the main brittle compression occurred in a NE-SW direction and developed a main fracture set with this orientation. The orientation and morphology from main cave passages is constrained by the orientation of the main foliation and the joint sets. There are oblique galleries (e.g. at the beginning of the cave, near the entry) associated with joint systems (Fig. 5.6, stations 10, 11 and 12) and the major collapse of previously oriented galleries.

The interdigitated lateral contacts between insoluble quartzites (as compared with marbles) provide for cave wall stability, thus preventing collapse. Finally, the presence of impermeable gneisses in contact with the marbles at the top of the sequence constitutes the lateral NE boundary of the karstic system.

### 5.7.2 The origin of the cave related to the presence of pyrite

The pyrite transformation is produced under certain environmental conditions. The disseminated pyrite is a primary mineral, and the contact with water and air (20% oxygen) could provoke its transformation into iron oxide, sulphates and hydroxides (Descotes *et al.*, 2003), according to equation (1). This is a very slow chemical process (Berner, 1984) which would result in acidic waters with high dissolution power in carbonate rocks (equation 2). This transformation took place in several stages in the Cerro del Castillo (Fig. 5.11). In the first stage, when the water table was located at the top of the hill (Fig. 5.11a), the pyrite was found under phreatic conditions without oxygen-free water. Hence, pyrite transformation was avoided. Subsequently, the hill underwent erosion of its contours and the water table descended, leaving the pyrite crystal under vadose conditions (Fig. 5.11b),

where oxygen was present. Rain infiltration, together with the presence of oxygen, initiated the transformation of pyrite into its secondary products. The low permeability of the marbles determines a very slow process: water mostly infiltrated along discontinuities parallel to the foliation or to the joints. These secondary products remain at the surface of the water table, where the lateral dissolution of the cave started due to the presence of acidic waters (Fig. 5.11c). Moreover, iron oxides and gypsum precipitated and covered the cave walls. After these early stages, permeability increased along the new conducts and the cave extended along the water table surface (Fig. 5.11d). Speleothems started to form in a final stage, after the end of the initial dissolution stages due to the pyrite reactions and other karstic processes (Fig. 5.11e). This evolutionary process was repeated during the development of the three levels (first taking place in the uppermost level).

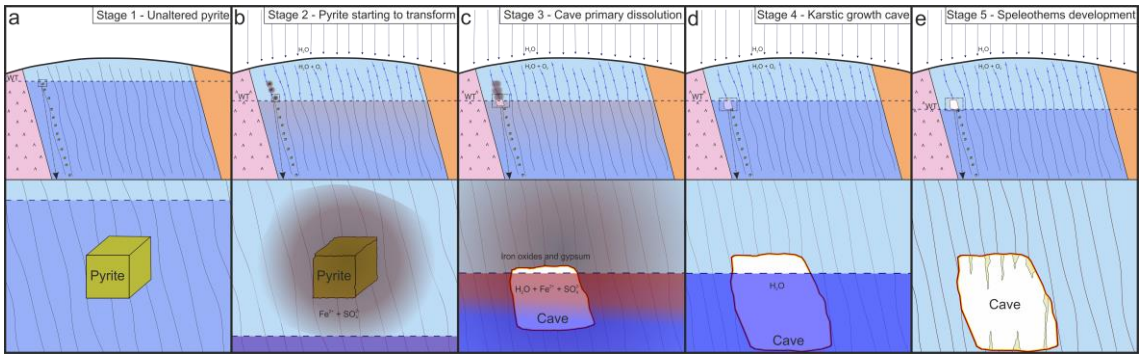


Figure 5.11: Schematic diagram of pyrite transformation and its evolution in Cerro del Castillo hill. (a) Pyrite under phreatic conditions. (b) Pyrite transforming to iron oxides, gypsum and acid waters. (c) Cave creation. (d) Cave evolution. (e) Speleothem construction and other predominant karstic processes.

The Raman spectroscopy results reveal that conditions changed during the cave formation. Sulphuric acid caves usually contain high quantities of gypsum crystal within the cavity. In the Gruta de las Maravillas cave, the gypsum is found between the host rock and the speleothems, in the form of thin layers of microcrystals. Moreover, hydrochemical analyis detects waters subsaturated in sulphates and, sometimes, in carbonates; hence, in the first stage of the cave formation the principal dissolution phenomenon would have been restricted to pyrite transformation. Later, the amount of pyrite present above the water table

decreased, and the dissolution of the cave mainly entailed water enriched in $CO_2$. The current cave dimensions are most likely tied to the amount of pyrite present in the hill during the cave formation. Nowadays, the proportions of pyrite crystal found near the cave are low, while iron oxides are the more widespread pyrite transformation results, and they are dragged into the cave by rainwater.

The cave position is closely linked to the pyrite band location (Fig. 5.12). As shown in the 3D model, the pyrite band is very close to the southern galleries of the cave and crosses the deep end of the cave, where major dissolution took place.

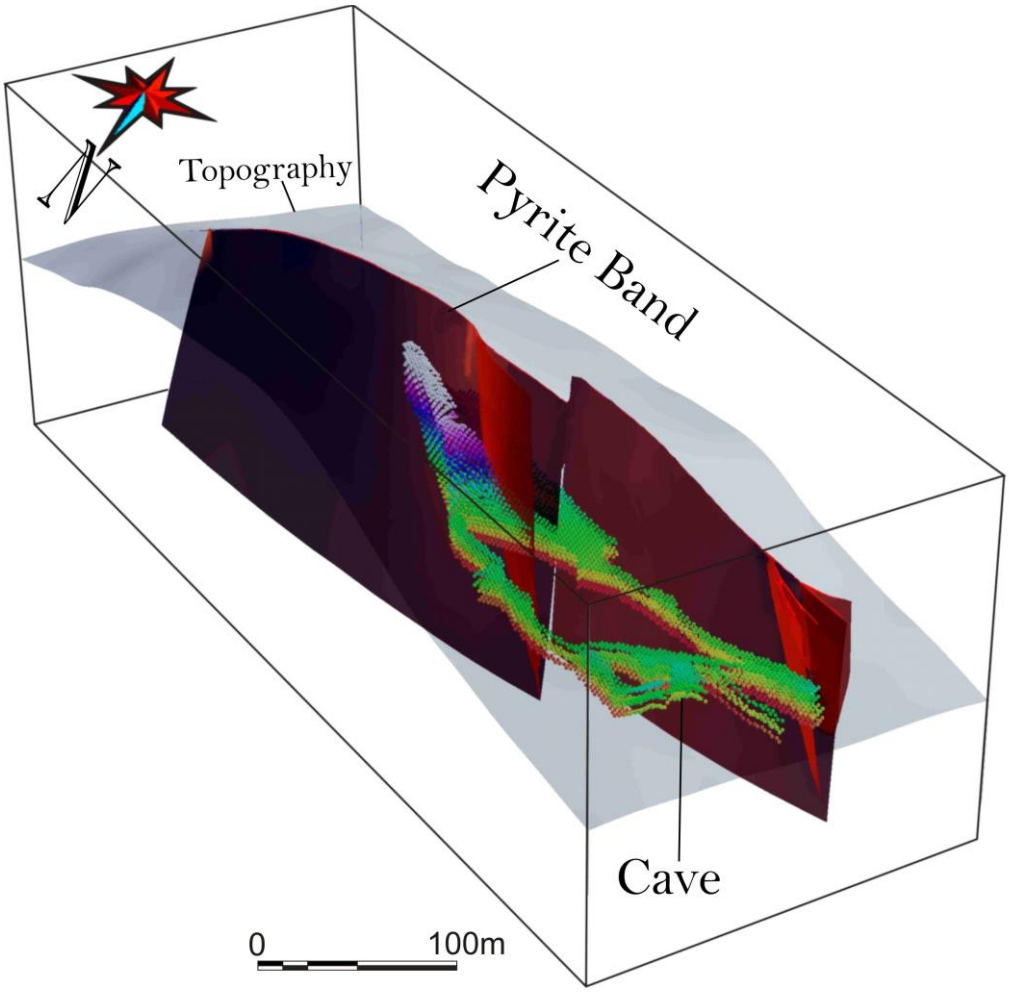


Figure 5.12: 3D view of the cave and pyrite band in their relative positions.

### 5.7.3 Evolution of the cave

The Gruta de las Maravillas, with its three levels and predominantly horizontal morphology (Fig. 5.7), is closely linked to outside hydrogeological changes. Dissolution (Fig. 5.13) started in the uppermost level 3, when the water table was located at the top of this level (~700 m.a.s.l., Fig. 5.13a). Later, the level of the water table descended as a consequence of the erosion of the hill contours, to become located at the top of level 2 (~675 m.a.s.l., Fig. 5.13b) and develop dissolution there. This level presents lower horizontal development, in part due to a slow but steady decline of the water table. Finally, the water table came to be located at the top of level 1 (~660 m.a.s.l., Fig. 5.13c), creating greater horizontal extension; this is where the entry lies, at the base of the hill. At present, the water table is located at 650 m.a.s.l. (Figs. 5.8a and 5.13d), probably building a new lower level. Throughout the cave evolution, water table fluctuations have given rise to speleothems of a vadose or phreatic nature.

The division into three predominantly horizontal levels evidences that the cave´s formation is directly linked with the evolution of the water table. Many speleothems can be traced to the first stage of the cave formation, entailing rapidly dissolving phreatic waters. In the second stage, speleothems formed in vadose and/or phreatic conditions. Later, in the third stage, rain water padded the galleries, creating gours and starting calcite precipitations. Finally, water found an outlet and began to form speleothems corresponding to the vadose zone, over the previous ones. Therefore, the rapid dissolution of the first stage along the main foliation direction, parallel to the pyrite bands, was followed by a stage of slow deposit creation.

The deep end of the cave —at the centre of the hill, beneath the highest topographic levels— is interrupted by chaotic blocks as a consequence of a major collapse (Fig. 5.8c)

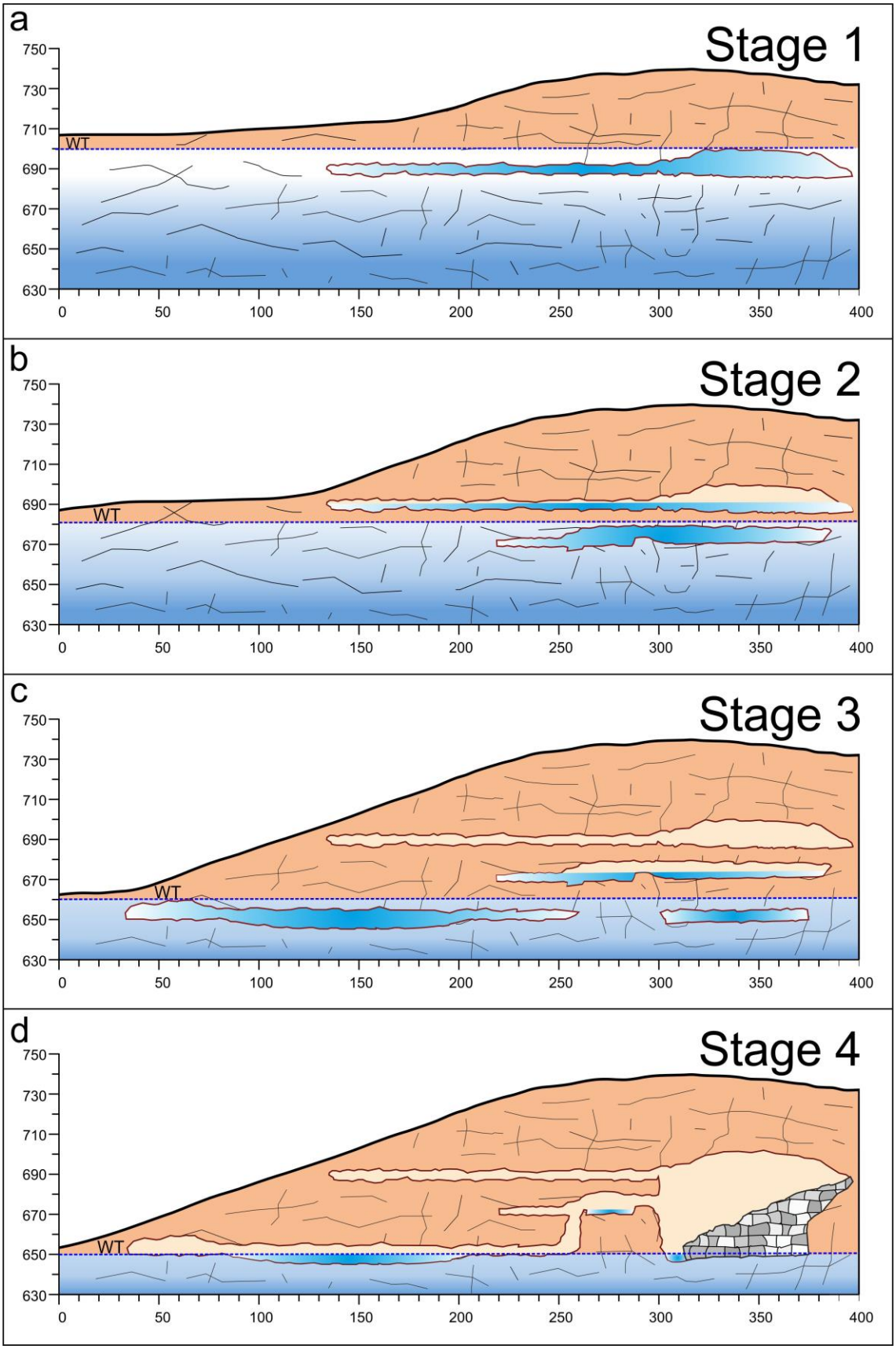


Figure 5.13: Interpretive sketch of the Gruta de las Maravillas evolution.

that mixed rocks from the bottoms of levels 2 and 3. Afterwards, with more rock mass to be dissolved, there was a tendency of destabilization and collapse. Other parts of these levels with less vertical development remain stable.

Currently, the cave evolves into a normal epigenic regime in which the dissolution of the host rock owes to meteoric waters entering the subsaturated carbonate aquifer. The role of sulphide oxidation as a source of acidification source seems to have lost significance at this stage.

It would appear logical that the visible pyrite mineralization is the origin of sulfuric acid in the early stages of karstification. The large size of the cavity and the morphologies developed within it suggest a hypogenic origin favoured by early $H_2S$-laden rising deep fluid.

## 5.8 CONCLUSIONS

The Gruta de la Maravillas is developed in the marbles of the Cerro del Castillo hill of the Aracena Metamorphic Belt. Marbles are interfingered with quartzites and located between granodiorites at the bottom, and gneisses at the top. These igneous and metamorphic rocks are deformed in ductile conditions by isoclinal folds, SC-fabrics and boudins. The late brittle deformation is related to NE-SW compression and orthogonal extension that develops a main NE-SW tensional fracture set, and locally two shear or hybrid joint sets.

The cave morphology is directly linked with structural control in conjunction with a progressive water table drop. The principal galleries have a predominantly N110ºE direction and a dip towards the NE, defined mainly by the host rock foliation and secondarily by the main fractures. The water table was located at three different levels in the past, determining the cave´s horizontal extension, the gallery morphologies and

speleothem development. In addition, gravity processes were active in galleries such as the Great Lake, formed by the collapse of destabilization zones and direct dissolution.

The origin of the Gruta de las Maravillas is linked to the presence of the disseminated pyrite bands in marbles. On the one hand, its transformation into iron oxides provides acidic waters that accelerate dissolution of the cave. On the other hand, iron oxides and gypsum remain covering the cave walls. The host igneous and metamorphic rocks, after marble dissolution, stabilize the cave.

The particular combination of lithological, structural and hydrogeological conditions of the Gruta de las Maravillas cave lead one to suspect the presence of cavities elsewhere, formed in similar settings. The fact that pyrite disseminated in marbles near or inside the cave is closely related with the cave formation could contribute to the discovery of new caves by means of surface field observation.

## ACKNOWLEDGEMENTS

We would like to thank to the ExoMars project (developing the Raman instrument for mission ExoMars of the ESA [ESP2013-48427-C3-2-R], Science and Innovation Ministry, Spanish Government) for the Raman results performed inside the cave. We thank Carlos Marín for help in the preparation of figures. Moreover, we gratefully acknowledge the support provided by the Gruta de las Maravillas staff and Aracena City Council. This research was funded by Aracena City Council projects C-3726–00, C-3727–00, the Spanish Government through projects CGL2010-21048 and P09-RNM-5388, and the RNM148 research group of the Junta de Andalucía.

# Chapter 6

## Geophysics of Gruta de las Maravillas karst system

# Integrated geophysical methods for studying the karst system of Gruta de las Maravillas (Aracena, Southwest Spain)

F.J. Martínez-Moreno[a], J. Galindo-Zaldívar[a,b], A. Pedrera[b], T. Teixido[c], P. Ruano[a,b], J.A. Peña[c], L. González-Castillo[a], A. Ruiz-Constán[d], M. López-Chicano[a], W. Martín-Rosales[a]

[a] Departamento de Geodinámica, Universidad de Granada, 18071-Granada, Spain

[b] Instituto Andaluz de Ciencias de la Tierra, CSIC-Universidad de Granada, 18071-Granada, Spain

[c] Instituto Andaluz de Geofísica y Prevención de Desastres Sísmicos, Universidad de Granada, 18001-Granada, Spain

[d] Instituto Geológico y Minero de España, Ríos Rosas 23, 28003-Madrid, Spain

Published on:

**Journal of Applied Geophysics**

Vol. 107, 149-162

*DOI: 10.1016/j.jappgeo.2014.05.021*

Received 7 March 2014

Accepted 23 May 2014

**ABSTRACT**

In this study we contrast the results of different geophysical methods in order to describe the karst system surrounding of the Gruta de las Maravillas cave (Aracena, Spain). A comprehensive study of the geophysical responses of the known cavity was carried out, after which several sections were studied to detect the karst architecture and cave continuity. To ensure precision, the inner 3D-topography of the cave was determined by classical geodetic techniques and a digital terrain model was performed with differential GPS. The microgravity method was used to obtain the residual gravity map of the entire study zone, whose minima could be related to caves. Then, the negative gravity anomalies were analyzed to plan several lines for implementing further geophysical methods: magnetic profiles (MP), electrical resistivity tomography (ERT), induced polarization (IP), 2D seismic prospection (refraction tomography and reflection sections) and ground penetrating radar (GPR). The resulting models for each line explored were integrated with detailed geological maps to establish the unknown continuity of the caves. Finally, we discuss the suitability of each geophysical technique for cave detection in marble with sulfur host rock and propose the best procedures to constrain their geometries.

**HIGHLIGHTS**

- Combined geophysical methods are integrated in cave prospecting.
- Microgravity survey with differential GPS is the best reconnaissance method.
- ERT, seismic, GPR and magnetic researches provide precise results.
- The response in a known cave is extrapolated to research unknown areas.
- Aracena cave, located in marbles, is formed by sulfur related acid waters.

**Keywords:** Geophysical cave detection; Residual gravity anomaly; Electrical resistivity tomography (ERT); Magnetic anomaly profiles; Seismic prospection; Ground penetrating radar (GPR)

## 6.1 INTRODUCTION

Geophysical methods are commonly applied to detect the presence of caves, given the high contrast with the host rock in terms of density, electrical and seismic properties. Single geophysical prospecting methods such as gravimetric prospecting (Chico, 1964), electrical resistivity tomography (ERT) (Martínez-Pagán *et al.*, 2013), ground penetrating radar (GPR) (McMechan *et al.*, 1998 and Robert and de Bosset, 1994) or seismic methods (Rechtien and Stewart, 1975) have provided possible solutions for determining cave geometry and the surrounding subsurface geological structure. Yet in some specific geological contexts, such as complex karst systems, a particular geophysical method can only give partial information. This occurs because it is focused on a specific physical property, and the recorded data tends to be masked by the special environment conditions. Additionally, when there is a strong contrast in physical properties between the cave and the host rock, the inverted models are more divergent and poorly fit the observed data, making the solutions less reliable (Loke, 2013). In order to reduce uncertainty and avoid misinterpretations based on a single method, combinations of several geophysical methods have been applied in cave studies (Table 6.1).

The selection of the most appropriate methods and their success rate on cave detection depends on several factors. These include: i) The size, depth and morphology of the cave; ii) The lithology where the cave is enclosed (rocks, homogeneity, isotropy, fractures; etc.); iii) Water content of the rock matrix, and the presence of air, water or both within the cave; and iv) The salinity of the water filling the cave and the nature of the precipitates (i.e. the presence of decalcification clay).

The aim of this research is to test different geophysical methods and their combination in cavity detection in mineralized marbles. We carried out a microgravity

survey, two magnetic profiles (MP), four ERT profiles, four induced polarization (IP) profiles, four seismic refraction and reflection profiles, and two GPR profiles, testing and comparing their capacity to detect cavities in the karst system of the Gruta de las Maravillas (Aracena, Spain).

| *Author, year* | *Methods* |
|---|---|
| Beres *et al.* (2001) | GPR and MG |
| Bozzo *et al.* (1996) | EM, ERT, SRT |
| Brown *et al.* (2011) | MG, GPR, ERT, IP |
| Butler (1984) | MG and G gradient |
| Cardarelli *et al.* (2003) | GPR, SR, SRT |
| Cardarelli *et al.* (2010) | ERT and SRT |
| Carriere *et al.* (2013) | ERT and GPR |
| Chamon and Dobereiner (1988) | ERT, M, G, EM |
| El-Qady *et al.* (2005) | ERT and GPR |
| Gambetta *et al.* (2011) | G and ERT |
| Gautam *et al.* (2000) | GR and ERT |
| Gibson *et al.* (2004) | ERT and MG |
| Gómez-Ortiz and Martin-Crespo (2012) | GPR and ERT |
| Holub and Dumitrescu (1994) | ERT and VES |
| Keydar *et al.* (2010) | SW and DW |
| Lange (1999) | EM, G, NP |
| Lazzari *et al.* (2010) | GPR and ERT |
| Leucci (2006) | GPR and ERT |
| Leucci and Giorgi (2005) | ERT and GPR |
| Leucci and Giorgi (2010) | GPR and MG |
| Martínez-Moreno *et al.* (2013) | MG, ERT, IP |
| McGrath *et al.* (2002) | MG and ERT |
| Mochales *et al.* (2008) | G, M, GPR |
| Orlando (2013) | GPR and ERT |
| Rădulescu *et al.* (2007) | ERT and VES |
| Ulugergerli and Akca (2006) | GPR, ERT, SRT |
| Vadillo *et al.* (2012) | CCG and GPR |
| Valois *et al.* (2010) | ERT and SRT |
| Xia *et al.* (2007) | RW and ERT |

Table 6.1. Combination of geophysical methods applied to the study of cavities. Electrical methods: CCG — Capacity-Coupled Geoelectrics, ERT — Electrical Resistivity Tomography, IP — Induced Polarization, VES — Vertical Electrical Soundings; Electromagnetic methods: GPR — Ground Penetration Radar, NP — Natural Potential, EM — Electromagnetic, GR — Gamma Ray; Gravity methods: G — Gravimetry, MG — Microgravimetry; Magnetic methods: M — Magnetometry; Seismic Methods: SRT — Seismic Reflection/Refraction Tomography, SR — Seismic Refraction, DW — Diffracted waves, RW — Rayleigh waves, SW — Seismic Wavefield.

## 6.2 GEOLOGICAL SETTING AND CAVE DESCRIPTION

The Gruta de las Maravillas lies in a hill called Cerro del Castillo, in the town of Aracena (Huelva province, southwest Spain, Fig. 6.1a). The cave developed in marbles included within the Aracena Metamorphic Belt (Crespo-Blanc and Orozco, 1988). This band, together with the Beja-Acebuches Ophiolites, forms the Aracena Massif (Bard and Moine, 1979), with a width of 10 km and a length of 100 km. The Aracena Massif is located at the boundary between the Ossa-Morena Zone (OMZ) and the South-Portuguese Zone (SPZ), two major tectono-stratigraphic units of the Iberian Massif.

The studied area is restricted to the hill formed by marbles and quartzites — highly deformed in ductile conditions — as well as granodiorites and gneiss (Fig. 6.1b). The marble containing the cave shows a penetrative compositional banding that trends N110°E and dips 70°–80° toward the NE. The cave extends 300 m in a WNW–ESE direction controlled by the presence of mineralized braided bands of pyrite mainly parallel to the metamorphic bands. The dissolution of the pyrite provides iron oxides that can be recognized in the walls of the cave. The cave is formed by three main dissolution levels: level 1 (~ 650 m.a.s.l.), level 2 (~ 665 m.a.s.l.) and level 3 (~ 685 m.a.s.l.) (Martín-Rosales *et al.*, 1999 and Pulido-Bosch *et al.*, 1997). That is, dissolution progressed from level 3 (shallowest) to level 1 (deepest). At present the lower level is partially submerged in 10 m of water. The cave morphology comprises long narrow passages with dimensions under 5 × 5 m, and local large cavities over 40 × 40 m. The two main cave ramifications are artificially connected forming a loop. The largest cavity is located beneath the central part of the hill, where the three dissolution levels are connected leading to a maximum height of 40 m from base to top. A great collapse interrupts continuity of the cave toward the ESE.

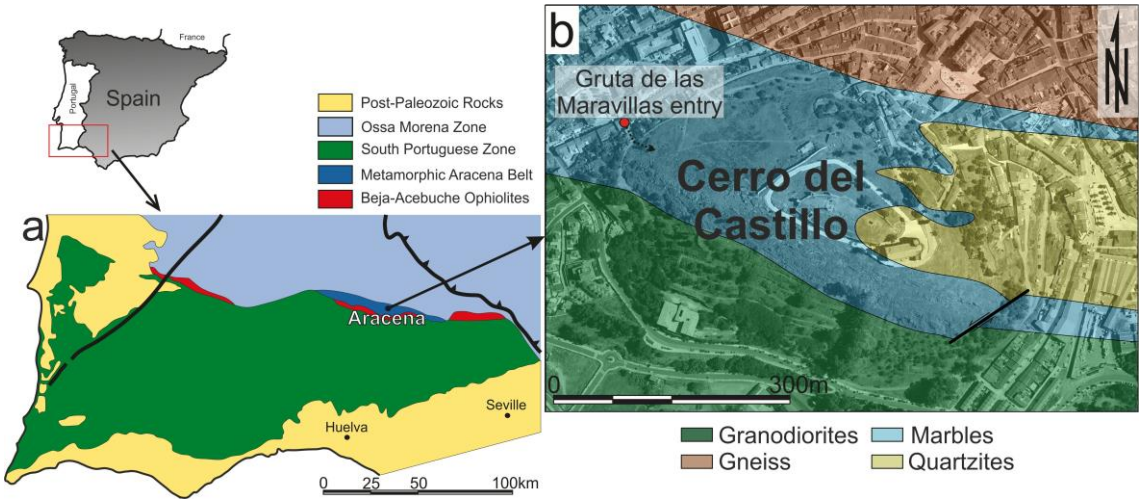


Figure 6.1. Location of the studied area in southwest Spain, by the town of Aracena. (a) Simplified geological scheme. (b) Synthetic geological map of the studied zone. A sinistral fault is identified in the southeast part of the studied zone.

## 6.3 GEODETICAL AND GEOPHYSICAL METHODS

Before carrying out the geophysical exploration, a detailed inner geometry of the cave was obtained using geodesic polygonal methods, and a digital terrain model (DTM) was derived in order to place the cave as well as possible respect to the hill topography. In a second extensive reconnaissance step, a microgravity study was performed to calculate the residual anomaly map and determine the minima, which we related to the presence of cavities. The third step was to define a reference Line 1 over the known cave to test other geophysical methods and correlate their responses. Finally, over the residual anomaly map we defined further inspection lines, mainly focusing on the sectors with relative gravity minima, to investigate the presence of unknown caves at different karstic levels.

### 6.3.1 Cave cartography and local DTM

The inner 3D-mapped cave contours were projected using topographic polygonal methods. A laser distance-meter on a tripod was used to establish distance, pitch, and

azimuth between consecutive reference stations. Moreover, horizontal and vertical distances to the cave walls were noted in each reference site. Thus, a total of 94 reference stations were measured throughout 1037 m, with 188 lateral measurements. The position of the first three stations, located outside the cave, was constrained with differential GPS. Measurements were made forming a loop, where the first point and the last point should share the same position. This procedure allows for correction of errors produced along the track: a RMS error of 1.03% for the horizontal measures, and 0.2% for the vertical distance were corrected (Montoriol-Pous, 1973).

A differential GPS Leica 1200 (reference station) and Leica 1200 + (Real Time Kinematic) connected by a one-watt radio transmitter were used to generate the local DTM. The Leica 1200 GPS system uses error-correction data to fine-tune the position accuracy of each point to ± 0.5–20 mm. A fixed GPS reference station gave coverage of the whole studied area; it was established on a point whose coordinates were determined with respect to the Andalusian Positioning Network, known as RAP (Junta de Andalucía, 2011). The DTM was constructed using a mesh size of 10 × 10 m, which matched the gravimetric measuring point, and geophysics profiles were carefully measured. The coordinate system used was UTM ETRS89.

### 6.3.2 Microgravity prospection

Underground density changes cause variations in the gravity value. Therefore, microgravity prospection serves to find near-surface karstic cavities because there is a good density contrast — i.e. voids with a density of ~ 0 g/cm3, or filled by water ~ 1 g/cm3 enclosed within marbles with ~ 2.7 g/cm3. In the residual gravimetric map we can associate the caves with the negative residual anomalies, and model (approximately) their geometry (McGrath *et al.*, 2002).

A Scintrex CG-5 Autograv gravity meter on a tripod, with an accuracy of ± 0.001 mGal, was used to obtain the gravity data. The gravity survey covers the hill with 1798 measurements sites, taken in cycles shorter than 3 h, and spaced in a 10 × 10 m regular grid. Before measurements, the gravimeter was leveled and calibrated on the tripod to minimize hysteresis effects. The measurements were referred to the Huelva gravimetric base (IGN, 2005). On each gravity site, measurements were repeated during 60–90 s until minimizing the obtained error under ± 0.005 mGal. After tidal and instrumental corrections, the Bouguer anomaly was determined using the standard density of 2.67 g/cm3, close to the median density of the lithologies present in the studied area: granodiorites (2.73 g/cm3), marble (2.7 g/cm3), quartzite (2.63 g/cm3) and gneiss (2.69 g/cm3). Densities were obtained by double weight (air/water) in laboratory experiments. The terrain correction was calculated with Hammer's circle method (Hammer, 1939 and Hammer, 1982) using our local DTM combined with the digital terrain model of IGN, which has a horizontal resolution of 5 m as the topographic base. The maximum radius covered during the terrain correction was 9902 m around each gravity site (zones B to K).

The residual gravity anomaly was calculated after removing the regional anomaly trend by polynomial regression on the Bouguer anomaly tendency. The Bouguer anomaly shows an elongated shape and one degree polynomial regression was applied to remove regional effects. In addition, we performed gravity profiles crossing the most interesting sectors. These profiles were forward modeled using GRAVMAG v.1.7 from the British Geological Survey (Pedley *et al.*, 1993), with 2.5D approximation according to the geological information.

### 6.3.3 Magnetic anomaly profiles

Magnetic research aims to detect the mineralized bands of pyrite that cross the hill and related iron oxides. Total magnetic field data were acquired along two N-S profiles. The profiles cross both sides of the hill with a mean spacing of 10 m between stations. Magnetic measurements were taken using a GSM-8 proton precession magnetometer with an accuracy of ± 1 nT at a mean height of 2 m above the topography level. As anthropic noise (such as ferromagnetic materials or electric power lines) distorts the natural magnetic field, magnetic measurements were not acquired close to the village. Calculation of total magnetic field anomalies was performed by means of a standard procedure, including reduction to the IGRF 2010 (IAGA, 2010); the reference to correct the diurnal variation was the permanent magnetic station located in San Fernando (Cádiz, Spain; www.intermagnet.org). In addition, susceptibility values were measured with an Exploranium KT-9 kappameter.

### 6.3.4 DC electrical methods

The equipment employed for electrical methods in continuous current mode (DC) was a Terrameter SAS 4000 (ABEM, Inc.). This equipment injects current to measure the resistivity of the underground, subsequently stopping injection to measure the IP, with the transient voltage decay in a number of time intervals. The resolution of the equipment is about ± 1 μV.

Four profiles were acquired with a 4-channel multiple gradient electrode array in two combined protocols: GRAD4LX8 and GRAD4S8 (ABEM, 2006). The gradient protocol uses a Wenner-Schlumberger electrode array configuration and it was developed for multi-channel resistivity meter systems (Dahlin and Zhou, 2006). The GRAD4S8 protocol complements the upper data coverage of the GRAD4LX8. Both offer a great

amount of shallow data and sparse deeper data. Considering the accuracy and depth penetration target, electrodes were deployed at 1 m, 2.5 m and 5 m spacing for different profiles, reaching effective penetration depths of ~ 14 m, ~ 30 m and 70 m, respectively.

The inversion data was calculated with RES2DINV software (v.3.59; Geotomo Inc.), using a standard least-square inversion method (Degroot-Hedlin and Constable, 1990, Loke *et al.*, 2003 and Sasaki, 1992) and a model refinement constraint due to the large amount of data. A mesh made up of model cells was applied, increasing in size at greater depth, with 4 nodes per unit electrode spacing and an initial damping factor of 0.3, which reduces the effects of side blocks. The inversion was carried out with finite-elements. Topography modeling involved the use of the least-square straight line and Schwartz–Christoffel transformation (Spiegel *et al.*, 1980).

The empirical depth of investigation (DOI) index method (Marescot *et al.*, 2003 and Oldenburg and Li, 1999) was calculated carrying out two data inversions using different resistivity backgrounds (Loke, 2013). The main difficulty in computing the normalized empirical DOI lies in deciding the cut-off value where the inversion values are reliable. Marescot *et al.* (2003) recommended a cut-off value of 0.1 or 0.2, and for this work we use the more restrictive value of 0.1.

*6.3.4.1. Forward modeling*

In order to understand the resistivity response of the known cave, we generated 2D forward models (Loke, 2002) using RES2DMOD software (v.3.0, Geotomo Inc.) to examine the effect of the void within marble for certain cases, for instance when cave walls are covered by a conductive layer of pyrite and iron oxides, as in many sectors of the Gruta de las Maravillas. The synthetic apparent resistivity pseudo-sections obtained were inverted using the same inversion software (RES2DINV; v3.59) as used to process

the pseudo-sections measured in the field; and we applied the same parameters and treatment flow.

Five forward models with marbles (50,000 Ω·m), air (1,000,000 Ω·m) and a different distribution of iron oxides (1 Ω·m) are shown in Fig. 6.2. We modeled a cave completely covered by iron oxides (model 1), one with iron oxides only in the lateral wall and the roof (model 2), or only in the roof (model 3), disseminated iron oxide only in the roof (model 4), and a cave without iron oxides (model 5). The inversion parameters used are the same as those applied on the field profiles. The cave without iron oxides gets the expected resistivity response in the ERT profiles (Gómez-Ortiz and Martín-Crespo, 2012). In contrast, caves with different iron oxide wall coverage show lower resistivity values than cave without them.

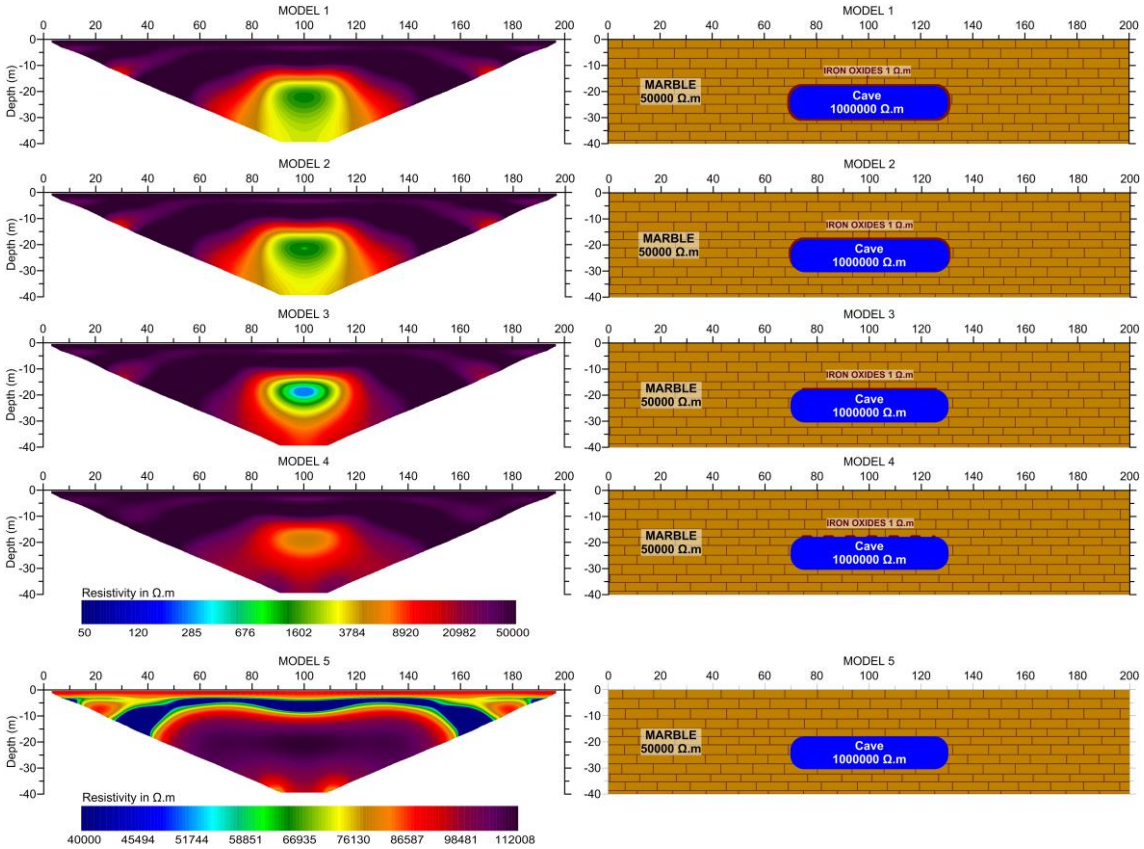


Figure 6.2. Forward modeling of ERT profiles including synthetic models and inverted pseudosections.

### 6.3.5 GPR profiles

GPR profiles are commonly used in shallow cave detection because the amplitudes of reflected-diffracted electromagnetic (EM) waves generated atop a cavity can be detected on the radargram section (Boubaki *et al.*, 2011, Lee, 2011, McGraw, 2010 and Ulugergerli and Akca, 2006). GSSI equipment with 80 and 40 MHz antennas was employed, respectively, with 2 m and 3 m of transmitter–receptor separation. In both cases, the measurement interval was 0.1 m, with 1024 samples for a time window of 400 ns. The commercial software RADAN (v.6.5, GSSI, Inc.) was used to process the collected data. In this case, only a simple flow (background removal, filtering horizontal pass-band and topographic correction) was applied because the objective was to emphasize only the relevant diffraction-reflections due to the top and the lateral walls of the cave; this meant not compensating the amplitude attenuation due to geometrical divergence and not migrating the radargrams.

Since the EM wave velocities could then be estimated, approximate depth is given. In the study zone the EM waves in the marbles were taken about 0.4 m/ns and the average distances to the top test cave from the GPR test profile were 16 m (coinciding with a section of the cave). Thus, reflections from top-walls should be observed within the 80 ns, while the rest of the GPR facies would contain information about other subsurface reflectors. Due to the sharp topography, however, only two GPR profiles were acquired.

### 6.3.6 Seismic exploration

We applied several seismic techniques to the raw data in order to determine, as precisely as possible, the karst cavities and then evaluate their detection capability. The seismic wave fronts interact with the walls of a cavity, related to inversion of velocities due to the presence of air. This low-velocity body produces diffractions, amplitude

absorptions and frequency changes, and ray-path anomalous coverage (Di Fiore *et al.*, 2013, Flecha *et al.*, 2004 and Grandjean and Leparoux, 2004).

A Stratavisor-NZ seismometer of 24 channels was used, with a steel plate and a hammer of 8 kg for the shots. Explosives were used to obtain deeper information in some profiles. For all seismic profiles, the sample time interval was 0.021 ms, with a time window of 500 ms. The geophone interval ranges were 5 m, 3 m and 1.5 m. In all cases, reflection spread data acquisition is based on a short offset shooting, placing the shot at half distance of geophone spacing in front of the first active station, selected with a roll-along switch (48I/24O). When all seismic profiles had been acquired, inverse offset shooting was performed. As result, 24-fold CDP coverage is available. Additionally, planned shots were executed in order to obtain good refraction spread coverage.

To process the raw seismic data, various packages were used: 1) the RayFract TM (v.32; Intelligent Resouces, Inc.) seismic refraction tomography code allowed us to obtain the P-wave velocity field and its ray tracing coverage map. The effects of a cavity in seismic refraction tomography are smeared, while smoothed velocities are due to the presence of air. In some cases, little or filled cavities, such effects are indistinguishable from the surrounding host rocks. The ray coverage around a cavity is decreased because of the low velocity, creating a defocusing of effect (Riddle *et al.*, 2010). 2) The VSUNT-Pro21 (Geosoft, Inc.) commercial code and SU (Seismic Unix, Center of wave phenomena) free routines code were used to process the seismic reflection sections. In this case, we generated common offset short-receiver sections over the instantaneous frequency images to better define the cavities. They are given by changes in the amplitude trace and the high frequency absorption (Teixidó, 2000). The seismic reflection section was also carried out.

## 6.4 GEOPHYSICAL RESULTS

### 6.4.1 Gravity anomalies

The Bouguer anomaly map presents values ranging from 36.1 to 39 mGal (Fig. 6.3a) and the variation of the regional anomaly goes from 38.7 mGal to 36.0 mGal — a range of 2.7 mGal, decreasing from SW to NE (dashed black lines in Fig. 6.3b). The residual gravity anomaly map (Fig. 6.3b) shows three major domains elongated in a WNW–ESE direction, coinciding with the main Gruta de la Maravillas direction. Two positive anomalies with values ranging from 0.15 mGal to 0.45 mGal are located at the northeastern and southwestern borders of the hill. Relative minimum anomalies with shorter spatial wavelength are recognized in between the positive anomaly edges associated with isolated fractures or small cavities. The minimum values of the residual anomaly (-0.7 to -0.5 mGal) are concentrated in the central part of the hill and suggest shallow cavities that could be related with an uppermost karstic level. Around them, a large secondary minima anomaly (between − 0.5 and − 0.1 mGal) matches the known mapped cave toward the NW. This band fits with the largest rooms of the known cave, suggesting the detection of karstic levels 3 and 2. However, the narrow ducts of karstic level 1 with loop morphology do not generate enough measurable gravity anomalies, owing to their small dimensions and high depth (34 to 60 m from the surface). Minima of residual gravity anomalies, even more intense than those linked to the known cave and elongated in the same direction, are found in the southeastern part of the hill. Particularly prominent is the minimum located at coordinates 4,196,400N and 714400E, which reaches values as low as -0.7 mGal.

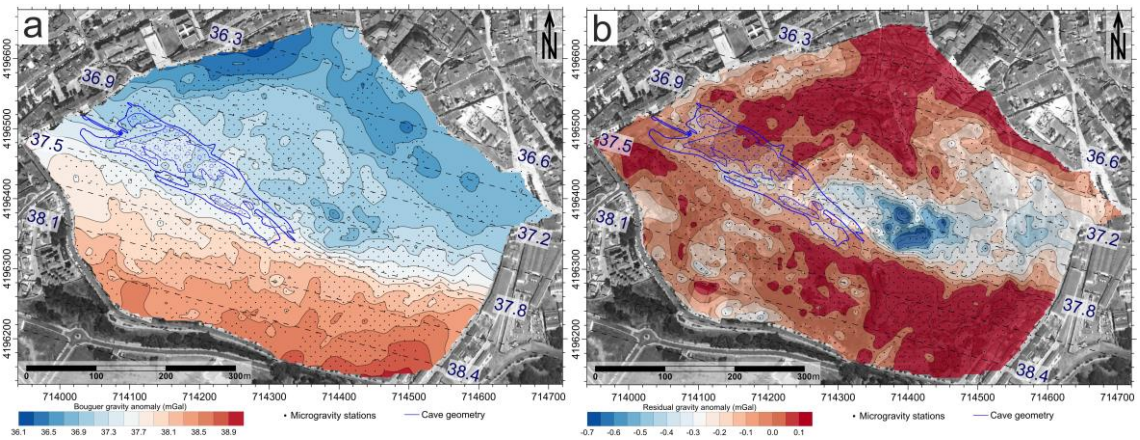


Figure 6.3. Gravity anomaly maps of the Cerro del Castillo hill. (a) Bouguer anomaly map. (b) Residual anomaly map including regional anomalies marked with dashed lines. The cave contour is traced with black lines west of the hill in both maps. The measured microgravity stations are marked with dots.

### 6.4.2 Magnetic anomalies

The Aeromagnetic map (Fig. 6.4a; IGME, 1997) shows large dipoles parallel to geologic structures with total magnetic field intensity values from 43,200 nT to 43,500 nT. The hill is characterized by a SW minimum and a NE maximum, the two related to different dipoles extending outside the study area.

In order to determine shallow and local anomalies, two field magnetic profiles were measured. They show a prominent residual magnetic minimum (Fig. 6.4b) related to a shallow mineralized band with remnant magnetism. The profile in the western side of the hill crossing the known cave detects a residual magnetic minimum of − 1.3 × 103 nT at latitude 4,196,415N. Meanwhile, the profile in the eastern part of the hill intersects a minimum of − 1 × 103 nT at latitude 4,196,280N. Both minima (150 m along the profile, Fig. 6.3b) are aligned in a N110°E direction (red line in Fig. 6.4b), according to the geological information.

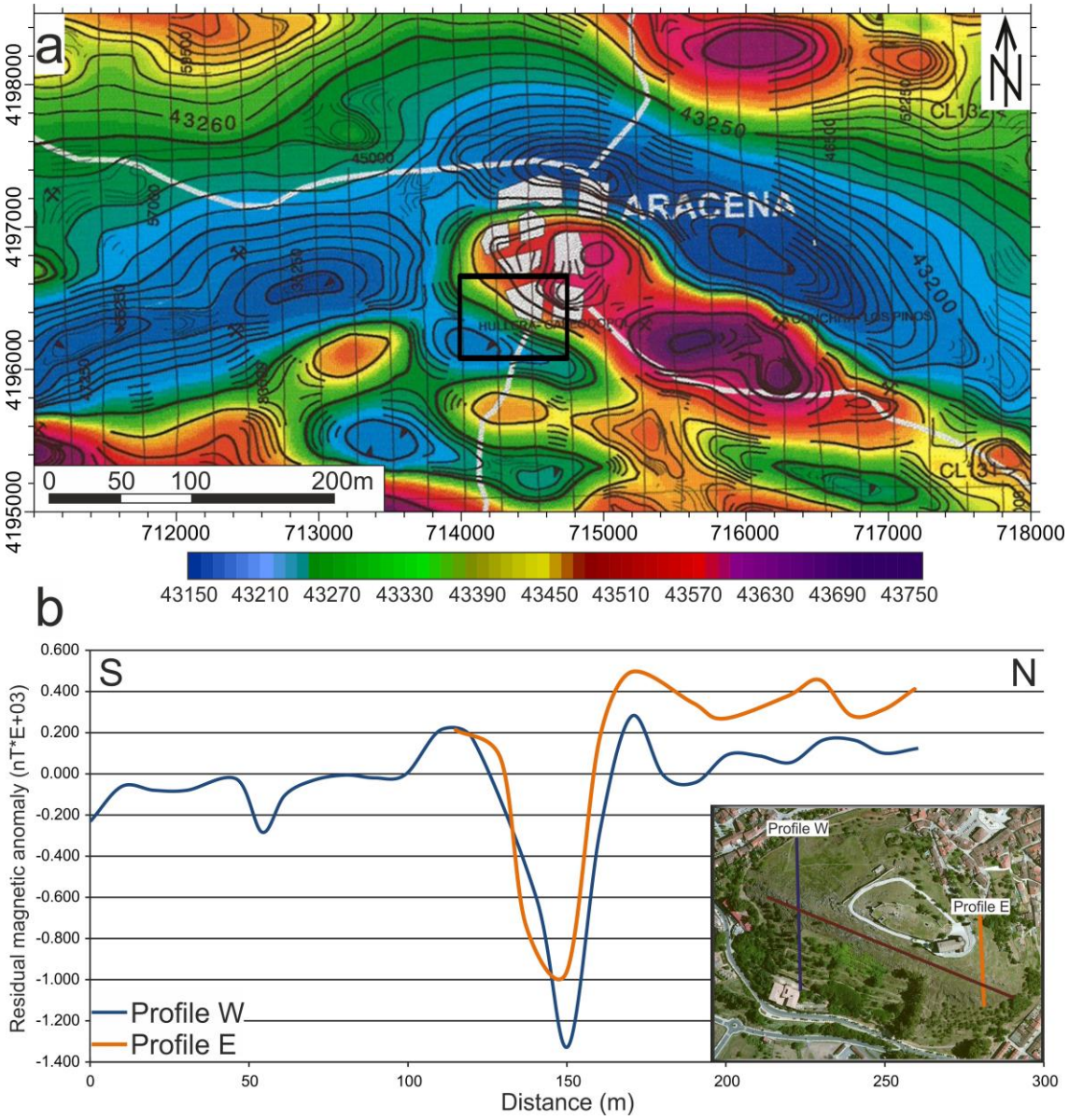


Figure 6.4. Magnetic research: (a) Regional aeromagnetic map of Aracena (IGME, 1997). The studied area is highlighted with black squares. (b) Magnetic profiles East and West of the hill. The position of the profiles is represented on the aerial photo of the studied zone. The red line that crosses the profiles indicates the magnetic minima.

### 6.4.3 Combined geophysical survey and inversion models

Through analysis of the residual gravity map, four lines defined in the most interesting zones were selected to be recognized by other geophysical methods. Fig. 6.5 shows the layout of profiles carried out, the preferred direction of karstification and the boundary zones between minimum and maximum gravity values taken into account;

obviously the layout was also conditioned by the rugged topography of the hill. Firstly, a Test Line 1 was traced above the known cave, close to its entry by one of the shallowest sectors. Afterwards, three lines were performed lengthwise, along the detected gravity anomalies, to investigate possible karstic levels (Lines 2, 3 and 4).

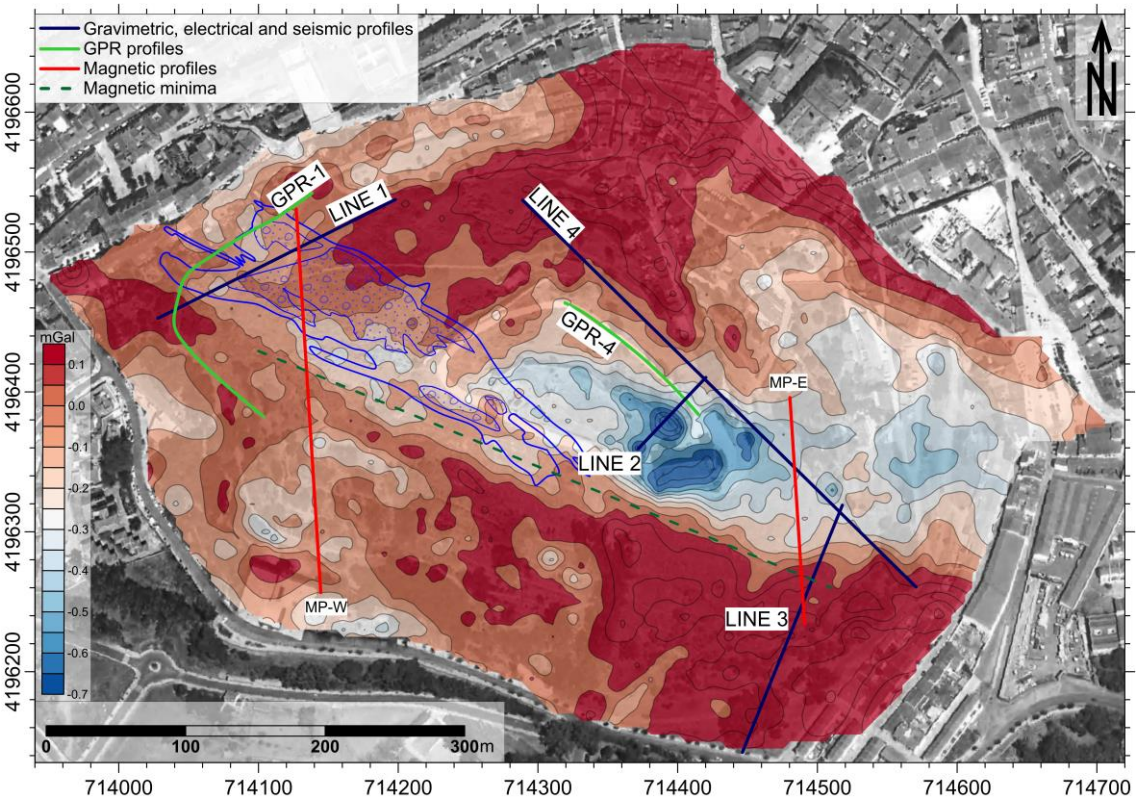


Figure 6.5. Position of measured lines by geophysical methods, plotted over the residual anomaly map. The GPR profiles are parallel and displaced from the lines due to the irregular topography. The position of magnetic profiles shown in Fig. 6.4 is marked with a red line.

### *6.4.3.1 Geophysical profiles above Line 1 — known cave, karstic levels 1 and 2*

Test Line 1 is close to the cave entry where the top is known (~ 15 m depth). The microgravity profile (Fig. 6.6a) crosses an asymmetric minimum residual anomaly between meters 30 and 160, and its minimum reaches − 0.28 mGal at meter 50 in length. The main 2.5D modeled bodies (Fig. 6.6b) have a perpendicular extension of 20 m (cavity 1) and 40 m (cavity 2). These caves were established taking into account the geometry of

the known cave. Yet better fitting the data, four probable new cavities were detected under points at lengths 30 m (cavity 4), 50 m (cavity 6), 110 m (cavity 3) and 145 m (cavity 5) with a perpendicular extension of 10 m. These cavities were modeled in view of the results from the other methods, as resistivity, velocity model and ray tracing coverage. In addition, the sharp intensity of anomalies at meters 50 and 95 suggests the presence of additional small shallow cavities. However, the trend of the greatest anomaly perfectly fit with the main caves detected by the other applied methods. The interpolated magnetic minimum of N110°N direction detected on magnetic profiles is indicated on the microgravity profile.

The resistivity model (Fig. 6.6c) reveals a shallow low resistivity layer (50 Ω·m) 5 m thick. Beneath it, a high resistivity layer of 50000 Ω·m is assigned to marble. The known caves coincide with sectors of intermediate resistivity values ranging from 2000 to 6000 Ω·m, where the shape of the resistivity contours roughly fits the cave morphology. Moreover, the high resistivity of the environment slightly masked the cave signal. The modeled caves of level 2 are registered with high resistivity values. The IP model (Fig. 6.6d) identifies high chargeability values of 15–20 ms coinciding with the known cave position and the pyrite band. Cavity 4 is located deeper than the maximum depth reached by the ERT and IP models. The DOI calculated shows the results to be reliable for most of the profile.

The velocity model (Fig. 6.6e) detects low velocities (~ 400 m/s) at the shallowest subsurface and progressively increasing with depth. This general pattern is sharply interrupted by lower velocity zones matching caves. Whereas cavity 1 fits this low velocity only at the edges, the ray tracing coverage (Fig. 6.6f) shows a large number of rays over the top of cave l and low ray coverage where cavity 1 is located. The same

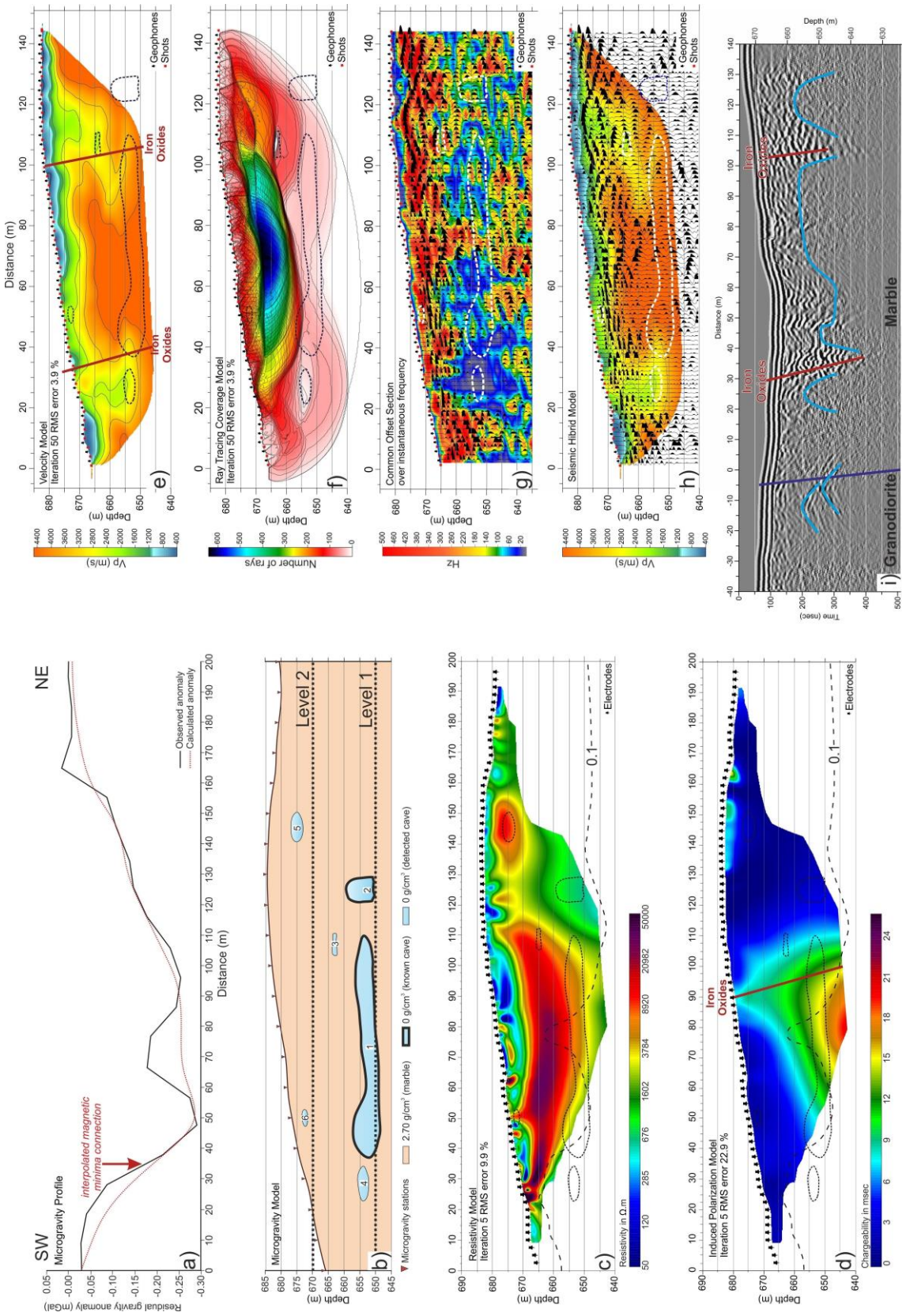
SW
NE
Microgravity Profile
Interpolated magnetic minima connection
Observed anomaly
Calculated anomaly
Residual gravity anomaly (mGal)
Distance (m)
a)
Microgravity Model
Level 2
Level 1
Depth (m)
Microgravity stations
2.70 g/cm³ (marble)
0 g/cm³ (known cave)
0 g/cm³ (detected cave)
b)
Resistivity Model
Iteration 5 RMS error 9.9 %
Electrodes
Resistivity in Ω.m
c)
Induced Polarization Model
Iteration 5 RMS error 22.9 %
Iron Oxides
Chargeability in msec
d)
Velocity Model
Iteration 50 RMS error 3.9 %
Iron Oxides
Geophones
Shots
Vp (m/s)
e)
Ray Tracing Coverage Model
Iteration 50 RMS error 3.9 %
Number of rays
f)
Common Offset Section
over instantaneous frequency
Hz
g)
Seismic Hibrid Model
h)
Time (msec)
Iron Oxides
Granodiorite
Marble
i)

Figure 6.6. Geophysical profiles above Test Line 1. (a) Microgravity profile with station equidistance of 10 m. (b) Microgravity forward model constructed from the residual gravity anomalies where the known cave contour is marked with a thick black dashed line. (c) Inversion model of ERT and (d) IP profiles with 0.1 DOI value marked. The electrode spacing is 2.5 m and the profile reaches a length of 200 m. (e) Vp field obtained from seismic refraction tomography and (f) Ray-path coverage for the final Vp model. The geophone separation is 3 m. (g) Common offset section (1.5 m of shot-geophone distance) over its trace instantaneous frequency. Time to depth conversion was made with a constant 3000 m/s. (h) Stacked seismic reflection section over Vp refraction velocity field (hybrid seismic image), using the same constant velocity of 3000 m/s for time to depth conversion. (i) GPR profile with hyperbolic reflectors marked.

interpretation can be made at other sectors where we detected low ray coverage. Note that cavity 2 is not detected in either profile.

Fig. 6.6g shows the common offset section with low frequencies at the zones probably containing cavities. This trend is more marked beneath meter 30 in length, with a large zone of high frequency abortion. Refraction and reflection data were combined to create the seismic hybrid model (Fig. 6.6h), which shows the coincidence between the absorption of high frequencies and low velocity in zones occupied by cavities.

The GPR profile (Fig. 6.6i) shows absorption signals associated with the presence of granodiorites from − 40 to − 5 m. Hyperbolic reflectors associated with caves in the contact between granodiorite and marble are detected under distance − 10 m long. The iron oxide bands under distances 30 and 105 m identified at the surface, and matching the minimum detected in magnetic profiles, are characterized by strong reflections. These bands are limited on both sides by transparent sectors with reflections on top, which we correlated with cave 4 and 1.

*6.4.3.2 Geophysical profiles above Line 2 — new uppermost karstic level*

This line crosses the most prominent minimum detected in the residual anomaly map, situated in the center of the hill (Fig. 6.3). The microgravity profile (Fig. 6.7a) presents two pronounced gravity minima (-0.7 mGal) at distances of 0 and 30 m. The

microgravity model (Fig. 6.7b) was constrained taking into account the other geophysical methods as described below, reaching 740-710 m.a.s.l. Two large cavities (1 and 2) were modeled with respective perpendicular extensions of 20 and 40 m; they are located at the beginning and center of the model. The cavity 2 model reaches deeper than the other methods applied, while cavities 3, 4 and 5 have small dimensions and a perpendicular extension of 5 m.

The resistivity model (Fig. 6.7c) gives a background value of 50-100 Ω·m, probably associated with the resistivity of the outcropping quartzite. Between 25 and 35 m length and beneath 735 m.a.s.l., the profile shows intermediate resistivity values (1000–3000 Ω·m) that are interpreted to be caused by the large cave 2. The smaller cavities are also associated with intermediate resistivity values, except cavity 4, which is conductive. All the cavities have inward increasing resistivity. The induced polarization model (Fig. 6.7d) displays high chargeability (4–6 ms) associated with cavities 1 and 2, and intermediate chargeability (3 ms) in the zone occupied by the small cavities. In both profiles cavity 1 is outside the models. The DOI is below the big cave, and crosses through the middle of the smaller ones.

The Vp model (Fig. 6.7e) detects cavities 2, 3, 4 and 5 by the velocity inversion sectors, but cavity 1 does not allow any transmission of seismic waves, leading to a blank zone in the model. The same sectors are in accordance with the zones of low ray coverage (Fig. 6.7f). At the beginning of the profile, a significant absence of ray coverage may mark the top and side wall of cavity 1 and the entire contour of cavity 2. The bottom of cavity 2 has little ray coverage, probably due to the presence of clays. We chose a constant Vp velocity for time to depth conversion of 2000 m/s by converting the common offset section (Fig. 6.7g). This represents average velocity for the first 15 m of depth. This seismic section reveals a band of low frequencies (< 100 Hz) and amplitude absorption

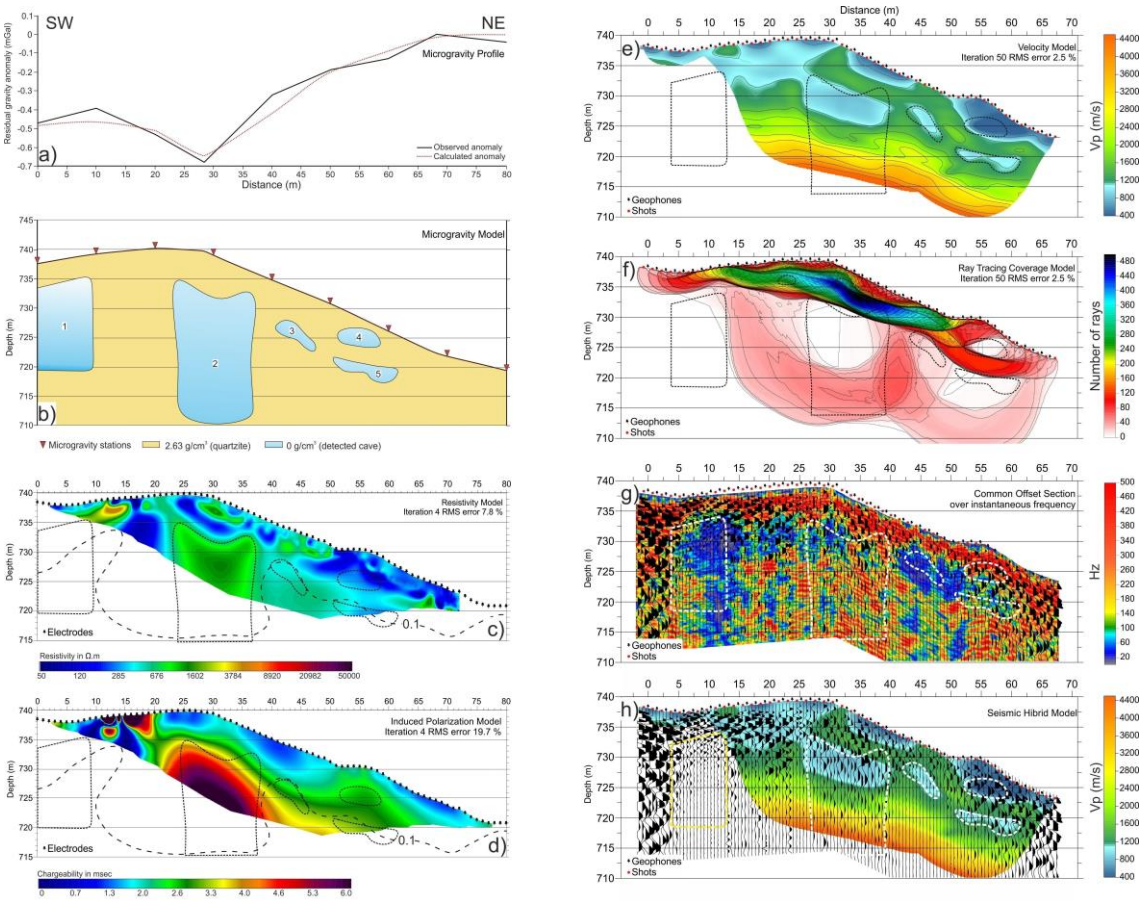


Figure 6.7. Geophysical profiles above Line 2. (a) Microgravity profile with station equidistance of 10 m. (b) Microgravity forward model constructed from the residual gravity anomalies. (c) ERT and (d) IP inversion model profiles with 0.1 DOI value marked. The electrode spacing used was 1 m. (e) Field P-velocity model obtained from seismic refraction tomography and (f) Ray-path coverage for the final VP refraction model. The geophone spacing was 1.5 m. (g) Common offset section over its instantaneous trace frequency. Offset distance is 3 m and the approximate time to depth conversion was made with a constant 2000 m/s of P wave velocity. (h) Stacked seismic section over its refraction velocity field (hybrid seismic model). CDP distance was 0.75 m and the approximate time to depth conversion was made with a constant 2200 m/s of P wave velocity.

effects in agreement with the karstification levels. In the hybrid model (Fig. 6.7h) we can see the correlation between the velocity inversion sectors and the absorption amplitudes related to possible cavities.

*6.4.3.3 Geophysical profiles above Line 3 — karstic levels 1, 2 and 3*

This line was designed perpendicular to foliation, crossing the pyrite band spatially related with the cave. Moreover, the profile passes through granodiorites, marbles and quartzites. The microgravity profile (Fig. 6.8a) presents three gravimetric minima at the beginning (10 to 35 m long), the middle (90 to 125 m long) and the end (160 to 200 m long). The two first relative minima reach a gravimetric value of − 0.2 mGal, and the final minimum attains − 0.4 mGal. Considering the outcropping lithology, the microgravity model (Fig. 6.8b) includes granodiorites from the beginning to meter 100; marbles from meters 100 to 190; and quartzites in the last 10 m. The caves modeled according to the other methods have perpendicular extensions of 40 m (cavity 1) or 20 m (cavities 2, 3 and 4). The intersection with the magnetic minimum is indicated in the Figure.

The resistivity model (Fig. 6.8c) presents a low resistivity shallow zone (~ 50 Ω·m) from a distance of 0 to 100 m, pertaining to outcropping granodiorites, and a high resistivity shallow zone (~ 40000 Ω·m) from 100 to 160 m corresponding to marbles. This resistivity zone is interrupted by a thin subvertical layer with low resistivity that coincides at surface with the pyrite band. Only cavity 2 is identified in the ERT model as a sector with intermediate resistivity value (~ 1500 Ω·m) and as an increasing of resistivity values inward. The IP model (Fig. 6.8d) presents a high chargeability sector at the bottom of the profile that partially matches the position of cave 2. This area contains water and clays, according to the measured water table in the known cave. The pyrite band is highlighted as a north-dipping band with intermediate chargeability.

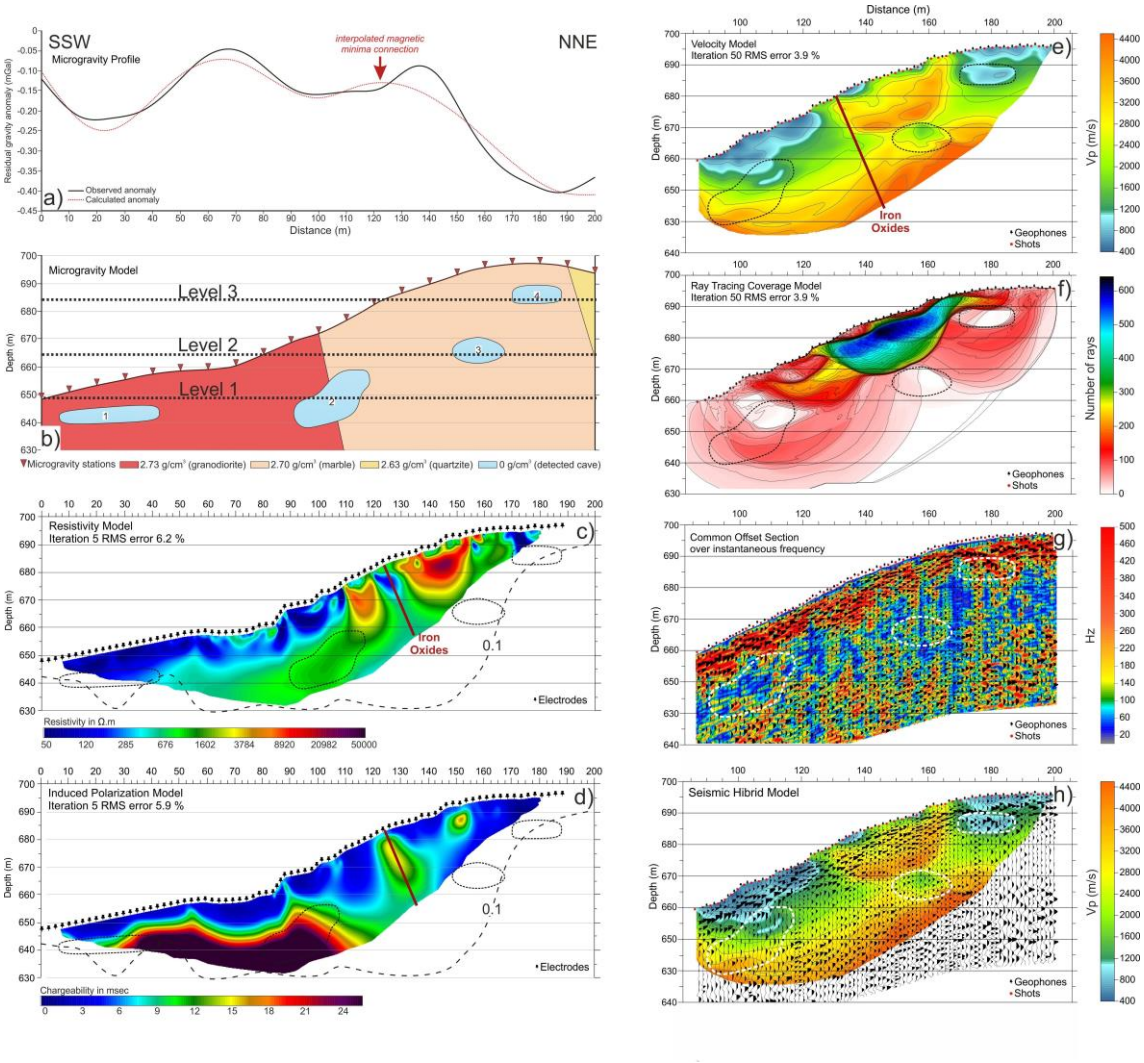


Figure 6.8. Geophysical profiles above Line 3. (a) Microgravity profile with station equidistance of 10 m. (b) Microgravity forward model fitting the residual gravity anomalies. (c) Inversion model of ERT and (d) IP profiles with 0.1 DOI value marked. The electrode separation was 2.5 m. (e) Field P-velocity model obtained from seismic refraction tomography and (f) Ray-path coverage for the final refraction velocity model. The geophone spacing was 2.5 m. (g) Common offset section over its instantaneous trace frequency. In this case, the shot-geophone distance is 1.25 m and the approximate time to depth conversion was made with a constant 3000 m/s of P wave velocity. (h) Stacked seismic section over its refraction velocity field (hybrid seismic model), the seismic reflection section extending the seismic refraction model; thus the rest of the model is in a homogeneous color.

The velocity inversion detected in three sectors in the refraction model (Fig. 6.8e) is interpreted to be caused by caves 2, 3 and 4. The ray coverage model (Fig. 6.8f) presents a central part with a high number of rays associated with compact marbles, and three sectors with low ray density that clearly show the probable cave locations. The bottom of cavity 2 has ray coverage associated with the presence of water. In the common offset model (Fig. 6.8g), the detected caves are revealed as a band with high absorption frequencies (> 100 Hz). The hybrid model (Fig. 6.8h) shows the located caves with inversion velocities and amplitude absorption zones.

*6.4.3.4 Geophysical profiles above Line 4 — karstic levels 2, 3 and 4*

The microgravity profile (Fig. 6.9a) shows a broad minimum between 140 and 360 m of distance, while other minima with shorter wavelengths, most likely related to shallow bodies, are superposed on the general gravity pattern. Five caves, enclosed within both marbles and quarzites, are modeled to fit the observed gravity data (Fig. 6.9b). The contact between marbles and quarzites, recognized at surface, is located at meter 250. Cavity 1 is the largest, featuring a section 120 m long, a maximum height of 30 m, and a modeled perpendicular extension of 60 m. Cavity 2, shallower than cavity 1, has a perpendicular extension of 20 m and is located at meters 290–360. The smaller cavities (3, 4, 5, 6 and 7) were modeled with a perpendicular extension of 10 m.

Three distinct parts are recognized in the ERT model (Fig. 6.9c): a sector with a resistivity of ~ 40,000 Ω·m extends from the beginning until meter 140, associated with marbles. Intermediate resistivity values of 2000 Ω·m placed from meter 140 to 260 are interpreted to be caused by marble enclosing caves. Quartzites also enclosing cavities lead to low resistivity values from meter 260 to the end. The cavities produce sectors with

intermediate resistivity, and they present high resistivity values at their edges that progressively decrease toward the center of the void. Cavity 7 produces a different situation, with high resistivity values. The residual gravity map (Fig. 6.3) indicates that the line may run through the cave by its wall, and the resistivity model registers marble resistivity. The shallow low resistivity values beneath meter 45 there are associated with sparse pyrite observed at the surface. The induced polarization model (Fig. 6.9d) recorded high chargeability values inside cavities 1 and 4, and also under the pyrite detected. The DOI index calculated remains beneath the caves modeled.

The seismic refraction profile trace matches the electrical and microgravity profiles from meter 65 onward. The shallow caves and the upper part of cavity 1 are detected as zones with inversion velocities (Fig. 6.9e) and as zones with low ray tracing coverage (Fig. 6.9f), which are in accordance with the absorption zones in the common offset section (Fig. 6.9g). The hybrid model (Fig. 6.9h) reveals coincidences between the low velocity zones and frequency absorption for the shallowest caves.

The GPR profile (Fig. 6.9i) is displaced toward the south from the other profiles to avoid the irregular topography (Fig. 6.5). The radargram shows a shallow zone with high electromagnetic signal down to 35 m, and hyperbolic anomalies associated with the presence of caves at ~ 35 m depth. There is signal absorption beneath the hyperbolic reflectors. At the southeastern edge of the radargram, a NW-dipping longitudinal reflector is the consequence of rebounding electromagnetic waves due to the cave walls.

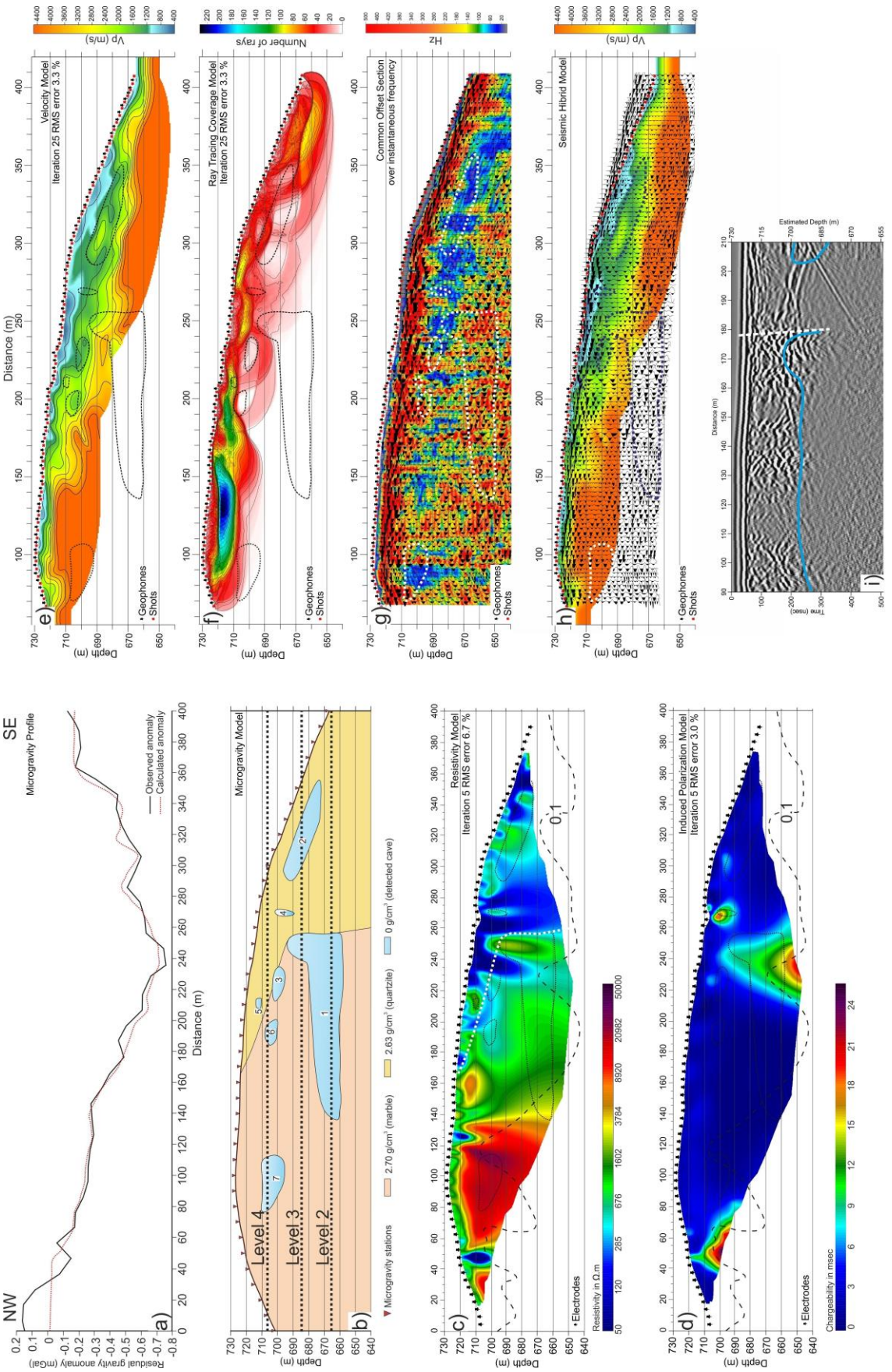
Velocity Model
Iteration 25 RMS error 3.3 %
Ray Tracing Coverage Model
Iteration 25 RMS error 3.3 %
Common Offset Section
over instantaneous frequency
Seismic Hibrid Model
Vp (m/s)
Number of rays
Hz
Geophones
Shots
Depth (m)
Distance (m)
Estimated Depth (m)
Time (msec)
Microgravity Profile
Observed anomaly
Calculated anomaly
Residual gravity anomaly (mGal)
NW
SE
Microgravity Model
Level 4
Level 3
Level 2
2.70 g/cm³ (marble)
2.63 g/cm³ (quartzite)
0 g/cm³ (detected cave)
Microgravity stations
Resistivity Model
Iteration 5 RMS error 6.7 %
Induced Polarization Model
Iteration 5 RMS error 3.0 %
Electrodes
Resistivity in Ω.m
Chargeability in msec

Figure 6.9. Geophysical profiles above Line 4. (a) Microgravity profile with station equidistance of 10 m. (b) Microgravity forward model fitting the residual gravity anomalies. (c) Inversion model of ERT and (d) IP profiles with 0.1 DOI value marked. The electrode spacing applied was 5 m. (e) Field P-velocity model obtained from seismic refraction tomography. (f) Ray-path coverage for the final refraction velocity model. (g) Common offset section over its trace instantaneous frequency. In this case the shot-geophone distance is 5 m, and the time to depth conversion was made with a constant 3000 m/s. (h) Stacked seismic section over its refraction velocity field (hybrid seismic model). Obviously, the seismic reflection section extends the seismic refraction model; so the rest of the model is in a homogeneous color. (i) GPR profile with reflectors associated to the modeled cave displayed. The profile is slightly displaced from other profiles, so that the distances are approximate.

## 6.5 JOINT INTERPRETATION AND DISCUSSION

The presence of the Gruta de las Maravillas leads one to suspect the presence of other cavities emplaced in the hill, undiscovered to date. Moreover, the end of the known cave, located beneath the center of the hill and formed by a collapse of karstic levels 2 and 3, suggests that the cavity continues behind the fallen rocks. The difficulty in exploring new cavities from the inside of the known cave forces researchers to explore them externally by means of geophysical methods.

### 6.5.1 Methodological flow diagram in geophysical cave prospecting

Fig. 6.10 summarizes our methodological approximation to achieve the maximum efficacy in marbles with sulfur cave prospecting. Once detailed geologic and topographic information are gathered, we propose that an extensive field microgravity survey be carried out, positioning differential GPS to focus on zones likely to contain caves. Due to the high density contrast between air and rock, such zones are detected as relative minima within the residual gravity anomaly map, whose cell size should be decided in light of the

anticipated size of the caves and the desired resolution. Prominent gravimetric anomaly minima are probably associated with small and shallow caves, while broad and moderate anomalies are linked to larger and deeper cavities or lithological changes. This uncertainty makes it necessary to apply other geophysical methods to ensure the cave presence, matching zones in view of the residual anomaly map. Whenever possible we advise that

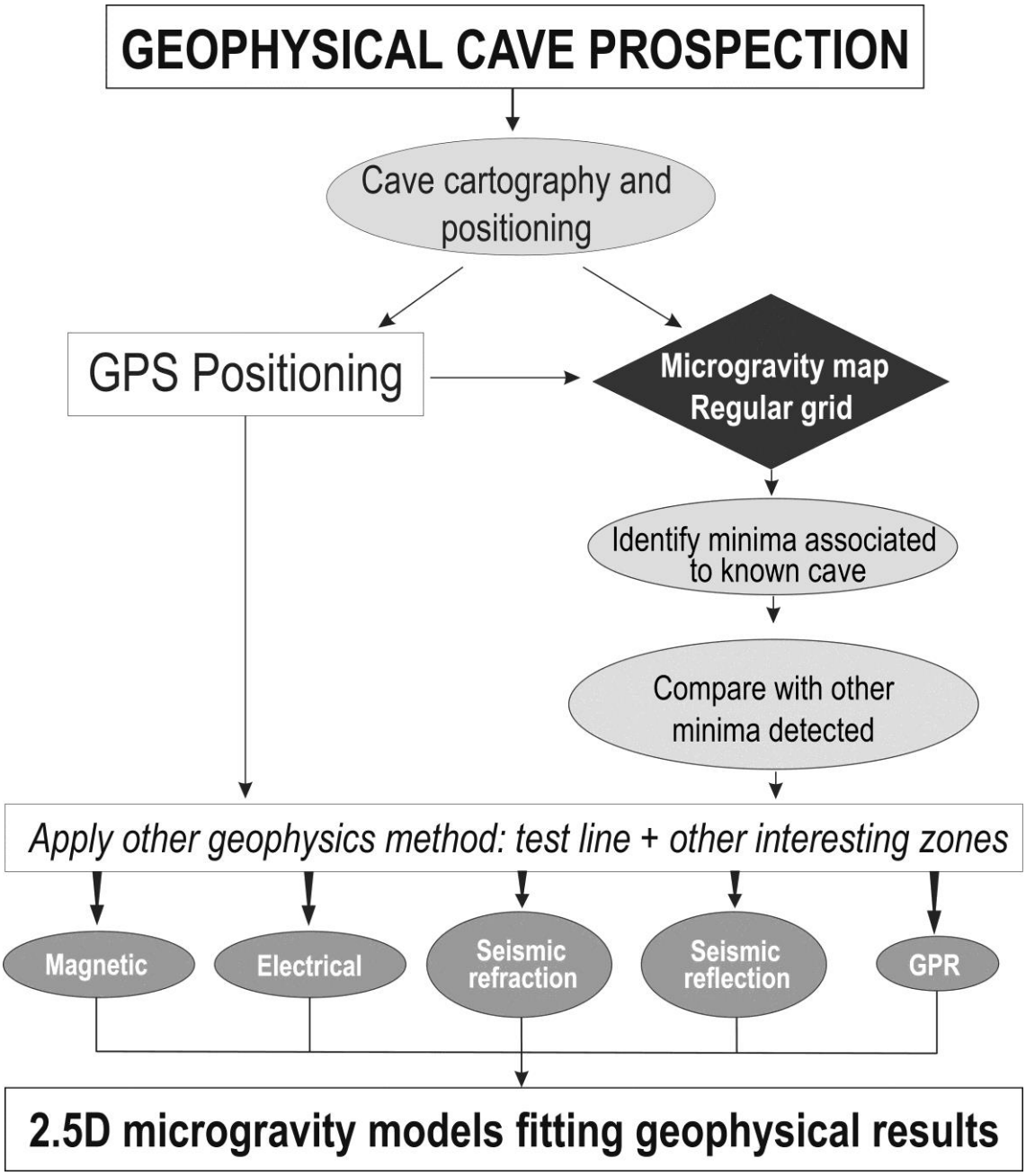


Figure 6.10. Proposed flowchart implementing geophysical methods in cave detection research.

a test line over the known cave be performed to obtain the responses of different geophysical methods. At that point, we are ready to extend the exploration surface techniques to the other planned lines. In karstic systems, where a mineral band (e.g. pyrite) and iron oxides are frequent, magnetic profiles and induced polarization are also recommended to provide contacts with mineralized bodies that most likely are close to caves. Insofar as it is possible, we propose matching geophysical profiles at the same place and creating 2.5D microgravity models.

### 6.5.2 Response of the geophysical methods to cavity presence

To test a given karst system related to sulfur mineralizations, the magnetic profile is a useful tool. It serves to detect zones with mineralized bands and a high probability of harboring caves (Chamon and Dobereiner, 1988). Giving the particular presence of iron oxides and sulfurs in the Gruta de las Maravillas (Fig. 6.4b), this method is highly reliable in this context.

Empty caves are generally seen as high resistivity values in the ERT models due to air presence. But the presence of iron oxides on cave walls dramatically reverts and enhances the resistivity contrast between host rocks and the cave boundary (e.g. caves 1 and 5 of Fig. 6.6), as the forward model demonstrates (Fig. 6.2). In addition, we observed that the IP profiles detect only caves with high iron oxide content (e.g. cave 1 of Fig. 6.6d and cave 2 of Fig. 6.8d), and provide only the cave position without information regarding morphology. In our karst system, with iron oxides on the cave walls, DC electrical methods provide adequate reliability for cave detection.

The seismic refraction tomography profiles distinguish cavities as zones with low or inversion Vp velocity combined with the anomalous low ray tracing coverage (caves 2, 4 or 5 Fig. 6.7e and f). Shallow and intermediate cavities (up to ~ 30 m) are detected

and delineated with intermediate to high reliability by combining these two models; obviously their top is located more accurately than their bottom. Moreover, deepest caves are not well detected for these methods (e.g. cave 1 of Fig. 6.9).

In the seismic common offset section, the distances between shot-geophone sets indicate the depth of the cavity inspection. In our case, a short offset was selected to achieve the karstic shallow levels. When size and depth of a cave are above the detection threshold established by the experimental device, the traces corresponding at this zone present a content of absorption in its amplitude and its high frequencies (Figs. 6.6g and 8g). We found that these seismic images have a lower reliability than velocity refraction combined with ray tracing coverage models when dealing with the shape of isolated cavities, but they marked the karstification levels very well. In cavities studied with the seismic method, a high density shooting is necessary, meaning that the seismic reflection section is an easily obtained sub-product. Although the CDP staking attenuated the cavity detection, we recommend generating the seismic hybrid model (reflection section over refraction Vp field) to analyze the underground image.

Finally, the radargrams show hyperbolic events associated with the presence of cavities or strong reflections at the top of a cavity when it has bigger dimensions (Figs. 6.6i and 9i). In either case, signal absorption is produced. Although the cave morphology is not accurate, this method detects with precision the top of the cave. An occasional lateral reflection due to the cave walls may occur, as observed in the southeastern edge of the radargram GPR4 (Fig. 6.9i).

### 6.5.3 Karst system of the Gruta de las Maravillas

The combination of geophysical methods together with detailed geologic information helped to define the area surrounding the Gruta de las Maravillas, where the

karstic system is more developed (Fig. 6.11). The new cavities detected can be grouped into four predominant dissolution levels, three of them already confirmed by direct cartography of the cave (~ 650, 665 and ~ 685 m.a.s.l.), while the uppermost level (~ 710 m.a.s.l.; in Line 2, Fig. 6.7) was detected by the geophysical models.

The residual gravity anomaly map suggests that the karst system developed mainly in a N110°E direction, in agreement with the geologic and cartographic information of the known cave. The new caves and galleries discovered present the same orientation and karstic levels as the Gruta de las Maravillas. The map shows the different levels and their extension, although it is difficult to delineate them with accuracy. In turn, the seismic prospection models show that the karstic levels are highly interconnected, according to the quasi-vertical dip of marbles. The connection between the known cave and new caves

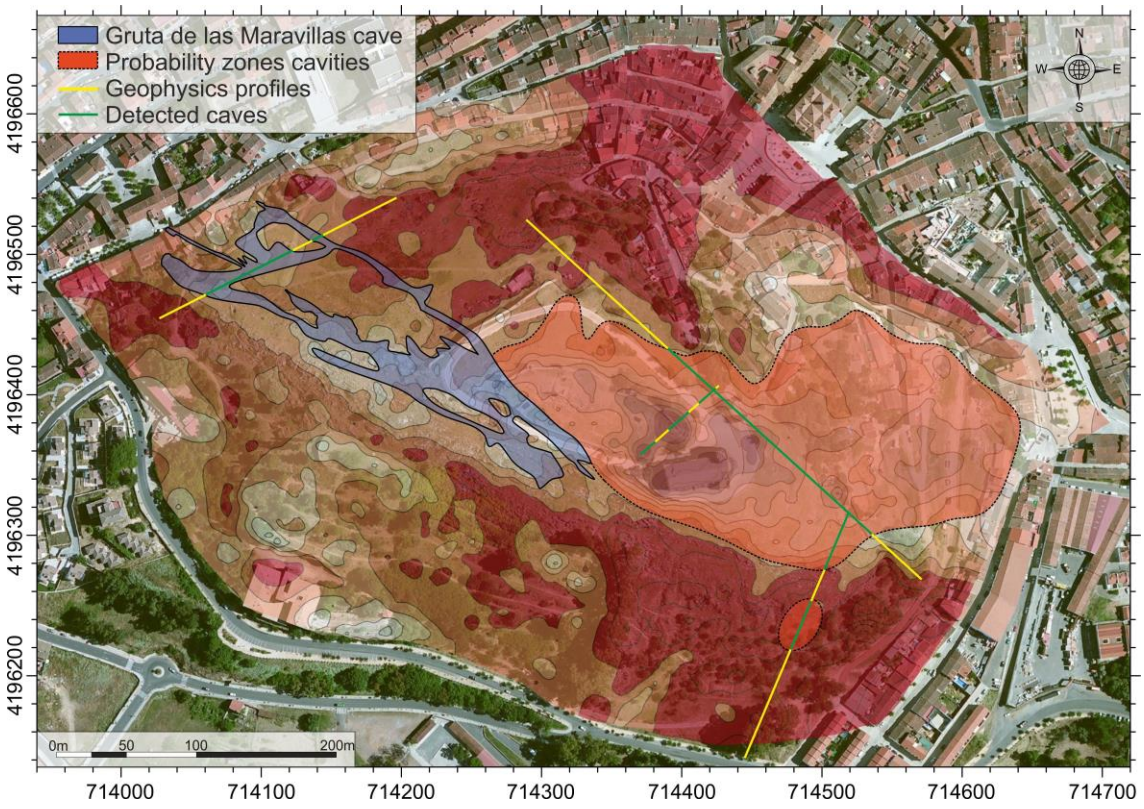


Figure 6.11. Interpreted karstic system around Gruta de las Maravillas. This image is built by joining geophysical models and shows the main areas where the ducts are more developed.

discovered occur in the central part of the hill, probably crossing the major collapse present at the end of the known Gruta de las Maravillas.

## 6.6 CONCLUSIONS

Near-surface geophysical methods are a useful tool to study karst systems. In the present study, a complete set of these techniques was used to detect the continuity of the Gruta de las Maravillas system.

According to our test results, the most suitable combination of geophysical methods to establish the main dissolved ducts would begin with deriving microgravimetry and microtopography maps of the entire study area. This enables one to identify typical anomalies related to ducts that may be recognized as relative gravimetric minima in the residual anomaly map.

When cavities have special conditions — e.g. iron oxides covering the walls and mineralized bands associated with them — the magnetic profiles (MP) are the second step in the procedure. The anomalies are related to the presence of oxides and sulfurs associated to the origin of the cavity.

Afterwards, in view of the microgravity map and MP, a series of strategic surveys can be defined to perform other geophysical profiles. We found the ERT and IP methods to be very sensitive in cave detection. Their models are highly dependent on special conditions between the cave and surrounding rocks. Iron oxides covering walls, the high resistivity of marble, or the nature of filling fluid can change the resistivity associated with caves. In this context, we recommend generating synthetic models a priori to describe the particular geologic setting, and analyzing the resulting models to establish the general responses expected.

In our case, shallow seismic prospection is presented as a more reliable method, especially refraction tomography with ray tracing coverage. This combined technique is useful to detect the top of cavities, though the bottom is "hidden" due to the high acoustic impedance. Indeed, when the wave-front propagates through the compact formation (e.g. marble) and reaches the top of the cavity, the high reflection coefficient at the interface interferes with the refracted seismic energy, and the lower layers cannot be measured. In contrast, the seismic offset section combined with trace instantaneous frequency image reliably locates the main dissolution tracts, but introduces uncertainty in the detection of individualized cavities. In turn, seismic reflection sections mainly provide information on the arrangement of the strata, as CDP staking (increasing the signal–noise relationship) is opposed to individual body detection (i.e. the case of caves).

The GPR profiles are also a sound method to detect cavities, because they afford a dielectric contrast between the cavity (air) and the surrounding materials. Still, their behavior is similar to seismic prospection in that only the top and laterals of cavities are well defined, due to the relationship between the refraction and refraction dielectric coefficients. Another limitation of this method is the difficulty of collecting data on rugged terrain, a situation that is fairly common when dealing with karst systems.

Starting from the results of the microgravity survey, the combination of magnetic, electric and seismic methods is the best tool for cave detection that has allowed to highlight the continuity of the Gruta de las Maravillas cave formed in mineralized marbles of the Cerro del Castillo Hill. These new data contribute to improve the knowledge on the cave and to propose the presence of an upper 4 karstic level.

**ACKNOWLEDGMENTS**

We thank two anonymous reviewers for their insightful reviews which significantly helped to improve the manuscript. We would like to thank the Aracena City Council and the Gruta de las Maravillas staff for permitting our fieldwork and cave data acquisition. Moreover, we wish to acknowledge the assistance provided in the field by Rafael R. Durán and Adela Hodar. This research was supported by projects 3726–00, 3727–00, CGL2010-21048, P09-RNM-5388 and RNM148.

# Chapter 7

## Regional and residual anomaly separation

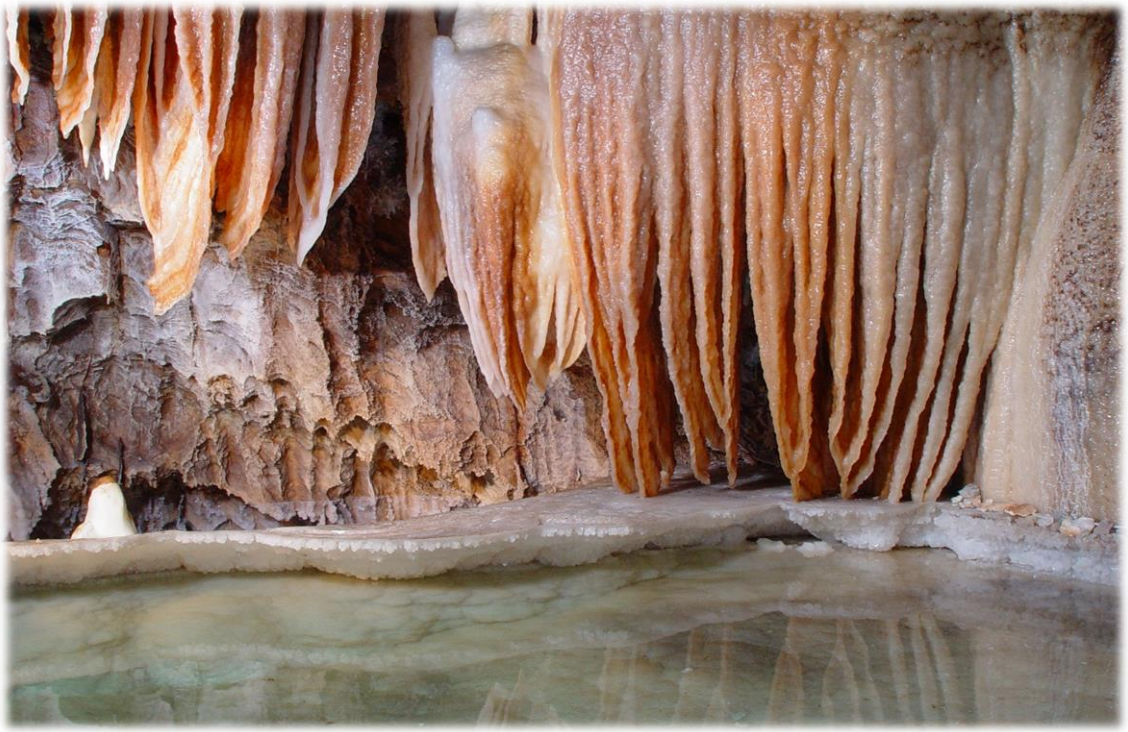

# Regional and residual anomaly separation in microgravity maps for cave detection: the case study of Gruta de las Maravillas (SW Spain)

F.J. Martínez-Moreno[a], J. Galindo-Zaldívar[a,b], A. Pedrera[b], T. Teixido[c], J.A. Peña[c], L. González-Castillo[a]

[a] Departamento de Geodinámica, Universidad de Granada, 18071-Granada, Spain

[b] Instituto Andaluz de Ciencias de la Tierra, CSIC-Universidad de Granada, 18071-Granada, Spain

[c] Instituto Andaluz de Geofísica y Prevención de Desastres Sísmicos, Universidad de Granada, 18001-Granada, Spain

Published on:

**Journal of Applied Geophysics**

Vol. 114, 1-11

*DOI: 10.1016/j.jappgeo.2015.01.001*

Received 15 September 2014

Accepted 5 January 2015

**ABSTRACT**

Gravity can be considered an optimal geophysical method for cave detection, given the high density contrast between an empty cavity and the surrounding materials. A number of methods can be used for regional and residual gravity anomaly separation, although they have not been tested in natural scenarios. With the purpose of comparing the different methods, we calculate the residual anomalies associated with the karst system of Gruta de las Maravillas whose cave morphology and dimensions are well-known. A total of 1857 field measurements, mostly distributed in a regular grid of 10 x 10 m, cover the studied area. The microgravity data were acquired using a Scintrex CG5 gravimeter and topography control was carried out with a differential GPS. Regional anomaly maps were calculated by means of several algorithms to generate the corresponding residual gravimetric maps: polynomial first-order fitting, Fast Fourier Transformation with an upward continuation filter, moving average, minimum curvature and kriging methods. Results are analysed and discussed in terms of resolution, implying the capacity to detect shallow voids. We propose that polynomial fitting is the best technique when microgravity data are used to obtain the residual anomaly maps for cave detection.

## HIGHLIGHTS

- Microgravity geophysical method and differential GPS are applied in cave detection.
- Diverse methods in regional-residual anomaly separation are tested and compared.
- Polynomial, FFT-upward continuation, moving average, kriging and minimum curvature.
- These methods are compared for a known cave with detailed morphology information.
- The best results are discussed to propose the optimal method for microgravity maps.

**Keywords:** Microgravity data; cave detection; regional gravity anomaly; residual gravity anomaly; Bouguer anomaly separation.

## 7.1 INTRODUCTION

The Earth´s gravitational field, which may be observed at different surface points, is sensitive to lateral and vertical underground density variations (Nettleton, 1971). A qualitative identification of bodies with anomalous densities in view of the Bouguer anomaly calls for their decomposition into regional and residual anomalies (Agarwal and Sivaji, 1992). Residual gravity is a concept arising from the fact that conventional Bouguer gravity maps reflect the superposition of local gravity fields, owing shallow geological structures, upon a regional gravity field caused by deeper geological structures (Griffin, 1949). Hence, the concept of residual gravity refers to the part of the Bouguer gravity anomaly remaining after subtracting a smooth regional effect (Skeels, 1967).

Yet the best means subtracting the regional effect from the Bouguer anomaly is a crucial problem in gravity interpretation (Dobrin, 1976). Applying digital filters is an increasingly popular option (Gupta and Ramani, 1980). Still, there are non-unique solutions, and all separation techniques rely on some hypothesis regarding the source distribution (Keating and Pinet, 2011). It can therefore be helpful to collect information on the structure and density of the residual anomaly sources distributed in the study area prior to performing Bouguer anomaly decomposition.

Microgravity is commonly applied in cave detection studies given the high-density contrast between cave and host rock. The determination of residual anomalies (minima values) produced by caves is a key step when processing such data. Several filtering techniques can be applied to this end (Table 7.1): polynomial fitting, finite element methods, diverse filters, kriging, minimum curvature, moving average and fast Fourier transformation, among others. Yet the literature to date lacks discussion of which might be the optimal method.

The methods proposed by Griffin (1949) – involving relaxation techniques, fractals, Green's equivalent layer concept, graphical separator, wavelet transform or optimal robust separator, among others – led to limited success as most of them only filter gravity profiles, and have since been relegated (Table 7.1).

Further approaches that can be successfully applied to filter Bouguer gravity maps or profiles would include gridding methods such as polynomial fitting, minimum curvature, kriging or moving average, all of them easily calculated with commercial software. Fast Fourier Transformation is an option that may be used with a great variety of filters, and it is therefore more frequently applied for regional-residual gravity anomaly separation.

Gridding interpolation methods such as kriging or minimum curvature (Mickus *et al.*, 1991; Izarra, 2008) and moving average (Abdelrahman and El-Araby, 1993 and 1996) call for additional data outside the area of interest (Table 7.2). These methods are more suitable for regional gravity surveys (e.g. Nitescu *et al.*, 2003); when microgravity prospection involves a small local area, they do not yield sufficient accuracy. In contrast, polynomial fitting and FFT-upward continuation can be applied in local and regional surveys with high-resolution results (e.g. Martín *et al.*, 2011; Sedighi *et al.*, 2009).

The aim of this research is to compare the existing regional-residual filtering methods and their suitability for gravity studies in the framework of shallow cave detection. To do so, we calculated the residual anomalies associated with the karst system of a cave with well-known morphology and dimensions: the Gruta de las Maravillas (Aracena, SW Spain).

| METHOD | AUTHORS |
|---|---|
| **Polynomial** | Al-Zoubi *et al.*, 2013<br>Agarwal and Sivaji, 1992<br>Abdelrahman *et al.* 1989<br>Agocs, 1951<br>Beltrao *et al.*, 1991<br>Camacho *et al.*, 1994<br>Davis, 1986<br>Martín *et al.*, 2011<br>Martínez-Moreno *et al.*, 2014<br>Montesinos *et al.*, 1999<br>Ojo and Kangkolo, 1997<br>Rybakov *et al.*, 2001<br>Sedighi *et al.*, 2009<br>Simpson, 1954<br>Stern, 1979<br>Swarz, 1954<br>Thurston and Brown, 1992<br>Wren, 1973<br>Zeng, 1989 |
| **Fast Fourier Transformation – Upward Continuation** | Carbó *et al.*, 2003<br>Gupta and Ramani, 1980<br>Fuller, 1967<br>Nettleton, 1954<br>Sedighi *et al.*, 2009 |
| **Moving Average** | Abdelrahman and El-Araby, 1993, 1996 |
| **Minimum Curvature** | Mickus *et al.*, 1991<br>Nitescu *et al.*, 2003 |
| **Kriging and Cokriging** | Izarra, 2008<br>Marcotte and Chateau, 1993 |
| **Finite Element Method** | Agarwal and Srivastava, 2010<br>Kaftan *et al.*, 2005<br>Mallick and Sharma, 1999<br>Sarma *et al.*, 1993 |
| High and/or Low pass filter | Dobrin and Savit, 1988<br>Lodolo *et al.*, 2007<br>Sedighi *et al.*, 2009 |
| Global Geopotential Model | Featherstone, 1997<br>Hackney *et al.*, 2004 |
| Spectral factorization | Chávez *et al.*, 2007<br>Gupta and Ramani, 1980 |
| Optimal Robust separator | Wessel, 1998 |
| Geological Stripping | Weiland, 1989 |
| 3D Magnetic inversion algorithm | Li and Oldenburg, 1998 |
| Wavelet transform and spectrum analysis | Xu *et al.*, 2009<br>Fedi and Quarta, 1998 |
| Graphical separator | Gupta and Ramani, 1980 |
| Green's equivalent layer concept | Pawlowski, 1994<br>Guo *et al.*, 2013 |
| Fractals | Chapin, 1996 |
| Relaxation Techniques | Agarwal and Sivaji, 1992 |
| Horizontal gradient | Al-Zoubi *et al.*, 2013<br>Eppelbaum *et al.*, 2008 |
| Bilinear saddle regression | Al-Zoubi *et al.*, 2013 |

Table 7.1: Methods applied by different authors for regional and residual gravity field separation. The ones most used are highlighted in bold type, as opposed to other methods not currently considered for separation.

## 7.2 THE KARST SYSTEM OF GRUTA DE LAS MARAVILLAS

The Gruta de las Maravillas is located in Cerro del Castillo hill, in the town of Aracena (Huelva province, SW Spain) (Fig. 7.1a). The hill is made up of a Precambrian-Cambrian sequence belonging to the so-called Aracena Metamorphic Belt, within the Iberian Massif. It is formed by marbles (ρ = 2.7 g/cm3), quartzites (ρ = 2.67 g/cm3), granodiorites (ρ = 2.73 g/cm3) and gneisses (ρ = 2.69 g/cm3) (Martínez-Moreno *et al.*, 2014). There is a positive relief of 100 m with respect to the surrounding areas, and Cerro del Castillo is covered by vegetation and several constructions. The cave itself is emplaced in marbles with a foliation trending N110ºE and dipping 70-80º towards the NE, observable along the path of the cavity (Fig. 7.1b), towards the NW. The cave presents a longitudinal development of 300 m following the direction of the marbles.

This endokarst system comprises three main dissolution levels (Fig. 7.1c): level 1 (~650 m.a.s.l.), level 2 (~665 m.a.s.l.) and level 3 (~685 m.a.s.l.) (Martín-Rosales *et al.*, 1999; Pulido-Bosch *et al.*, 1997, Martínez-Moreno *et al.*, 2014). The cave morphology is one of narrow passages with dimensions lower than 5 x 5 m, featuring large cavity-halls over 40 x 40 (Fig. 7.1d). The largest passage is located beneath the central part of the hill connecting towards the East with the so-called Great Lake Hall; it has a maximum height of 40 m from base to top, where the three dissolution levels collapsed and are joined (Fig. 7.1b). An accumulation of collapsed rocks interrupts the possible continuity of the cave towards the ESE sector of the hill.

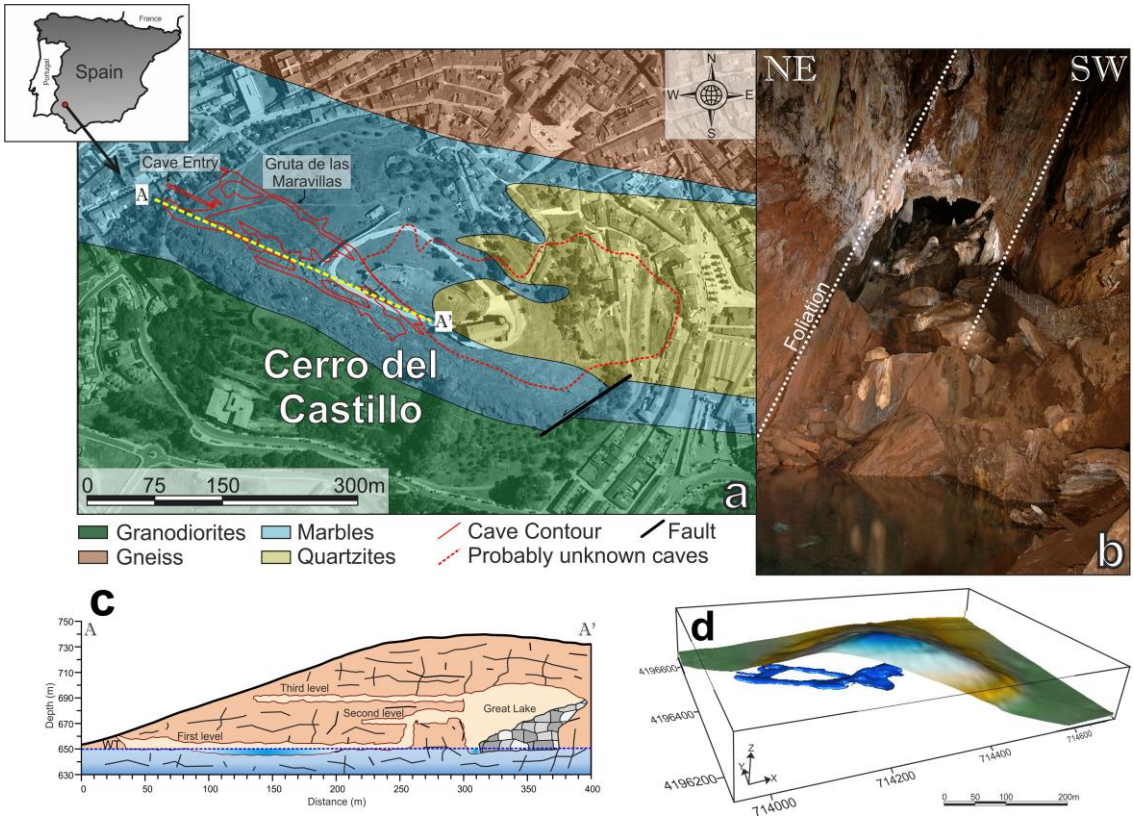


Figure 7.1: Location of the study area in southwest Spain. (a) Gruta de las Maravillas cave morphology and zone with probable new caves over synthetic geological map in Cerro del Castillo hill. (b) Great Lake gallery of the Gruta de las Maravillas with foliation trending marked. (c) Cave profile and its division in three levels. The position of the profile is marked on (a). (d) 3D cave model and its depth position relative to the surface.

## 7.3 DATA ACQUISITION AND APPLIED METHODS

Residual and regional separation from the Bouguer anomaly map is highly sensitive to the quality of the microgravity dataset. Careful consideration was given to certain of data acquisition to ensure accurate results (for more details see Martínez-Moreno *et al.*, 2014).

### 7.3.1 Microgravity acquisition

Microgravity variations are produced by local density changes, and the range of values can be very small or pronounced, depending on the cave/rock density contrast and the dimensions of the cave.

A Scintrex CG-5 gravity meter on a tripod with an accuracy of ±0.001 mGal was used in this study. The acquisition data was filed in two kinds of microgravity measurement stations: a regular grid spacing of 10 x 10 m within the hill, where the endokarst system is located, and isolated profiles extending 350 m beyond the hill (Fig. 7.2). Inside the hill, 1786 station measurements were taken; around the hill, 70 stations were measured.

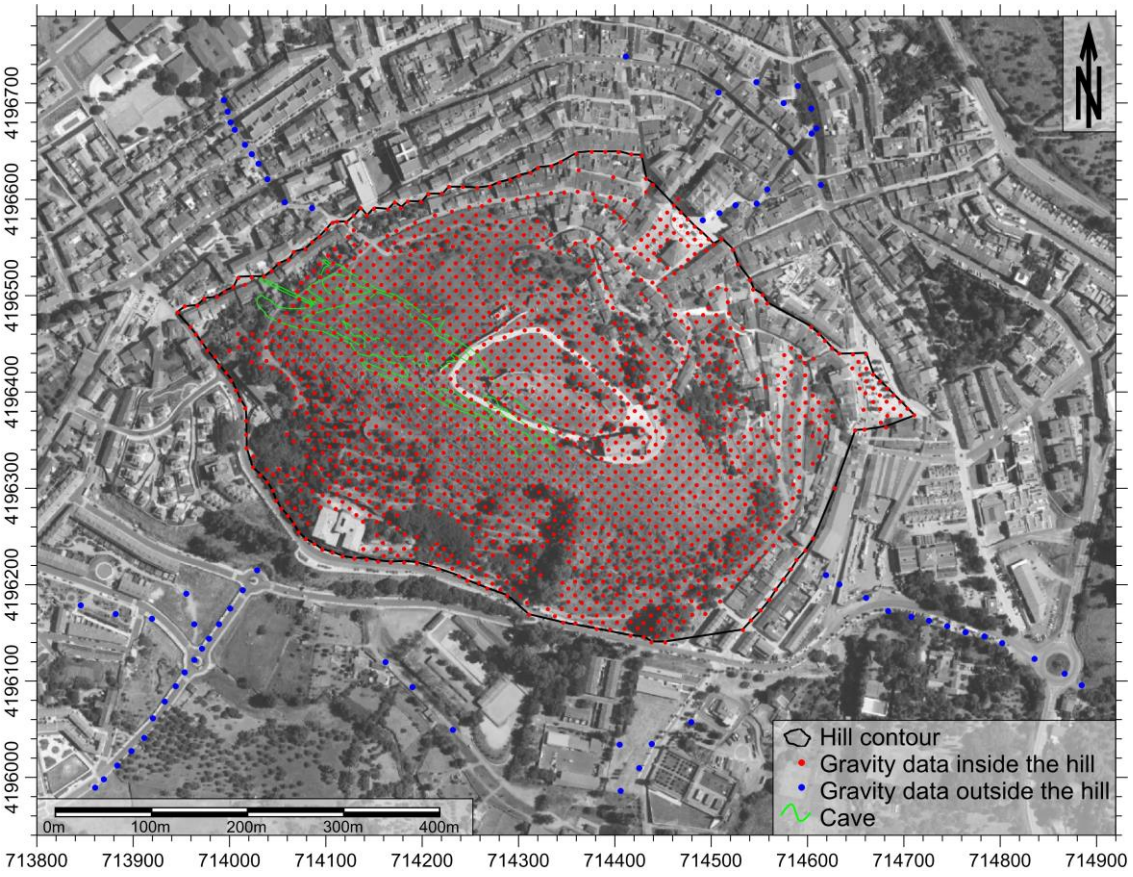


Figure 7.2: Microgravity dataset distribution. The gravity station data inside the hill has a grid size of 10 x 10 m, and outside the hill the stations reach up to 350 m. Hill contour and cave position are marked.

A differential GPS with a Leica 1200 as the reference station and a Leica 1200+ as the mobile station (Real Time Kinematic mode), connected by a one-watt radio transmitter, served to position the microgravity data and to obtain the local digital terrain model (DTM). Full coverage of the studied area was provide by a fixed GPS reference station established on a point whose coordinates were determined by means of the

Andalusian Positioning Network (RAP; Junta de Andalucía, 2011). Afterwards, the grid microgravity station coordinates were calculated using the GPS stakeout programme.

The forward models of cave sections were calculated using GRAVMAG v.1.7 software from the British Geological Survey (Pedley *et al.*, 1993). A 2.5D approximation was used adopted in view of cave features and geological information. The section selected lies at the centre of the hill, where the cavity is larger.

### 7.3.2 Separation between Regional and Residual gravity fields

The microgravity field data set was obtained with reference to the Huelva gravimetric first order base (IGN, 2005). After tidal and instrumental corrections, the Bouguer anomaly map (Fig. 7.3) was derived using a standard density of 2.67 g/cm$^3$. The terrain correction effect, calculated with Hammer's circle method (Hammer, 1939, 1982), was from 2 m to 100 km around each gravity station.

First, we selected specific extraction trend methods to determine the regional gravity field, which led us to envisage three possible situations arising from the two data sets: (a) all microgravity data; (b) only the stations measured inside the hill, with higher coverage; and (c) only the data from surrounding, "outside" stations, with sparse measures. The regional trends were then calculated using Surfer V12 (Golden Software Inc.) and Oasis Montaj (Geosoft) codes, and they were subtracted from the Bouguer anomaly map to obtain the corresponding residual anomaly maps. Some methods could only be applied over data with a certain resolution (Table 7.2).

#### *7.3.2.1 Polynomial fitting method*

This method is used to define large-scale trends and patterns over the Bouguer data to obtain the regional anomaly. In view of the elongated shape of the Bouguer anomaly, it seemed logical to use a low-degree polynomial adjustment (Martín *et al.*, 2011). In this case, a first-order polynomial was used to fit the Bouguer anomaly in three

| | DATASETS | | |
|---|---|---|---|
| Method | Total Data | Inside Study Area | Outside Study Area |
| Polynomial fitting | X | X | X |
| Kriging | - | - | X |
| Minimum Curvature | - | - | X |
| Moving Average | - | X | - |
| FFT-Upward Continuation | X | X | - |

Table 7.2: Validity of the application the interpolation methods in the two dataset distributions, where (X) means that the method can be applied, and (-) means that the method should not be applied.

data positions: (i) over all the data; (ii) only using the sparse data surrounding the cave, and finally, (iii) only using the 10 x 10 grid focused on the hill.

#### *7.3.2.2 Fast Fourier Transformation - Upward continuation*

The grid data $a_i(x_i,y_i)$ were converted to the dual Fourier domain by means of the Fast Fourier transformation (FFT) algorithm (Blakely, 1995), to produce a folded 2D transform map that represents a sum of sine and cosine terms with different spatial frequencies (Kx and Ky) defined by data sampling (dx and dy) in x and y directions. The properties of the Fourier transform (symmetry, linearity, shift and derivative properties) allow for several computational operations to be performed in the Fourier-transformed frequency (Kx, Ky) domain more efficiently than in the spatial (x, y) domain. As part of this process, the radially averaged energy spectrum was calculated and the map was obtained by applying a regional_upward continuation filter (Dean, 1958). The upward continuation method was applied over all data but only using the 10 x 10 grid, in order to approximate a regional map (Fuller, 1967; Henderson, 1960; Peters, 1949). Notwithstanding, the accuracy of the upward continuation method depends on the filter height selected, making it somewhat subjective and difficult to estimate. Our study used the hill height –100 m– as the value of reference for cave enclosure.

*7.3.2.3 Moving Average method*

This is a simple landmark technique described by Griffin (1949), while the application of least-square to the moving average is described by Agocs (1951). The moving average residuals, which are proportional to the second derivate values (Rao and Radhakrishnamurthy, 1965) have high resolving power (Abdelrahman and El-Araby, 1993). The method was used to fit the data from the 10 x 10 grid.

*7.3.2.4 Minimum curvature*

This gridding method was first employed by Briggs (1974); the algorithm was later formulated by Swain (1976) and modified by Webring (1981). It relies on a two-dimensional differential equation for the displacement of a thin sheet under the influence of point forces, equivalent to a third-order spline (Briggs, 1974). To calculate the regional trend, the gravity measurements over the study area were removed (Mickus *et al.*, 1991).

*7.3.2.5 Kriging interpolation method*

This geostatistical gridding method produces visually intriguing maps from irregularly spaced data (Marcotte and Chateau, 1993). The kriging method can express trends suggested by the Bouguer data. It was applied, in our cases, through the linear variogram analysis of sparse data surrounding the cave.

## 7.4 GRAVITY FORWARD MODEL

In order to estimate the expected residual gravity anomaly produced by the cave, the 2.5D forward model performed cross-cut the largest rooms within the Gruta de las Maravillas (Fig. 7.3). The cavity has a length of 50 m, a height of 20 m and perpendicular extension of 60 m, and it lies partially below the water table. The unsaturated cave has a density of 0 g/cm$^3$; the saturated cave has a standard density of 1 g/cm$^3$. The host rock of

the cave is mostly composed by marbles with a density of 2.7 g/cm$^3$. The minimum residual gravity anomaly produced by the cave is -0.25 mGal in this section.

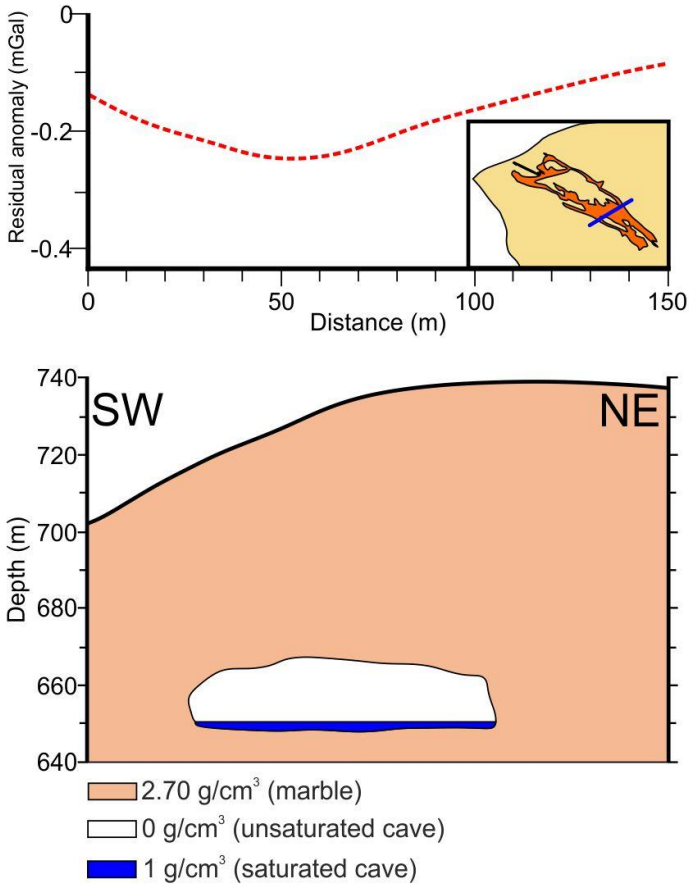


Figure 7.3: Microgravity forward model on the biggest galleries of the Gruta de las Maravillas cave. The morphology of the cave in this section is used to calculate the residual gravity anomaly produced by the cave.

## 7.5 RESULTS

### 7.5.1 Bouguer anomaly map

The Bouguer anomalies show a linear trend elongated in a WNW-ESE direction decreasing to the NE (Fig. 7.4). The values range from 38.6 mGal to 36.0 mGal. The highest values are associated with outcropping granodiorites, which present a slightly higher density than marbles, quartzites and gneisses. The projection of Gruta de las Maravillas cave coincides with Bouguer anomaly values of 36.8 mGal to 37.2 mGal. A

zone possibly presenting new cavities (Martinez-Moreno *et al.*, 2014) gives lower values, ranging from 36.4 mGal to 36.8 mGal.

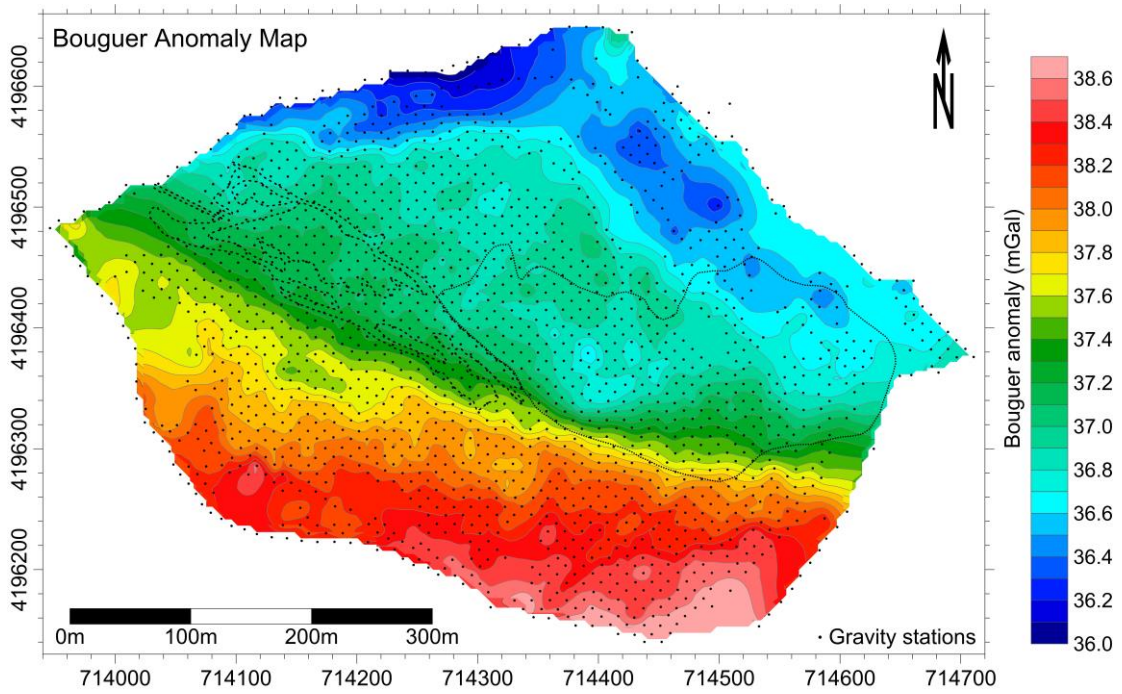


Figure 7.4: Bouguer anomaly map. The gravity stations are marked with black dots. Gruta de las Maravillas cave and the probable zone of new cavities (complete karst system) are highlighted with dashed black line.

### 7.5.2 Regional and residual gravity anomaly maps

Different regional and residual maps were obtained by applying the proposed methods (listed in Table 7.2). The overall quality of each method was evaluated by studying the residual anomalies obtained with the position and morphology of the mapped Gruta de las Maravillas, then comparing them with the residual anomaly estimated using the forward model (Fig. 7.3). We moreover took into account any new cavities indirectly detected by means of other geophysical methods (from Martínez-Moreno *et al.*, 2014).

#### *7.5.2.1 Methods that include all gravity data*

The regional map obtained with first-order polynomial fitting presents a linear trend with N105ºE elongation (Fig. 7.5a), giving values that vary from 36.0 mGal to 38.2

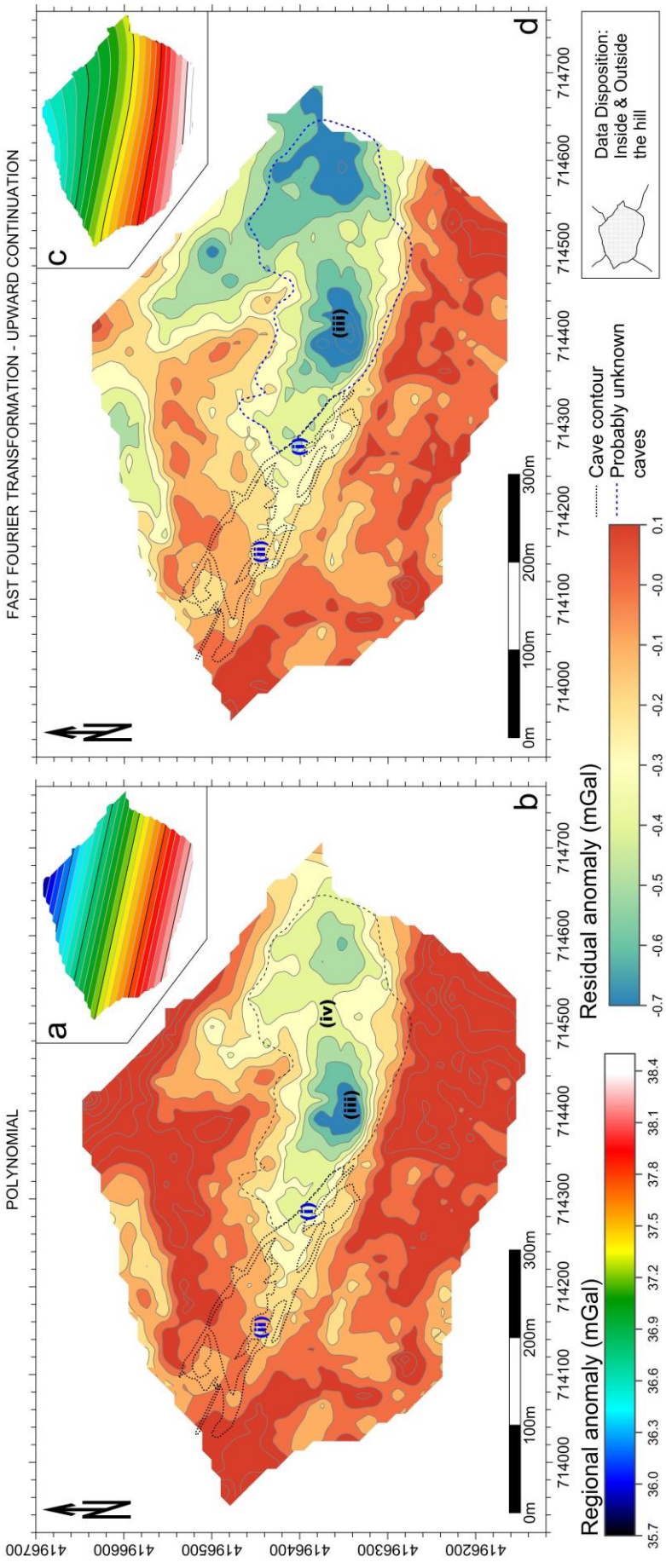


Figure 7.5: Regional and residual separation from Bouguer anomaly map calculated on gravity data in and beyond the hill. Regional (a) and residual (b) anomaly maps obtained with first-order polynomial fitting. Regional (c) and residual (d) anomaly maps calculated by Fast Fourier Transformation and upward continuation filter.

mGal, from NE to SW. After subtracting these values from the Bouguer map, the residual map derived (Fig. 7.5b) indicates a central zone of negative anomalies, elongated in a WNW-ESE direction. The projection of Gruta de las Maravillas cave fits with minima of -0.3 to -0.2 mGal that is particularly evident over the largest galleries, designated as (i) in Fig. 7.5a. The lower galleries (ii) coincide with a minimum of -0.1 mGal, while the zone containing unexplored cavities shows locally pronounced minima (iii) as well as more widespread minima (iv).

The Fast Fourier Transformation method reflects a regional anomaly of slightly curvilinear morphology (Fig. 7.5c). The variation in the values is less than in polynomial fitting, ranging from 36.4 mGal to 38.0 mGal, again from NE to SW. The residual anomaly map (Fig. 7.5d) shows the Gruta de las Maravillas cave to be less highlighted, presenting values of -0.5 mGal to -0.3 mGal for the largest galleries (i), and -0.2 mGal for the lower ones (ii). Moreover, in the zone of the unexplored cavities (iii), an extended minimum of -0.9 mGal is obtained.

*7.5.2.2 Methods that include only the high resolution data (10 x 10 grid)*

In this case, the regional anomaly obtained using the polynomial fitting method shows a linear trend (Fig. 7.6a) with a N105ºE strike, the values decreasing towards the NE. The regional anomaly varies between 35.8 mGal to the N, and 38.3 mGal to the S. The residual anomaly map (Fig. 7.6b) shows minima of -0.2 mGal to -0.4 mGal fitting with the biggest galleries of the cave (i), and -0.1 mGal coinciding with the smaller ones (ii). In the zone where the presence of new caves has been suggested, a pronounced minimum of -0.8 mGal (iii) and a smoother one of -0.3 mGal (iv) were obtained.

The regional map derived using the Fast Fourier Transformation method features a slightly curved anomaly in the central part of the study area (Fig. 7.7a), with an average N100ºE direction and values decreasing towards the N from 38.5 to 36.1 mGal. The

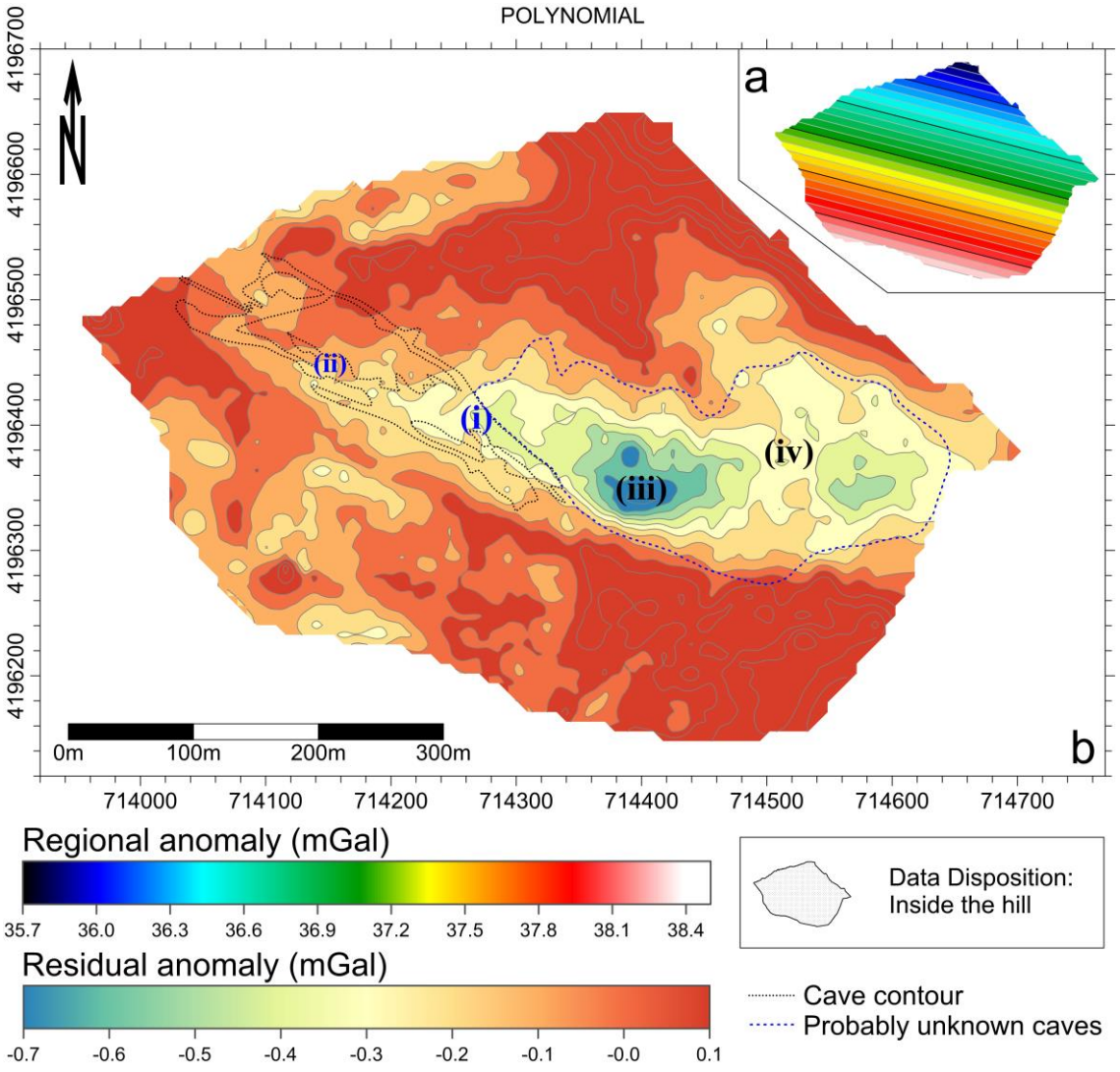


Figure 7.6: Regional and residual separation from Bouguer anomaly map calculated by first-order polynomial fitting on gravity data measured inside the hill. Regional (a) and residual (b) anomaly maps.

residual anomaly map (Fig. 7.7b) reflects the largest galleries of the cave (i) with -0.3 to -0.4 mGal, and the smaller ones (ii) with values of -0.1 mGal. The cavities indirectly detected coincide with values of -0.8 mGal on the pronounced minimum (iii) and -0.4 mGal over the extended minima (iv).

Finally, the regional anomaly map obtained by means of the moving average method (Fig. 7.8a) shows a curved trend with an average N100ºE strike. The anomaly decreases towards the NW, ranging from 36.7 to 37.8 mGal. The residual anomaly (Fig.

7.8b) shows two major zones: a minimum to the NE (i) and a maximum to the SW (ii). The largest galleries (iii) coincide with minima of -0.3 mGal to -0.4, and the smaller cavities (iv) present a minimum of -0.2 mGal. The new cavities detected indirectly by Martinez-Moreno *et al.* (2014) again appear as two minima: one is more pronounced (v) and reaches -0.6 mGal, whereas the other is smoother (vi), -0.3 mGal.

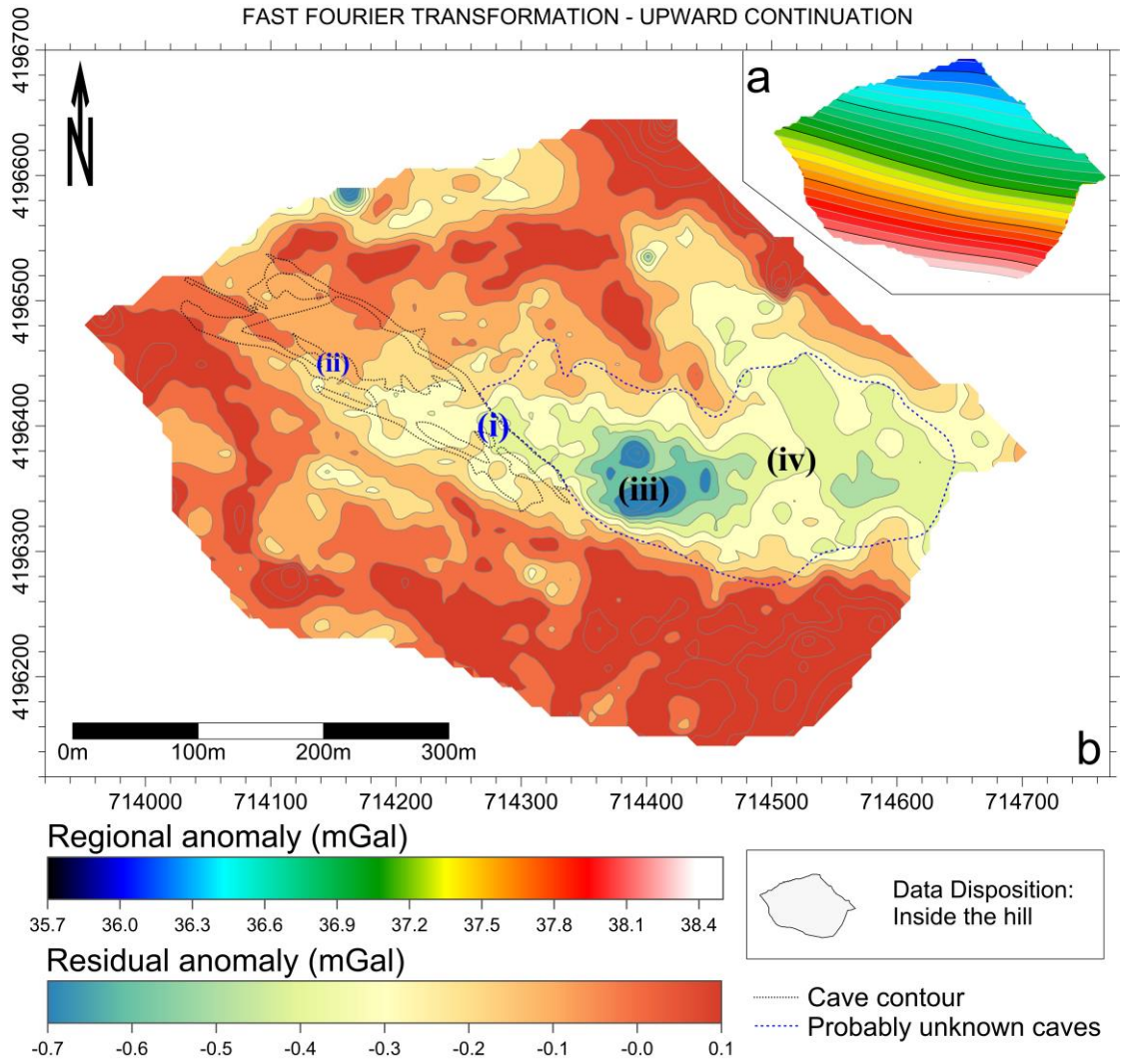


Figure 7.7: Regional and residual separation from Bouguer anomaly map calculated with Fast Fourier Transformation and upward continuation filter on gravity data measured inside the hill. Regional (a) and residual (b) anomaly maps.

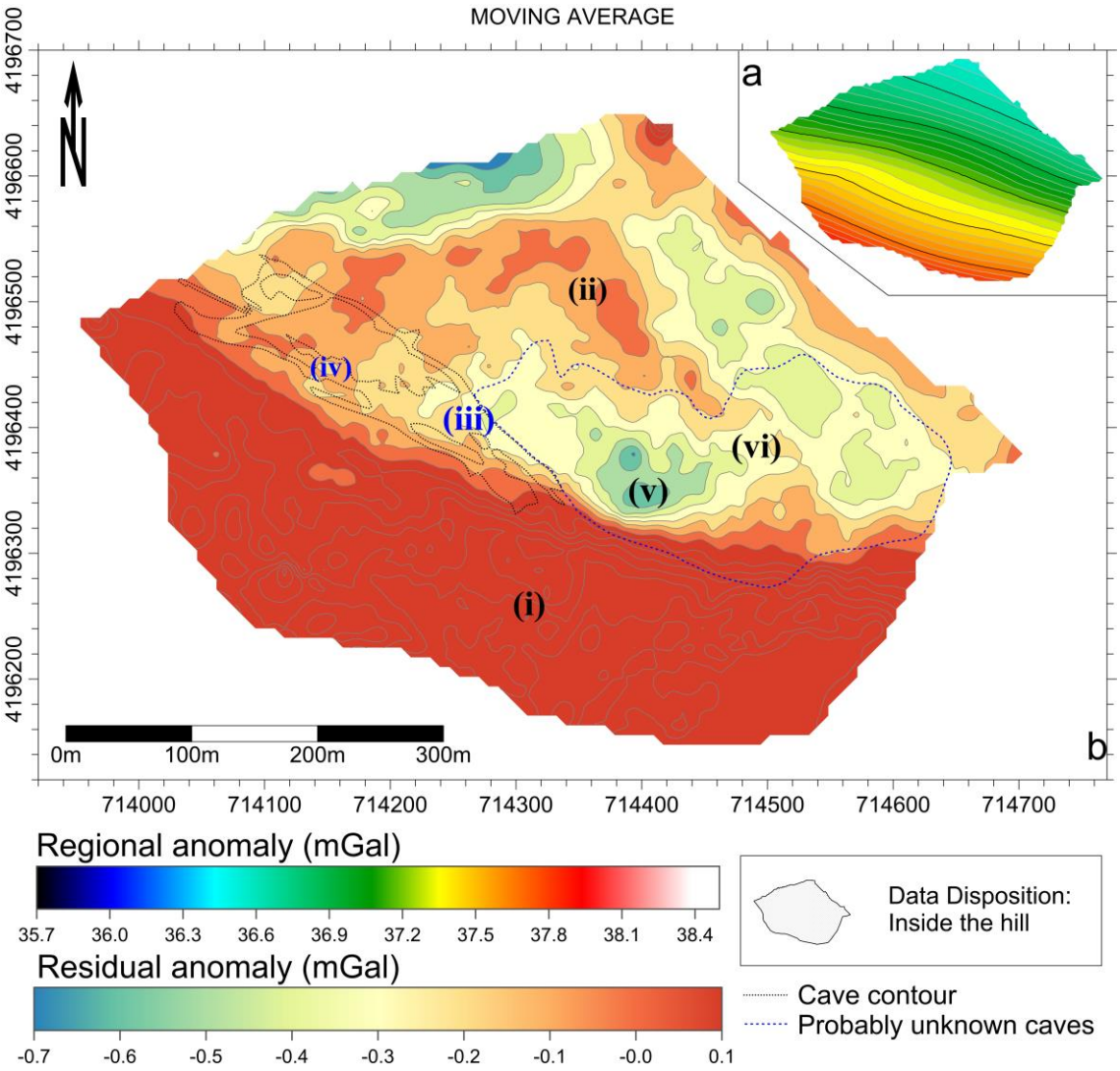


Figure 7.8: Regional and residual separation from Bouguer anomaly map calculated on gravity data measured inside the hill. Regional (a) and residual (b) anomaly maps obtained by moving average method.

### *7.5.2.3 Methods that include only the surrounding sparse data*

In turn, the polynomial fitting method considering only the sparse gravity data that surround Cerro del Castillo hill shows a regional map with a WSW-ENE linear elongated morphology (Fig. 7.9a). The values decrease towards the WNW from 38.7 to 36.5 mGal. The residual map (Fig. 7.9b) detects the biggest galleries of the cave (i) with values of -0.6 mGal to -0.7 mGal in the residual anomaly map. The smaller galleries (ii) have values of -0.2 mGal, and the unexplored cavities are detected as a broad and smooth minimum (iii) of -1 mGal.

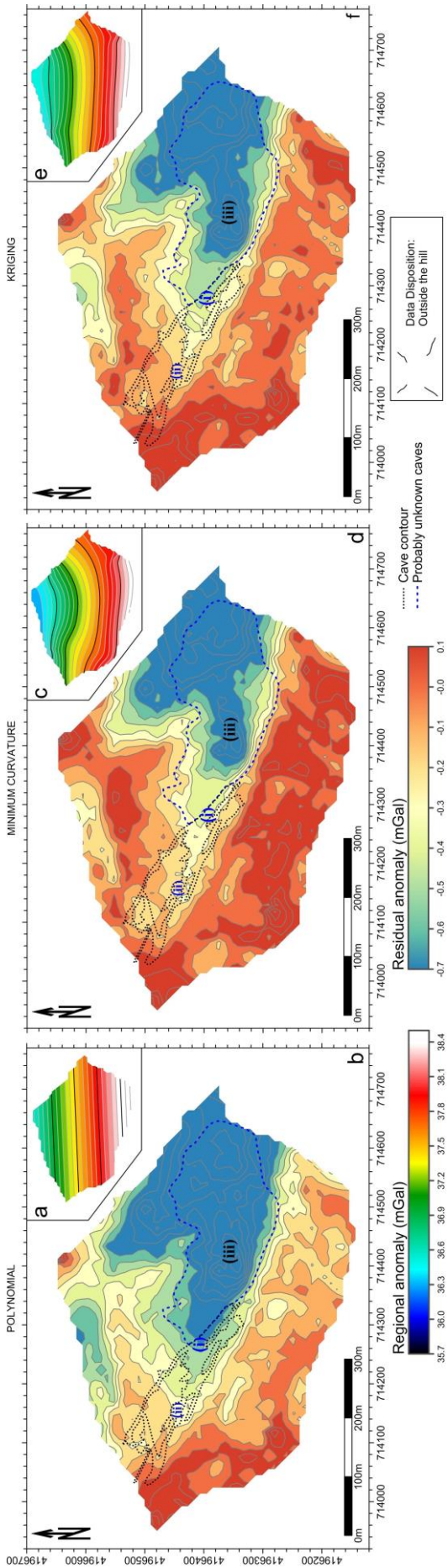


Figure 7.9: Regional and residual separation from Bouguer anomaly calculated on gravity data measured outside the hill. Regional (a) and residual (b) anomaly maps calculated with first-order polynomial fitting. Regional (c) and residual (d) anomaly maps obtained by minimum curvature. Regional (e) and residual (f) maps obtained by kriging.

The regional map obtained using the minimum curvature method presents a curvilinear trend with values decreasing towards the N from 38.6 to 36.3 mGal (Fig. 7.9c). The residual anomaly (Fig. 7.9d) reflects the cave contours pertaining to the largest galleries (i) with minima of -0.4 to -0.5 mGal, and the smaller galleries (ii) with -0.1 mGal. The new cavities (iii) are identified with an extended minimum of -1 mGal.

The regional map obtained with the kriging method also presents curvilinear contour lines (Fig. 7.9e), but mainly elongated in an E-W direction. The values decrease towards the N, from 38.6 to 36.4 mGal. The calculated residual anomaly map (Fig. 7.9f) assigns values of -0.4 to -0.2 mGal to the largest galleries (i), and -0.1 mGal to the smaller ones (ii). Again, the newly detected yet unexplored cavities (iii) are related to a smooth minimum of -1 mGal.

## 7.6 DISCUSSION

As we show in the previous section, the calculation of residual anomaly maps provides quite different results depending on the methods applied.

### 7.6.1 Data distribution

The regional anomaly obtained only with the data sets from beyond the hill (Fig. 7.9) presents morphologies that do not match the geological information regarding the hill itself. The trend obtained is oriented W-E, while the foliation tendency is N110ºE. Moreover, the residual maps obtained mask the presence of the Gruta de las Maravillas cave, and the zone containing "unexplored" cavities appears as minima with high spatial wavelength. Therefore, the separation of regional and residual maps is not restricted to the anomalies pertaining to the study area. This effect is further observed in the residual

anomaly maps obtained with FFT-upward continuation (Fig. 7.5d) applied to the data both inside and outside the study area, although less extended.

The residual maps created only with data from inside the hill highlight the cave and the unexplored cavities better. The results obtained using polynomial fitting with all data sets versus data only inside the hill are actually very similar (Figs. 7.5b and 7.6b). In some cases, measuring stations far from the area of interest present added difficulty. Therefore, in cave research with microgravity prospection covering a given area in a regular grid, the residual anomaly may be derived more accurately with measurements from inside the area of interest.

### 7.6.2 The optimum regional-residual gravimetric separation

All applied methods detect the largest galleries of Gruta de las Maravillas cave as gravimetric minima (Fig. 7.10). Nevertheless, some methods achieve more minimum associated to cave presence than others. Choice of the optimal regional-residual separation is based on the gravity anomaly calculated in the forward model (Fig. 7.3). The value associated with the cave in that section and with the corresponding cave features is -0.25 mGal.

The residual anomaly values associated with the largest parts of the Gruta de las Maravillas cave range from -0.6 mGal (polynomial fitting, Fig. 7.9b; FFT, Fig. 7.5d) to -0.3 mGal (polynomial fitting, Figs. 7.5b and 7.6b; FFT-upward continuation, Fig. 7.7b; minimum curvature, Fig. 7.8b; moving average, Fig. 7.9d; kriging, Fig. 7.9f). Some match the cave morphology and its continuation towards the E better than others.

Methods including FFT-upward continuation, polynomial fitting, kriging or minimum curvature, when applied on data from beyond the hill, detect the largest galleries as prominent minima, whereas the new caves are detected as smooth minima.

The Gruta de las Maravillas continuation is elongated in the direction of the cave, and the areas towards the SW and NE should be detected as residual anomaly maxima. This effect disappears when the regional anomaly is calculated with data from outside, in which case the regional anomaly is restricted to geological structures beyond the hill.

Polynomial fitting, FFT-upward continuation or moving average methods estimate the cave position more precisely while pointing to its possible continuation. The cave modelled in 2.5D is a better match with the values obtained using these methods. They detect the central part of the hill, where the cave lies, as minima enclosed by maxima towards the NW and SE, where the granodiorites and gneiss prevail. In contrast, the moving average method does not detect the maximum to the NW, and the FFT-upward continuation detects a less prominent NW maximum. One major in applying these procedures resides in the selection of the optimal parameters for regional anomaly calculation. As adjusting the parameters in upward continuation filters might condition results, the comparison with geological information is key. Selection of the polynomial degree could be easy in the case of elongated Bouguer anomaly shapes, yet difficult for complicated maps. A low degree is always recommended (Martín *et al.*, 2011), given that a high degree can mask relevant information in the residual anomaly map.

In light of the above, the method found to provide the most accuracy in terms of regional-residual separation and cave morphology is first-order polynomial fitting applied to data from inside the hill. In addition, the regional anomaly obtained, with an elongated morphology according to foliation, fits better with the geological information.

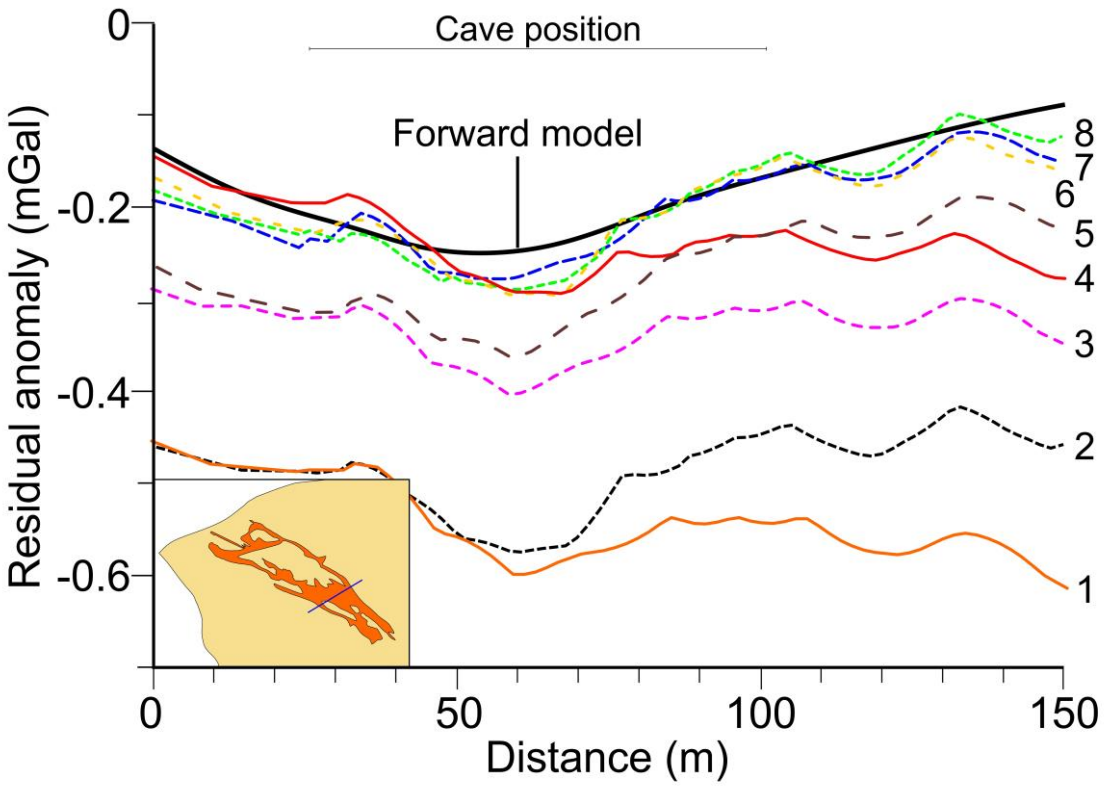


Figure 7.10: Microgravity profile measured over the biggest galleries of Gruta de las Maravillas cave in the different residual anomalies obtained. Total datasets: (2) FFT-upward-continuation and (7) Polynomial fitting. Inside study area data: (4) Moving average, (6) FFT-upward continuation and (8) Polynomial fitting. Outside study area data: (1) Polynomial fitting, (3) Kriging and (5) Minimum Curvature.

## 7.7 CONCLUSIONS

In cave detection studies entailing microgravity prospection, the separation of regional and residual anomalies from the Bouguer anomaly is a crucial processing step. Uncertainty about which method provides the best results calls for analyses such as this comparison of results obtained with various procedures using the same data.

We analysed the data from microgravity stations measured in a regular grid of 10 x 10 m covering the area of interest, located in the Cerro del Castillo hill where the Gruta de las Maravillas karst system is emplaced. Data surrounding the area of interest were additionally taken into account for the regional-residual separation, and data were interpreted both jointly and separately. The obtained results, when compared with well-

established information from a known cave, reveal that microgravity prospection for cave detection requires only the data measured over the area of interest in a regular grid. However, the data must pertain to an area large enough so as to allow for the cave to be highlighted.

Polynomial fitting, a popular method applied by numerous authors (Table 7.1), proves to be the best technique for detecting the caves involved in our study. In addition, this method yields a regional anomaly that better fits the geological information. We therefore recommended calculating the regional-residual separation from the Bouguer anomaly through polynomial fitting of a low-degree over data corresponding strictly to the area of interest.

## ACKNOWLEDGMENTS

We thank Dr. Ardestani and another anonymous reviewer for their insightful comments that helped to improve the manuscript substantially. The studies present here were part of projects 3726–00, 3727–00, CGL2010-21048, P09-RNM-5388 and RNM148. Moreover, we would like to thank the Aracena City Council and the Gruta de las Maravillas staff for permitting our fieldwork and cave data acquisition. We also wish to acknowledge the assistance provided in the field by Rafael R. Durán and Adela Hodar.

# Chapter 8

## Cave detection with geophysical methods and drills exploration in Cerro del Castillo

## 8.1 INTRODUCTION

The geophysical results obtained in the Cerro del Castillo (Aracena, SW Spain) make suspect the presence of uncovered cavities in relation with the Gruta de las Maravillas cave. In addition, the geological data suggest the continuity of the cave toward the ESE.

In order to check the presence of new cavities predicted by near-surface geophysics, it has been performed shallow drill exploration. The drilling technique require a few of meters exploration without a great expending of time and money. This fact ensures the geophysical results and its interpretation, and they can be extrapolated to other parts with analogous geophysics results (Keys and MacCary, 1971; Finger, 1984; Keys, 1989).

In gravity surveys, a decrease of the residual anomaly can be attributed to the presence of buried caves but also to lithological changes. These uncertainties shall be removed performing a drill. In the case of the Cerro del Castillo, the minima of residual anomaly coincides with outcropping quartzites, a lithology where the karstic caves does not develop. However, the high complexity of the geology of the hill, including shear bands and folds composed of marbles and quartzites, leaves open the possibility to find karstified marbles under the quartzites. Moreover, the other geophysical methods applied on these areas also point out anomalies that suggest the cave presence (Martínez-Moreno et al., 2014).

The aim of this exploration is to test the cave presence under the areas marked with minima of residual gravity anomaly. For this purpose, we have performed a borehole in best zones where considering geophysical, geological and accessibility criteria.

## 8.2 DRILLING MACHINE

The boreholes were performed with the equipment Rolatec RL 48-M, from Rolatec Inc. (Fig. 8.1). The drilling machine, whose weight is about 4500 kg and mast length of 4.5 m, has a maximum drilling depth of 200 m, with a diameter up to 200 mm with conventional drilling system and HQ. The rotation head has 100 mm pitch striated hollow shaft and threat for coupling direct rotation. The rotation speed go from 0 to 900 revolution per minute (r.p.m.), variable from the control panel. The maximum torque is 450 kg, the hydraulic clamp installed on the head has 90 mm (HQ) diameter rod capacity, and the hydraulic retainer has a guide and retention capacity until 200 mm with dual retainer releaser. The head travel has a diameter of 2400 mm with a maximum traction of 7000 kg. The drilling angle is from 0º to 20º, with four adjustable cylinders plate and control to check valves. The water pump has regulated flow from 0 to 140 (liter per minute) l.p.m. and regulated pressure from 0 to 45 bar. In addition, it has a wire line winch of 1000 kg capacity in direct pull with 200 m of cable with 6 mm diameter.

Figure 8.1: Rolatec RL 48-M equipment on the borehole 1.

The borehole performed has a depth of 52 m excavated with diamond core drill bit for hard rocks. The collaring go from 0 to 1.5 m with a hole diameter of 101 mm and a core diameter of 98 mm. From 1.5 to 27 m the hole diameter is 86 mm with a core diameter of 74 mm. Due to the fracturing of the explored zones, the drill system was changed to avoid too much spend of time recovering samples. For this purpose, the samples were recollected inside the core drill with a diameter of 48 mm and a hole diameter of 76 mm (NQ). The drill was performed with rotation system to avoid stabilization problems and preserve the karst system. The rotation velocity was from 100 to 200 r.p.m. and the water pump flow was 12.5 l.p.m.

## 8.3 DRILL EXPLORATION LOCATION AND ITS RELATIONSHIP WITH GEOPHYSICAL RESULTS AND GEOLOGICAL SETTINGS

The best location of the drill exploration has been decided according to certain parameters. First, it has been taken into account the main minima of residual anomaly detected in the hill. Secondly, geological settings as pyrite band location related to cave occurrence and quartzite-marble contact, have marked the second approach. Finally, the machine accessibility has restricted the final location of the drill exploration.

The drill has been located at the E of the hill (Fig. 8.2), at 713 m.a.s.l. The residual anomaly highlight that area with minima values from -0.3 to -0.5 mGal. It is located in the continuity of the elongated shape of the minimum, in the cave development direction. In addition, it is close to the profiles 3 and 4 (Chapter 6, Figs. 6.5, 6.8 and 6.9), which detect shallow and deep cavities. Moreover, the drill is located over outcropping quartzites close to the contact with marbles (Fig. 8.3). This contact presents an elongated shape, with the foliation trending N110ºE and dipping 70º toward NE. In addition, the

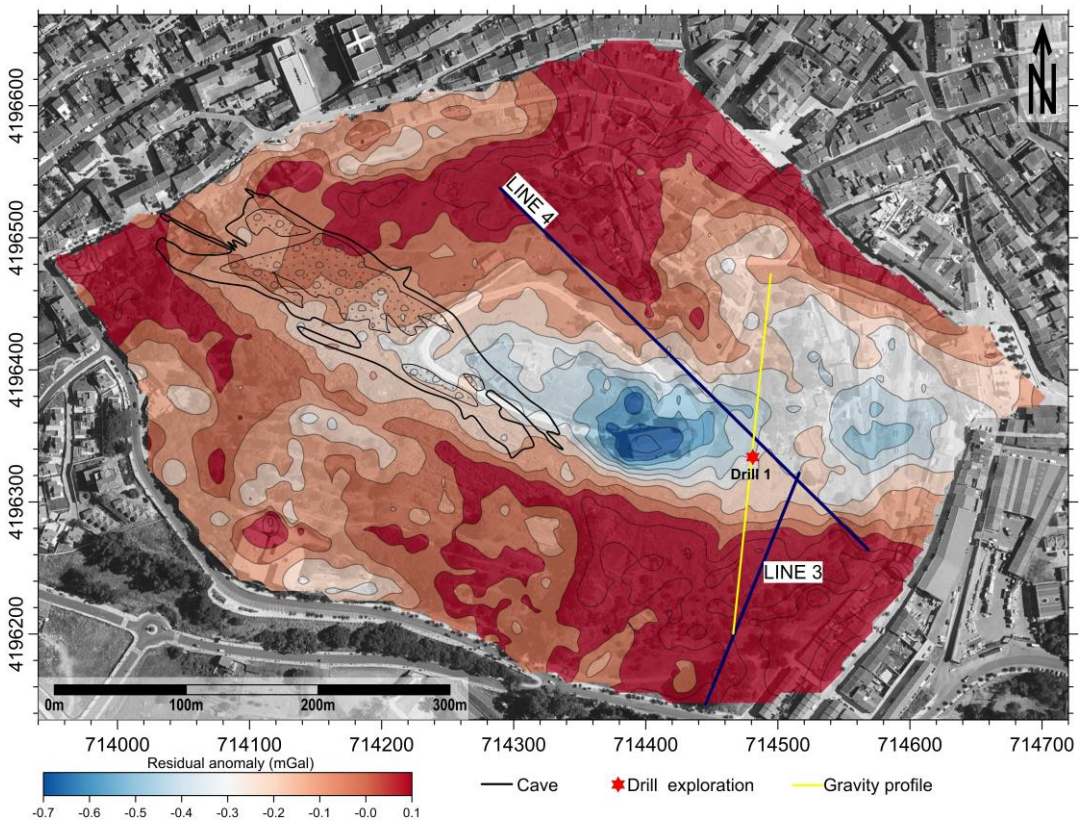


Figure 8.2: Location of the drill exploration over the residual anomaly map. The cave morphology is marked, as well as the gravity profiles modelled.

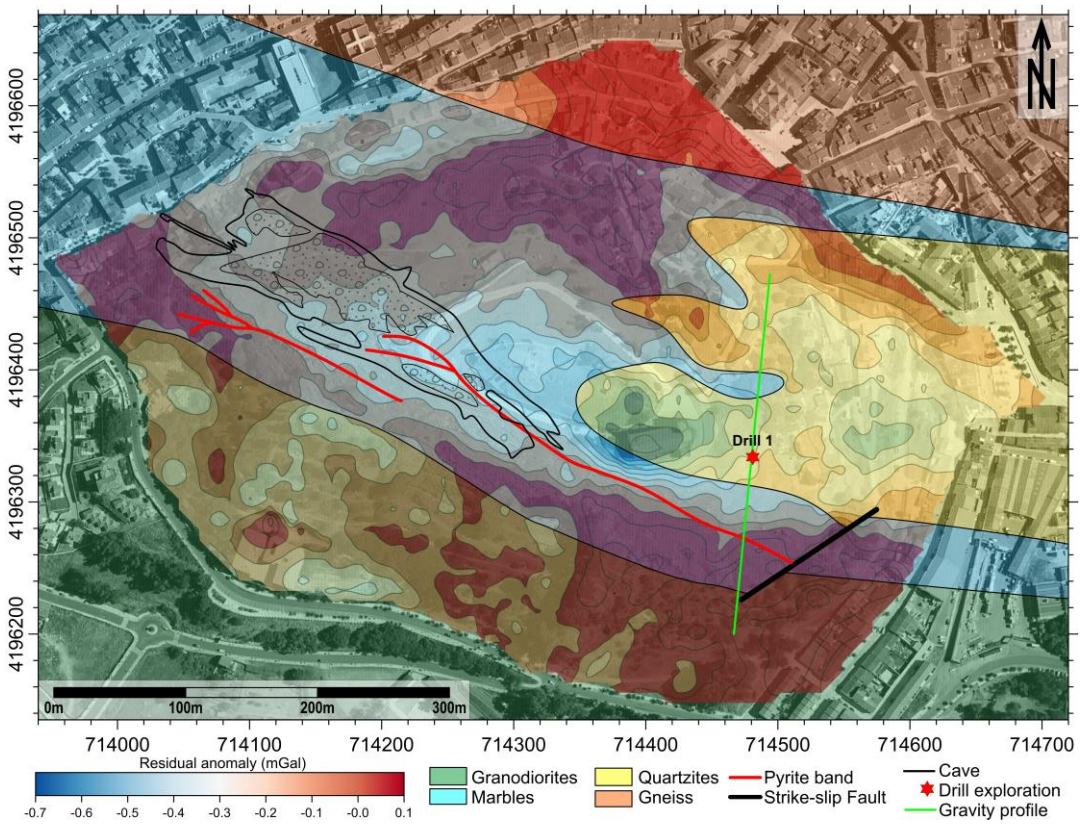


Figure 8.3: Location of the drill exploration over the geological sketch and the residual anomaly map. The cave morphology is marked, as well as the gravity profiles modelled.

pyrite band, which is an essential element in the cave formation, is found at the SW to the drill location is similar to the location of this band in respect to the Gruta de las Maravillas. Finally, the precise area selected responds to machine accessibility and architectural barriers. The point selected is the unique area where the ground is practically flat, which is essential to perform the drill exploration.

There are another possibilities which were raised for the drills location. For example, the profile 2 of the geophysical methods applied (Chapter 6, Fig. 6.7) detects a shallow cave which could be explored with drills. However, the accessibility of the machine, the steep slope and the absence of flat ground, in addition with the archaeological protection of the area, prevented its drilling. Moreover, another possibility is perform an inclined drill. However, from the path it needed an angle of 45º in the drill to achieve the cave detected, and the angle limitation from the machine is until 20º.

## 8.4 RESULTS

At the top of the borehole, from 0 to 0.90 m is cover with vegetal soil (Fig. 8.4). Under this vegetal layer appears quartzites, from 0.90 m to 27 m. This quartzite layer presents different colour changes, from light colours at the top to more darks ones in deep. In addition, there are thick layers from 1 to 3 centimeters formed by calcite and quartz interlayered in the quartzites. The fracturing of the layer increase with the depth. At 14.75 m depth appear a thick layer with abundant pyrite, under which the density in the fractures increase notably. In some areas, appears quartzites with calcite layers dissolved and with decalcification clays filling the voids (Fig. 8.5).

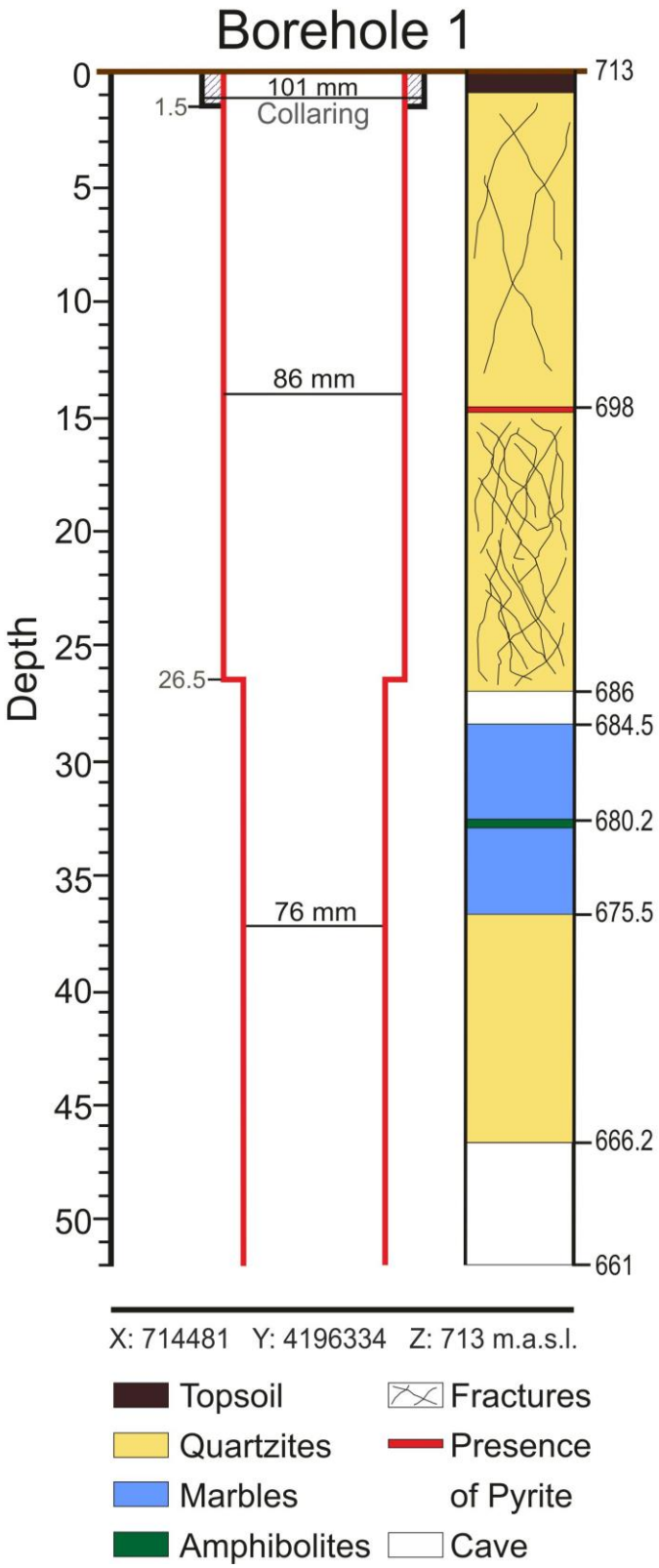


Figure 8.4: description of the drill exploration. The depth and the elevation is marked. The hole diameter is indicated, and the lithological column is described.


Figure 8.5: Quartzite sample with calcite veins dissolved and decalcification clays filling the voids

At 27 m deep it was found a hole of 1.5 m high. It is located from 684.5 to 686 m.a.s.l. Under this void, appear a marble layer, from 28.5 to 37 m deep. The marbles has less dissolution than upper quarzites. A small intercalation of amphibolites is located at 32.75 m deep with a thickness of 0.6 m. At 37 m deep is found quartzites with very low dissolution. Finally, a new void is found from 46.80 to 52 m deep. The hole has a high of 5.20 m, from 666.2 to 661 m.a.s.l. Under this hole the vibration of the drill exploration machine during the rotation prevented the continuation of the drill.

## 8.5 DISCUSSIONS AND CONCLUSIONS

The results obtained in the drill exploration confirm the geological data and the geophysical results obtained. The presence of marbles intercalated with quartzites is observed both, shallow and deep. These intercalations leave open the possibility to find caves in any place of the hill where marbles and quartzites crop out indistinctly.

The dissolution level at the upper part of the borehole (Fig. 8.5) influences the geophysical results. In gravity results produce decreasing in residual anomaly values due to this dissolved areas. In electrical results, these zones are detected as shallow and small resistivity areas, as well as in velocity profiles in seismic refraction produce a decreasing in velocities values. The ray tracing highlight small and shallow areas with ray tracing absence, greater than the dissolved area because this small fractures behave as major barriers. Finally, the GPR detect these zones with hyperbolic reflectors without signal absorption.

In view of the data obtained, has been performed a forward model in residual gravity anomaly (Fig. 8.6). The model include the three lithologies present along the profile (Fig. 8.3): granodiorites (2.73 g/cm$^3$), marbles (2.7 g/cm$^3$) and quartzites (2.63 g/cm$^3$). The caves have been modeled with a density of 0 g/cm$^3$. In the first case (Fig. 8.3a), only has been taken into account the caves detected belonging to the level 2 and 3 of the Gruta de las Maravillas karst system (Fig. 8.3c). The calculated anomaly do not fit with the observed anomaly requiring an additional low density body in the borehole area. A new uncovered cave has been fitting the observed anomaly (Fig. 8.3b and c).

The borehole performed has detected two of the three levels observed in the Gruta de las Maravillas cave. Altogether, they are located at the same elevation than the levels of the cave. The horizontal development of the Gruta de las Maravillas allow make this interpretation and correlated the levels at both place of the hill. In addition, the borehole confirms the cave levels detected in the profile 3 in chapter 6 (Fig. 6.8) and the caves modeled in the profile 4 in chapter 6 (Fig. 6.9). Moreover, the borehole ensures that the minima of residual anomaly are produced by voids and not by a density decreasing associated with quartzites.

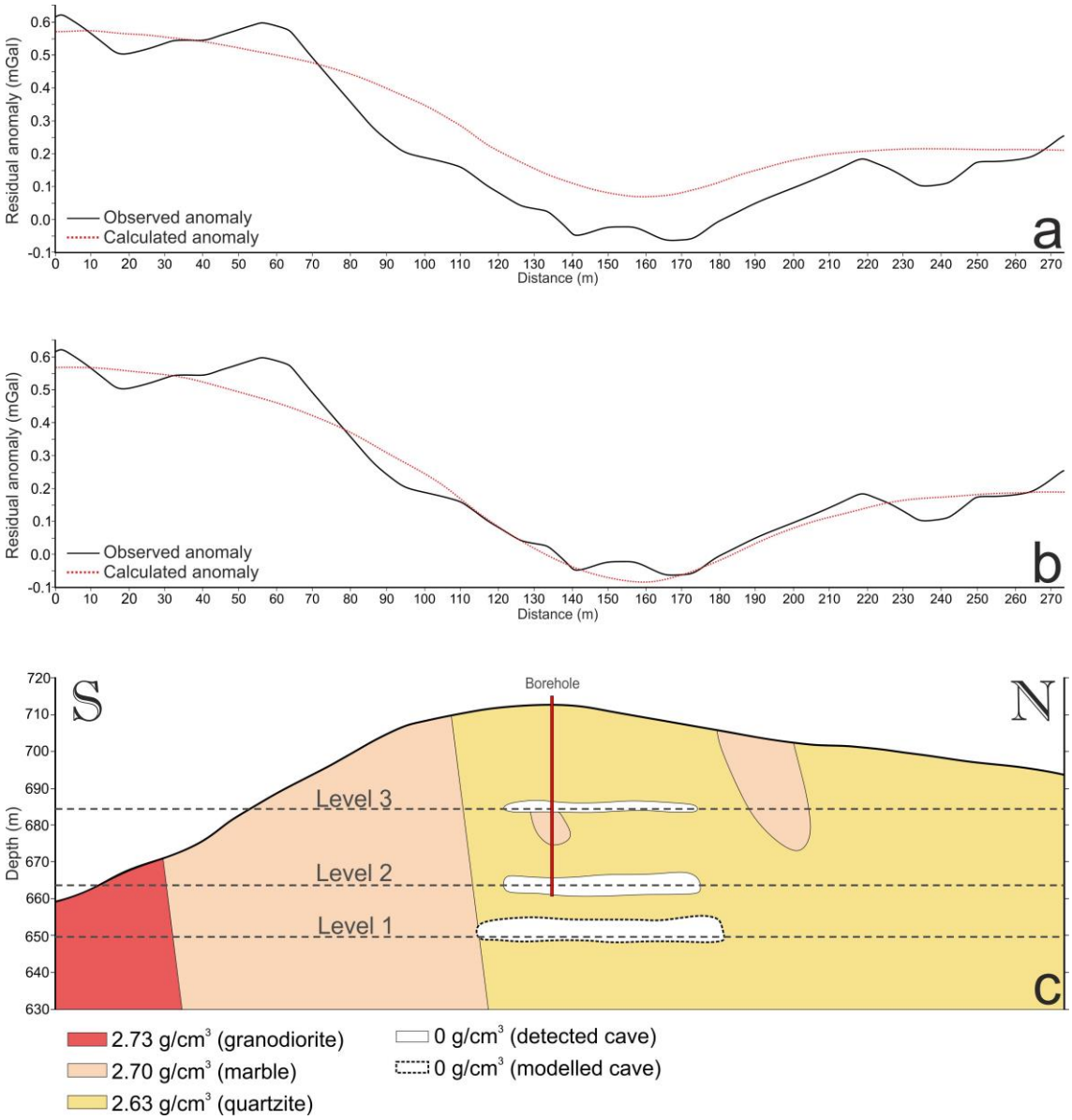


Figure 8.6: Residual anomaly profile over the borehole, pinpointed on Figures 8.2 and 8.3. (a) Gravity profile modelled only with the caves discovered. (b) Gravity profile modelled with the cave discovered and a new one located at the same deep than Level 1 in Gruta de las Maravillas. (c) Microgravity forward model constructed from the residual gravity anomalies where the detected caves contour is marked with a thick black line, and the uncovered level is marked with black dashed line.

In view of the results it is concluded that the geophysical results are a good tool to detect caves. The borehole performed has confirmed that the minima of residual anomaly are associated to caves and the interpretation of the geophysical profiles is fitted with the

geology of the Cerro del Castillo hill. In addition, the borehole has detected new cavities which belong to the continuity of the Gruta de las Maravillas, probably connected through the collapse from the Great Lake of the cave.

# Chapter 9

## Algaidilla cave

# Combined microgravity, electrical resistivity tomography and induced polarization to detect deeply buried caves: Algaidilla cave (Southern Spain)

F.J. Martínez-Moreno[a], A. Pedrera[b], P. Ruano[a,b], J. Galindo-Zaldívar[a,b], S. Martos-Rosillo[c], L. González-Castillo[a], J.P. Sánchez-Úbeda[a], C. Marín-Lechado[c]

[a] Departamento de Geodinámica, Universidad de Granada, 18071-Granada, Spain

[b] Instituto Andaluz de Ciencias de la Tierra, CSIC-Universidad de Granada, 18071-Granada, Spain

[c] Instituto Geológico y Minero de España, Ríos Rosas 23, 28003-Madrid, Spain

Published on:

**Engineering Geology**

Vol. 162, 67-78

*DOI: 10.1016/j.enggeo.2013.05.008*

Received 11 August 2011

Accepted 17 May 2013

## ABSTRACT

The suitability of the combined microgravity and electrical tomography to detect and characterize caves deeply buried in limestones is tested. We have selected the buried Algaidilla cave, in the Estepa range (western Betic Cordillera), which is partially submerged below the water table and which was intersected between 26 and 66 m in depth by two boreholes. At that location, microgravity, electrical resistivity tomography (ERT) and induced polarization (IP) data was collected along four profiles. Algaidilla cave is associated with a − 0.5 mGal residual gravity anomaly minimum. Microgravity models reveal an approximately horizontal N–S elongated shape with a maximum length of 150 m and a width of 40 m. Resistivity variations provide information on the cave sectors remaining above, as well as below the water table. Forward modelling and depth of investigation (DOI) support the suitability of ERT to constrain the cave geometry. The cave is identified as having an intermediate to low-resistivity feature, which approximately matches the 250 Ω·m contour line along its ceiling. In addition, induced polarization models show high chargeability anomalies probably associated with decalcification clays. The location and approximately geometry of Algaidilla cave estimated from geophysical modelling suggests that nearby overburden may develop cave-ins and collapse sinkholes. Microgravity is proved as a powerful tool to detect caves at this depth, but this method alone fails to estimate the geometry. ERT results delineate the cavity both above and below the water table. Although the deepest sectors of the models should be interpreted with caution since they are less constrained by the data, below the water table the cavity shows great resistivity contrast with regard to the background carbonate. In addition, this study points out the usefulness of the IP method for detecting decalcification clays, often present at the base of karstic caves.

**HIGHLIGHTS**

- We use the combination of nondestructive geophysics methods to detect deeply caves.
- We use microgravity, electrical resistivity tomography and induced polarization.
- Forward modelling supports the suitability of the response of ERT and IP profiles.
- The DOI index discriminates the unreliable parts of the electrical profiles.
- The high resolution of the measurement allows obtaining a trusted model of the cave.

**Keywords:** Microgravity; Electrical resistivity tomography; Induced polarization; Deep-cave geometry; DOI index; Forward modelling.

## 9.1 INTRODUCTION

The study of karst cavities is of great interest in the fields of civil engineering and hydrogeology. Firstly, subsidence by the collapse of karst cavities can have particular impacts on transport infrastructure and building. Secondly, karst cavities determine the hydrodynamics of carbonate aquifers, which constitute an important water resource in arid and semiarid regions, since these aquifers have a high rate of recharge, large storage capacity, and good water quality. Some karstic cavities are accessible from the surface and their size allows direct description and mapping. However, many caves remain disconnected from the surface or are connected by narrow fissures. These cavities must be characterized indirectly by geophysical methods.

Gravity methods have been used to detect near-surface caves since the 1960s (Chico, 1964 and Butler, 1984), and electrical prospecting has been used since the 1980s (Smith and Randazzo, 1975, Owen, 1983, Chamon and Dobereiner, 1988 and Rodríguez Castillo and Reyes Gutierrez, 1992). In recent years, electrical resistivity tomography (ERT) has developed as a key technique to image near-surface geological structures, including cave detection (McGrath *et al*., 2002, Zhou *et al*., 2004, El-Qady *et al*., 2005, Leucci and De Giorgi, 2005, Carpenter and Ekberg, 2006, Leucci, 2006, Rădulescu *et al*., 2007, Vargemezis *et al*., 2007, Abu-Shariah, 2009, Cardarelli *et al*., 2010, Lazzari *et al*., 2010, Ortega *et al*., 2010, Pánek *et al*., 2010, Ravbar and Kovačič, 2010, Valois *et al*., 2010 and Gambetta *et al*., 2011). Numerous combinations of gravity and electrical methods with other geophysical techniques have been used to detect superficial caves (Table 9.1). However, rarely these combinations of techniques reaches a depth greater than 40 m. Focusing on the combined microgravity and ERT methods, McGrath *et al*. (2002) successfully documented karstic voids up to 5 m deep. Recently, Gambetta *et al*.

(2011) satisfactorily tested the gravity and electrical response of a known shallow cave segment located at, or about, 30 m from the ground surface.

| **Author, year** | ***Methods** | **Depth (meters)** |
|---|---|---|
| Leucci and Giorgi, 2005 | GPR and ERT | 4 |
| Zhou *et al*., 2004 | ERT | 4 |
| Leucci and Giorgi, 2010 | GPR and MG | 5 |
| Brown *et al*, 2011 | MG, GPR, ERT, IP | 10 |
| El Qady *et al*., 2005 | GPR and ERT | 10 |
| McGrath *et al*., 2002 | G and ERT | 10 |
| Ortega *et al*, 2010 | ERT | 12 |
| Beres *et al*., 2001 | MG and GPR | 14 |
| Leucci, 2006 | GPR and ERT | 15 |
| Vargemezis *et al*., 2007 | ERT | 15 |
| Abu-Shariah, 2009 | ERT | 16 |
| McCann *et al*., 1987 | SRT and Seismic Resonance, Cross-hole, ERT, G, M and EM | 16 |
| Smith and Randazzo, 1975 | VES | 16 |
| Carpenter and Ekberg, 2006 | GPR and ERT | 19 |
| Bozzo *et al*., 1996 | EM, ERT, SRT | 20 |
| Lazzari *et al*., 2010 | GPR and ERT | 20 |
| Ravbar and Kovačič, 2009 | ERT | 20 |
| Cardarelli *et al*., 2010 | ERT and SRT | 25 |
| Mochales *et al*., 2008 | G, M and GPR | 28 |
| Butler, 1984 | G and G gradient | 30 |
| Gambetta *et al*., 2011 | G and ERT | 30 |
| Santos and Afonso, 2005 | ERT | 30 |
| Valois *et al*., 2010 | ERT and SRT | 30 |
| Guérin *et al*., 2009 | ERT, MRS, "mise-à-la-masse" electrical mapping and SRT. | 40 |
| Pánek *et al*, 2010 | ERT | 40 |
| Rodríguez and Reyes, 1992 | VES | 40 |
| Gibson *et al*., 2004 | ERT and M | 44 |
| Chamon and Dobereiner, 1988 | ERT, M, G and EM | 50 |
| Lange, 1999 | EM, G and NP | 80 |
| Rădulescu *et al*., 2007 | ERT and VES | 80 |

Table 9.1. Studies using gravity and/or electrical methods, and their combination with other geophysical techniques used for detecting caves. The approximate penetration depth is also indicated. Electrical methods: IP—induced polarization tomography; ERT—2D electrical resistivity tomography; VES—vertical electrical soundings. Electromagnetic methods: EM—electromagnetic; GPR—ground penetration radar; NP—natural potential. Magnetic methods: M—magnetometry; MRS—magnetic resonance sounding. Gravity methods: G—gravimetry. Seismic methods: SRT—seismic refraction tomography.

The aim of the present study is to test the suitability of combining microgravity, ERT and IP in order to detect and characterize karstic caves buried more than 30 m below the ground surface. We selected a buried cave located in the Estepa range (western Betic Cordillera), intersected by two boreholes between 26 and 66 m depth, in order to characterize its geometry combining these geophysical techniques.

## 9.2 GEOLOGICAL AND HYDROGEOLOGICAL SETTING

The Betic Cordillera is the westernmost end of the European Alpine Chain and, together with the Rif, forms the Gibraltar Tectonic Arc. Three major geological zones are recognized in the Betic Cordillera: the Internal Zones, the Campo de Gibraltar Flysch Complex, and the External Zones. The External Zones are composed mainly of Mesozoic limestones that extensively crop out WSW–ENE along the north-western border of the Betic Cordillera (Fig. 9.1a). These are divided into the Prebetic and Subbetic sedimentary sequences deposited close and far, respectively from the South Iberian paleomargin (García-Hernández *et al*., 1980). These rocks are deformed by folds and thrusts with a general vergence towards the NW (Fig. 9.1b). In the western part of the Betic Cordillera, the rocks of the External Zones underwent accretion and fragmentation above, with a thick plastic tectonic mélange unit of a highly deformed rock assemblage, the so-called Subbetic Chaotic Complex (Vera and Martín-Algarra, 2004) where carbonates frequently constitute isolated ranges deformed by fold-and-thrusts (Frizon de Lamotte *et al*., 1991, Crespo-Blanc and Campos, 2001 and Pedrera *et al*., 2012).

The Estepa range is one of these isolated ranges, composed of several carbonate outcrops: the Becerrero, Hacho, Mingo, Águilas, and Pleites hill (Fig. 9.1b). The sedimentary sequence starts in a thick mélange unit with a matrix formed mainly by

Triassic Keuper clays and evaporites (Pedrera *et al*., 2012 and Ruiz-Constán *et al*., 2012). Detached above this unit, lies a Mesozoic-Paleogene sequence. This starts with 20 to 50 m of dolomitic breccias. Over these lie 200 to 300 m of Middle Jurassic limestones (Molina, 1987). A unit of argillaceous nodular limestones was deposited above during the Middle Jurassic to Early Cretaceous. On the top, Cretaceous to Paleocene marls and marly limestone are heterogeneously distributed with large thickness changes and sedimentary gaps (Castro and Ruiz-Ortiz, 1991). A unit of white marls, calcareous sands, limestones,

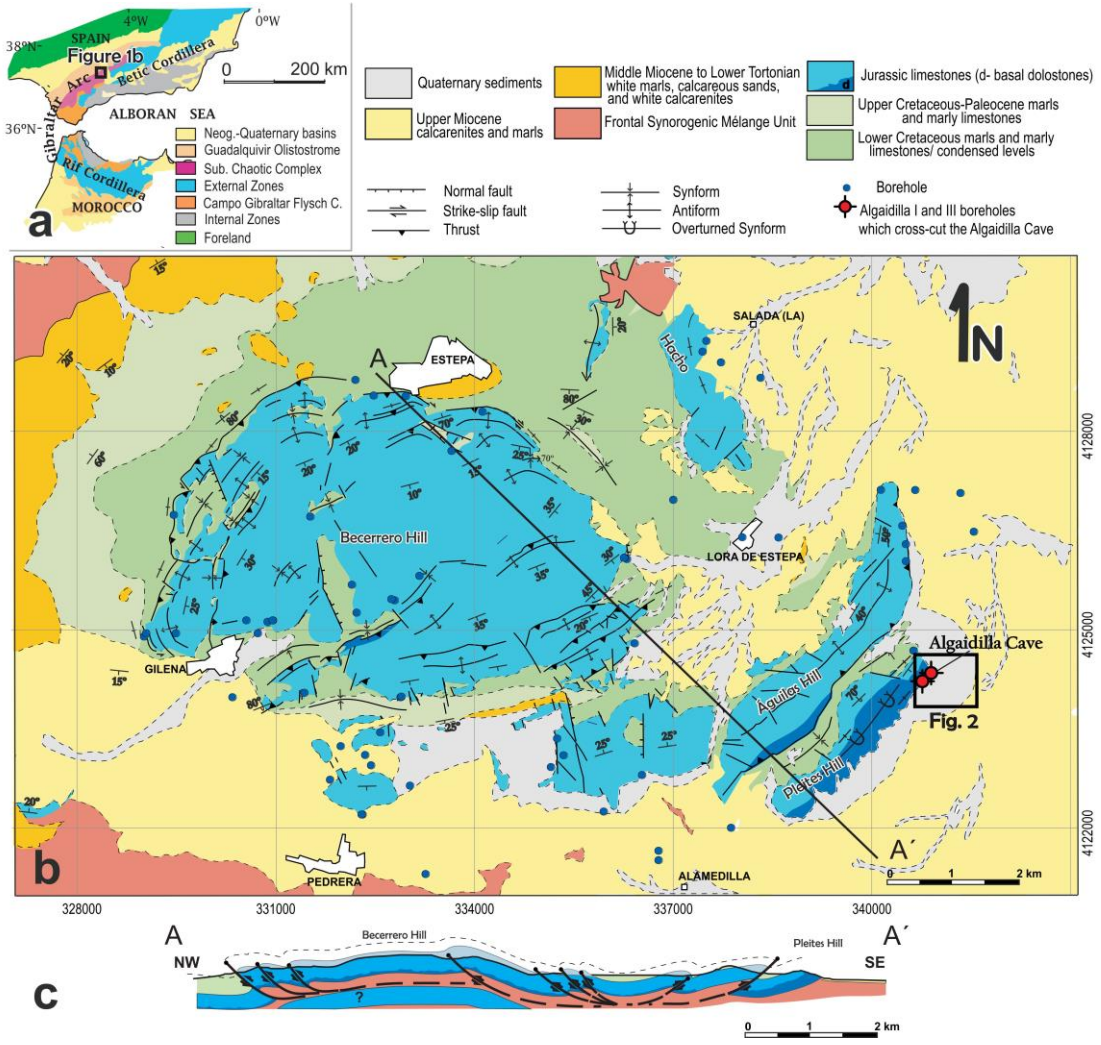


Figure 9.1. (a) Synthetic geological map of the Gibraltar Arc, formed by the Betic and Rif Cordilleras. (b) Geological map of the Estepa Range. The locations of geological cross-section of Figure 9.1c and Figure 9.2 are marked. (c) Geological cross-section of the Estepa Range, note that the Pleites hill corresponds to a SE-vergent fold above a thrust. Modified from Pedrera *et al*., 2012.

and white calcarenites unconformably overlie the Mesozoic-Paleocene Subbetic rocks, which appear to belong to the Middle Miocene. Upper Tortonian marine calcarenites, sands, and marls unconformably overlie the previous units. Plio-Quaternary continental detrital sediments belonging to the piedmont, alluvial fan, and river deposits discordantly overlie the older rocks. The piedmont and alluvial fans are particularly well developed in the SE boundary of the Pleites hill.

The Jurassic limestones and dolostones of Pleites hill also constitute a small aquifer (1.5 $km^2$ of outcropping carbonates). Hydrodynamic and hydrochemical studies indicate that the Pleites aquifer has a behavior independent of the nearby aquifers that occupy the Estepa Range: the Mingo, Hacho, Águilas, and Becerrero aquifers (Martos-Rosillo *et al.*, 2009). All its boundaries are closed to the groundwater flow, except the south-eastern border, which is partially covered by permeable Pliocene and Quaternary detrital sediments. Pumping tests enabled the calculation of a transmissivity of 2000–2500 m2/day in the aquifer. In addition, a well storage effect was detected during the pumping tests, which was probably related to the presence of karstic cavities (Martos-Rosillo, 2008). The recharge occurs by rain water infiltration (0.38 $hm^3$/year, 35% of the average annual rainfall). The sharp topography of the Pleites Hill (29% of average slope gradient) leads to a lower infiltration coefficient than in the nearby aquifers. The infiltration is concentrated mainly in the south-eastern hillside, where the water flows along the epikarst and infiltrates the hillside toe. The water discharge of the Pleites aquifer occurs along the south-eastern border towards a wetland sector, which is dry at present as a consequence of the intensive exploitation of the aquifer. This setting provokes a fast drop in their water table with the frequent desiccation of the discharge zone, and deterioration in the water quality. Therefore, the freshwater is mixed with the salt water from the Triassic evaporites

of the basal mélange unit, inducing an increase in the water's electric conductivity, from 450 μS/cm to 1700–2000 μS/cm.

The carbonates present an early state of karstification characterized by the development of karrens, limestone pavements, and few dolines. At the top of the hills an epikarst is developed. The thickness of the epikarst increases in the sector with a low slope, as occurs at the top of Becerrero hill. Along the south-eastern border of Pleites hill, some karstification features have been recognized (Martos-Rosillo *et al*., 2013). The most prominent karstic forms are dolines developed after the collapse of the carbonate and Pliocene to Quaternary alluvial sedimentary rocks (Cruz-Sanjulian, 1977). There, two water-supply boreholes, the Algaidilla I and Algaidilla III, perforated a buried cave between 26 and 66 m and between 49 and 66 m depth respectively, the so-called Algaidilla cave (Fig. 9.1).

## 9.3 METHODS

The deeply buried Algaidilla cave was studied combining microgravity, ERT, and IP techniques.

### 9.3.1 Survey stations

The precise determination of the coordinates of each geophysical site is decisive for proper accurate geophysical data acquisition, processing, modelling and interpretation. The precise altitude determination is especially important in microgravity surveys, where a miscalculation of ± 1 m induces a deviation of up to ± 0.2 mGal. Therefore, we attempted to make a precise determination of the altitude at each site. To do so, we used two combined microtopography techniques:

– Differential GPS. A fixed GPS reference station, consisting of a Leica 1200 GPS receiver, GPS antenna and one-watt radio transmitter was established on a point with coordinates determined in respect to the Andalusian Positioning Network known as RAP (Red Andaluza de Posicionamiento, http://www.juntadeandalucia.es; http://rap.uca.es; Junta de Andalucía, 2011). The Leica 1200 GPS system uses error-correction data to fine-tune the position accuracy of each geophysical site to ± 0.5–20 mm. This system provides local-area error corrections for the satellite signals.

– A laser level SP30 and LC-2 laser receptor were used for high-precision determination of the relative altitude of the geophysical sites using reference points of known coordinates. The altitude accuracy of each point was to ± 0.17 mm.

### 9.3.2 Microgravity

Microgravity enables the detection of near-surface bodies of small dimensions with a different density than that of their surroundings. The presence of caves constitutes a reduction in the density (0 g/cm$^3$ above and roughly 1 g/cm$^3$ below the water table) with respect to the host rock, and, therefore, in the gravity value. The negative gravity anomaly (McGrath *et al*., 2002) could be quantitatively modelled to determine the cave geometry.

We used an Autograv Scintrex CG-5 gravity meter with an accuracy of 0.001 mGal. The 305 gravimetric measurement stations were referred to the Granada gravimetric base (Instituto Geográfico Nacional, www.ign.es). The profile has a length of 200 m formed by measurement sites spaced 2.5 and 5 m (Fig. 9.2). Three profiles had a N–S orientation (profiles 1, 2 and 3) and one had an E–W orientation (profile 4) (Fig. 9.2). In addition, 19 additional gravity stations were measured around these profiles to draw the Bouguer anomaly map. After tidal and instrumental drift corrections, the Bouguer anomaly was determined using a reference density of 2.67 g/cm$^3$ and applying the terrain correction by

the method of Hammer's circles (Hammer, 1939 and Hammer, 1982). This correction was calculated from the digital terrain model of Andalusia (Junta de Andalucía, 2005) with a resolution of 10 m up to 4469 m around each measurement station (Zones B to I). The residual gravity anomaly was calculated from the Bouguer anomaly by trend removal, and also the regional anomaly determined on the basis of the 1:1,000,000 regional Bouguer anomaly maps (I.G.N., 1975).

Finally, the residual anomalies determined were forward modelled along profiles using 2.5D approximation (from 20 to 30 m orthogonal lengths) using GRAVMAG V.1.7 from the British Geological Survey (Pedley *et al*., 1993). Forward microgravity modelling is rather limited if the geometry of the modelled object is not partially known beforehand.

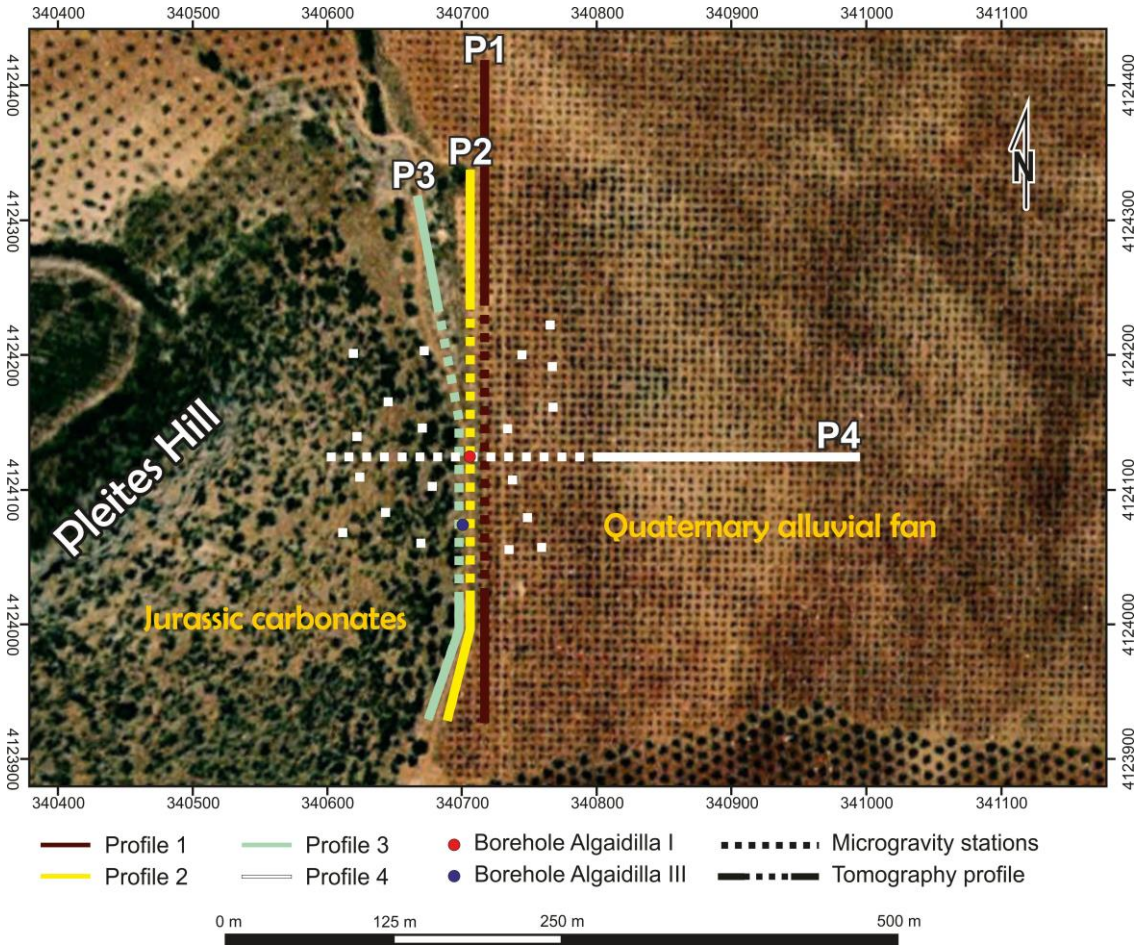


Figure 9.2. Aerial photography of the study sector with the location of the geophysical sites.

Therefore, field geological and borehole data, as well as morphologies defined in the 2D resistivity inversion models, were considered during gravity forward modelling.

### 9.3.3 Electrical resistivity tomography (ERT) and induced polarization (IP)

ERT and IP methods are electrical geophysical techniques that provide detailed information of the subsurface resistivity and induced polarization distribution. ERT method consists on a lineal electrode array, where an electrical current is consecutively injected through a source electrodes pair and the potential difference is recorded between other electrode pairs. The apparent resistivity ($\varphi_a$) is determined by the ratio of the potential (V) and the current intensity (I) multiplied by a geometric factor (k) ($\varphi_a = (V/I) \cdot k$). The apparent resistivity can be equal to the effective resistivity in homogeneous and isotopic mediums. Each measurement of apparent resistivity is represented on a pseudo-section. Resistivity is sensitive to small changes in rock porosity, interconnectivity, and water salinity (Worthington, 1976).

IP method measures chargeability by the voltage decay over a specified time interval after the removal of the artificial current. The voltage does not return to zero instantaneously and decays slowly, indicating that charge has been stored in the rocks. This charge accumulates mainly at interfaces between clay minerals and around metallic conductors, which induce dielectric polarization of the ionic charges present in an aqueous medium.

We used the ABEM Terrameter SAS 4000, an electrode selector ES10-64C, 4 Lund automatic cables with 21 takeouts on each, 81 steel electrodes and 12 V DC battery, which constitutes a high-resolution electric imaging system. It consists of a multielectrode arrangement simultaneously used to determine both horizontal and vertical resistivity and chargeability variations along a profile (ABEM, 2006). The equipment has a resolution

of 25 mV (theoretical, 1 second integration time), three automatic measurement ranges (± 250 mV, ± 10 V and ± 400 V) and an accuracy of 1% at all temperatures.

*9.3.3.1. Forward modelling*

Using a priori information from the two existing boreholes, we constructed 2D forward models, using RES2DMOD software (Loke, 2002), with simplified geometries to examine the expected range of resistivity and chargeability contrasts in different settings. This program calculates the apparent resistivity pseudosection for a defined 2D synthetic model. The apparent resistivity pseudosections were inverted using RES2DINV software. ERT and IP forward model inversion was performed using the finite difference method based on field measurements (Dey and Morrison, 2005 and Loke, 1994). Forward modelling calculation allows us to select the optimum electrode array configuration by checking the resolution, penetration and geometry of the derived anomalies (e.g. Gómez-Ortiz and Martín-Crespo, 2012). The best results for our study area were obtained using a Wenner–Schlumberger array with an electrode spacing of 5 m.

*9.3.3.2. Field acquisition*

Four profiles were acquired using a 4-channel multiple gradient electrode array and two combined protocols (GRAD4LX8 and GRAD4S8; ABEM, 2006) which use the Wenner–Schlumberger electrode array configuration previously tested in the forward models. The gradient array is developed for multi-channel resistivity meter system (Dahlin and Zhou, 2006). A multi-channel system can make several measurements simultaneously with the same position of the current electrodes and different localizations of the potential electrode pairs. GRAD4S8 was designed to supplement GRAD4LX8 at the shortest electrode spacing. Electrodes were deployed at a 5 m and 2.5 m spacing, with effective penetration depths of ~ 70 and ~ 35 m, respectively. In addition, we combined

different total lengths of profiles, between 400 and 500 m. Along profile 2, which was placed in a central position (Fig. 9.2), two different electrode spacings (5 m and 2.5 m) were combined, including common points, with the aim of reaching maximum penetration and a good near-surface resolution. Iterative 2D inversion of the data was performed using the smoothness-constrained least-square method (deGroot-Hedlin and Constable, 1990, Sasaki, 1992 and Loke *et al*., 2003). The inversion process tries to reduce the RMS (root-mean-squared) value after each iteration in an attempt to find a better model. We used a mesh made up of model cells increasing in size at greater depth, using 2 nodes per unit electrode spacing and an initial damping factor of 0.3.

*9.3.3.3. Normalized depth of investigation index (DOI)*

The empirical depth of investigation (DOI) index method was introduced by Oldenburg and Li (1999) and modified by Marescot *et al*. (2003). To determine the DOI it is necessary to carry out, at least, two inversions of the data using different resistivity backgrounds. The second reference model should be obtained from an initial resistivity background 10 to 100 times higher than the first one (Loke, 2012). The equation below makes it possible to calculate a DOI index (R) of the model cell by cell:

$$R_{1,2}(x,z) = \frac{m_1(x,z) - m_2(x,z)}{m_{1r} - m_{2r}} \quad (1)$$

where $m_{1r}$ and $m_{2r}$ are the resistivity of the first and second reference models, and $m_1$ (x, z) and $m_2$ (x, z) are the resistivity of each cell of these models. The DOI index (R) will approach zero where the two inversions produce the same resistivity values, regardless of the value of the reference model. In cells where the value is far from zero, it means that the resistivity value depends on the background resistivity value assigned to the reference model; such a result is not reliable. The normalized DOI index is calculated to reduce the effect of the damping factor and the selection of the initial reference model (Robert *et al*.,

2011). To normalize the DOI index, we use the maximum value of R ($R_{max}$) calculated with Eq. (1):

$$R(x,z) = \frac{m_1(x,z) - m_2(x,z)}{R_{max}\ (m_{1r} - m_{2r})} \quad (2)$$

The main difficulty lies in deciding the cut-off value where the inversion values are trusted. For the normalized DOI index, Marescot *et al*. (2003) recommended a cut-off value of 0.1 or 0.2. In our case, we used a more restrictive 0.1 cut-off value. We carried out two inversions with a background resistivity of the second reference model that was 100 times the first one. The computation of the normalized DOI index was performed with RES2DINV v.3.59, and it is shown on the ERT and IP profile (e.g. Robert *et al*., 2011).

## 9.4 RESULTS

### 9.4.1 Microgravity results

#### *9.4.1.1 Bouguer anomaly*

We calculated the Bouguer anomaly map of the study sector from 305 new microgravity measurement stations (Fig. 9.3). The sector had a surface area of 40,000 $m^2$ and a maximum height difference of 31 m from the lowest point (385 m.a.s.l.) to the highest (416 m.a.s.l.). The variation of the Bouguer anomaly is − 94.274 mGal to − 93.239 mGal, a range of 1.04 mGal.

The highest Bouguer anomaly value coincided with the highest sector, where the Jurassic carbonate rocks are located. The anomaly value decreased progressively towards the east in the area with a lowest topography, where low-density Quaternary alluvial rocks crop out. Superimposed over this general trend were low-amplitude negative Bouguer

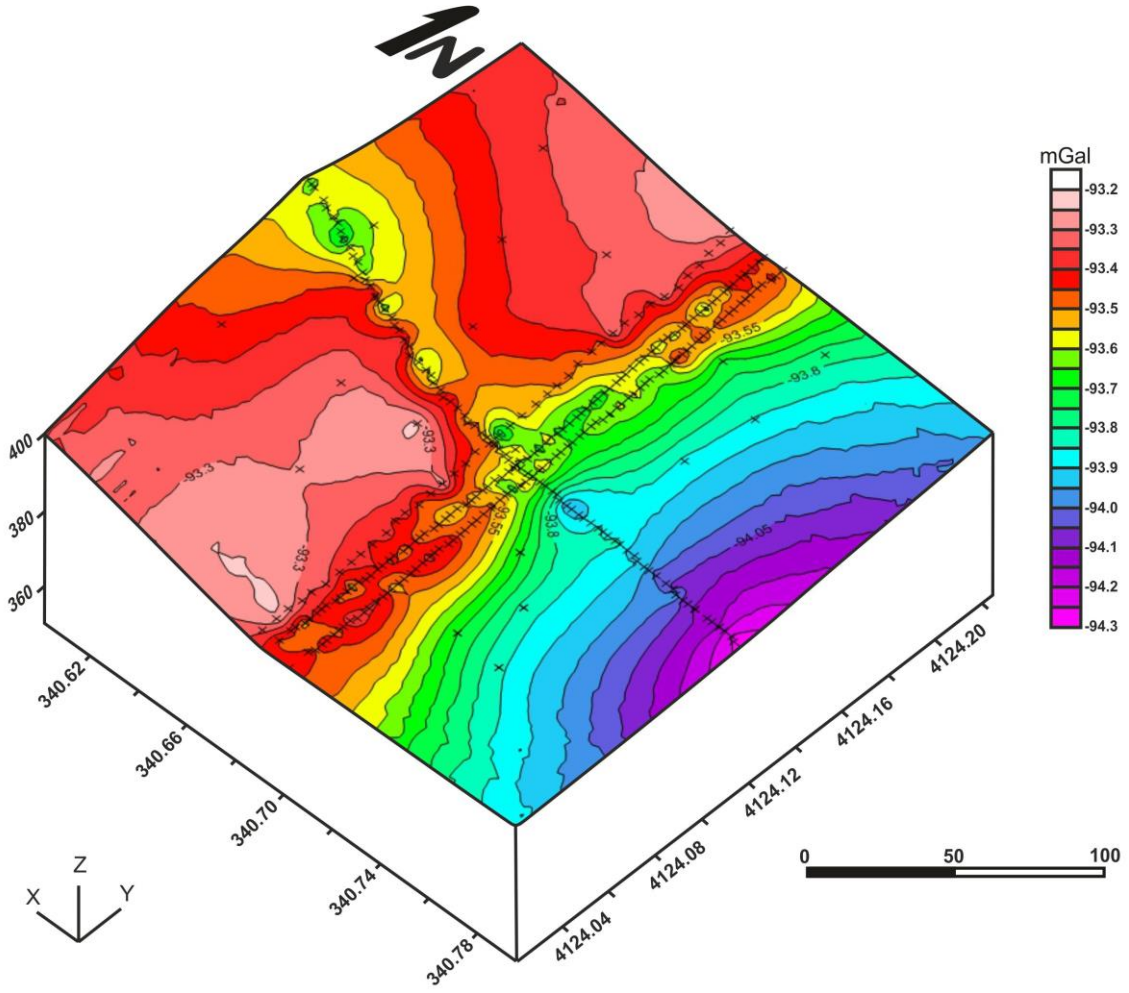


Figure 9.3. Bouguer anomaly map plotted above the digital elevation model. The gravity sites are marked as black dots.

anomalies presumably associated with buried caves. At the top of the mountain (340.60 to 340.66 km E and 4124.125 km N), a gravity minimum is ranged between − 93.5 and − 93.7 mGal. The most prominent low-amplitude Bouguer anomaly minimum (− 93.8 mGal) had a N–S elongated shape coinciding with the position of the buried cave of Algaidilla, in the central part of the map (340.66 to 340.70 km E; 4124.12 to 4124.18 km latitude N). The Bouguer anomaly resolution slightly decreases towards the boundaries.

*9.4.1.2 Microgravity models*

The N–S trending microgravity profiles (profile 1, 2, and 3) revealed an asymmetric minimum residual anomaly slightly displaced towards the N associated with Algaidilla cave. This minimum reached − 0.45 mGal in profile 1, − 0.4 mGal in profile 2, and − 0.5 mGal in profile 3. In the E–W oriented profile 4, the minimum caused by the cave was masked by lithological changes. Nevertheless, there were two minima, at meter 0 and at meter 20, which could be related to buried caves (Fig. 9.4).

We modelled the Pliocene to Quaternary alluvial detrital sediments with densities of 2.2–2.3 g/cm$^3$. This formation, located in the shallowest part of profiles 1 and 2, progressively decreases in thickness towards the W until completely disappearing in profile 3. These Pliocene to Quaternary alluvial sediments unconformably overlie

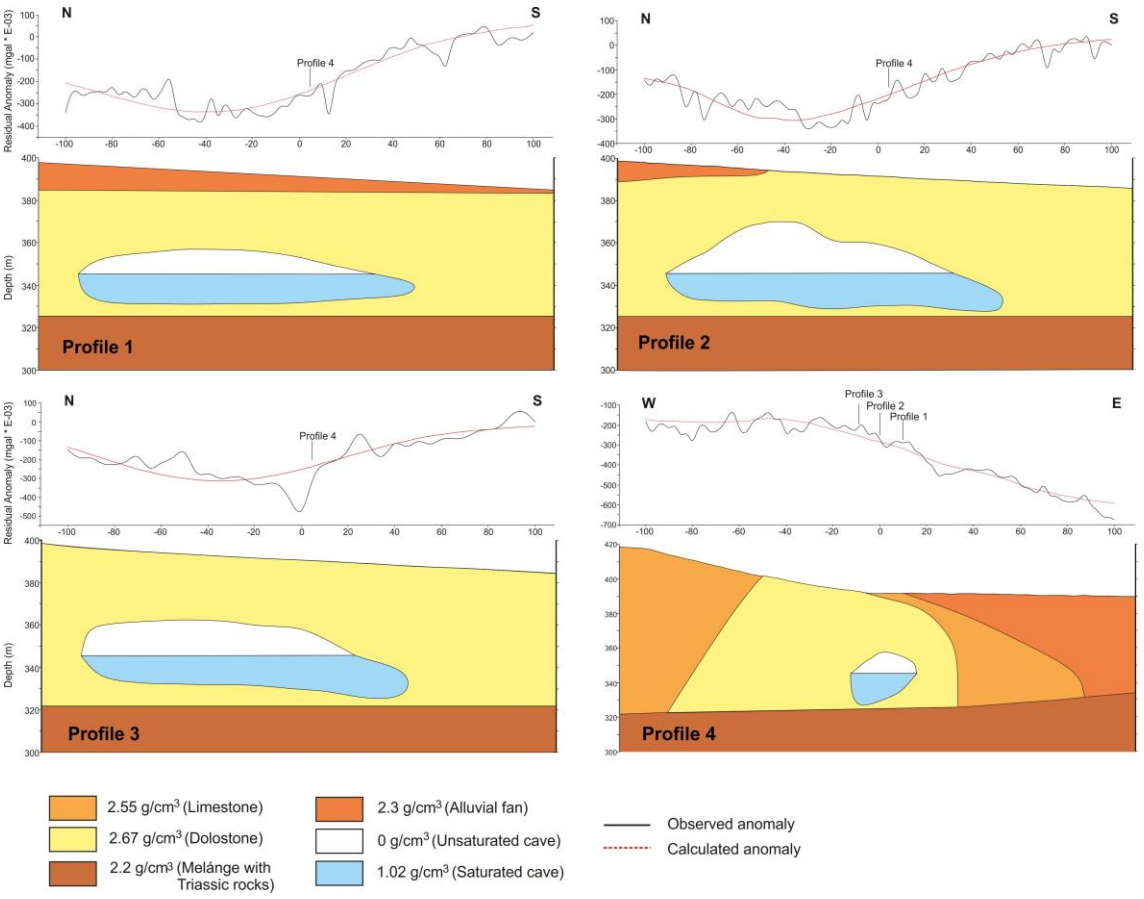


Figure 9.4. 2D forward models constructed from the residual gravity anomalies.

Jurassic limestones and dolostones with density 2.55 and 2.7 g/cm$^3$, respectively. These carbonate rocks, with an average thickness of 60 m in the profiles modelled, enclose Algaidilla cave. The cave is located near the contact with the mélange unit having a matrix composed mainly of Triassic clay and evaporites.

Algaidilla cave is partially submerged below the water table. During the data collection, the water table is located at 345 m.a.s.l in the Algaidilla I and III boreholes. We assigned 1.02 g/cm$^3$ density to the water according to its salinity and temperature. To model Algaidilla cave, we used different orthogonal lengths according the plan view of the Bouguer anomaly minimum associated with the cave. The boundaries of Algaidilla cave modelled in each profile fit the results of the 2D inversion models of the electrical resistivity tomography and the available borehole data. The cave had an approximately horizontal N–S elongated morphology with a maximum length of 150 m and a width of 40 m along the E–W direction. The maximum vertical thickness located in the central zone was 25 m.

*9.4.1.3 Electrical resistivity tomography and induced polarization*

This section presents the forward modelling and measured profiles in the study area. Moreover, we describe the results of the forward modelling as well as the ERT and IP models with the trusted zone determined by calculating the DOI index.

9.4.1.3.1 Forward modelling profiles

The forward modelling profiles are shown in Fig. 9.5, and panel a illustrates the influence of the steel pipes installed in the two boreholes. We assigned a resistivity of 1 Ω·m to the steel tubes and a background resistivity of 200 Ω·m linked to limestones. The model shows a conductive anomaly coinciding with the borehole position and a higher resistivity anomaly between the boreholes in the shallowest zone. These anomalies

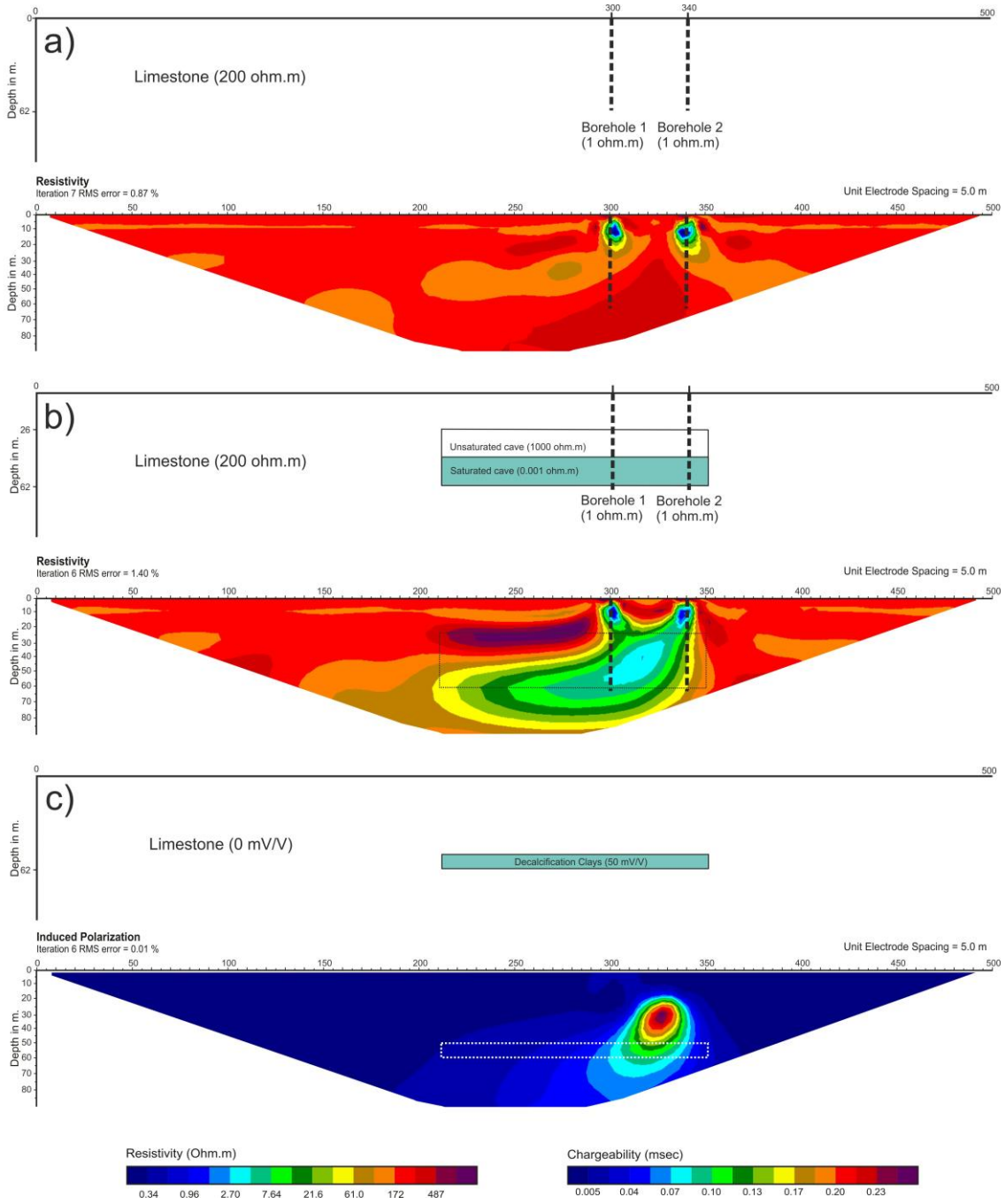


Figure 9.5. Forward modeling of ERT profiles including synthetic models and inverted pseudosections. (a) Resistivity profile with two boreholes embedded in a homogeneous half-space, (b) resistivity profiles with a partially saturated cave located between the two boreholes and (c) induced polarization profile of decalcification clays associated at the base of the cave.

disappear at depth, where the value of the background is homogeneous. In a second setting (Fig. 9.5b) we performed an ERT forward modelling considering both the cave and the steel pipes. In the ERT forward model, the simplified geometry of the cave was constructed in two separate parts: a saturated cave with 0.001 Ω·m (measured water conductivity of 1171 μS/cm), and an unsaturated cave with very high resistivity, considering a value of 1000 Ω·m. Although the obtained ERT forward model of Fig. 9.5b presents the same conductive effect in the shallowest part linked to the steel pipes, it delineates the geometry of the cave with remarkable resolution. Therefore, we discern the transition from high resistivity values (unsaturated cave) to low resistivity values (saturated cave). The IP model with decalcification clays (Fig. 9.5c) located high values of chargeability above the modelled body.

9.4.1.3.2. ERT and IP models

Resistivity models resulting from 2D numerical inversions are displayed in Fig. 9.6. The models for profiles 1, 2, and the eastern part of profile 4 show a relatively low resistive surface layer (~ 50 to 75 Ω·m), corresponding to the Pliocene-Quaternary detrital sediments. A resistive zone (~ 857 Ω·m) extends downwards from the surface and from the lower boundary of the low resistive surface layer in all the 2D resistivity models, coinciding with the Jurassic limestones and dolostones (Fig. 9.6). The resistive values are abruptly distorted by vertical lower resistivity bodies, which match with the location of the Algaidilla I and III steel-cased boreholes. The Algaidilla I borehole (390 m.a.s.l) cut the cave between 26 and 66 m (between 364 and 328 m.a.s.l.) and the Algaidilla III borehole (388 m.a.s.l.) between 49 and 66 m (between 339 and 322 m.a.s.l.). The boreholes are placed closely to meters 0 and 40 in the N–S oriented profiles (profiles 1, 2 and 3) and to the meter 0 in profile 4 (vertical dashed black lines in Fig. 9.6). The intersection of the boreholes with the cave coincides with an intermediate to low

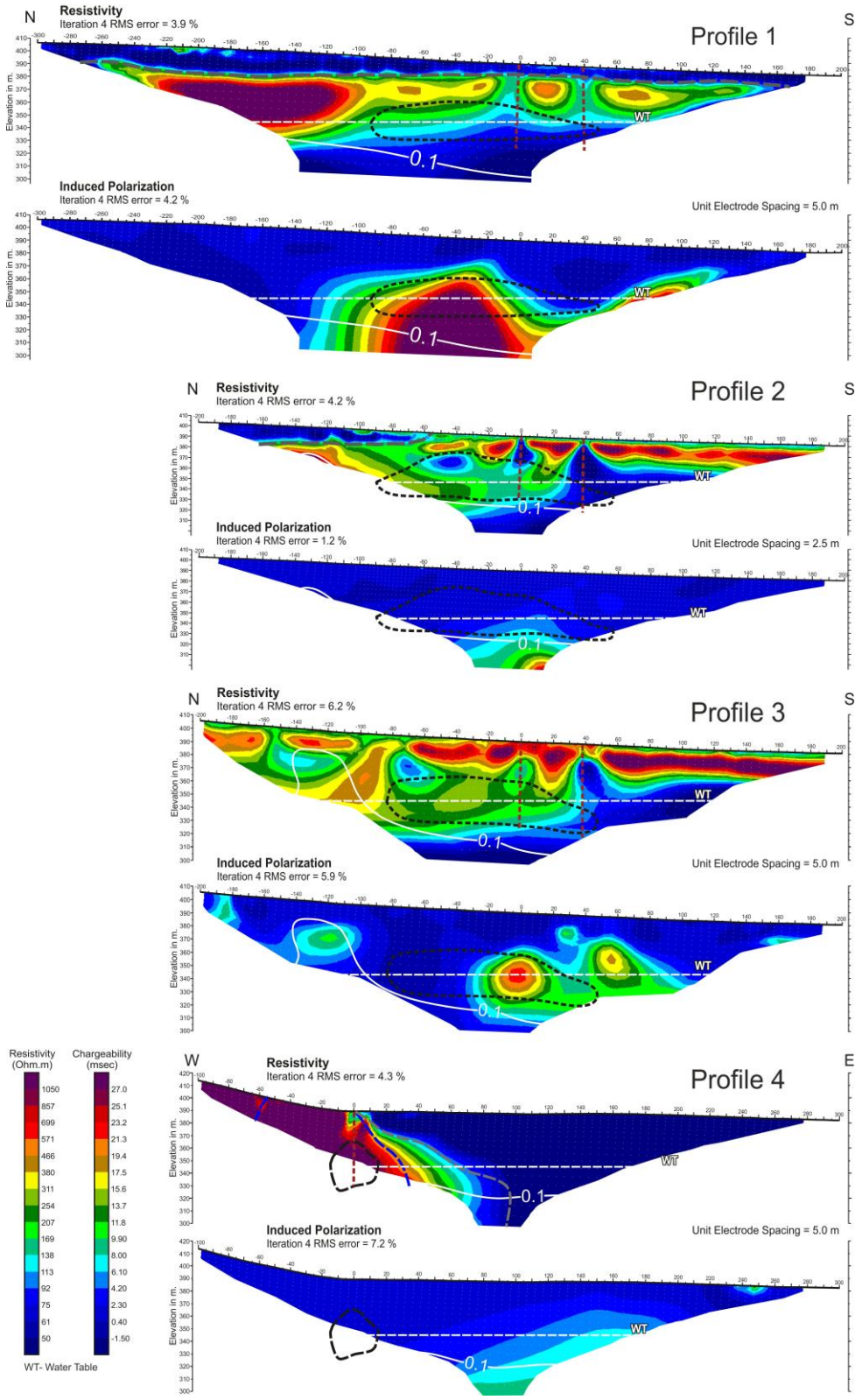


Figure 9.6. Inversion models of electrical resistivity and induced polarization tomography. RMS error and number of iterations are marked. The cave contour is marked with a black dashed line and the water table (WT) is indicated with a white dashed line. The DOI index 0.1 cut-off value is marked on each profile.

resistivity feature with a boundary that approximately matches the 250 Ω·m resistivity contour line. These intermediate resistivity values are presumably associated with the presence of moderately saline groundwater in the cave. The morphology of the resistivity anomaly has been used to constraint the models of the microgravimetry data. The models show a low resistive zone towards the base, potentially indicating the location of the mélange unit, with a matrix composed mainly of Triassic clay and evaporites, beneath the Jurassic carbonates.

The IP models resulting from 2D numerical inversions show a high chargeability body partially coinciding with the location of Algaidilla cave (profiles 1, 2 and 3 in Fig. 9.6). We interpreted these chargeability values as clays derived from the dissolution of carbonate rocks that must be deposited at the bottom of the cave.

The incidence of the cave in the E–W oriented profile 4 is unclear, apparently due to its limited depth resolution. The resistivity value coinciding with the top of the cave, according to the borehole Algaidilla I, matches with the background resistivity assigned to the limestones and dolostones. The IP model reveals a high chargeability sector at the base of the model towards the E (profile 4, Fig. 9.6) which could belong to the Triassic Keuper clay-in-matrix mélange.

We computed the depth of investigation for surveyed data, based on the DOI index method, following the recommendations given by Oldenburg and Li (1999) and Marescot *et al*. (2003). The 0.1 cut-off value of the DOI index obtained is highlighted on the profiles with a continuous white line (Fig. 9.6). The zones above the line marked, which have a DOI value between 0 and 0.1, show an overall high resolution. Underneath the line, where the DOI index begins to point towards high values, it indicates the untrusted zones of the profile. Note that reliable zones delimited by the DOI index of the models extend to a

depth of 70–80 m in the middle sectors. This is greater than the depth of the bottom of the cave, as derived from the resistivity models.

## 9.5 TENTATIVE 3D MODEL

From the combined electric tomography, microgravity, and borehole data, we constructed an approximate 3D model of Algaidilla cave (Fig. 9.7). For this, the cave's boundaries were defined in each interpreted section (rounded dashed black lines in Fig. 9.6). The sections interpreted were integrated with the topography and water table altitude data. We used Geomodeller software, which employs potential fields to build a 3D surface (Aug *et al*., 2005) from the sections interpreted.

Based on the geophysical models, Algaidilla cave has N–S trending tubular morphology being narrower in its southern part and progressively widening towards the north. The cavity should be roughly horizontal in the central and northern regions, whereas in the southern part the cave slopes towards the south. The estimated volume of the cavity is of ~ 150,000 $m^3$, of which 78,000 $m^3$ belongs to the unsaturated zone and 72,000 m3 to the volume of water contained in the cave.

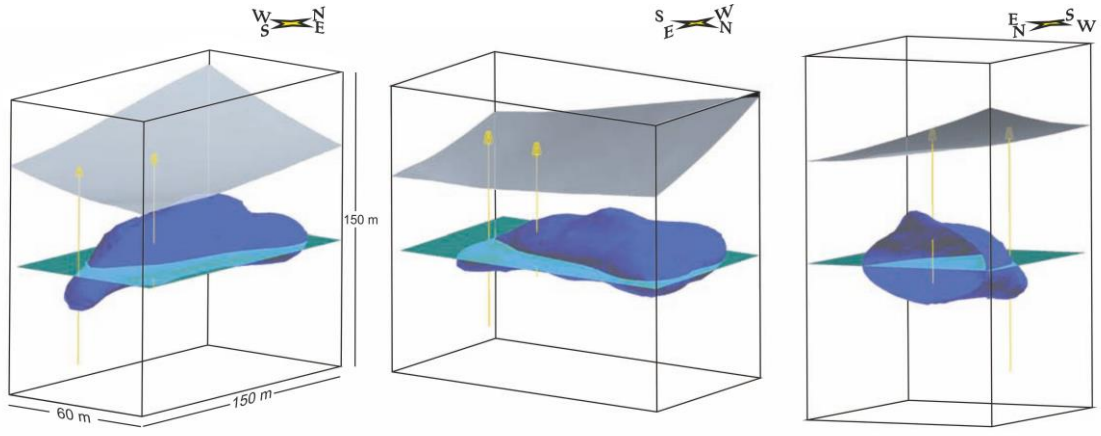


Figure 9.7. Three-dimensional construction of the Algaidilla cave from the geophysical results found using a 3D potential field (Aug *et al*., 2005).

## 9.6 DISCUSSION

Electrical tomography has been successfully used to find cavities at more than 20 m in depth (Noel and Xu, 1992, Manzanilla *et al*., 1994, Shi *et al*., 1997, El-Qady *et al*., 2005 and Kaufmann *et al*., 2011). However, in the case of caves located in carbonate rocks, due to the resistive character of the host rock (1000–100,000 Ω·m, Palacky, 1987), detection depends on the size and depth of the cave and its content (air and/or water). On the other hand, the caves have an associated minimum gravity residual anomaly that can be modelled quantitatively (Al-Rawi and Rezkalla, 1987). The present study provides information on the sensitivity of electrical tomography and microgravity prospecting to detect partially flooded caves located more than 30 m below the ground surface.

### 9.6.1 Methodological implications

The high resolution achieved with Bouguer anomaly data (305 microgravity stations) allowed the qualitative identification of anomaly minima that could potentially be produced by karst cavities. Therefore, Algaidilla cave, which was highlighted by borehole data, gave a − 0.5 mGal residual gravity minimum. Thus, these results validate the approach of using a high-resolution Bouguer anomaly map as a preliminary step to the qualitative identification of buried caves and the selection of sectors most of interest to be investigated in detail using other geophysical methods.

However, when quantitative microgravimetric direct modelling is used alone, it fails because unlimited models are able to adjust the data of gravity residual anomaly. In our case, borehole data and 2D ERT and IP results were used together for better constraint of the possible models. It is well known the non-uniqueness and instability of ERT inverse solution and the diverse anomaly shapes resulting from different selected electrode arrays. We have checked the resolution of different electrode arrays and compared the resulting

images from various configurations. Although the iterative inversion process minimizes this non-linear problem, the ratio layer thickness and layer conductivity could be solved with multiple solutions due to principle of equivalence. In our example the boundaries of the cave are constrained by boreholes partially resolving the void thickness. Thus, the value of 250 Ω·m was used to delineate the contours of top of Algaidilla cave in 2D resistivity inversion models 1, 2 and 3 (corresponding to profiles of the same name). The 2D resistivity inversion model 4 did not detect the cave because the profile of the cavity runs parallel to the hillside slope and the abrupt topography limits the penetration. Although steel tubes of two boreholes affect the shallow part of the ERT models, as in the forward models, the geometry of the cave is well resolved by the tomography data and it can delineated at a depth between 26 and 66 m. In addition, the obtained DOI guarantees reliable results in the ERT and IP models with 0.1 cut-off values down to 70–80 m or beneath, which is greater than the depth of the cave bottom.

There was a difference in the resistivity values associated with the cave between profile 1 and profile 3. The profile 1 showed a progressive change from higher resistivity values in the upper part of the cave to lower values towards the base. In profile 3 the maximum value of resistivity coincided with the central part of the cave. This discrepancy between the values of resistivity profiles potentially indicates that the section below the water table is larger than the unsaturated zone in profile 1. In this setting, the moderately saline water filling the bottom of the cave produces low resistivity values. However, in profile 3, most of the cavity remains above the unsaturated zone, which is reflected in the high resistivity values. Our results suggest that in karstified carbonate massifs, cavities lying below the water table have a larger resistivity contrast with the resistive host bedrock than above the water table. However deepest sectors of the models should be interpreted with caution since they are less constrained by the data.

IP models show areas with high polarization values located mainly at the bottom of the cave. Although, the deepest parts of the models are less constrained, these chargeability positive anomalies are probably associated to decalcification clays generated from the dissolution of the calcite from the rock. Therefore, these red decalcification clays were cross-cut by the Algaidilla I and III boreholes. A decalcification clays residuum commonly occurs in karstic caves. Calcite dissolves in water saturated in carbonic anhydride and the impurities, red clays with iron oxide, precipitate. These clays are transported by the water and deposited in the base of the cavity. IP is observed when a steady current through two electrodes is shut off and the voltage does not return to zero instantaneously, indicating that charge has been stored mainly at interfaces between clay minerals. This study illustrates the strong potential of the IP method to highlight decalcification clays and therefore to complement other geophysical techniques during cave detection.

While caves commonly have a highly resistive electrical signature (e.g. El-Qady *et al*., 2005 and Gambetta *et al*., 2011), our study reveals that caves that develop below the water table have lower resistivity than do the surrounding carbonates. Therefore, while Algaidilla cave has sharp resistivity contrast in the saturated part, the resistivity contrast is lower above the water table.

This study demonstrates the reliability of ERT and IP, combined with gravity prospecting, for deep and saturated cave detection, compared with the GPR method. On the one hand, GPR penetrates up to 15 m, but it fails in high-conductivity materials such as water or saturated clays. Thus, while it is a suitable method for detecting shallow unsaturated caves, the low penetration below the water table rules out its use for deep saturated caves. Moreover, in this setting, we have demonstrated the sensitivity of IP

prospecting to detect the clays that are commonly associated with the carbonate dissolution in karstic caves.

### 9.6.2 Cave development, hydrogeological and engineering implications

The geophysical results show that Algaidilla cave developed from karstification along a N–S direction coinciding with the boundary strike between dolostones and the mélange unit, which is saturated in saline water. The mélange unit acts as an aquitard saturated in highly saline water. At present, the conductivity values measured show moderate salinity. The intensive exploitation of the Pleites carbonate aquifer would lead to the mixture between deeper saline waters and the shallow freshwater. This would result in deteriorated water quality that could limit its use for irrigation.

The location and geometry of Algaidilla cave estimated from geophysical modelling serve as a warning against nearby overexploitation, to prevent cave-in situations. Collapsed caves have been described along the eastern hillside of the Pleites hill (Cruz-Sanjulian, 1977), close to and with an equivalent setting as the cave studied. Therefore, load-addition by the construction of buildings or roads with heavy vehicular traffic could cause Algaidilla cave to collapse. At present, there is a minor country road with very little road traffic above the cave. Increasing the traffic or passing with heavy machinery could cause minor destabilization which, in the future, could result in a collapse.

## 9.7 CONCLUSIONS

The combined application of microgravity and electrical tomography, including resistivity (ERT) and induced polarization (IP) techniques, yields important information about the location and geometry of karstic caves deeply buried in carbonates. Algaidilla

cave, which is partially saturated, has a − 0.5 mGal residual gravity anomaly minimum. ERT results delineate the cavity both above and below the water table. The cave is identified as a feature having intermediate to low resistivity, its top boundary approximately matching the 250 Ω·m in the 2D ERT inversion model. The saturated part of the cave, below the water table, has lower resistivity than the surrounded carbonates, contrary to the commonly found highly resistive electrical signature of the caves. In addition, IP models show high chargeability anomalies probably associated with decalcification clays accumulated at the base of the cave. Both electrical and microgravity models reveal a cave between 20 and 66 m depth with an approximately horizontal N–S elongated shape with a maximum length of 150 m and a width of 40 m. The obtained normalized depth of investigation index (DOI) — considering a cut-off value of 0.1 — guarantees reliable results in the ERT and IP models down to 70 m–80 m, which is greater than the depth of the base of the cave. In this setting, microgravity may constitute a preliminary regional reconnaissance method while ERT and IP results roughly constrain the geometry of the void, although it is necessary to combine them to gain accurate results for deep caves.

## ACKNOWLEDGMENTS

We are sincerely grateful to D. Francisco Jose Cabello, who facilitated the field work. We appreciate the thoughtful comments and suggestion made by Dr. Teresa Teixidó, Dr. José Peña and the support of Dr. M. H. Loke. We thank two anonymous reviewers for their insightful reviews which significantly helped to improve the manuscript. This research was supported by the CSD2006-00041, CGL-2008-03474-E/BTE, CGL2010-21048, P09-RNM-5388 and RNM148 projects.

# Chapter 10

El Bosque cave

# Detecting gypsum caves with microgravity and ERT under soil water content variations (Sorbas, SE Spain)

F.J. Martínez-Moreno[a]*, J. Galindo-Zaldívar[a,b], A. Pedrera[b], L. González-Castillo[a], P. Ruano[a,b], J.M. Calaforra[c], E. Guirado[c]

[a] Departamento de Geodinámica, Universidad de Granada, 18071-Granada, Spain

[b] Instituto Andaluz de Ciencias de la Tierra, CSIC-Universidad de Granada, 18071-Granada, Spain

[c] Water Resources and Environmental Geology, University of Almería, 04120-Almería, Spain

*Under review*

Submitted on June 25, 2014 to

**Engineering Geology**

**ABSTRACT**

The detection of caves developed in gypsum and marls through geophysical methods is tested in the gypsum karst of Sorbas (SE Spain). We applied microgravity and electrical resistivity tomography (ERT) in the Covadura cave system, which features a large variety of shapes developed in a multilayer structure. The response of caves in different conditions of host rocks and cave dimensions is analysed by means of synthetic models. Gravity studies require very accurate conditions in data acquisition and processing to highlight the associated minima, given the low density contrast between caves and gypsum or marl host rock. Different microgravity station spacing was tested to find the best configuration for the detection of such caves. The suitability of ERT under different conditions of soil humidity is discussed in conjunction with the low resistivity contrast between gypsum bedrock and cave conduits. After measuring 2D ERT parallel profiles coincident in space, yet in wet versus dry soil conditions, the results were compared, and a 3D model was drawn up for the two different humidity conditions. The best results for cave detection are obtained when combining gravity and ERT in wet conditions, as they provide for a higher contrast in physical properties and an optimal setting for instrumental measurements.

**HIGHLIGHTS**

- ERT and microgravity prospection are applied to a cave in gypsum and marls.
- A combination of geophysical methods is recommended to distinguish caves in gypsum.
- Resistivity measurements under different humidity soil conditions are compared.
- Different microgravity station spacings are tested to optimize the gravity survey.

**Keywords:** gypsum caves; microgravity; residual anomalies; ERT time-lapsed; Sorbas, SE Spain.

## 10.1 INTRODUCTION

Cave detection by means of geophysical methods is an increasingly widespread practice. Such research aims to check the geophysical response of a known cave (Chico, 1964; McMechan *et al.*, 1998; Jardani *et al.*, 2007; Martínez-Pagán *et al.*, 2013) and later explore unknown cavities in the same host rock. Combinations of geophysical methods have been applied to this end (Bozzo *et al.*, 1996; Mochales *et al.*, 2008; Brown *et al.*, 2011; Martínez-Moreno *et al.*, 2013), mostly involving caves developed in limestones and marbles, the most common host rocks of dissolution (Chandra *et al.*, 1987; Vadillo *et al.*, 2012).

The density, resistivity and seismic velocity propagation contrasts between host rock and caves —whether or not filled by water— produce prominent geophysical anomalies (Martínez-Moreno *et al.*, 2014). Few geophysical studies have focused on cave detection in lithologies such as gypsum, the second most widespread rock enclosing solution caves, after limestones (Klimchouk, 2012). Gypsum dissolves about one hundred times faster than limestone (Klimchouk, *et al.*, 1996). Subsidence and collapse are common engineering problems associated with gypsum dissolution (e.g. Nicod, 1993; Gutierrez *et al.*, 2007), and gypsum caves tend to have a poorer geophysical signature than limestone ones (Ulugergerli and Akca, 2006). The density contrasts between caves —filled by air (~0 g/cm$^3$) or water (~1 g/cm$^3$)— and the host rock is higher within the context of limestone-marble (~2.67 to ~2.7 g/cm$^3$) than in gypsum (~2.35 g/cm$^3$) or marls (~2.3 g/cm$^3$). The very high resistivity of gypsum and air-filled caves further complicate the detection of gypsum caves by means of electrical methods.

The collapse of zones with gypsum is a well-known engineering geohazard (Poupelloz and Toulemont, 1981; Cooper, 1986, 1995; Paukštys *et al.*, 1999; Cooper and Saunders, 2002; Alberto *et al.*, 2008). Given that gypsum is associated with dissolution

processes and caves (Yilmaz, 2001), there may beunstable areas nearby where new constructions can produce sinkholes under increased weight. Previous constructions could also suffer collapse owing to a progressive dissolution of terrain over years, as under dams in Oklahoma and New Mexico (Brune, 1965). In Zaragoza (Spain), the construction of a high speed railway line upon gypsum layers (Galve *et al.*, 2008, 2009) was interrupted in 2003 due to the onset of collapse by weight increment (Simón *et al.*, 2009).

Despite its apparent consistency, gypsum, can dissolve inwardly. This element of instability means that construction in such zones should be controlled. The deterministic spatio-temporal approach is not suitable for appraising the stability of areas bordering on gypsum; hidden unstable zones should instead be identified through geophysical methodology.

This study tested the applicability of microgravity and electrical resistivity tomography (ERT) for cave detection in a well constrained cave within the gypsum karst system of Sorbas (SE Spain). First, we aimed to determine the optimal spacing of microgravity stations in order to detect small shallow caves. Secondly, by measuring parallel ERT profiles under two different soil humidity conditions, we constructed a 3D model to reflect different soil humidity conditions.

## 10.2 GEOLOGICAL SETTING

The studied caves are located in the Gypsum Karst of Sorbas Natural Park (Tabernas-Sorbas Basin, Almería, SE Spain; Fig. 10.1a). This intramontane Neogene basin within the Betic Cordillera contains a 120 m thick Messinian unit (Yesares Member, Fig. 10.1b) comprising alternating gypsum and marls (Krijgsman *et al.*, 2001; Calaforra and Pulido-Bosch, 2003) among other pre- and post- Messinian sediments that do not

crop out in the study area. The stratigraphy sequence (Fig. 10.1b) comprises evaporites, mainly selenite with different crystal arrangements (Dronkert, 1985), including massive selenite or conical clusters (nucleation cones). The latter occur locally within the gypsum layers (Dronkert, 1977), especially in water drainage areas. These partially dissolved zones inside the more homogeneous gypsum can be traced to large selenitic gypsum crystals separated by voids.

The emersion of the sector since the Pliocene favoured the dissolution of gypsum layers, thereby creating a karstic landscape. The present-day arid climate predominating in the region —precipitation less than 210 mm/y (Esteban-Parra *et al.*, 1998)—, has helped conserve the karst system. More than 1000 caves have been catalogued, some several kilometres long (e.g. Cueva del Agua, over 9 km in total surveyed length, Baquero and Calaforra, 1992).

From the geomorphic standpoint, the study area is at the headwater of a small hydrographic basin that drains into the Aguas River. The basin is dissected by a network of flat-bottom infilled valleys; its headwater area shows a slightly undulating landscape featuring elongated low-lying depressions and sinkholes (Fig. 10.1a).

This study focuses on the the Covadura system. One of its galleries, known as El Bosque (Fig. 10.1a), has a length of approximately 100 m, a width of 4-5 m, a height of 2-3 m, and an elongated morphology in the N-S direction. The cave of study is located at 4-5 m depth (Fig. 10.1c). Its development entailed two stages, under phreatic and vadose conditions (Calaforra and Pulido-Bosch, 2003). Whereas the multilayer system constitutes an aquifer formed by karstified (gypsum) and low-permeability (marls) layers, dissolution of the gypsum levels started under phreatic conditions, forming proto-conduits in post-Messinian times (Calaforra and Pulido-Bosch, 2003). In a second stage, the piezometric level fell and the marls experimented erosion along the proto-conduits.

The results are caves with V morphology (Fig. 10.1c) developed in marl levels, having gypsum roofs and floors (top and bottom strata between marls). Thus, according to the morphology of the multilayer karst system, levels may be interconnected, vertically or horizontally, through the gypsum layers.

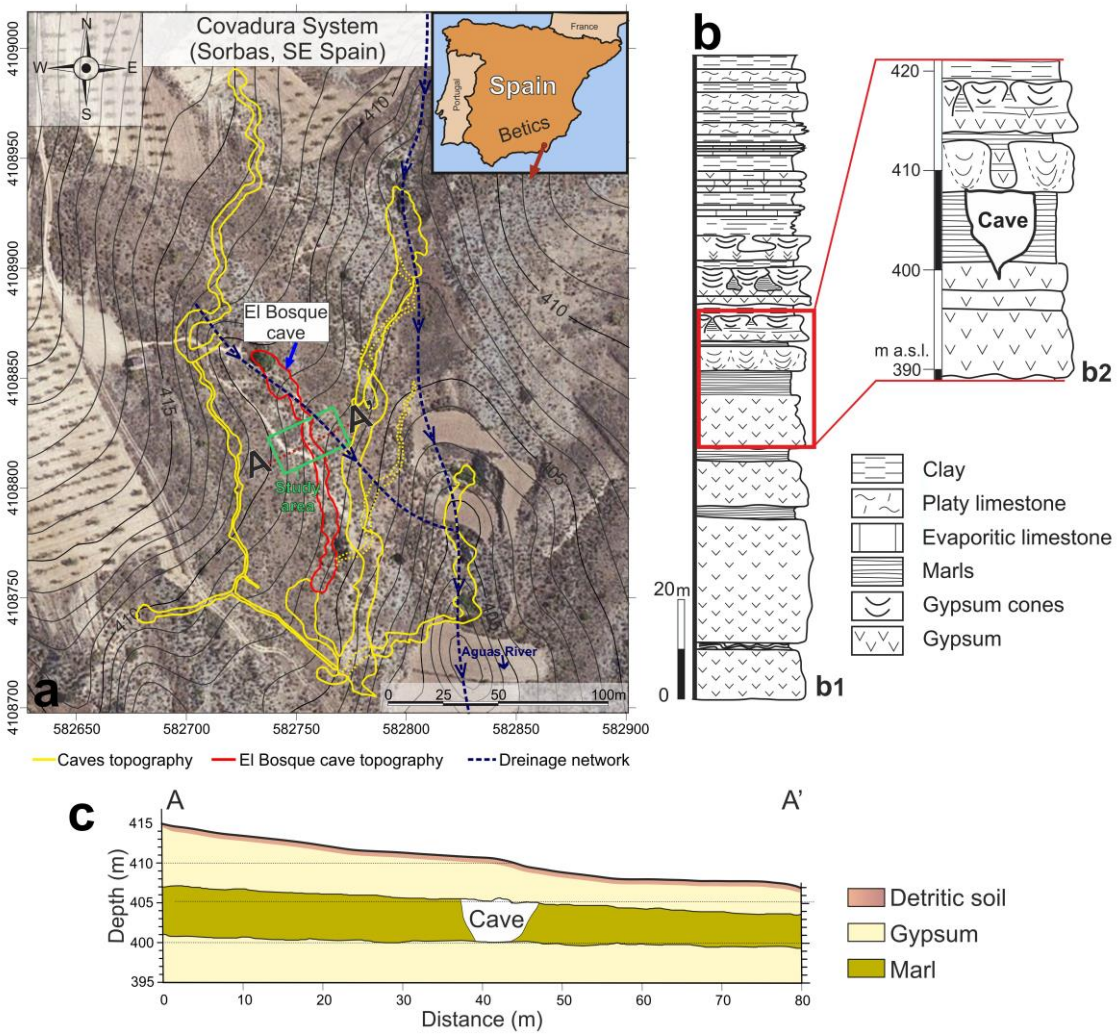


Figure 10.1: Location of the studied area. (a) Sorbas karst system (Almería, southeastern Spain) and topography of the study area. The gypsum cave selected is El Bosque, belonging to the Covadura karst system. (b) Lithological column of the Yesares Member alternating gypsum beds and/or evaporitic limestones with marls or clays (modified from Krijgsman *et al.*, 2001). (c) El Bosque cave section. A multilayer system, composed by gypsums and marls, encloses the cave.

## 10.3 METHODS

Investigation of the suitability of geophysical methods for cave detection in gypsum involved different procedures. First we mapped the cave morphology using classical geodetical techniques. Microgravity and two ERT measurement campaigns were then performed under different soil humidity conditions. Differential GPS allowed for the planning and positioning of measurement points in the studied area, after which the distribution of field measurements could be carried out in view of the cave position (Fig. 10.2).

### 10.3.1 Microgravity measurements

Microgravity can detect small underground density contrasts with high accuracy, identifying such changes as gravity minima when, for example, a cave with density 0 g/cm$^3$ is inside limestone with 2.67 g/cm$^3$ or gypsum with 2.35 g/cm$^3$. Other parameters to be taken into account are the dimensions and depth of the structures.

We used a gravity meter (Scintrex CG-5 Autograv) on a tripod, with an accuracy of ±0.001 mGal. Microgravity conditions involved measurements under ±0.005 mGal error, cycles shorter than 3 hours, charging on a levelled tripod 12 h before the field measurements, and 15 minutes on a levelled tripod before each cycle to minimize the spring hysteresis effects.

The microgravity stations were situated at distances of 1 m, 2 m and 4 m. A total of 444 measurements were taken, covering an area of 2585 m$^2$ (Fig. 10.3). The microgravity stations were measured in a 1x1 m grid above the cave, a 2x2 m grid beside the cave, and a 4x4 m grid beyond.

The microgravity position was determined using a differential GPS Leica 1200 (as reference station) and a Leica 1200+ (as Real Time Kinematics). The position of the GPS reference station was obtained through the Andalusian Positioning Network (RAP, Junta de Andalucía, 2014) with an accuracy of ±5 cm. This station, which sends the correction

to real time kinematic equipment that registers the measurements with an error under ±1 cm, relies on the coordinate system of reference UTM ETRS89.

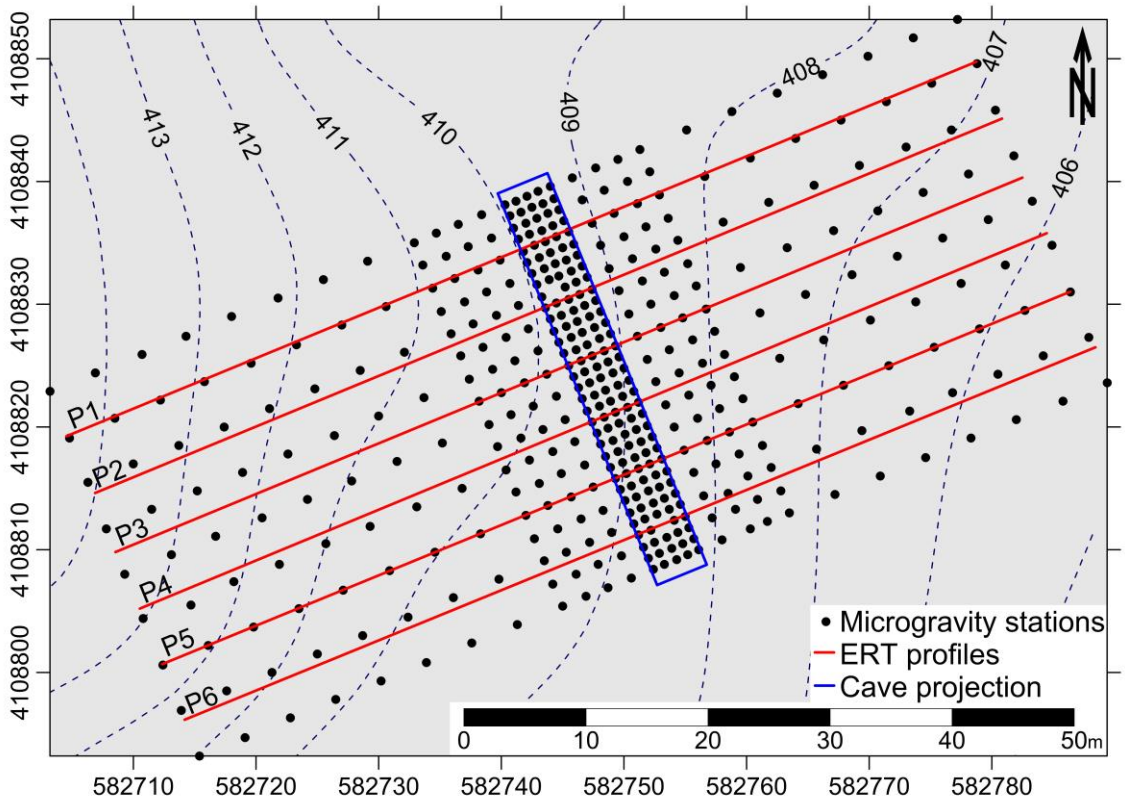


Figure 10.2: Locations of the ERT profiles (red line), over microgravity measurement stations (black dots). The cave contour is also plotted.

The recorded gravity was referred to the Almería gravimetric base (Instituto Geográfico Nacional, www.ign.es). The Bouguer anomaly was determined after tidal and instrumental corrections using a 2.67 g/cm$^3$ standard density. The terrain correction was calculated with Hammer's circle method (Hammer, 1939, 1982) by means of the digital terrain model of the IGN (Instituto Geográfico Nacional, 2005) with a 5 m horizontal resolution. A polynomial regression (one degree) was applied to the Bouguer anomaly map to obtain the trend of the regional anomaly, giving the residual anomaly map. Moreover 2.5D synthetic models of gravity and field gravity profiles were created to match the ERT lines. The profiles were forward modelled using GRAVMAG v.1.7 from

the British Geological Survey (Pedley *et al.*, 1993) according to the geological information (Calaforra and Pulido-Bosch, 2003).

### 10.3.2 ERT measurements

Resistivity profiles were measured using Terrameter SAS 4000 (ABEM, Inc.) 4-channel equipment, which introduces current in the terrain by means of a pair of steel electrodes while measuring potential difference in another pair of steel electrodes. The equipment resolution is about ±1μV. The profiles were acquired by a multiple gradient electrode array with GRAD4LX8 and GRAD4S8 protocols (ABEM, 2006). The gradient protocol uses an 'alfa' type electrode arrangement where the potential electrodes are between the current ones (ABEM, 2006; Loke, 2014). This array was developed for a multi-channel resistivity meter system (Dahlin and Zhou, 2006).

The ERT method was applied under various temperature and humidity soil conditions. For instance, dry conditions (October, 2013) imply close to 0% relative soil humidity and an air temperature of 20ºC to 24ºC. Wet conditions (January, 2014) meant 20-40% relative soil humidity and air temperature between 13-19 ºC. These data were provided by the National Meteorology Agency of Spain (AEMET, www.aemet.es). Soil humidity —measured in function of soil type, its development, the vegetation present and soil uses—depends on the precipitation and the evapotranspiration produced at a certain point in time.

Accordingly, six parallel profiles were obtained for each of the soil humidity conditions. The ERT profiles, spaced 5 m apart and with an electrode separation of 1m, were collected inside the microgravity area; some of them ran along microgravity stations. The positions of both campaigns were therefore gauged with differential GPS. Previous to the data inversion process filters were applied to adjust for: extermination bad datum

points and RMS error statistics (discarding data above 40% error, following Loke, 2014). Inverse calculation of the apparent resistivity data was carried out with the same parameters, under software Res2Dinv (v. 3.59, Geotomo Inc.). This entailed standard least-square inversion and model refinement constraint, in conjunction with a mesh made up of model cells, 4 nodes per unit electrode spacing, and an initial damping factor of 0.3. Furthermore, because the studied area has a smooth topography, the least square straight line and uniformly distorted grid were used for topography modelling. For the 3D models, the parallel profiles were coupled in 3D format to calculate the inversion data using Res3Dinv (v. 2.1, Geotomo Inc.). The 3D inversion parameters selected were the same as in 2D inversion.

The resolution of the ERT profiles was tested by calculating the empirical depth of investigation (DOI) index. This process consists of performing two model inversions with different resistivity backgrounds on each profile. The first model has a resistivity background of 10 Ω.m, as opposed to the second one of 1000 Ω.m. The two are compared to obtain the depth under which the model has low resolution (Loke, 2014). The DOI index calculation, as introduced by Oldenburg and Li (1999) and modified by Marescot *et al.* (2003), recommends a cut-off value of 0.1 or 0.2 to consider data as reliable. We applied the more restrictive cut-off value of 0.1, the area above being fully consistent with measured data.

## 10.4 RESULTS

### 10.4.1 Microgravity results

The gravity response of caves enclosed in low density rocks was tested by means of synthetic models created using 2D modelled software for a cave with a density of 0 g/cm$^3$. This enabled us to analyse the influence of cavity dimensions, depth to the top,

and density contrast on the gravity anomaly (Fig. 10.3). Three host rock densities were applied: gypsum or marls (2.3 g/cm$^3$), marbles/limestone (2.7 g/cm$^3$) and basalts (3.0 g/cm$^3$). In terms of cave dimensions and depth to the top (Fig. 10.3a), the residual anomaly was seen to increase with cave dimension, although the rise was not linear for the same density. Considering different host rock densities (Fig. 10.3b) and a setting similar to that of the studied cave, the incidence on the gravity anomaly of the cave distance to the surface decreases exponentially with depth. This decay is equivalent regardless of the host rock density. The next diagram (Fig. 10.3c) represents the relationship between cave dimensions and depth-to-the-top to preserve the same minimum residual gravity anomaly. For shallow caves, the ratio is more homogeneous than for deeper cavities, where the curves separate. The final diagram (Fig. 10.3d) maintains the top of the cave at the same depth, increasing the cave size to double its volume, which would mean a linear decrease in gravity values for larger caves. The features of El Bosque cave and its produced anomaly are signalled by a red dot.

For field measurements, the Bouguer anomaly map (Fig. 10.4a) shows values ranging from -3.8 to -3.4 mGal, from SW to NE. The regional anomaly (Fig. 10.4b) goes from -3.83 to -3.43 mGal —a range of 0.4 mGal— decreasing from ESE to WNW. Seven residual anomaly maps were created with different spacing measures and disposition. The 1x1 m grid (Fig. 10.4c), focused on the cave position, shows a minima of residual anomaly gravity from -0.05 to -0.1 mGal that matched the known cave position. Two other spacing were calculated for the next grids, one focused on the cave, and another beyond it. The 2x2 m grid focused on the cave (Fig. 10.4d) shows a similar minima morphology as regards cave position, though less sensitive to its shape. The minima value is slightly lower than in the first grid, whereas slightly beyond the cave (Fig. 10.4e) more

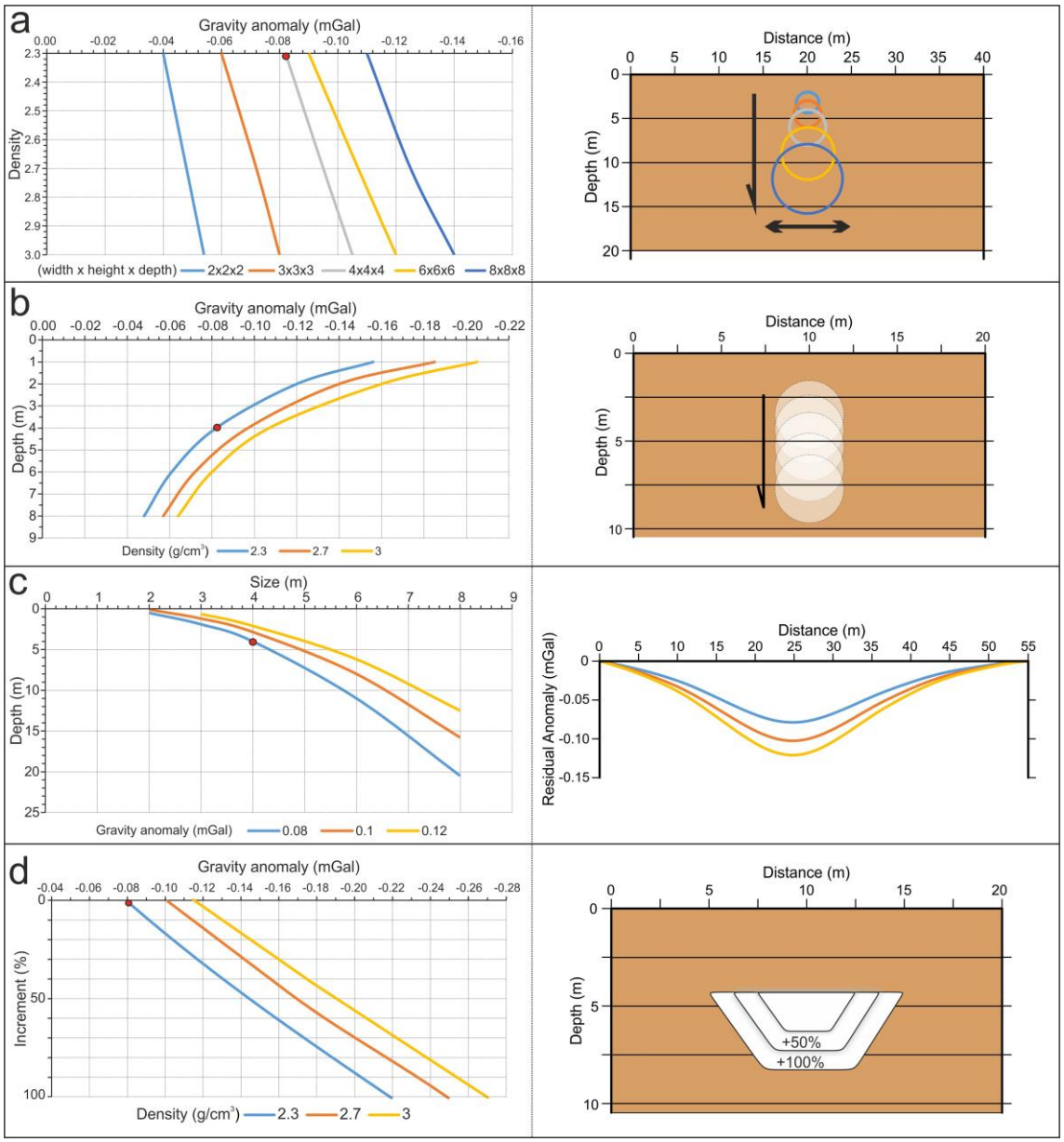


Figure 10.3: Synthetic gravity models. (a) Gravity anomaly variation with increasing density, in different cave dimensions. (b) Gravity anomaly variation with increasing depth of a cave having the same dimensions as El Bosque cave (4x4 m). (c) Variation of the size and depth of a cave for different gravity anomaly values. (d) Gravity anomaly variation for cave size increment in %, and maintaining the same top depth. The red dots mark study cave conditions.

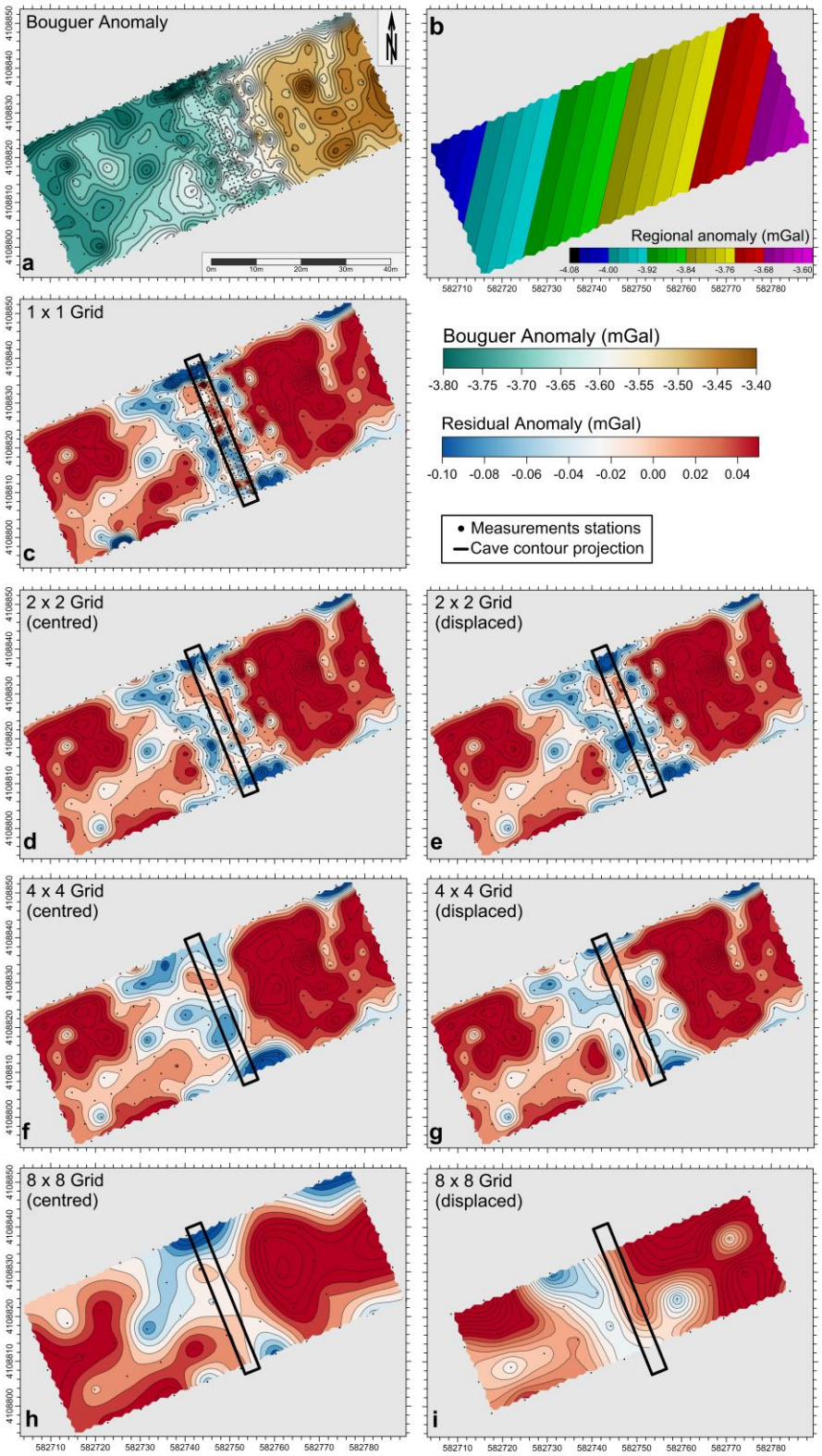


Figure 10.4: Gravity anomaly maps. (a) Bouguer anomaly map and (b) regional anomaly map. Different measurement spacings are displayed: 1x1 m on the cave (c), 2x2, centred (d) and displaced (e) from cave, 4x4 centred (f) and displaced (g) from cave and 8x8 centred (h) and displaced (i) from the cave. Displaced grids allow one to check the effect of the selected reference sites. The cave contour projection is shown in the maps.

expanded minima are seen. In the 4x4 m grid centred on the cave (Fig. 10.4f), we observe a more widespread minima gravity zone associated with the cave. In contrast, the same grid displaced (Fig. 10.4g) shows that the narrow conduct defined with microgravity disappears, and only extended zones with minima associated with the cave are visible. Finally, a grid with 8x8 m spacing either focused or not on the cave (Figs. 10.4h and 10.4i) does not detect the narrow minima; yet it detects the cave as a broad smooth minima identified by a few points, and the residual anomaly has values lower than in the other grids.

### 10.4.2 ERT prospection

The ERT profiles, measured under different humidity conditions, present differences both in the number of data and in data accuracy (Table 10.1). Statistical analysis reveals that fewer original data were obtained in dry conditions than in wet conditions, due to the poor contact between electrodes and soil, implying some disconnected electrodes. Even when the ground near each electrode is moistened with salted water, they remained unconnected in this sense. The quality of data in wet conditions is better, and fewer filters are needed during the processing stage. Hence, in the inversion process, the electrical model obtained in wet conditions had a lower RMS error for the same iteration number.

| PROFILE | Original Data number | | Filter Data number (Error<40%) | | % Error DATA | | RMS error (Iteration 4) | |
|---|---|---|---|---|---|---|---|---|
| | Dry | Wet | Dry | Wet | | Dry | Wet | Dry |
| P1 | 981 | 947 | 903 | 947 | P1 | 981 | 947 | 903 |
| P2 | 638 | 1010 | 619 | 994 | P2 | 638 | 1010 | 619 |
| P3 | 768 | 1038 | 716 | 1029 | P3 | 768 | 1038 | 716 |
| P4 | 912 | 1168 | 850 | 1155 | P4 | 912 | 1168 | 850 |
| P5 | 1034 | 1055 | 977 | 1055 | P5 | 1034 | 1055 | 977 |
| P6 | 884 | 1052 | 820 | 1043 | P6 | 884 | 1052 | 820 |

Table 10.1: Data points and RMS error (iteration 4) from the ERT profiles measured in dry and wet conditions.

The profiles measured in dry conditions (Fig. 10.5) present a shallow higher-resistivity sector (>1000 Ω.m) associated with the gypsum layer. Beneath this resistive layer, the profiles show a lower resistivity sector (~50 to ~100 Ω.m) corresponding to marl layers. In the central part of this lower-resistivity sector, between 40-45 m length and 400-405 m depth, there is a higher-resistivity zone of 500-1000 Ω.m matching the cave position and its approximate dimensions. Around the cave and below the gypsum layers there are values from ~200 to ~500 Ω.m corresponding to marls, but influenced by the presence of the resistive cave and therefore increasing its resistivity value. The DOI index line crosses under the detected cave in most profiles.

The ERT profiles measured in wet conditions (Fig. 10.6) show the same pattern as in dry conditions. The resistivity anomaly linked to the marl layer is similar in both (~50 to 100 Ω.m); however, the high resistive anomalies associated with the cave and with the shallow gypsum layer are slightly different. In wet conditions, the cave (~900 to 1500 Ω.m) and the gypsum layer (>2000 Ω.m) are seen to have higher resistivity than in dry conditions. In addition, the anomaly related to the cave presents a more circular shape and slightly bigger morphology. The gypsum layer at the bottom of the cave was not reflected in the inversion models, probably masked by the lower-resistivity marl layer situated above.

In both dry and wet conditions, the continuity of the elongated resistive body orthogonal to the profiles is concordant with the cave position (Fig. 10.7). The resistivity contrast for the shallow layers is sharp in both humidity conditions, although the resistivity anomaly associated with the cave is greater in wet than in dry conditions. In addition, there are differences in the shallowest parts of the two profiles. The W shallow

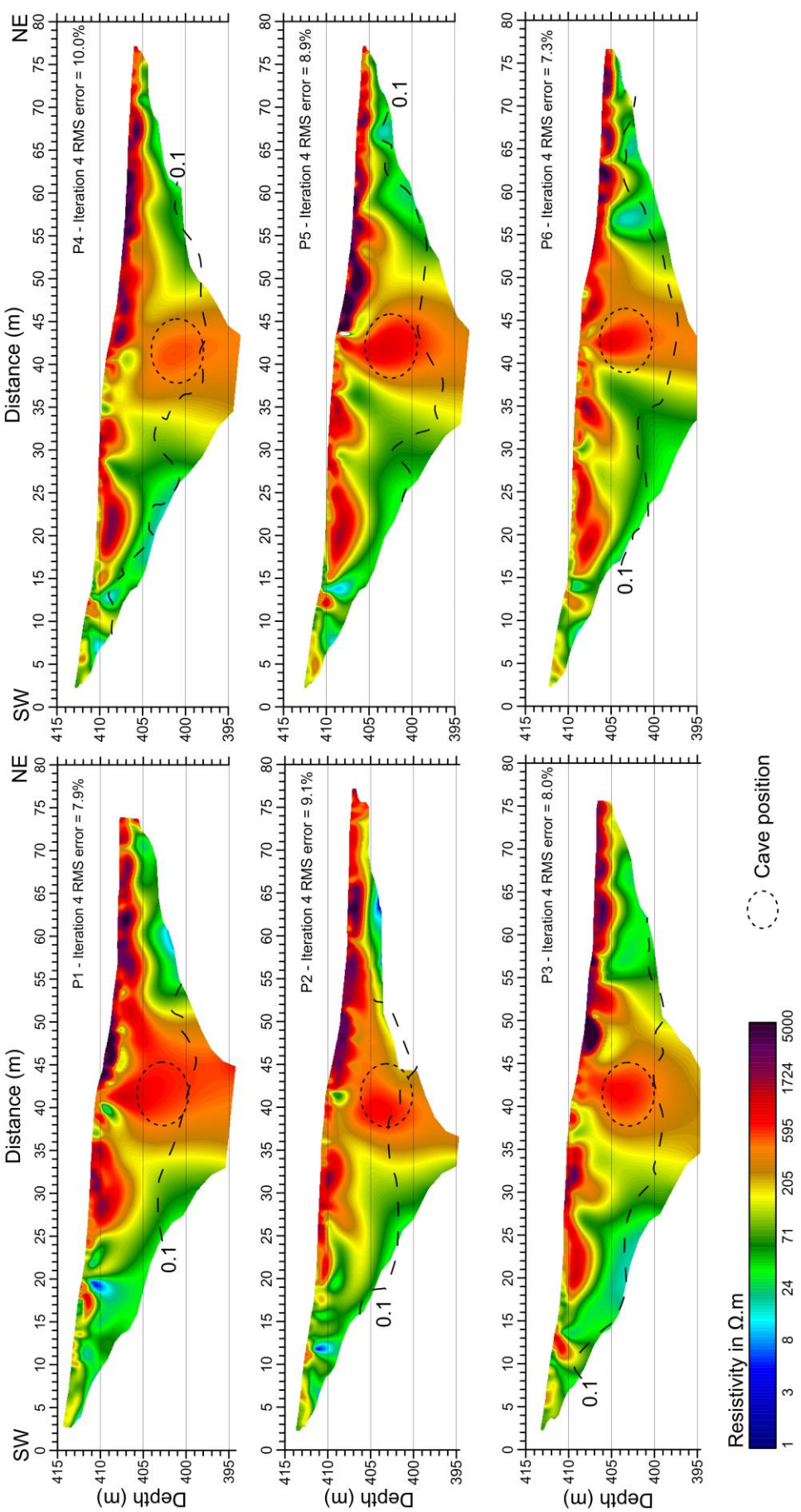


Figure 10.5: ERT profiles in dry soil humidity conditions (October 2013, 0% relative soil humidity). The cave shape is marked in the centre of the profiles with a small dashed line. The 0.1 DOI index value is displayed on each profile (large dashed line).

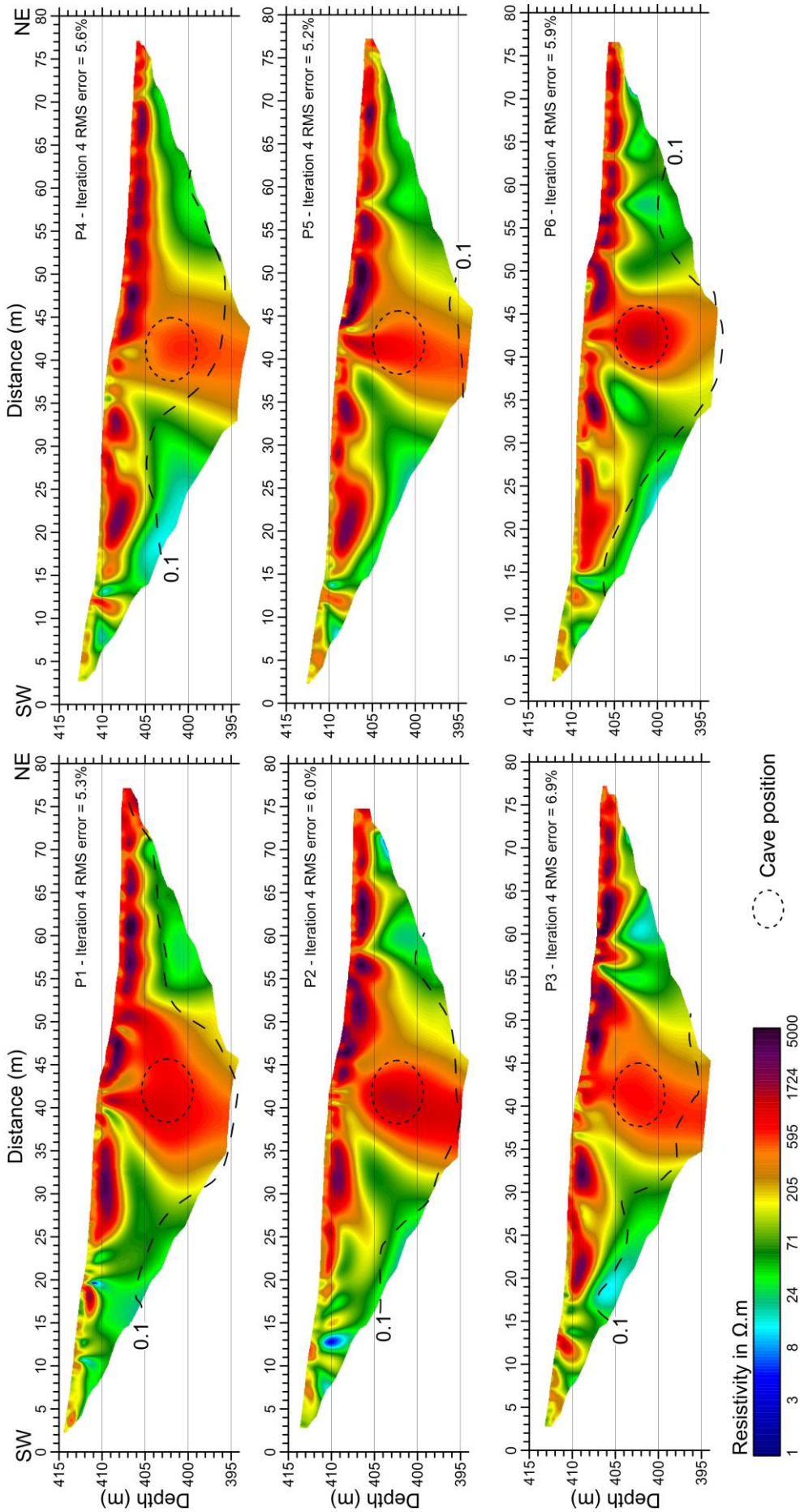


Figure 10.6: ERT profiles in wet soil humidity conditions (January 2014, 20-40% relative soil humidity). The cave shape is marked in the centre of the profiles with a small dashed line. The 0.1 DOI index value is displayed on each profile (large dashed line).

zones contain profiles with higher resistivity values than the E ones, most likely due to more detritic soil content and less nucleation cones toward the western zones of the profiles.

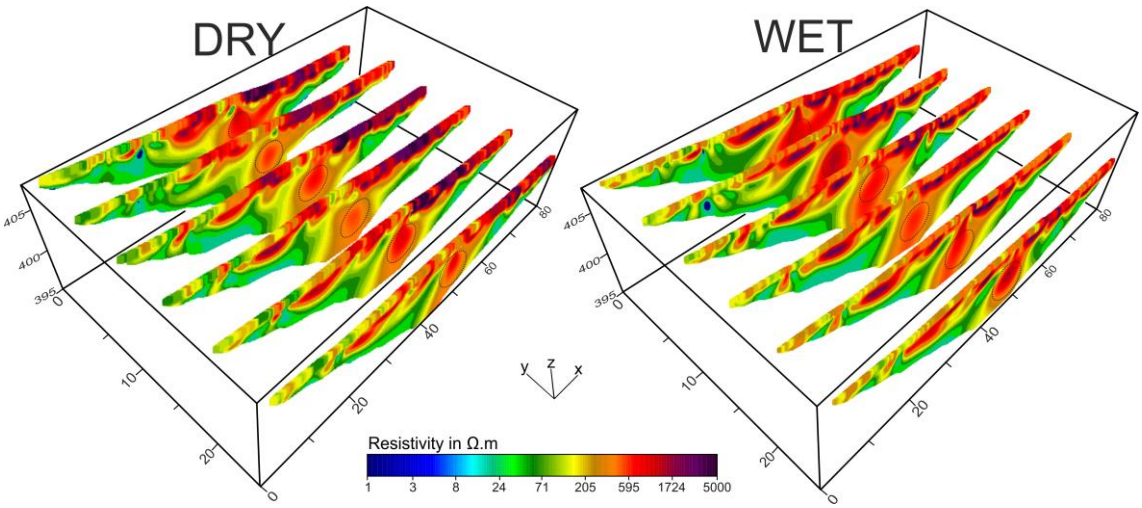


Figure 10.7: ERT profiles placed in their spatial position with cave position marked (dashed line). Both humidity conditions are shown.

Figure 10.8, which presents the 3D inversion results, shows different contour values matching the cave contour. The resistivity contour used was 900 Ω.m for the dry model, and 1150 Ω.m for the wet model. These resistivity contours approximately fit the morphology of the cave. The selected contour value also delineates the bottom of the shallow gypsum layer located above the cave. The RMS error (17.1%) and the number of iterations obtained in dry conditions are higher than those obtained in wet conditions (RMS of 13.6%). Both 3D models indicate a broadly similar morphology.

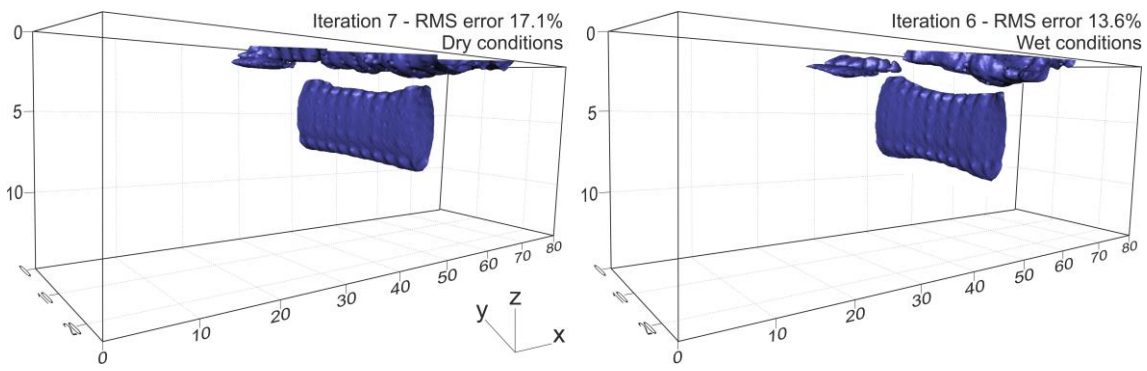


Figure 10.8: 3D inversion results of both measurement campaigns. The selected contour value (900 Ω.m in dry conditions and 1150 Ω.m in wet ones) adjusts cave morphology.

### 10.4.3 Gravity and ERT joint interpretation

To minimize uncertainty in the interpretation of the gravity and electrical anomalies, a joint interpretation of the 2D ERT and 2.5D gravity models was attempted. The profile 5 has been selected to this aim, where the gravity measurements and electrical positions largely coincided (Figure 10.9). Some microgravity minima were pronounced, while others were slight.

The pronounced negative anomaly located in the centre of the profile is associated with El Bosque cave. This minimum has values of -0.1 mGal, fitting the resistive anomaly registered in the ERT model also linked to the cave. The density assigned to the modelled cave is 0 g/cm$^3$, with a perpendicular extension of 100 m. Other minima of a longer wavelength reaching values of -0.02 to -0.04 mGal— coincide with shallow resistivity zones inside the gypsum layer, pertaining to nucleation cones formed by the growth of large selenitic gypsum crystals. The density assigned to these cones is 1.4 g/cm$^3$, since gypsum crystals are frequently separated by voids filled by air. Because the model fits both the observed gravity minima and the high resistivity anomalies, associated with the cave and the nucleation cones, it leads to more reliable interpretations.

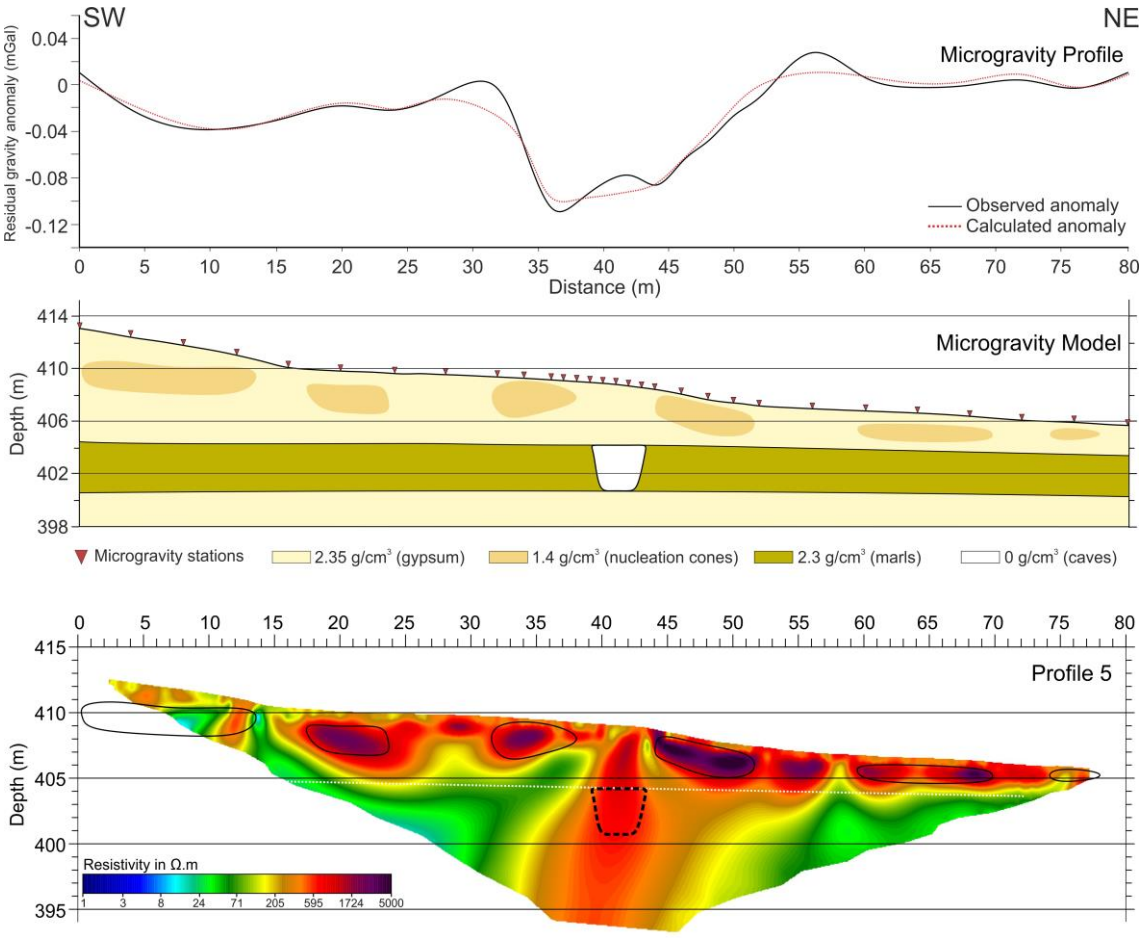


Figure 10.9: 2D forward model constructed from the residual gravity anomalies and P5 ERT profile in wet conditions.

## 10.5 DISCUSSION

### 10.5.1 Density contrast and small gypsum cave detection

Our results demonstrate that the density contrast and cave dimensions play a key role in deriving residual anomaly results (Fig. 10.3). Shallow caves with small dimensions produce local residual gravity anomaly with shorter spatial wavelengths than higher and deeper ones, thus implying greater difficulty in their detection. Caves developed in gypsum produce lower anomalies than caves in more dense lithologies, making them more difficult to detect, especially in the case of small caves. In such settings, microgravity prospection requires high accuracy in order to detect very minor changes in the residual gravity anomaly (~0.8 mGal), which may closely approach the error of

microgravimeters (e.g. Scintrex CG-5). Finally, for a given density contrast in the case of gypsum host rocks (2.3 g/cm$^3$), a large cave size and small depth to the top would be needed to obtain a residual gravity anomaly highlighting a cave in a residual anomaly map.

The spacing of gravity measurements is an important factor to be considered: a small residual anomaly leaves shallow and small caves practically undetectable, unless very narrow measurements are carried out, or a larger grid is focused over the cave by chance. In large study areas, this might involve numerous and time consuming measurements. Accordingly, Figure 10.4 shows real residual anomaly grids, the first two with respective spacing of 1x1 m and 2x2 m, for which the anomaly detected is quite similar. There is a well highlighted minimum linked to the cave, especially when the 2x2 grid is centred over the cave. This gravity minimum associated with the cave located at 4-5 m depth, and dimensions of 3 m height and 5 m width, has a value of -0.05 to -0.1 mGal, in line with those calculated using the synthetic models. This spacing makes it possible to detect and differentiate caves with accuracy. Nevertheless, grids with spacing 4x4 and 8x8 detect an extended area with smooth minima associated with cave location, though the morphology and precise position are not well defined. Only when the 4x4 spacing is focused on the cave can it be inferred. Such findings demonstrate that microgravity measurement spacing should be, at least, about half the size of the cave, so that one of the stations along a profile might be located over the cavity.

The relatively low contrast between host rock and caves is another important point to be addressed. Massive gypsum, with an approximate density of 2.3 g/cm$^3$, provides a good contrast for highlighting caves. However, gypsum rock may present partially dissolved zones of lower density, such as nucleation zones with a density of about 1.4 g/cm$^3$. Low contrast can lead to confusion in cave detection, as it is necessary to

distinguish between minima associated with caves and partially dissolved zones in gypsum. For this reason, precisely, it is very important to combine methods.

### 10.5.2 Qualitative variation in different humidity contexts on ERT profiles

This study demonstrates the importance of soil humidity conditions when detecting caves in gypsum using resistivity methods. Our profiles were measured with a 20-40% difference in soil humidity conditions (AEMET), a high value given the arid climate involved (Calaforra and Pulido-Bosch, 2003). The profiles measured in dry conditions (0% relative soil humidity) had lower quality, fewer useful data, and reached higher RMS model-errors (Table 10.1). Furthermore, the depth where the model had a good resolution (DOI index calculated) was shallower in dry models than in wet ones. His can be attributed to the very dry and resistive superficial layer near the ground, which impedes good contact between the electrodes and terrain, reducing the number of available electrodes along the profile and decreasing the number of data (and therefore the profile quality). In turn, the resistivity contrast between the cave and its surrounding material is emphasized in wet conditions.

An additional aspect to highlight in time lapse profiles is the resistivity differences between wet and dry profiles. Air temperature changes in electrical profiles necessarily produce resistivity changes (Keller and Frischknecht, 1966; Hayley *et al.*, 2007). Profiles measured under 15ºC detect resistivity values about ~100 Ω.m higher than the measurements at 20ºC (Revil *et al.*, 1998; Hayley, 2007), depending on other parameters such as grain size, porosity and moisture content (Harmon and Hajicek, 1992; Bernstone *et al.*, 2000; Guerin *et al.*, 2004; Chambers *et al.*, 2009; Hayley *et al.*, 2009). Such resistivity changes have been demonstrated in more recent research (Peciller *et al.*, 2012).

According to our results, the profiles measured in time-lapse point to two kind of changes. On the one hand, marl layers register lower resistivity values due to their

increase in moisture content, in contrast to the changes causes by the temperature decreasing; while on the other hand, the cave and gypsum layers are detected as higher resistivity zones when measurements are performed in wet conditions due to the temperature decrease. The decreasing resistivity of zones close to the cave and nucleation cones would provoke an increment in resistivity contrast, thus giving rise to higher resistivity values for these areas.

When calculating the resistivity differences between dry and wet 2D inversion models (Figure 10.10), we determined that the cave and partially dissolved gypsum zones (nucleation cones; Dronkert, 1977) continued to show resistivity increments (white zones), whereas the resistivity of the environment decreased (coloured areas). This contrast could serve to underline the cave position.

In sum, ERT profiles under wet conditions are better able to detect a cave developed in gypsum. The resistivity contrast is higher than in dry conditions, and the quality of the profiles increases along with the degree of humidity. We furthermore found that the RMS error obtained in iteration 4 of the inversion process in wet profiles was lower than 7%, and in the dry ones, between 7.3% and 10% (Table 10.1). It should be stressed that the resistivity layer underneath the cavity could not be detected due to the low resistivity layer located immediately above the gypsum layer and the gradient array used (Loke, 2014). The detection of resistivity layers under low resistivity cover is a well-known problem in electrical methods (Kirsch, 2009).

Finally, 3D inversion also serves to detect differences in the dimensions of the resistivity anomaly linked to the cave. Even in the case of small caves with lower resistivity contrast in dry conditions, the shape and resistivity contrast are higher in wet conditions.

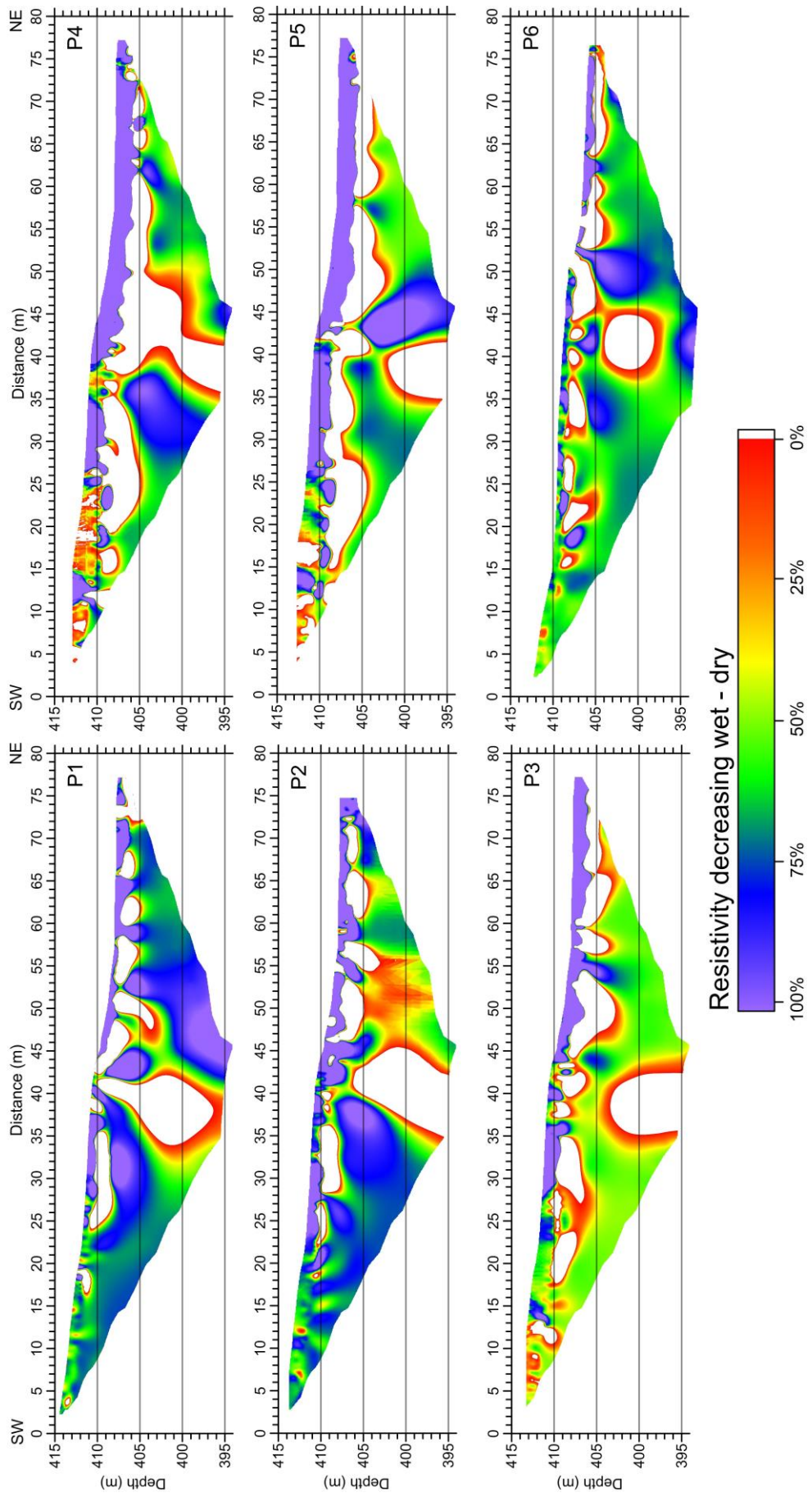


Figure 10.10: Comparison of the profiles in wet and dry soil conditions. The wet profiles were subtracted from the dry ones. Coloured areas represent resistivity decreasing, while white areas depict resistivity increment associated with the cave.

### 10.5.3 Integrated interpretation

The promising results of the different geophysical techniques applied here call for an integrated interpretation of models in future research efforts. Our study entailed a 2.5D gravity model that fit the resistivity anomalies observed for the ERT model. When dealing with air-filled caves developed in gypsum, the associated resistivity could be assigned to the host-rock, as the caves themselves have a low resistivity contrast. Gravity models are therefore crucial for distinguishing between the cave, the gypsum, and the zones partially dissolved between gypsum layers. In addition to revealing known caves beneath the gypsum layer and surrounded by marls, there may be nucleation cones —sectors formed by large selenitic gypsum crystals separated by voids— inside the more homogeneous gypsum layer. Gypsum nucleation cones could therefore be identified as small high resistivity zones featuring small wavelength residual minima.

## 10.6 CONCLUSIONS

Different soil humidity conditions and microgravity research techniques may provide results that improve our knowledge about the application of ERT methods in gypsum cave prospection. Modelled gravity profiles complement and enhance ERT results, enriching the information obtained by each method separately.

The detection of caves within gypsum and surrounded by marls is a complicated task, which this study approached in a novel way. Two different geophysical methods were applied: microgravity and ERT. Both demonstrated high success rates in detecting and locating caves in the study area. Applied separately, however, they may give rise to misleading interpretations.

Microgravity, which detects slight density contrast, is highly sensitive to the density variation in lithology adjacent to a cave. In gypsum caves, the density contrast is lower than in caves surrounded by higher density lithology. The calculated theoretical model demonstrates that caves developed in lithologies with high densities (limestones, marbles) are better detected than those within lower contrast lithologies (gypsum, marls). Moreover, planning the spacing between measuring stations can prove to be determinant for the success of such research. For cave dimensions similar to those dealt with here, we propose microgravity station spacing that is half the minimum width of the cavity projection.

The ERT method ensures positive results in the detection of cavities where the resistivity contrast between gypsum and the cave could be masked. Because the case at hand involved a cave surrounded by a low resistivity marl layer, it was possible to detect the cavity under the gypsum layer. We can also conclude that wet conditions provide for better data and inversion results than dry conditions. The 3D model obtained represents the cave morphology with different resistivity values owing to humidity variation.

Gravity and ERT models may be misleading when they are examined separately. A coordinated interpretation of the results of these geophysical models can point researchers to more reliable interpretations.

Clearly, these two methods are appropriate for combined application in the case of gypsum caves. The success rate of this combined methodology is high when applied to the detection of cavities with low-contrasting physical parameters, as is the case of evaporite karsts. Such an approach may prove valuable within a framework of engineering or structural design and risk assessment.

**ACKNOWLEDGEMENTS**

We would like to express our appreciation to the four reviewers for their comments and suggestions which served to substantially improve this research paper. We thank Jean Sanders for reviewing the English grammar. Moreover, we would like to acknowledge the helpful collaboration of Sorbas Natural Park, and GLOCHARID (Global Change in Arid Zones). Our research was supported by projects CGL2010-21048, P09-RNM-5388 and RNM148.

# Part III

11. Discussion

12. Conclusion / Conclusiones

13. Future perspectives

# Chapter 11

Discussion

This Ph.D. Thesis demonstrates that geophysical methods are a good tool to detect near surface caves. In some cases, the cavities that lack outside access or are not fully accessible. This fact makes necessary to identify how the caves are detected by means of different geophysical methods in diverse geological settings, environment conditions and cave features. Sometimes the methods applied require certain special settings that prevent its applications. These conditions could be architectural barriers, as buildings and walls, where only is applicable methods as GPR or microgravity; vegetation or areas not opencast, which reduce the probabilities to apply microgravity and GPS; or areas with firm ground (asphalted, paved or rocks) which complicates the electrical or seismic data acquisition.

Moreover, there are geological settings and cave features which benefit the results obtained with some methods in respect to others. Hence, it is necessary to perform a detailed geological study of the study area in order to establish the main cave features and the probable location and sources of geophysical anomalies. Parameters as foliation and dip of the host rock influence the cave development (Chapters 5, 8 and 9). In addition, the water-table location and hydrodynamic of the study area also affect to the cave morphology, position and development (Chapters 5 and 8). Finally, in caves with ferromagnetic metallic mineralization (Chapter 5), the mapping of these ore minerals could improve the cave detection and location due to delimit areas with cave presence.

In some settings, it is possible to perform a drill exploration to confirm the location of the caved highlighted by the geophysics. In Chapter 6, the geophysical methods applied have been tested with mechanic drill exploration. In that area, the residual anomaly map shows an area with minima elongated in WNW-ESE direction. These minima, which are more pronounced than the corresponding to the known cave, matches with the foliation trend and it is near to the pyrite bearing band, although they are placed within outcropping

quartzites. Moreover, it is close to the profiles 3 and 4 in Chapter 6, which a combination of geophysical methods reveals near surface caves. The drilled cavities expose the accuracy and resolution of the geophysical methods. In Aracena, drill exploration confirms the presence of caves emplaced in quartzites, as consequence of dissolution of marbles inside them. Moreover, the previous drill exploration make in Algaidilla cave (Chapter 8) have been used for interpreting the ERT profiles and, in addition, to make forward gravity models. The information provided for these drills fit with the theoretical geophysical models calculated, which proves the effectiveness of the applied geophysical methods and the interpretation offered.

For an overview of the geophysical methods suitability in different contexts, in Table 11.1 is summarized the results obtained in different geological settings, cave features and using different geophysical methods in this PhD. Thesis. The first geological feature to consider is the nature of the host rock, due to their contrast in density and resistivity, which could be carbonates (marbles, limestones and dolostones, Chapter 6 and 8) and gypsum (Chapter 9). Secondary minerals present in some cavities are discussed, as ferromagnetic metallic minerals (iron oxides at the cave walls, Chapter 6) or product from carbonates dissolution (decalcification clays at the cave bottom, Chapter 8). Another important cave feature is the water content, giving three possible cases: unsaturated caves (Chapter 9), saturated caves, and partially saturated caves (Chapter 6 and 8). The size and deep of the cavity is examined in this section because there are shallow small (Chapter 6 and 9) and large caves (Chapter 6), as well as deep small (Chapter 6) and large cavities (Chapter 6 and 8). Finally the soil moisture is a feature taken into account since it influences in some of the geophysical methods applied.

Microgravity, which detects shallow density changes, is a good method for most of the cases in terms of host rock and cave features (Butler, 1984). The caves are detected

| GEOLOGICAL SETINGS AND CAVE FEATURES / METHODS | | MAGNETIC | ELECTRICAL | | SEISMIC REFRACTION | | SEISMIC REFLECTION | GROUND PENETRATING RADAR |
|---|---|---|---|---|---|---|---|---|
| | | | RESISTIVITY | IP | VELOCITY | RAY TRACING COVERAGE | COMMON OFFSET | |
| LITHOLOGY | CARBONATES | Intense minima of residual anomaly | Resistive cave within less resistive host rock | | Very low velocities | Absence of rays | Low frequencies | Hyperbolic reflectors over the cave |
| | GYPSUM | Low intense minima of residual anomaly | Resistive cave within less resistive host rock | | Low velocities | Absence of rays | Low frequencies | Hyperbolic reflectors over the cave |
| METALLIC MINERALIZED CAVES | | Intense minima of residual anomaly | Low resistivity cave with increment inward | High chargeability values | Low velocities | Absence of rays | Low frequencies | Strong reflectors can mask caves |
| DECALCIFICATION CLAYS DEPOSITS | | Decrease the minima intensity | Low resistivity in the lower parts of the cave | High chargeability values | Increasing velocity in the lower parts of the cave | Poorly ray tracing coverage in the lower parts of the cave | No low frequencies in the lower part of the cave | |
| WATER CONTENT | UNSATURATED | Intense minima of residual anomaly | Resistive cave within less resistive host rock | | Very low velocities | Absence of rays | Low frequencies | Hyperbolic reflectors over the cave |
| | PARTIALLY SATURATED | Minima of residual anomaly | Low resistive cave within resistive host rock | Low chargeability values with salted water | Low velocities at the top and intermediate down | Absence of rays at the top | Low frequencies | Hyperbolic reflectors over the cave |
| | SATURATED | Low intense minima of residual anomaly | Low resistive cave within resistive host rock | Low chargeability values with salted water | Intermediate velocities | Poorly ray tracing coverage in the lower parts of the cave | Intermediate frequencies | |
| DEPTH | SHALLOW SMALL | Only detectable with small measurement spacing | Resistive contours | | Very low velocities | Absence of rays | Low frequencies slightly masked | Hyperbolic reflectors over the cave |
| | SHALLOW LARGE | Intense and located minima of residual anomaly | Resistive contours | | Very low velocities | Absence of rays | Low frequencies | Hyperbolic reflectors over the cave |
| | DEEP SMALL | | | | | Very small zones with absence of rays | | |
| | DEEP LARGE | Smooth minima of residual anomaly | Well delineated resistive contours. | | Low velocities | Absence of rays | Low frequencies slightly masked | Hyperbolic reflectors over the cave |
| HUMIDITY SOIL CONDITIONS (UNSATURATED ZONE) | WET | Intense minima of residual anomaly | Resistive cave within less resistive host rock | | Low velocities | Absence of rays | Low frequencies | |
| | DRY | Intense minima of residual anomaly | Resistive cave within slightly less resistive host rock | | Low velocities | Absence of rays | Low frequencies | Hyperbolic reflectors over the cave |

Table 11.1: Cave detection in different methods and geological settings. The green squares highlight the best method in the cave features. Yellow ones marks the method applied could result confuse. Finally, the red squares mean the method not detect the cave with such features.

as residual gravimetric minima in all cases (Chico, 1964; Colley, 1963), but with different wavelength in function of the host rock conditions and cave features. Regarding the lithology where the cave is emplaced, this method is more effective in carbonates (Brown, *et al.*, 2011; Chapter 6 and 8), due to their higher density contrast between host rock and voids (2.6-2.7 g/cm$^3$ versus ~0 g/cm$^3$), than in gypsum (~2.3 g/cm$^3$ versus ~0 g/cm$^3$, Chapter 9), where there are less density contrast. In addition, gypsum as host rock could present shallow features, as nucleation cones or small shallow holes, which produce residual minima anomaly not associated with the cave. This fact creates widespread and smoothed minima zones that may mask the cave identification. Metallic mineralization associated with some caves is not a determinant feature for microgravity, however large accumulation of decalcification clays at the bottom of the caves decrease slightly the minima associated with them, especially in small caves.

Saturated caves produce less density contrast than the cavities filled by air (~0 g/cm$^3$), since the water increases the density associated to the cave (~1 g/cm$^3$) (Van Camp *et al.*, 2006). Therefore, depending on the amount of water into the cave, the residual anomaly minima will be more outstanding (Kaufmann *et al.*, 2011). In caves with variable water table level is recommendable perform the microgravity study with its lower water table (e.g. before the first rains into the hydrological cycle -in natural hydrogeological conditions-). Cave size and depth is another important feature (Beres *et al.*, 2001). Shallow and small caves produce local prominent minima, whereas deep and large ones create less prominent and more widespread minima. For this reason, it is necessary estimate the cave size and depth expected before carry out the microgravity survey in map distribution to plan the station spacing (Chamon and Dobereiner, 1988). In this respect, in one hand for shallow small caves is necessary a close spacing (2x2 m, Chapter 9) to detect all the possible cave irregularities and, in other hand, a more distant measurement

sites spacing is enough to characterize deep and large caves (10x10 m, Chapter 6). In this way, it is more probably that at least one measurement station is located on the cave, which facilitates its detection. Finally, humidity soil conditions are not a decisive feature for cave detection with microgravity (Lange, 1999). However, soils with more water content increase slightly the density contrast between host rock and cave, resulting in a better cave detection.

The cave detection in gravity researches requires the residual anomaly maps calculation, which separates the shallow anomalies from the deeper ones. The regional-residual separation is an important procedure in cave microgravity researches. Depending on the technique applied, different map results could be obtained which can varied the interpretation of the data (Dobrin, 1960). There are several regional-residual separation techniques (Table 7.1, Chapter 7) that have been applied for many authors. The most popular of them has been tested over different data distribution (inside, outside and both cave surrounding area; Chapter 5) determining that the best method for regional-residual separation, in terms of easy method application and residual map results is polynomial fitting low order over data inside cave and surrounding area. Some commercial software products are able to apply polynomial fitting over data in map distribution, in which is more feasible to apply this technique (Gupta and Ramani, 1980).

Magnetic methods are only applied for detect the position of caves with ferromagnetic mineralized features (Chamon and Dobereiner, 1988; Chapter 6). The cave position is detected as a magnetic anomaly due to the cave walls present mineralized conditions. This geophysical method can be applied in profiles (Mochales *et al.*, 2008) or in map to detect those anomalies highlighting the mineralized caves position. For this reason, in this case is important to know this cave feature specifically (e.g. comparing with near caves or surficial geological observation) to be able to detect this kind of cave.

Unfortunately, this method does not allow estimating cave parameters such as depth and size with accuracy. The areas detected with these methods must be explored with other geophysical methods to confirm the cave presence in such areas.

Electrical methods are other good tools to detect caves (Alastruey *et al.* 2002; Thierry *et al.* 2005; Rybakov *et al.* 2005; Mochales *et al.* 2006). In one hand, resistivity contrast between host rock and cave (both carbonates and gypsum) locates the voids presence with highest resistivity values (El-Qady *et al.*, 2005). In some cave features this resistivity contrast can be perturbed by different cave conditions. With mineralized cave walls, such as iron oxides (Chapter 6), the cavity is detected with low resistivity values, which increasing inward. Most carbonate caves present decalcification clays at the bottom producing that caves were detected with low resistivity values at the lower zones. The water content of the cave also varies the expected cave resistivity (Lazzari *et al.*, 2010), such that saturated caves are detected with low resistivity, whereas that unsaturated caves are distinguished with high resistivity values. Subsaturated caves produce intermediate conditions (Chapter 8), where the top is detected with high resistivity decreasing toward the saturated bottom. As in microgravity, it is recommended to perform the electrical survey with the lower water table position. Size and depth of the cave is also important (Mochales *et al.*, 2008) due to small and deep caves are practically undetectable. As in most geophysical techniques, the method resolution decreases with the deep. Finally, soil humidity conditions are a very important feature for cave detection (Leucci and De Giorgi, 2005; Chapter 9). As have been demonstrated, unsaturated caves in wet soils are better detected than the same caves in dry soils. The resistivity contrast increase in wet conditions allowing improve cave detection.

Induced polarization (IP) is an appropriate tool to study cavities linked to metallic mineralization or containing clays deposits (Brown *et al.*, 2011). There are few examples

of cave detection throughout IP in the literature. However, this technique is successfully applied in the Chapter 6 and 8. This method does not detect strictly the cave, but detect the products which can be originated during and/or associated with its formation. Secondary cave products are detected as high chargeability values which match with the cave bottom (decalcification clays, Chapter 8) or cave walls (metallic mineralized, Chapter 6). Anyway, this is an inaccurate technique that only provides the cave position, but its measurement is performed in conjunction with the resistivity data without too much time acquisition increasing for 4 channels equipment (Brown *et al.*, 2011). Consequently is recommended to take this data to compare with resistivity profiles and then improve the obtained results.

Seismic methods provide consistent results in most of the cave situations. Using refraction methods, as velocity profiles, the caves are detected as low velocity values (Cardarelli *et al.*, 2003 and 2010). Lithological changes in the host rocks are unappreciated for cave detection. Probably the velocity contrasts is lower in gypsum as host rock due to this lithology is less compact than carbonates (Ulugergerli and Akca, 2006). If decalcification clays amount is really high in the cave bottom, this is not well detectable because that zone experience a velocity values increment (Valois *et al.*, 2010). For saturated caves the velocity contrasts are lower and then the cave is less emphasized. As in the other methods, small and deep caves are practically undetectable. Soil humidity conditions are not a determinant feature for this method.

Ray tracing coverage, within refraction seismic methods, becomes the simplest but most effective method for cave detection (Zelt and Smith, 1992). This method provides information about fractures and voids. This zones experience an absence of ray tracing and the voids zones appear as white zones. Thus, for this method only negatively influences the cavity fillings such as decalcification clays or water content. For other

cases the caves are detected as zones with ray absence. Detection of small deep caves turns out to be more complicated due to they can be masked. Nevertheless, this method would be able to detect these caves. The approximate real morphology of the caves are not fitted with this method, which requires to be compared with the combination of other methods as microgravity, ERT or velocity profiles in seismic refraction.

Seismic reflection methods as common offset over instantaneous frequencies detect caves with low frequencies zones (Daniels, 1988). This is a method that only is affected by the cavity fillings and dimensions, like ray tracing coverage method. However it is not a really accurate method due to are only well detectable large and shallow cavities (Chapter 6).

Finally, electromagnetic methods as ground penetrating radar (GPR) detect the top of the caves as hyperbolic reflectors with signal absence under them (Beres *et al.*, 2001; El-Qady, 2005). They can be applied over any lithology in dry conditions to obtain accurate results, whenever this lithology was anisotropic (Carrière *et al.*, 2013). Caves with metallic mineralized at the walls or surrounding them can mask the cave presence in GPR methods, due to these deposits produce strong reflectors. Decalcification clays are not a determining factor for this method because it only detects the cave ceiling. For saturated caves or areas with high clay content, this method is not applicable due to the electromagnetic waves are not transmitted in humidity conditions (Laurens *et al.*, 2002). Therefore, detecting the top of the cave can be disturbed for the water content. Therefore, the soil humidity is a determinant feature due to the method is exclusively applicable to dry soils. The cave dimensions is also important, due to small deep caves are undetectable. Moreover, for caves with different levels (Chapter 6) this method detect only the more shallow level due to under it there is signal absence masking others deeper levels. Only small shallow caves lead the detection of caves deeper and greater.

For cave researches is not only essential the detection of them, but also the estimation of approximate morphology, depth and size. Not all applied methods have enough resolution to provide cave morphologies and most of them have uncertainties that can lead to misinterpretation. Microgravity let create forward models to fit the observed anomaly to the calculated anomaly fitting lithological and cave morphologies. But there are multiple models to fit those anomalies (Zhdanov, 2002). This method requires of other methods to perform a joint interpretation. Electrical resistivity method provides a resistivity map contours with morphologies which can be tested with microgravity models (Chapters 6, 8 and 9). Induced polarization not provide morphology, size or depth of the cave, but it can differentiate zones belong to the caves (Chapters 6 and 8). Velocity profiles in seismic refraction, as electrical resistivity, offers a velocity map contour whose morphologies can be verified with microgravity models or resistivity profiles (Chapter 6). The ray tracing coverage in seismic refraction methods not provide cave morphologies but it provides an estimation of the size and depth. This method discriminates between caves or not from the velocity or resistivity contours. Common offset in seismic reflection also provide morphologies, depth and sizes of the cave, however is a more inaccurate method for this purpose. Mainly this method detects zones with probably to contain caves. Finally, GPR method only detects the top of the cave, and the approximate depth where it is emplaced.

To estimate the cave morphology, depth and size, is enough the combination of two methods as microgravity models joint to electrical resistivity or velocity profiles. Moreover, this combination can be supported by the other methods to estimate safely the cave depth (ray tracing coverage or GPR), distinguish between the presence of cave or not (ray tracing coverage), locate mineralized caves (IP or magnetic) or cave deposits (IP), or pinpoint zones with probably to content caves (common offset over instantaneous

frequencies). The combination of more than 2 methods provides more fitted and trusted results.

The best combination of geophysical techniques is formed by microgravity and ray tracing coverage. Both are very sensitive to cave presence and allow to distinguish between caves and other underground features.

# Chapter 12

## Conclusions/Conclusiones

# CONCLUSIONS

Geophysical methods applied from the surface are the optimal means of detecting and characterizing cavities that lack outside access. However, it is necessary to perform a previous geological survey to identify the settings and main features of a cave. The geological study is decisive to pinpoint the contrast in physical properties that determine responses provided by the geophysical methods.

Cavities are much more than voids located underground. They have numerous individual features: lithological contrasts with respect to the host rock, water content, ferromagnetic metallic mineralization in the cave walls, decalcification clays at the base, soil moisture, and size and depth where the cavity is located. Altogether, these factors are determinant when anticipating the response of each geophysical method applied to cave detection.

In view of all the geophysical techniques used, microgravity stands as the first regional reconnaissance approach, to locate areas most likely containing cavities. The microgravity study should entail an equidistant grid designed according to the size of the expected cavity. This survey will provide the residual anomaly map where gravity minima are shown, probably associated with cavities. Then the minima can be analysed by means of additional geophysical methods to confirm the presence or absence of cavities nearby. For cavities associated with ferromagnetic mineralization, regional magnetic prospecting is a second step towards identifying areas likely to contain cavities.

Geophysical techniques such as electrical tomography, seismic tomography or GPR are applied in a posterior stage of the survey, along profile arrays over the areas identified as gravity minima or magnetic anomalies. Electrical resistivity and velocity profiles provide contour maps with fitted morphologies that must be confirmed by gravity forward

models, which in turn distinguish between the cavity and other structures of the host rock. Induced polarization models only provide locations of cavities when they include decalcification clays in carbonate caves or metallic mineralized walls. Ray tracing coverage in seismic refraction is the most conclusive method overall, as ray absence is caused by the presence of voids. Moreover, this method can approximately locate voids in depth. The common offset in seismic reflection can pinpoint areas probably containing cavities, although it is a less accurate method. Finally, GPR effectively locates the cavity ceiling and gauges its approximate depth.

Taking into account the different techniques and the studied field examples, it is concluded that the geophysical methods that best provide for detection and localization of cavities are microgravity and ray tracing coverage in seismic refraction. If these methods are accompanied with electrical resistivity tomography or velocity profiles in seismic refraction, the morphologies, dimensions and depth of cavities can also be obtained, to be tested at a later date by boreholes.

## CONCLUSIONES

Los métodos geofísicos aplicados desde la superficie son la mejor herramienta para detectar y caracterizar cavidades que no tienen acceso desde el exterior. Sin embargo, es necesario realizar un reconocimiento geológico previo para identificar las características que puede presentar la cavidad y su entorno. El estudio geológico es crucial para conocer el contraste de propiedades físicas que determina la respuesta de los distintos métodos geofísicos.

Las cavidades no solamente se presentan como espacios vacíos emplazados en el subsuelo. Existen características como contrastes litológicos respecto a la roca encajante, contenido en agua, mineralizaciones ferromagnéticas metálicas en sus pareces, arcillas de descalcificación en su base, humedad del suelo, tamaño y profundidad de la cavidad, las cuales hacen variar la respuesta esperada en la detección de dicha cavidad para cada método geofísico aplicado.

De todos los métodos geofísicos aplicados, la microgravimetría se convierte en una primera aproximación de reconocimiento regional para localizar zonas con presencia de cavidades. En este estudio se usa una malla equidistante diseñada en función del tamaño de la cavidad esperada. Este estudio determina un mapa de anomalía residual donde se muestran mínimos gravimétricos posiblemente asociados a cavidades. En un segundo paso, se deberán caracterizar dichos mínimos con otra u otras metodologías geofísicas para confirmar la presencia o no de cavidad. Para cavidades asociadas a mineralizaciones ferromagnéticas metálicas, la prospección magnética se convierte en una segunda técnica regional para identificar zonas susceptibles de contener cavidades.

Métodos geofísicos como tomografía eléctrica, tomografía sísmica o GPR son aplicados en una segunda etapa del estudio a lo largo de perfiles sobre las zonas

identificadas con mínimos gravimétricos o con anomalías magnéticas. Los perfiles eléctricos de resistividad y los perfiles de velocidades ofrecen mapas de contornos con morfologías aproximadamente reales de las cavidades que deberán ser confirmados con modelos gravimétricos. Estos modelos diferenciarán entre cavidad u otras estructuras de la roca encajante. El método de polarización inducida solo ofrece localizaciones de cavidades cuando estas tienen arcillas de descalcificación en cuevas carbonatadas o paredes recubiertas por minerales con elementos metálicos. La cobertura del trazado de rayos en sísmica de refracción es el método más determinante, ya que localiza zonas con ausencia de rayos debidas exclusivamente a la presencia de vacíos. Además, este método localiza aproximadamente en profundidad los huecos. El método de offset común en sísmica de reflexión localiza zonas con posibilidad de contener cavidades, aunque se trata de un método menos preciso. Finalmente, el método de GRP localiza el techo de la cavidad y su profundidad aproximada.

Por todo esto se concluye que los métodos geofísicos que mejor detectan y localizan las cavidades son la microgravimetría y la cobertura de trazado de rayos en sísmica de refracción. Si estos métodos se utilizan combinadamente con tomografía eléctrica de resistividad o perfil de velocidades en tomografía sísmica de refracción, además se podrán obtener morfologías, dimensiones y profundidades de la cavidad, que finalmente deben de ser comprobadas mediante sondeos mecánicos.

# Chapter 13

## Future perspectives

The continuous development of the geophysical methods, its application fields and the progress in inversion and modelling programs will allow obtain more accurate results in the detection and characterization of caves in karst system in the near future. Moreover, the interpretation of the data will be more precise with the advance of new techniques.

Furthermore, the use of the geophysical methods in other geological settings and cave features, as glacier or volcanic caves (primary caves) is not widespread. The touristic interest aroused in this kind of caves makes that its detection through geophysical methods gain importance. However, it will have to take into account the difficulty involving these environments, as the hardness of the ground, equipment transport or inaccessibility.

The integration of geophysical methods calls for the development of joint data treatment. For this purpose, it must develop and optimize joint inversion programs for different types of data. It will be able to make joint inversions in 2D and 3D arrays of microgravity and resistivity data, microgravity and seismic refraction data, and resistivity and seismic refraction data, inter alia. The basis of these programs will lie in computerize the actual observation made by analysis and with the naked eye. The programs divide the half space in areas with similar physical properties in the so-called 'clusters'. In subsequently inversion step these *clusters* are compared in both or several geophysical data until the area delimited match in them. Finally, the joint inversion will separate the areas belong to caves and the areas belong to the host rock or another different geological features. In this way, the analysis conducted by the naked eye will be corroborated for these joint inversions of the geophysical data.

Moreover, the requirement to know theoretical morphologies of the unknown and detected caves from the surface calls for the advance in inversion programs which offers such morphologies following the patterns marked by the geophysical results. The

electrical resistivity tomography and velocity profiles in seismic refraction methods provide theses morphologies more fitted to the real ones. However, in the inversion programs the results has non-unique solution, and the difficulty lies in determine which of the contour interval belongs to the cavity. For this purpose, it will be necessary the advance in inversion programs with microgravity data in 3D array, and its comparison with electrical or seismic data.

The detection and characterization of cavities is essential in civil engineering to assess the ground stability. In addition, the uncover of new cavities and it opening for touristic use, always with the utmost respect to the cave integrity, its environment and surrounding areas, will be another future perspective. In this manner, it will be essential new detailed geophysical surveys which enable the analysis of optimal areas to open and explore the new caves.

The study of cave through geophysical methods awakens a wide range of possibilities which must be addressed in the future. These developments will help to detect cavities more accurately and efficiently.

# Chapter 14

References

Abdelrahman, E., Bayoumi, A., Abdelhady, Y., Gobashy, M., El-Araby, H., 1989. Gravity interpretation using correlation factors between successive least-squares residual anomalies. Geophysics, 54, 1614-1621. doi: 10.1190/1.1442629.

Abdelrahman, E., El-Araby, T., 1993. A least-squares minimization approach to depth determination from moving average residual gravity anomalies. Geophysics, 58, 1779-1784. doi: 10.1190/1.1443392.

Abdelrahman, E.M., El-Araby, T.M., 1996. Shape and depth solutions from moving average residual gravity anomalies. Journal of Applied Geophysics, 36, 89-95. doi: 10.1016/S0926-9851(96)00038-9.

ABEM., 2006. Instruction Manual Terrameter SAS 4000/SAS 1000. ABEM Instrument AB, Sundbyberg, Sweden, 136 pp.

Abu-Shariah, M.I.I., 2009. Determination of cave geometry by using a geoelectrical resistivity inverse model. Engineering Geology, 105, 239-244. doi: 10.1016/j.enggeo.2009.02.006.

Agarwal, B.N.P., Sivaji, C.H., 1992. Separation of regional and residual anomalies by least-squares orthogonal polynomial and relaxation techniques: a performance evaluation. Geophysical Prospecting, 40, 143-156. doi: 10.1111/j.1365-2478.1992.tb00368.x.

Agarwal, B.N.P., Srivastava, S., 2010. A FORTRAN program to implement the method of finite elements to compute regional and residual anomalies from gravity data. Computers, Geosciences, 36, 848-852. doi: 10.1016/j.cageo.2009.11.002.

Agocs, W., 1951. Least squares residual anomaly determination. Geophysics, 16, 686-696. doi: 10.1190/1.1437720.

Al, T.A., Martin, C.J., Blowes, D.W., 2000. Carbonate-mineral/water interactions in sulfide-rich mine tailings. Geochimica et Cosmochimica Acta, 64, 3933-3948. doi: 10.1016/S0016-7037(00)00483-X.

Alastruey, I., Alastruey, J., Ayuso, N., Cuchí, J., Lera, F., Mediano, A., Molina, P., Villarroel, J., Viñals, V., 2002. Inducción magnética y técnicas asociadas en el estudio del karst. Karst and Environment, pp 505-510.

Alberto, W., Giardino, M., Martinotti, G., Tiranti, D., 2008. Geomorphological hazards related to deep dissolution phenomena in the Western Italian Alps: Distribution, assessment and interaction with human activities. Engineering Geology, 99, 147-159. doi: 10.1016/j.enggeo.2007.11.016.

Al-Rawi, F.R., Rezkalla, J.S., 1987. The application of microgravity survey for cave detection in a karstic area. Large Rock Caverns, Proceedings of the International Symposium, Helsinki, Finland, 2, 25-28.

Al-Zoubi, A., Eppelbaum, L., Abueladas, A., Ezersky, M., Akkawi, E., 2013. Removing Regional Trends in Microgravity in Complex Environments: Testing on 3D

Model and Field Investigations in the Eastern Dead Sea Coast (Jordan). International Journal of Geophysics, 2013, 1-13. doi: 10.1155/2013/341797.

Angelucci, D.E., Boschian, G., Fontanals, M., Pedrotti, A., Vergès, J.M., 2009. Shepherds and karst: the use of caves and rock-shelters in the Mediterranean region during the Neolithic. World Archaeology, 41, 191-214. doi: 10.1080/00438240902843659.

Arzi, A., 1975. Microgravimetry for engineering applications. Geophysical Prospecting, 23, 408-425. doi: 10.1111/j.1365-2478.1975.tb01539.x.

Audra, P., Hofmann, B., 2004. Les cavités hypogènes associées aux dépôts de sulfures métalliques (MVT). [Hypogenic cave systems related to metallic sulphide deposits (MVT)]. Le Grotte d'Italia, 5, 35-56.

Aug, C., Chilès, J.-P., Courrioux, G., Lajaunie, C., 2005. 3D Geological Modelling and Uncertainty: The Potential-field Method. In: Leuangthong, O., Deutsch, C. (eds.) Geostatistics Banff, 2004. Springer Netherlands, 145-154.

Auler, A.S., Smart, P.L., 2003. The influence of bedrock-derived acidity in the development of surface and underground karst: evidence from the Precambrian carbonates of semi-arid northeastern Brazil. Earth Surface Processes and Landforms, 28, 157-168. doi: 10.1002/esp.443.

Ballard, R.F., Cuenod, Y., Jenni, J.P., 1982. Detection of karst cavities by geophysical methods. Bulletin of the International Association of Engineering Geology - Bulletin de l'Association Internationale de Géologie de l'Ingénieur, 26-27, 153-157. doi: 10.1007/bf02594210.

Baquero, J.C., Calaforra, J.M., 1992. Sistema de la Cueva del Agua, Sorbas (Almería). Tecno Ambiente, 12, 1-8.

Bard, J.P., Moine, B., 1979. Acebuches amphibolites in the Aracena hercynian metamorphic belt (southwest Spain): Geochemical variations and basaltic affinities. LITHOS, 12, 271-282. doi: 10.1016/0024-4937(79)90018-5.

Bar-Matthews, M., Ayalon, A., Kaufman, A., 1998. Middle to Late Holocene (6,500 Yr. Period) Paleoclimate in the Eastern Mediterranean Region from Stable Isotopic Composition of Speleothems from Soreq Cave, Israel. In: Issar, A., Brown, N. (eds.) Water, Environment and Society in Times of Climatic Change. Springer Netherlands, 203-214.

Beltrão, J., Silva, J., Costa, J., 1991. Robust polynomial fitting method for regional gravity estimation. Geophysics, 56, 80-89. doi: 10.1190/1.1442960.

Beres, M., Luetscher, M., Olivier, R., 2001. Integration of ground-penetrating radar and microgravimetric methods to map shallow caves. Journal of Applied Geophysics, 46, 249-262. doi: 10.1016/S0926-9851(01)00042-8.

Berner, R.A., 1964. Distribution and diagenesis of sulfur in some sediments from the Gulf of California. Marine Geology, 1, 117-140. doi: 10.1016/0025-3227(64)90011-8.

Bernstone, C., Dahlin, T., Ohlsson, T., Hogland, H., 2000. DC-resistivity mapping of internal landfill structures: two pre-excavation surveys. Environmental Geology, 39, 360-371. doi: 10.1007/s002540050015.

Blakely, R.J., 1995. Potential Theory in Gravity and Magnetic Applications. Cambridge University Press, New York, 435pp.

Blížkovský, M., 1979. Processing and applications in microgravity surveys. Geophysical Prospecting, 27, 848-861. doi: 10.1111/j.1365-2478.1979.tb01002.x.

Booth, J., Hong, Q., Compton, R.G., Prout, K., Payne, R.M., 1997. Gypsum overgrowths passivate calcite to acid attack. Journal of colloid and interface science, 192, 207-214. doi: 10.1006/jcis.1997.4978.

Boubaki, N., Saintenoy, A., Tucholka, P., 2011. GPR profiling and electrical resistivity tomography for buried cavity detection: A test site at the abbaye de l'Ouye (France). Advanced Ground Penetrating Radar (IWAGPR), 2011 6th International Workshop on, 1-5.

Bozzo, E., Lombardo, S. and Merlanti, F., 1996. Geophysical studies applied to near-surface karst structures: the dolines. Annals of geophysics, 39, 23-38. doi: 10.4401/ag-3948.

Briggs, I., 1974. Machine contouring using minimum curvature. Geophysics, 39, 39-48. doi: 10.1190/1.1440410.

Brown, W.A., Stafford, K. W., Shaw-Faulkner, M. and Grubbs, A., 2011. A comparative integrated geophysical study of Horseshoe Chimney Cave, Colorado Bend State Park, Texas. International Journal of Speleology, 40, 9-16. doi: 10.5038/1827-806X.40.1.2.

Brune, G., 1965. Anhydrite and gypsum problems in engineering geology. Bulletin Association Engineering Geologists, 3, 26-38.

Butler, D.K., 1984. Microgravimetric and gravity gradient techniques for detection of subsurface cavities. Geophysics, 49, 1084-1096. doi: 10.1190/1.1441723.

Calaforra, J.M., Pulido-Bosch, A., 2003. Evolution of the gypsum karst of Sorbas (SE Spain). Geomorphology, 50, 173-180. doi: 10.1016/S0169-555X(02)00213-1.

Calvari, S., Pinkerton, H., 1998. Formation of lava tubes and extensive flow field during the, 1991–1993 eruption of Mount Etna. Journal of Geophysical Research: Solid Earth, 103, 27291-27301. doi: 10.1029/97jb03388.

Camacho, A.G., Vieira, R., Montesinos, F.G., Cuéllar, V., 1994. A gravimetric 3D Global inversion for cavity detection Geophysical Prospecting, 42, 113-130. doi: 10.1111/j.1365-2478.1994.tb00201.x.

Canakci, H., 2007. Collapse of caves at shallow depth in Gaziantep city center, Turkey: a case study. Environmental Geology, 53, 915-922. doi: 10.1007/s00254-007-0802-y.

Carbó, A., Muñoz-Martín, A., Llanes, P., Álvarez, J., 2003. Gravity analysis offshore the Canary Islands from a systematic survey. In: Clift, P., Acosta, J. (eds.) Geophysics of the Canary Islands. Springer Netherlands, 113-127.

Cardarelli, E., Cercato, M., Cerreto, A., Di Filippo, G., 2010. Electrical resistivity and seismic refraction tomography to detect buried cavities. Geophysical Prospecting, 58, 685-695. doi: 10.1111/j.1365-2478.2009.00854.x.

Cardarelli, E., Marrone, C., Orlando, L., 2003. Evaluation of tunnel stability using integrated geophysical methods. Journal of Applied Geophysics, 52, 93-102. doi: 10.1016/s0926-9851(02)00242-2.

Carpenter, P.J., Ekberg, D.W., 2006. Identification of buried sinkholes, fractures and soil pipes using ground-penetrating radar and 2D electrical resistivity tomography. Proceedings of the Highway Geophysics - NDE Conference, 437-449.

Carrière, S.D., Chalikakis, K., Sénéchal, G., Danquigny, C., Emblanch, C., 2013. Combining Electrical Resistivity Tomography and Ground Penetrating Radar to study geological structuring of karst Unsaturated Zone. Journal of Applied Geophysics, 94, 31-41. doi: 10.1016/j.jappgeo.2013.03.014.

Castro, J.M., Ruiz-Ortiz, P.A., 1991. Nivel condensado con estromatolitos pelágicos en el Cretácico de la Sierra de Estepa (Subbético Externo, provincia de Sevilla. Revista de la Sociedad Geológica de España, 4, 305-319.

Chalikakis, K., Plagnes, V., Guerin, R., Valois, R., Bosch, F.P., 2011. Contribution of geophysical methods to karst-system exploration: an overview. Hydrogeology Journal, 19, 1169-1180. doi: 10.1007/s10040-011-0746-x.

Chambers, J., Meldrum, P., Gunn, D., Wilkinson, P., Kuras, O., Weller, A., Ogilvy, R., 2009. Hydrogeophysical monitoring of landslide processes using automated time-lapse electrical resistivity tomography (ALERT). 15th European Meeting of Environmental and Engineering Geophysics.

Chamon, N., Dobereiner, L., 1988. An example of the use of geophysical methods for the investigation of a cavern in sandstones. Bulletin of the International Association of Engineering Geology - Bulletin de l'Association Internationale de Géologie de l'Ingénieur, 38, 37-43. doi: 10.1007/bf02590446.

Chandra, P.C., Tata, S., Raju, K.C.B., 1987. Geoelectrical response of cavities in limestones: an experimental field study from Kurnool District, Andhra Pradesh, India. Geoexploration, 24, 483-502. doi: 10.1016/0016-7142(87)90017-2.

Chapin, D.A., 1996. A deterministic approach toward isostatic gravity residuals; a case study from South America. Geophysics, 61, 1022-1033. doi: 10.1190/1.1444024.

Chávez, R.E., Flores-Márquez, E.L., Suriñach, E., Galindo-Zaldívar, J., Rodriguez Fernández, J.R., Maldonado, A., 2007. Combined use of the GGSFT data base and on board marine collected data to model the Moho beneath the Powell Basin, Antarctica. Geologica Acta, 5, 323-335.

Chico, R.J., 1964. Detection of caves by gravimetry. International Journal of Speleology, 1, 101-108. doi: 10.5038/1827-806X.1.1.11.

Colley, G.C., 1963. The detection of caves by gravity measurements. Geophysical Prospecting, 11, 1-9. doi: 10.1111/j.1365-2478.1963.tb02019.x.

Cook, J.C., 1965. Seismic mapping of underground cavities using reflection amplitudes. Geophysics, 30, 527-538. doi: 10.1190/1.1439618.

Cook, K.L., Van Nostrand, R.G., 1954. Interpretation of resistivity data over filled sinks. Geophysics, 19, 761-790. doi: 10.1190/1.1438048.

Cooper, A.H., 1986. Subsidence and foundering of strata caused by the dissolution of Permian gypsum in the Ripon and Bedale areas, North Yorkshire (England). The English Zechstein and related topics, 127-139. doi: 10.1144/GSL.SP.1986.022.01.11.

Cooper, A.H., 1995. Subsidence hazards due to the dissolution of Permian gypsum in England: investigation and remediation. Karst geohazards: engineering and environmental problems in karst terrane. Proc. 5th conference, Gatlinburg, 1995, 33, 23-29.

Cooper, A.H., Saunders, J.M., 2002. Road and bridge construction across gypsum karst in England. Engineering Geology, 65, 217-223. doi: 10.1016/S0013-7952(01)00131-4.

Cravotta, C.A., Trahan, M.K., 1999. Limestone drains to increase pH and remove dissolved metals from acidic mine drainage. Applied Geochemistry, 14, 581-606. doi: 10.1016/S0883-2927(98)00066-3.

Crespo-Blanc, A., Campos, J., 2001. Structure and kinematics of the South Iberian paleomargin and its relationship with the Flysch Trough units: extensional tectonics within the Gibraltar Arc fold-and-thrust belt (western Betics). Journal of Structural Geology, 23, 1615-1630. doi: 10.1016/S0191-8141(01)00012-8.

Crespo-Blanc, A., Orozco, M., 1988. The southern Iberian shear zone: a major boundary in the Hercynian folded belt. Tectonophysics, 148, 221-227. doi: 10.1016/0040-1951(88)90130-8.

Cruz-Sanjulian, J., 1977. Formas Kársticas en materiales de pie de monte. Tecniterrae. Revista española de geología y minería, 16, 1-6.

Culver, D.C., White, W.B., 2005. Encyclopedia of caves. Elsevier Amsterdam (The Netherlands).

Dahlin, T., Zhou, B., 2006. Multiple-gradient array measurements for multichannel 2D resistivity imaging. Near Surface Geophysics, 4, 113-123. doi: 10.3997/1873-0604.2005037.

Daniels, D.J., 2004. Ground Penetrating Radar. 2º Edition. The institution of Electrical Engineers. 719 pp., London.

Daniels, J., 1988. Locating caves, tunnels and mines. The leading edge, 7, 32-52. doi: 10.1190/1.1439492.

Davis, D.G., 2000. Extraordinary features of Lechuguilla Cave, Guadalupe Mountains, New Mexico. Journal of Cave and Karst Studies, 62, 147-157.

Davis, J.C., 1986. Statistics and data analysis in geology. Wiley, New York.

De Giorgi, L., Leucci, G., 2014. Detection of Hazardous Cavities Below a Road Using Combined Geophysical Methods. Surveys in Geophysics, 35, 1003-1021. doi: 10.1007/s10712-013-9277-4.

Dean, W., 1958. Frequency analysis for gravity and magnetic interpretation. Geophysics, 23, 97-127. doi: 10.1190/1.1438457.

Debeglia, N., Bitri, A., Thierry, P., 2006. Karst investigations using microgravity and MASW; Application to Orléans, France. Near Surface Geophysics, 4, 215-225. doi: 10.3997/1873-0604.2005046

deGroot-Hedlin, C., Constable, S., 1990. Occam's inversion to generate smooth, two-dimensional models from magnetotelluric data. Geophysics, 55, 1613-1624. doi: 10.1190/1.1442813.

Del Val, J., Henández, M., 1989. El karst en el Macizo Hespérico. In: Durán, J.J., López-Martínez, J. (eds.) El Karst en España. Sociedad Española de Geomorfología, Madrid, 217-229.

Descotes, M., Beaucaire, C., Mercier, F., Savoye, S., Sow, J., Zuddas, P.P., 2002. Effect of carbonate ions on pyrite (FeS2) dissolution. Bulletin - Societe Geologique de France, 3, 265-270. doi: 10.2113/173.3.265.

Dey, A., Morrison, H., 1979. Resistivity modeling for arbitrarily shaped three-dimensional structures. Geophysics, 44, 753-780. doi: 10.1190/1.1440975.

Di Fiore, V., Angelino, A., Passaro, S., Bonanno, A., 2013. High resolution seismic reflection methods to detect near surface tuff-cavities: a case study in the Neapolitan area, Italy. Journal of Cave and Karst Studies, 75, 51-59. doi: 10.4311/2011ES0248.

Díaz Azpiroz, M., Fernández, C., 2005. Kinematic analysis of the southern Iberian shear zone and tectonic evolution of the Acebuches metabasites (SW Variscan Iberian Massif). Tectonics, 24. doi: 10.1029/2004TC001682.

Dobrin, M.B., Savit, C.H., 1960. Introduction to Geophysical Prospecting. McGraw-Hill, New York.

Dronkert, H., 1977. The evaporites of the Sorbas Basin. Rev. Inst. Invest. Geol. Diput. Prov. Barc., 32, 55-76.

Dronkert, H., 1985. Evaporite models and sedimentology of Messinian and recent evaporites. GUA papers of geology. Ser. 1.

Dublyansky, Y., 2014. Hypogene speleogeneis - Discussion of definitions. Hypogene Cave Morphologies, Proceedings of the International Symposium, San Salvador Islands, Bahamas.

Dutta, N., Bose, R., Saikia, B., 1970. Detection of Solution Channels in Limestone by Electrical Resistivity method. Geophysical Prospecting, 18, 405-414. doi: 10.1111/j.1365-2478.1970.tb02121.x.

Egemeier, S.J., 1971. A comparison of two types of solution caves: Unpublished report to Carlsbad Caverns National Park. April, 12, 7.

Egemeier, S.J., 1981. Cavern development by thermal waters. NSS Bull, 43, 31-51.

El-Qady, G., Hafez, M., Abdalla, M.A., Ushijima, K., 2005. Imaging subsurface cavities using geoelectric tomography and ground-penetrating radar. Journal of Cave and Karst Studies, 67, 174-181.

Eppelbaum, L., Ezersky, M., Al-Zoubi, A., Goldshmidt, V., Legchenko, A., 2008. Study of the factors affecting the karst volume assessment in the Dead Sea sinkhole problem using microgravity field analysis and 3-D modeling. Advances in Geosciences, 19, 97-115.

Esteban-Parra, M.J., Rodrigo, F.S., Castro-Díez, Y., 1998. Spatial and temporal patterns of precipitation in Spain for the period 1880-1992. International Journal of Climatology, 18, 1557-1574.

Featherstone, W.E., 1997. On the use of the geoid in geophysics: a case study over the North-West shelf of Australia. Exploration Geophysics, 28, 52-57. doi: 10.1071/EG997052.

Fedi, M., Quarta, T., 1998. Wavelet analysis for the regional-residual and local separation of potential field anomalies. Geophysical Prospecting, 46, 507-525. doi: 10.1046/j.1365-2478.1998.00105.x.

Fernández-Cortés, A., Calaforra, J.M., Jiménez-Espinosa, R., Sánchez-Martos, F., 2006. Geostatistical spatiotemporal analysis of air temperature as an aid to delineating thermal stability zones in a potential show cave: Implications for environmental

management. Journal of Environmental Management, 81, 371-383. doi: 10.1016/j.jenvman.2005.11.011.

Fernandez-Cortes, A., Sanchez-Moral, S., Cañaveras, J.C., Cuevas-Gonzalez, J., Cuezva, S., Andreu, J.M., 2010. Variations in seepage water geochemistry induced by natural and anthropogenic microclimatic changes: Implications for speleothem growth conditions. Geodinamica Acta, 23, 1-13. doi: 10.3166/ga.23.1-13.

Fernández-Rodriguez, C., Díaz Azpiroz, M., 2008. Estructuras de deformación en mármoles: el ejemplo del Cerro del Castillo en Aracena. In: Olías Álvarez, M., et al. (eds.) Geología de Huelva: lugares de interés geológico. 2º Edition. . University of Huelva, Huelva.

Finger, J.T. 1984. Investigation of percussion drills for geothermal applications. Journal of petroleum technology, 36, 2,128-122,136.

Flecha, I., Martí, D., Carbonell, R., Escuder-Viruete, J., Pérez-Estaún, A., 2004. Imaging low-velocity anomalies with the aid of seismic tomography. Tectonophysics, 388, 225-238. doi: 10.1016/j.tecto.2004.04.031.

Flohrer, C., Pöpel, M., 1996. Combination of a covermeter with a GPR-system: a tool for detecting prestressed bars in concrete structures. Proceedings of the Sixth International Conference on Ground Penetrating Radar, pp. 273-277.

Frizon de Lamotte, D., Andrieux, J., Guezou, J.C., 1991. Cinématique des chevauchements néogènes dans l'Arc bético-rifain: discussion sur les modèles géodynamiques. Bulletin - Societe Geologique de France, 162, 611-626.

Fuller, B.D., 1967. Two-dimensional frequency analysis and design of grid operators. Mining Geophysics, 2, 658-708. doi: 10.1190/1.9781560802716.

Galdenzi, S., Menichetti, M., 1995. Occurrence of hypogenic caves in a karst region: Examples from central Italy. Environmental Geology, 26, 39-47. doi: 10.1007/bf00776030.

Gale, S.J., 1984. The hydraulics of conduit flow in carbonate aquifers. Journal of Hydrology, 70, 309-327. doi: 10.1016/0022-1694(84)90129-X.

Galve, J.P., Bonachea, J., Remondo, J., Gutiérrez, F., Guerrero, J., Lucha, P., Cendrero, A., Gutiérrez, M., Sánchez, J.A., 2008. Development and validation of sinkhole susceptibility models in mantled karst settings. A case study from the Ebro valley evaporite karst (NE Spain). Engineering Geology, 99, 185-197. doi: 10.1016/j.enggeo.2007.11.011.

Galve, J.P., Gutiérrez, F., Lucha, P., Bonachea, J., Remondo, J., Cendrero, A., Gutiérrez, M., Gimeno, M.J., Pardo, G., Sánchez, J.A., 2009. Sinkholes in the salt-bearing evaporite karst of the Ebro River valley upstream of Zaragoza city

(NE Spain). Geomorphology, 108, 145-158. doi: 10.1016/j.geomorph.2008.12.018.

Gambetta, M., Armadillo, E., Carmisciano C., Stefanelli, P., Cocchi, L., Tontini, F.C., 2011. Determining geophysical properties of a nearsurface cave through integrated microgravity vertical gradient and electrical resistivity tomography measurements. Journal of Cave and Karst Studies, 73, 11-15. doi: 10.4311/jcks2009ex0091.

García-Hernández, M., López-Garrido, A.C., Rivas, P., Sanz de Galdeano, C., Vera, J.A., 1980. Mesozoic palaeogeographic evolution of the External Zones of the Betic Cordillera. Geologie en Mijnbouw, 59, 155-168.

Garofano, M., Govoni, D., 2012. Underground Geotourism: a Historic and Economic Overview of Show Caves and Show Mines in Italy. Geoheritage, 4, 79-92. doi: 10.1007/s12371-012-0055-3.

Gautam, P., Raj Pant, S., Ando, H., 2000. Mapping of subsurface karst structure with gamma ray and electrical resistivity profiles: a case study from Pokhara valley, central Nepal. Journal of Applied Geophysics, 45, 97-110. doi: 10.1016/S0926-9851(00)00022-7.

Gibson, P.J., Lyle, P. and George D.M., 2004. Application of resistivity and magnetometry geophysical techniques for near-surface investigations in karstic terranes in Ireland. Journal of Cave and Karst Studies, 66, 35-38.

Gómez-Ortiz, D., Martín-Crespo, T., 2012. Assessing the risk of subsidence of a sinkhole collapse using ground penetrating radar and electrical resistivity tomography. Engineering Geology, 149–150, 1-12. doi: 10.1016/j.enggeo.2012.07.022.

Grandjean, G., Leparoux, D., 2004. The potential of seismic methods for detecting cavities and buried objects: experimentation at a test site. Journal of Applied Geophysics, 56, 93-106. doi: 10.1016/j.jappgeo.2004.04.004.

Greenfield, R., 1979. Review of geophysical approaches to the detection of karst. Bulletin of the Association of Engineering Geologist, 16, 393-408.

Griffin, W., 1949. Residual gravity in theory and practice. Geophysics, 14, 39-56. doi: 10.1190/1.1437506.

Grotzinger, J., Jordan, T.H., 2010. Understanding earth. Macmillan.

Guérin, R., Baltassat, J.M., Boucher, M., Chalikakis, K., Galibert, P.Y., Girard, J.F., Plagnes, V., Valois, R., 2009. Geophysical characterisation of karstic networks – Application to the Ouysse system (Poumeyssen, France). Comptes Rendus Geoscience, 341, 810-817. doi: 10.1016/j.crte.2009.08.005.

Guerin, R., Benderitter, Y., 1995. Shallow karst exploration using MT-VLF and DC resistivity methods. Geophysical Prospecting, 43, 635-653. doi: 10.1111/j.1365-2478.1995.tb00272.x.

Guérin, R., Munoz, M.L., Aran, C., Laperrelle, C., Hidra, M., Drouart, E., Grellier, S., 2004. Leachate recirculation: moisture content assessment by means of a geophysical technique. Waste Management, 24, 785-794. doi: 10.1016/j.wasman.2004.03.010.

Gulley, J., 2009. Structural control of englacial conduits in the temperate Matanuska Glacier, Alaska, USA. Journal of Glaciology, 55, 681-690. doi: 10.3189/002214309789470860.

Guo, L., Meng, X., Chen, Z., Li, S., Zheng, Y., 2013. Preferential filtering for gravity anomaly separation. Computers, Geosciences, 51, 247-254. doi: 10.1016/j.cageo.2012.09.012.

Gupta, V.K., Ramani, N., 1980. Some aspects of regional-residual separation of gravity anomalies in a Precambrian terrain. Geophysics, 45, 1412-1426. doi: 10.1190/1.1441130.

Gutiérrez, F., Calaforra, J.M., Cardona, F., Ortí, F., Durán, J.J., Garay, P., 2007. Geological and environmental implications of the evaporite karst in Spain. Environmental Geology, 53, 951-965. doi: 10.1007/s00254-007-0721-y.

Hackney, R.I., Featherstone, W.E., Götze, H.-J., 2004. Regional-residual gravity field separation in the Central Andes using global geopotential models. ASEG Extended Abstracts, 2004, 1-4. doi: 10.1071/ASEG2004ab059.

Hammarstrom, J.M., Sibrell, P.L., Belkin, H.E., 2003. Characterization of limestone reacted with acid-mine drainage in a pulsed limestone bed treatment system at the Friendship Hill National Historical Site, Pennsylvania, USA. Applied Geochemistry, 18, 1705-1721. doi: 10.1016/S0883-2927(03)00105-7.

Hammer, S.I., 1939. Terrain corrections for gravimeters stations. Geophysics, 4, 184-194. doi: 10.1190/1.1440495.

Hammer, S.I., 1982. Critique of terrain corrections for gravity stations. Geophysics, 47, 839-840. doi: 10.1190/1.1441352.

Hancock, P.L., 1985. Brittle microtectonics: principles and practice. Journal of Structural Geology, 7, 437-457. doi: 10.1016/0191-8141(85)90048-3.

Hancock, P.L., Engelder, T., 1989. Neotectonic joints. Geological Society of America Bulletin, 101, 1197-1208.
doi: 10.1130/0016-7606(1989)101<1197:NJ>2.3.CO;2.

Harmon, E.J., Hajicek, M.F., 1992. Schlumberger Soundings and Sand-Column Resistivity Testing for Determining Stream-Aquifer Connection Great Sand Dunes Natl. Monument, Colorado. Symposium on the Application of

Geophysics to Engineering and Environmental Problems, 1992. Society of Exploration Geophysicists, 275-290.

Hayley, K., Bentley, L.R., Gharibi, M., Nightingale, M., 2007. Low temperature dependence of electrical resistivity: Implications for near surface geophysical monitoring. Geophysical Research Letters, 34. doi: 10.1029/2007gl031124.

Henderson, R., 1960. A comprehensive system of automatic computation in magnetic and gravity interpretation. Geophysics, 25, 569-585. doi: 10.1190/1.1438736.

Hill, C.A., 2000. Sulfuric acid, hypogene karst in the Guadalupe Mountains of New Mexico and West Texas (U.S.A.). National Speleological Society, 309-316.

Holub, P., Dumitrescu, T., 1994. Détection des cavités à l'aide de mesures électriques et du géoradar dans une galerie d'amenée d'eau. Journal of Applied Geophysics, 31, 185-195. doi: 10.1016/0926-9851(94)90057-4.

Hose, L.D., Macalady, J.L., 2006. Observations from active sulfidic karst systems: is the present the key to understanding Guadalupe Mountain speleogenesis. Caves and Karst of Southeastern New Mexico: New Mexico Geological Society, Guidebook, 57 Field Conference, 185-194.

Hose, L.D., Pisarowicz, J.A., 1999. Cueva de Villa Luz, Tabasco, Mexico: Reconnaissance study of an active sulfur spring cave and ecosystem. Journal of Cave and Karst Studies, 61, 13-21.

IAGA - International Association of Geomagnetism Aeronomy., 2010. International Geomagnetic Reference Field: the eleventh generation. Geophysical Journal International, 183, 1216-1230. doi: 10.1111/j.1365-246X.2010.04804.x.

IGME - Instituto Geológico y Minero de España., 1997. Mapa aeromagnético de la Península Ibérica - www.igme.es.

IGME - Instituto Geológico y Minero de España., 2006. Proyecto para la aplicación de las aguas subterráneas al abastecimiento mancomunado de los pueblos de la Sierra de Aracena (Huelva). Instituto Tecnológico Geominero de España; Consejería de Obras Públicas y Transportes de la Junta de Andalucía; Consejería de Medioambiente.

Instituto Geográfico Nacional (IGN)., 1975. Mapa de España de Anomalía de Bouguer (Scale 1:1000000).

Instituto Geográfico Nacional (IGN)., 2005. Elevation Digital Model, LiDAR-PNOA.

Izarra, C., 2008. Gravity analysis of Caracas Valley, Venezuela. CSPG CSEG CWLS Convention, 697-700.

Jardani, A., Revil, A., Santos, F., Fauchard, C., Dupont, J.P., 2007. Detection of preferential infiltration pathways in sinkholes using joint inversion of self-

potential and EM-34 conductivity data. Geophysical Prospecting, 55, 749-760. doi: 10.1111/j.1365-2478.2007.00638.x.

Jiménez-Sánchez, M., Stoll, H., Vadillo, I., López-Chicano, M., Domínguez-Cuesta, M., Martín-Rosales, W., Meléndez-Asensio, M., 2008. Groundwater contamination in caves: four case studies in Spain. International Journal of Speleology, 37, 5. doi: 10.5038/1827-806X.37.1.5.

Junta de Andalucía., 2005. Digitain Terrain Model of Andalusia. DVD.

Junta de Andalucía., 2014. Andalusian Positioning Network (RAP). http://www.juntadeandalucia.es/obraspublicasytransportes/redandaluzadeposicionamiento/rap/.

Kaftan, I., Salk, M., Sari, C., 2005. Application of the finite element method to gravity data case study: Western Turkey. Journal of Geodynamics, 39, 431-443. doi: 10.1016/j.jog.2005.04.003.

Kašpar, M., Pecen, J., 1975. Detection of caves in a karst formation by means of electromagnetic waves. Geophysical Prospecting, 23, 611-621. doi: 10.1111/j.1365-2478.1975.tb01548.x

Kaufmann, G., Romanov, D., Nielbock, R., 2011. Cave detection using multiple geophysical methods: Unicorn cave, Harz Mountains, Germany. Geophysics, 76, B71-B77. doi: 10.1190/1.3560245.

Keating, P., Pinet, N., 2011. Use of non-linear filtering for the regional–residual separation of potential field data. Journal of Applied Geophysics, 73, 315-322. doi: 10.1016/j.jappgeo.2011.02.002.

Keller, G.V., Frischknecht, F.C., 1966. Electrical methods in geophysical prospecting. Pergamon Press.

Keydar, S., Pelman, D., Ezersky, M., 2010. Application of seismic diffraction imaging for detecting near-surface inhomogeneities in the Dead Sea area. Journal of Applied Geophysics, 71, 47-52. doi: 10.1016/j.jappgeo.2010.04.001.

Keys, W.S. 1989. Borehole geophysics applied to ground-water investigations. National Water Well Association. Dublin, Ohio.

Keys, W.S. and MacCary, L.M. 1971. Application of borehole geophysics to water-resources investigations. U.S. Geological Survey.

Kirsch, R., 2009. Groundwater Geophysics: A tool for Hydrogeology. Springer.

Klimchouk, A., 2007. Hypogene Speleogenesis: Hydrogeological and Morphogenetic Perspective. National Cave and Karst Research Institute. Special Paper № 1. Carlsbad, NM.

Klimchouk, A., 2009. Morphogenesis of hypogenic caves. Geomorphology, 106, 100-117. doi: 10.1016/j.geomorph.2008.09.013.

Klimchouk, A., Forti, P., Cooper, A.H., 1996. Gypsum karst of the World: a brief overview. International Journal of Speleology, 25, 3-4.

Klimchouk, A.V., 2012. Gypsum Caves. Encyclopedia of Caves. 2nd edition. Ed: D. C. Culver, B. W. White. – Elsevier (USA). pp. 364-373.

Krijgsman, W., Fortuin, A.R., Hilgen, F.J., Sierro, F.J., 2001. Astrochronology for the Messinian Sorbas basin (SE Spain) and orbital (precessional) forcing for evaporite cyclicity. Sedimentary Geology, 140, 43-60. doi: 10.1016/S0037-0738(00)00171-8.

Lange, A.L., 1999. Geophysical studies at Kartchner Caverns State Park, Arizona. Journal of Cave and Karst Studies, 61, 68-72.

Laurens, S., Balayssac, J.-P., Rhazi, J., Arliguie, G., 2002. Influence of concrete relative humidity on the amplitude of Ground-Penetrating Radar (GPR) signal. Materials and Structures, 35, 198-203. doi: 10.1007/BF02533080.

Lazzari, M., Loperte, A., Perrone, A., 2010. Near surface geophysics techniques and geomorphological approach to reconstruct the hazard cave map in historical and urban areas. Adv. Geosci., 24, 35-44. doi: 10.5194/adgeo-24-35-2010.

Lee, K.F., 2011. A Case Study of Ground Penetrating Radar for Non-Destructive Testing Applied to Underground Culvert Structures. Journal of Emerging Trends in Engineering and Applied Sciences (JETEAS), 2, 1079-1082.

Leucci, G., 2006. Contribution of Ground Penetrating Radar and Electrical Resistivity Tomography to identify the cavity and fractures under the main Church in Botrugno (Lecce, Italy). Journal of Archaeological Science, 33, 1194-1204. doi: 10.1016/j.jas.2005.12.009.

Leucci, G., De Giorgi, L., 2005. Integrated geophysical surveys to assess the structural conditions of a karstic cave of archaeological importance. Nat. Hazards Earth Syst. Sci., 5, 17-22. doi: 10.5194/nhess-5-17-2005.

Leucci, G., De Giorgi, L., 2010. Microgravimetric and ground penetrating radar geophysical methods to map the shallow karstic cavities network in a coastal area (Marina Di Capilungo, Lecce, Italy). Exploration Geophysics, 41, 178-188. doi: 10.1071/EG09029.

Li, Y., Oldenburg, D., 1998. Separation of regional and residual magnetic field data. Geophysics, 63, 431-439. doi: 10.1190/1.1444343.

Lodolo, E., Lippai, H., Tassone, A., Zanolla, C., Menichetti, M., Hormaechea, J.-L., 2007. Gravity map of The Isla Grande de Tierra del Fuego and morphology of Lago Fagnano. Geologica Acta, 5.

Loke, M.H., 1994. The inversion of two-dimensional resistivity data. PhD Thesis, University of Birminghan.

Loke, M.H., 2002. Rapid 2D resistivity forward modeling using the finite-difference and finite-element methods. RES2Dmod v3.0 software. Geotomo Software Company.

Loke, M.H., 2014. Tutorial: 2-D and 3-D Electrical Imaging Surveys. Geotomo Software Company.

Loke, M.H., Acworth, I., Dahlin, T., 2003. A comparison of smooth and blocky inversion methods in 2D electrical imaging surveys. Exploration Geophysics, 34, 182-187. doi: 10.1071/EG03182.

Lopez Chicano, M., Martín-Rosales, W., Vadillo, I., 2010. Caracterización hidrogeoquímica de la Gruta de las Maravillas (Aracena, Huelva, España). In: Durán, J.J., Carrasco, F. (eds.) Cuevas: Patrimonio, Naturaleza, Cultura y Turismo. Asociación de Cuevas Turísticas Españolas, Madrid, 143-158.

Mallick, K., Sharma, K.K., 1999. A finite element method for computation of the regional gravity anomaly. Geophysics, 64, 461-469. doi: 10.1190/1.1444551.

Manzanilla, L., Barba, L., Chávez, R., Tejero, A., Cifuentes, G., Peralta, N., 1994. Caves and geophysics: an approximation to the underworld of Teotihuacan, Mexico. Archaeometry, 36, 141-157. doi: 10.1111/j.1475-4754.1994.tb01070.x.

Marcotte, D., Chouteau, M., 1993. Gravity Data Transformation by Kriging. In: Soares, A. (ed.) Geostatistics Tróia ’92. Springer Netherlands, 249-260.

Marescot, L., Loke, M.H., Chapellier, D., Delaloye, R., Lambiel, C., Reynard, E., 2003. Assessing reliability of 2D resistivity imaging in mountain permafrost studies using the depth of investigation index method. Near Surface Geophysics, 1, 57-67. doi: 10.3997/1873-0604.2002007

Martín, A., Núñez, M.A., Gili, J.A., Anquela, A.B., 2011. A comparison of robust polynomial fitting, global geopotential model and spectral analysis for regional–residual gravity field separation in the Doñana National Park (Spain). Journal of Applied Geophysics, 75, 327-337. doi: 10.1016/j.jappgeo.2011.06.037.

Martínez i Rius, A., 1992. Topografía espeleológica, Federación española de espeleología. Badalona, 1992.

Martínez-Moreno, F.J., Galindo-Zaldívar, J., Pedrera, A., Teixido, T., Ruano, P., Peña, J.A., González-Castillo, L., Ruiz-Constán, A., López-Chicano, M., Martín-Rosales, W., 2014. Integrated geophysical methods for studying the karst system of Gruta de las Maravillas (Aracena, Southwest Spain). Journal of Applied Geophysics, 107, 149-162. doi: 10.1016/j.jappgeo.2014.05.021.

Martínez-Moreno, F.J., Pedrera, A., Ruano, P., Galindo-Zaldívar, J., Martos-Rosillo, S., González-Castillo, L., Sánchez-Úbeda, J.P., Marín-Lechado, C., 2013. Combined microgravity, electrical resistivity tomography and induced

polarization to detect deeply buried caves: Algaidilla cave (Southern Spain). Engineering Geology, 162, 67-78. doi: 10.1016/j.enggeo.2013.05.008.

Martínez-Pagán, P., Gómez-Ortiz, D., Martín-Crespo, T., Manteca, J.I., Rosique, M., 2013. The electrical resistivity tomography method in the detection of shallow mining cavities. A case study on the Victoria Cave, Cartagena (SE Spain). Engineering Geology, 156, 1-10. doi: 10.1016/j.enggeo.2013.01.013.

Martín-Rosales, W., López-Chicano, M., Calaforra, J.M., Lauritzen, S.E., Rodríguez-Navarro, C.M., 2008. La Gruta de las Maravillas. In: Calaforra, J.M., Berrocal, J.A. (eds.) El Karst de Andalucía, Geoespeleología, Bioespeleología y Presencia Humana. Consejería de Medio Ambiente de la Junta de Andalucía, Sevilla (Spain), 209-215.

Martín-Rosales, W., Lopez-Chicano, M., Rodríguez Navarro, C.M., Pulido-Bosch, A., 1995. Morfología, Espeleotemas y Climatología de la "Gruta de las Maravillas" (Aracena, Huelva). Espeleotemas, 5, 51-62.

Martín-Rosales, W., López-Chicano, M., Vallejos, A., Pulido-Bosch, A., Calaforra, J.M., Gómez Jiménez, I., Rodríguez Navarro, C.M., 1999. Explotación turística y conservación de la Gruta de las Maravillas. Aracena (Huelva). XII Jornadas del Patrimonio de la Comarca de la Sierra. Aracena (Huelva), Diputación Provincial, 645-662.

Martín-Rosales, W., Romero-Bomba, E., López-Chicano, M., Guerra, M., 2012. Efectos de la gestión ambiental sobre la distribución temporal de los visitantes de la Gruta de las Maravillas (Aracena, Huelva, España). In: Durán, J.J., Robledo, P.A. (eds.) Las cuevas turísticas como activos económicos: conservación e innovación Asociación de Cuevas Turísticas Españolas (ACTE), Madrid, 448 pp.

Martos-Rosillo, S., 2008. Investigación hidrogeológica orientada a la gestión racional de acuíferos carbonáticos sometidos a un uso intensivo del agua subterránea. El caso de la Sierra de Estepa (Sevilla).PhD Thesis, Universidad de Granada.

Martos-Rosillo, S., Rodríguez-Rodríguez, M., Moral, F., Cruz-Sanjulián, J., Rubio, J., 2009. Analysis of groundwater mining in two carbonate aquifers in Sierra de Estepa (SE Spain) based on hydrodynamic and hydrochemical data. Hydrogeology Journal, 17, 1617-1627. doi: 10.1007/s10040-009-0464-9.

Martos-Rosillo, S., Rodríguez-Rodríguez, M., Pedrera, A., Cruz-Sanjulian, J., Rubio, J.C., 2013. Quantifying the groundwater recharge in semiarid carbonate aquifers with an intensive use: the Estepa range aquifers (Seville, South of Spain). Environmental Earth Sciences, 70, 2453–2468. doi:10.1007/s12665-013-2288-0.

McCann, D.M., Jackson, P.D., Culshaw, M.G., 1987. The use of geophysical surveying methods in the detection of natural cavities and mineshafts. Quarterly Journal of

Engineering Geology and Hydrogeology, 20, 59-73. doi: 10.1144/gsl.qjeg.1987.020.01.06.

McGrath, R.J., Styles, P., Thomas, E., Neale, S., 2002. Integrated high-resolution geophysical investigations as potential tools for water resource investigations in karst terrain. Environmental Geology, 42, 552-557. doi: 10.1007/s00254-001-0519-2.

McGraw, T.J., 2010. Assessment of Ground- Penetrating Radar and comparison with Resistivity for detecting subsurface cavities within karst topography in North-Central Ohio. Thesis of College of Bowling Green, State University of Ohio.

McMechan, G.A., Loucks, R.G., Zeng, X., Mescher, P., 1998. Ground penetrating radar imaging of a collapsed paleocave system in the Ellenburger dolomite, central Texas. Journal of Applied Geophysics, 39, 1-10. doi: 10.1016/S0926-9851(98)00004-4.

Mickus, K., Aiken, C., Kennedy, W., 1991. Regional-residual gravity anomaly separation using the minimum-curvature technique. Geophysics, 56, 279-283. doi: 10.1190/1.1443041.

Militzer, H., Rösler, R., Lösch, W., 1979. Theoretical and experimental investigations for cavity research with geoelectrical resistivity methods. Geophysical Prospecting, 27, 640-652. doi: 10.1111/j.1365-2478.1979.tb00991.x

Mochales, T., Casas, A.M., Pueyo, E.L., Pueyo, O., Román, M.T., Pocoví, A., Soriano, M.A., Ansón, D., 2008. Detection of underground cavities by combining gravity, magnetic and ground penetrating radar surveys: a case study from the Zaragoza area, NE Spain. Environmental Geology, 53, 1067-1077. doi: 10.1007/s00254-007-0733-7.

Molina, J.M., 1987. Análisis de facies del Mesozoico en el Subbético Externo (provincia de Córdoba y sur de Jaen). PhD Thesis, Universidad de Granada, 518 pp.

Montesinos, F.G., Camacho, A.G., Vieira, R., 1999. Analysis of gravimetric anomalies in Furnas caldera (São Miguel, Azores). Journal of volcanology and geothermal research, 92, 67-81. doi: 10.1016/S0377-0273(99)00068-2.

Montoriol-Pous, J., 1973. Sobre la tipología vulcanoespeleológica. Acta III Simposium Epeleología. Mataró, 268-273.

Moore, D.G., 1954. Origin and development of sea caves. National Speleological Society Bulletin, 16, 71-76.

Moore, G.W., Nicholas, B.G., 1967. Speleology: the study of caves.

Murphy, P., Westerman, A.R., Clark, R., Booth, A., Parr, A., 2008. Enhancing understanding of breakdown and collapse in the Yorkshire Dales using ground

penetrating radar on cave sediments. Engineering Geology, 99, 160-168. doi: 10.1016/j.enggeo.2007.11.015.

Nettleton, L.L., 1971. Elementary Gravity and Magnetics for Geologists and Seismologists. Society of Exploration Geophisicists (SEG Books).

Neumann, R., 1967. La gravimetrie de haute precision application aux recherches de cavites. Geophysical Prospecting, 15, 116-134. doi: 10.1111/j.1365-2478.1967.tb01776.x.

Nicholson, R.V., Gillham, R.W., Reardon, E.J., 1988. Pyrite oxidation in carbonate-buffered solution: 1. Experimental kinetics. Geochimica et Cosmochimica Acta, 52, 1077-1085. doi: 10.1016/0016-7037(88)90262-1.

Nicod, J., 1993. Recherches nouvelles sur les karts des gypses et des évaporites associeés. Karstologia, 21, 15-30.

Nitescu, B., Cruden, A.R., Bailey, R.C., 2003. Topography of the crust–mantle interface under the Western Superior craton from gravity data. Canadian Journal of Earth Sciences, 40, 1307-1320. doi: 10.1139/e03-042.

Noel, M., Xu, B., 1992. Cave detection using electrical resistivity tomography. Cave Science, 19, 91-94.

Ojo, S.B., Kangkolo, R., 1997. Shortcomings in the determination of regional fields by polynomial fitting: A simple solution. Journal of Applied Geophysics, 36, 205-212. doi: 10.1016/S0926-9851(96)00043-2.

Oldenburg, D.W., Li, Y., 1999. Estimating depth of investigation in dc resistivity and IP surveys. Geophysics, 64, 403-416. doi: 10.1190/1.1444545.

Onac, B.P., Wynn, J.G., Sumrall, J.B., 2011. Tracing the sources of cave sulfates: a unique case from Cerna Valley, Romania. Chemical Geology, 288, 105-114. doi: 10.1016/j.chemgeo.2011.07.006.

Orlando, L., 2013. GPR to constrain ERT data inversion in cavity searching: Theoretical and practical applications in archeology. Journal of Applied Geophysics, 89, 35-47. doi: 10.1016/j.jappgeo.2012.11.006.

Ortega, A.I., Benito-Calvo, A., Porres, J., Pérez-González, A., Martín Merino, M.A., 2010. Applying electrical resistivity tomography to the identification of endokarstic geometries in the Pleistocene Sites of the Sierra de Atapuerca (Burgos, Spain). Archaeological Prospection, 17, 233-245. doi: 10.1002/arp.392.

Owen, T.E., 1983. Detection and mapping of tunnels and caves. A.A Fitch (Ed.), Developments in Geophysical Exploration Methods, 5, 161-258.

Palacky, G.J., 1987. Resistivity characteristics of geological targets. E.B. Neitzel (Ed.), Electromagnetic Methods in Applied Geophysics—Theory, Vol. 1, Investigations in Geophysics Series, vol. 3, 53-129 (USA).

Palmer, A.N., 1991. Origin and morphology of limestone caves. Geological Society of America Bulletin, 103, 1-21. doi: 10.1130/0016-7606(1991)103<0001:oamolc>2.3.co;2.

Palmer, A.N., 2006. Support for a sulfuric acid origin for caves in the Guadalupe Mountains, New Mexico. 57º Field Conference, Caves and Karst of Southeastern New Mexico, 195-202.

Palmer, A.N., 2011. Distinction between epigenic and hypogenic maze caves. Geomorphology, 134, 9-22. doi: 10.1016/j.geomorph.2011.03.014.

Palmer, A.N., Palmer, M.V., 2000. Hydrochemical interpretation of cave patterns in the Guadalupe Mountains, New Mexico. Journal of Cave and Karst Studies, 62, 91-108.

Pánek, T., Margielewski, W., Tábořík, P., Urban, J., Hradecký, J., Szura, C., 2010. Gravitationally induced caves and other discontinuities detected by 2D electrical resistivity tomography: Case studies from the Polish Flysch Carpathians. Geomorphology, 123, 165-180. doi: 10.1016/j.geomorph.2010.07.008.

Paukštys, B., Cooper, A.H., Arustiene, J., 1999. Planning for gypsum geohazards in Lithuania and England. Engineering Geology, 52, 93-103. doi: 10.1016/S0013-7952(98)00061-1.

Pawlowski, R.S., 1994. Green's equivalent-layer concept in gravity band-pass filter design. Geophysics, 59, 69-76. doi: 10.1190/1.1443535.

Pedley, R.C., Busby, J. P., Dabeck, Z. K., 1993. GRAVMAG User Manual - Interactive 2.5D gravity and magnetic modelling. British Geological Survey, Technical Report.

Pedrera, A., Marín-Lechado, C., Martos-Rosillo, S., Roldán, F.J., 2012. Curved fold-and-thrust accretion during the extrusion of a synorogenic viscous allochthonous sheet: The Estepa Range (External Zones, Western Betic Cordillera, Spain). Tectonics, 31, n/a-n/a. doi: 10.1029/2012tc003119.

Pellicer, X.M., Zarroca, M., Gibson, P., 2012. Time-lapse resistivity analysis of Quaternary sediments in the Midlands of Ireland. Journal of Applied Geophysics, 82, 46-58. doi: 10.1016/j.jappgeo.2012.02.009.

Peters, L., 1949. The direct approach to magnetic interpretation and its practical application. Geophysics, 14, 290-320. doi: 10.1190/1.1437537.

Peterson, D., McKenzie, G., 1968. Observations of a Glacier Cave in Glacier Bay National Monument, Alaska. Bulletin of the National Speleological Society, 30, 47-54.

Piscitelli, S., Rizzo, E., Cristallo, F., Lapenna, V., Crocco, L., Persico, R., Soldovieri, F., 2007. GPR and microwave tomography for detecting shallow cavities in the

historical area of ‘‘Sassi of Matera’’(southern Italy). Near Surface Geophysics, 5, 275-284. doi: 10.3997/1873-0604.2007009

Polyak, V.J., McIntosh, W.C., Güven, N., Provencio, P., 1998. Age and origin of Carlsbad Cavern and related caves from 40Ar/39Ar of alunite. Science, 279, 1919-1922. doi: 10.1126/science.279.5358.1919.

Poupelloz, B., Toulemont, M., 1981. Stabilisation des terrains karstiques par injection le cas du lutetien gypseux de la region de Paris. Bulletin of the International Association of Engineering Geology - Bulletin de l'Association Internationale de Géologie de l'Ingénieur, 24, 111-123. doi: 10.1007/bf02595262.

Prokhorenko, V., Ivashchuk, V., Korsun, S., Stefanyshyn, I., 2006. Ground Penetrating Radar Survey in Podil’lya Karst Area. 11th International Conference on Ground Penetrating Radar, Columbus Ohio, USA.

Pulido-Bosch, A., Calaforra, J.M., Pulido-Leboeuf, P., Torres-García, S., 2004. Impact of quarrying gypsum in a semidesert karstic area (Sorbas, SE Spain). Environmental Geology, 46. doi: 10.1007/s00254-004-1062-8.

Pulido-Bosch, A., Martín-Rosales, W., López-Chicano, M., Rodríguez-Navarro, C.M., Vallejos, A., 1997. Human impact in a tourist karstic cave (Aracena, Spain). Environmental Geology, 31, 142-149. doi: 10.1007/s002540050173.

Rădulescu, V., Rădulescu, F., Diacopolos, C., Popescu, M., 2007. Geoelectrical study for delineating underground cavities in karst areas. Geo-Eco-Marina, 13, 89-95.

Rao, B.S., Radhakrishnamurthy, I.V., 1965. Some remarks concerning residuals and derivatives. Pure and applied geophysics, 61, 5-16. doi: 10.1007/bf00875755.

Ravbar, N., Kovačič, G., 2010. Characterisation of karst areas using multiple geo-science techniques, a case study from SW Slovenia. Acta Carsologica, 39, 51-60.

Rechtien, R.D., Stewart, D.M., 1975. A seismic investigation over a near-surface cavern. Geoexploration, 13, 235-245. doi: 10.1016/0016-7142(75)90026-5.

Revil, A., Cathles, L., Losh, S., Nunn, J., 1998. Electrical conductivity in shaly sands with geophysical applications. Journal of Geophysical Research: Solid Earth (1978–2012), 103, 23925-23936. doi: 10.1029/98JB02125.

Riddle, G.I., Riddle, C. J., Schmitt, R.D., 2010. ERT and Seismic Tomography in Identifying Subsurface Cavities GeoCanada - Working with the Earth.

Robert, A., de Bosset, C., 1994. Application du géoradar à la localisation de cavités, de nids de gravier et de zones karstiques. Journal of Applied Geophysics, 31, 197-204. doi: 10.1016/0926-9851(94)90058-2.

Robert, T., Dassargues, A., Brouyère, S., Kaufmann, O., Hallet, V., Nguyen, F., 2011. Assessing the contribution of electrical resistivity tomography (ERT) and self-

potential (SP) methods for a water well drilling program in fractured/karstified limestones. Journal of Applied Geophysics, 75, 42-53. doi: 10.1016/j.jappgeo.2011.06.008.

Rodriguez Castillo, R., Reyes Gutierrez, R., 1992. Resistivity identification of shallow mining cavities in Real del Monte, México. Engineering Geology, 33, 141-149. doi: 10.1016/0013-7952(92)90005-J.

Romero Bomba, E., Portero Moreno, J.R., Romero de la Osa Fernandez, O., Rodríguez García, M., Orquín Sánchez, J., 2010. La Gruta de las Maravillas, una mirada hacia su historia. In: Durán, J.J., Carrasco, F. (eds.) Cuevas: Patrimonio, Naturaleza, Cultura y Turismo. Asociación de Cuevas Turísticas Españolas, Madrid, 9-20.

Ruiz-Constán, A., Pedrera, A., Galindo-Zaldívar, J., Pous, J., Arzate, J., Roldán-García, F.J., Marin-Lechado, C., Anahnah, F., 2012. Constraints on the frontal crustal structure of a continental collision from an integrated geophysical research: The central-western Betic Cordillera (SW Spain). Geochemistry, Geophysics, Geosystems, 13, Q08012. doi: 10.1029/2012gc004153.

Rybakov, M., Goldshmidt, V., Fleischer, L., Rotstein, Y., 2001. Cave detection and 4-D monitoring: a microgravity case history near the Dead Sea. The leading edge, 20, 896-900. doi: 10.1190/1.1487303.

Rybakov, M., Rotstein, Y., Shirman, B., Al-Zoubi, A., 2005. Cave detection near the Dead Sea - a micromagnetic feasibility study. The leading edge, 24, 585-590. doi: 10.1190/1.1946210.

Sanchez Martos, F., Bosch, A.P., Calaforra, J.M., 1999. Hydrogeochemical processes in an arid region of Europe (Almeria, SE Spain). Applied Geochemistry, 14, 735-745. doi: 10.1016/S0883-2927(98)00094-8.

Sarma, G.S., Gadhinglajkar, V.R., Mallick, K., 1993. Finite element simulation of bright-spot structures. Journal Association of Exploration Geophysicists, 14, 43-47.

Sasaki, Y., 1992. Resolution of resistivity tomography inferred from numerical simulation. Geophysical Prospecting, 40, 453-463. doi: 10.1111/j.1365-2478.1992.tb00536.x.

Sedighi, M., Tabatabaee, S., Najafi-Alamdari, M., 2009. Comparison of different gravity field implied density models of the topography. Acta Geophysica, 57, 257-270. doi: 10.2478/s11600-008-0069-z.

Shackleton, E.H., 1911. The heart of the Antarctic: being the story of the British Antarctic Expedition, 1907-1909. W. Heinemann.

Shi, W., Morgan, F.D., Wharton, A.E., 1997. Application of electrical resistivity tomography to image Harrison Caves in Barbados, West Indies. SEG Technical Program Expanded Abstracts, 1997, 350-353. doi: 10.1190/1.1886100.

Simancas, J., Carbonell, R., Lodeiro, F.G., Estaun, A.P., Juhlin, C., Ayarza, P., Kashubin, A., Azor, A., Poyatos, D.M., Sáez, R., 2006. Transpressional collision tectonics and mantle plume dynamics: the Variscides of southwestern Iberia. Geological Society, London, Memoirs, 32, 345-354. doi: 10.1144/GSL.MEM.2006.032.01.21.

Simón, J.L., Soriano, M.A., Pocoví, A., Arlegui, L.E., Casas, A.M., Arancha Luzón, C.L.L., Pérez, A., Pueyo, Ó., Pueyo, E., Mochales, T., Gracia Abadías, F.J., Ansón, D., 2009. Riesgo de subsidencia kárstica en áreas urbanas: el caso de Zaragoza. Enseñanza de las Ciencias de la Tierra, 17.3, 303-315.

Simpson, S.M., 1954. Least squares polynomial fitting to gravitational data and density plotting by digital computers. Geophysics, 19, 255-269. doi: 10.1190/1.1437990.

Sjöberg, R., 1986. Caves indicating neotectonic activity in Sweden. Geografiska Annaler. Series A. Physical Geography, 393-398.

Skeels, D., 1967. What is residual gravity? Geophysics, 32, 872-876. doi: 10.1190/1.1439896.

Smith, D.L., 1986. Application of the pole-dipole resistivity technique to the detection of solution cavities beneath highways. Geophysics, 51, 833-837. doi: 10.1190/1.1442135.

Smith, D.L., Randazzo, A.F., 1975. Detection of subsurface solution cavities in Florida using electrical resistivity measurements. SouSoutheastern Geology, 16, 227-240.

Smith, G., 2007. Tectonic and talus caves at Pilchers Mountain. New South Wales, 11-20.

Spiegel, R., Sturdivant, V., Owen, T., 1980. Modeling resistivity anomalies from localized voids under irregular terrain. Geophysics, 45, 1164-1183. doi: 10.1190/1.1441115.

Steeples, D.W., Knapp, R.W., McElwee, C.D., 1986. Seismic reflection investigations of sinkholes Interstate Highway 70 in Kansas. Geophysics, 51, 295-301. doi: 10.1190/1.1442089.

Stern, T.A., 1979. Regional and residual gravity fields, central North Island, New Zealand. New Zealand Journal of Geology and Geophysics, 22, 479-485. doi: 10.1080/00288306.1979.10424156.

Swain, C.J., 1976. A FORTRAN IV program for interpolating irregularly spaced data using the difference equations for minimum curvature. Computers, Geosciences, 1, 231-240. doi: 10.1016/0098-3004(76)90071-6.

Swartz, C., 1954. Some geometrical properties of residual maps. Geophysics, 19, 46-70. doi: 10.1190/1.1437970.

Teixidó, T., 2000. Caracterización del subsuelo mediante sísmica de reflexión de alta resolución. PhD Univestity of Barcelona, Spain. .

Tennyson, R., Terry, J., Brahana, V., Hays, P.D., Pollock, E., 2008. Tectonic control of hypogene speleogenesis in the southern Ozarks -- Implications for NAWQA and beyond. U.S. Geological Survey Scientific Investigations Report, 2008-5023, 142 p.

Thierry, P., Debeblia, N., Bitri, A., 2005. Geophysical and geological characterisation of karst hazards in urban environments: application to Orléans (France). Bulletin of Engineering Geology and the Environment, 64, 139-150. doi: 10.1007/s10064-004-0247-4.

Thurston, J.B., Brown, J., 1992. The filtering characteristics of least-squares polynomial approximation. Canadian Journal of Exploration Geophysics, 28, 71-80.

Tisato, N., Sauro, F., Bernasconi, S.M., Bruijn, R.H., De Waele, J., 2012. Hypogenic contribution to speleogenesis in a predominant epigenic karst system: A case study from the Venetian Alps, Italy. Geomorphology, 151, 156-163. doi: 10.1016/j.geomorph.2012.01.025.

Ulugergerli, E., Akca, I., 2006. Detection of cavities in gypsum. Journal of Balkan geophysical society, 9, 8-19.

Vadillo, I., Benavente, J., Neukum, C., Grützner, C., Carrasco, F., Azzam, R., Liñán, C., Reicherter, K., 2012. Surface geophysics and borehole inspection as an aid to characterizing karst voids and vadose ventilation patterns (Nerja research site, S. Spain). Journal of Applied Geophysics, 82, 153-162. doi: 10.1016/j.jappgeo.2012.03.006.

Vaks, A., Bar-Matthews, M., Ayalon, A., Schilman, B., Gilmour, M., Hawkesworth, C.J., Frumkin, A., Kaufman, A., Matthews, A., 2003. Paleoclimate reconstruction based on the timing of speleothem growth and oxygen and carbon isotope composition in a cave located in the rain shadow in Israel. Quaternary Research, 59, 182-193. doi: 10.1016/S0033-5894(03)00013-9.

Valois, R., Bermejo, L., Guérin, R., Hinguant, S., Pigeaud, R., Rodet, J., 2010. Karstic morphologies identified with geophysics around Saulges caves (Mayenne, France). Archaeological Prospection, 17, 151-160. doi: 10.1002/arp.385.

Van Camp, M., Meus, P., Quinif, Y., Kaufmann, O., Ruymbeke, M., Vandiepenbeck, M., Camelbeeck, T., 2006. Karst aquifer investigation using absolute gravity. Eos, Transactions American Geophysical Union, 87, 298-298. doi: 10.1029/2006EO300005.

Vargemezis, G., Tsourlos, P., Papazachos, C., Kostopoulos, D., 2007. Application of electrical resistivity tomography to the detection of the Ermakia (Northern Greece) cavity system. Bulletin of the Geological Society of Greece XXXX, Proceedings of the 11th International Congress, Athens.

Vera, J.A., Martín-Algarra, A., 2004. Cordillera Bética y Baleares. J.A. Vera (Ed.), Geología de España (2004).

Vincenz, S., 1968. Resistivity investigations of limestone aquifers in Jamaica. Geophysics, 33, 980-994. doi: 10.1190/1.1439992.

Vogelsang, D., 1987. Examples of electromagnetic prospecting for karst and fault systems. Geophysical Prospecting, 35, 604-617. doi: 10.1111/j.1365-2478.1987.tb00838.x

Vouillamoz, J.M., Legchenko, A., Albouy, Y., Bakalowicz, M., Baltassat, J.M., Al-Fares, W., 2003. Localization of saturated karst aquifer with magnetic resonance sounding and resitivity imagery. Groundwater, 41, 578-586. doi: 10.1111/j.1745-6584.2003.tb02396.x.

Waters, A.C., Donnelly-Nolan, J.M., Rogers, B.W., 1990. Selected caves and lava-tube systems in and near Lava Beds National Monument, California. U.S. Geologycal Survey Bulletin.

Webring, M.E., 1981. Minc, a gridding program based on minimum curvature. U. S. Department of the Interior, Geological Survey, open-file rep. , 81-1224.

Weiland, W.L., 1989. Integrated approach to gravity anomaly separation by geologic stripping. In:, 1989 SEG Annual Meeting. Society of Exploration Geophysicists, 325-328.

Wessel, P., 1998. An Empirical Method for Optimal Robust Regional-Residual Separation of Geophysical Data. Mathematical Geology, 30, 391-408. doi: 10.1023/a:1021744224009.

White, W.B., Culver, D.C., Herman, J.S., Kane, T.C., Mylroie, J.E., 1995. Karst lands. American Scientist, 83, 450-459.

Wilkins, S.J., Compton, R.G., Taylor, M.A., Viles, H.A., 2001. Channel flow cell studies of the inhibiting action of gypsum on the dissolution kinetics of calcite: a laboratory approach with implications for field monitoring. Journal of colloid and interface science, 236, 354-361. doi: 10.1006/jcis.2000.7418.

Worthington, P.F., 1976. Hydrogeophysical Equivalence of Water Salinity, Porosity and Matrix Conduction in Arenaceous Aquifers. Ground Water, 14, 224-232. doi: 10.1111/j.1745-6584.1976.tb03107.x.

Wren, E.A., 1973. Trend surface analysis - a review. Journal of the Canadian Society of Exploration Geophysics, 9, 39-44.

Xia, J., Nyquist, J.E., Xu, Y., Roth, M.J.S., Miller, R.D., 2007. Feasibility of detecting near-surface feature with Rayleigh-wave diffraction. Journal of Applied Geophysics, 62, 244-253. doi: 10.1016/j.jappgeo.2006.12.002.

Xu, X., Zeng, Q., Li, D., Wu, J., Wu, X., Shen, J., 2010. GPR detection of several common subsurface voids inside dikes and dams. Engineering Geology, 111, 31-42. doi: 10.1016/j.enggeo.2009.12.001.

Xu, Y., Hao, T., Li, Z., Duan, Q., Lili, Z., 2009. Regional gravity anomaly separation using wavelet transform and spectrum analysis. Journal of Geophysics and Engineering, 6, 279-287. doi: 10.1088/1742-2132/6/3/007.

Yager, J., 1994. Speleonectes gironensis, new species (Remipedia: Speleonectidae), from anchialine caves in Cuba, with remarks on biogeography and ecology. Journal of Crustacean Biology, 14, 752-762.

Yılmaz, I., 2001. Gypsum/anhydrite: some engineering problems. Bulletin of Engineering Geology and the Environment, 60, 227-230. doi: 10.1007/s100640000071.

Zelt, C., Smith, R., 1992. Seismic traveltime inversion for 2-D crustal velocity structure. Geophysical Journal International, 108, 16-34. doi: 10.1111/j.1365-246X.1992.tb00836.x.

Zeng, H., 1989. Estimation of the degree of polynomial fitted to gravity anomalies and its applications. Geophysical Prospecting, 37, 959-973. doi: 10.1111/j.1365-2478.1989.tb02242.x.

Zhdanov, M.S., 2002. Geophysical inverse theory and regularization problems. Elsevier.

Zhou, Q.Y., Matsui, H., Shimada, J., 2004. Characterization of the unsaturated zone around a cavity in fractured rocks using electrical resistivity tomography. Journal of Hydraulic Research, 42, 25-31. doi: 10.1080/00221680409500044.

Ziemkiewicz, P., Skousen, J.G., Brant, D., Sterner, P., Lovett, R., 1997. Acid mine drainage treatment with armored limestone in open limestone channels. Journal of Environmental Quality, 26, 1017-1024. doi: 10.2134/jeq1997.00472425002600040013x.

The Big Lake (Gruta de las Maravillas)
Photo authors: Love the Frame